DISSERTATION

ENABLING AND UNDERSTANDING LOW-TEMPERATURE KINETIC PATHWAYS IN SOLID-STATE METATHESIS REACTIONS

Submitted by

Paul Kendrick Todd

Department of Chemistry

In partial fulfillment of the requirements

For the Degree of Doctor of Philosophy

Colorado State University

Fort Collins, Colorado

Spring 2020

Doctoral Committee:

Advisor: James Neilson

Rick Finke
Amy Prieto
Chuck Henry
Kaka Ma

Copyright by Paul Kendrick Todd 2020

All Rights Reserved

ABSTRACT

ENABLING AND UNDERSTANDING LOW-TEMPERATURE KINETIC PATHWAYS IN SOLID-STATE METATHESIS REACTIONS

For the kinetic pathway to influence the outcome of a solid-state reaction, diffusion barriers must be lowered or circumvented through low-temperature chemistry. Traditional ceramic synthesis use high temperatures to overcome diffusion, yet they result in the thermodynamically stable product. If the desired product lies higher in energy, they are unattainable at such temperatures. Extrinsic parameters, like pressure, can be used to change the stability of products (kinetic trapping), yet require extreme conditions. Another strategy involves kinetically controlling the energy barriers of the reaction to select for a given product. Here, we use solid-state metathesis reactions to understand and control kinetic pathways in the formation of complex oxides and binary metal sulfides. Through simple changes to precursor composition, three unique polymorphs of yttrium manganese oxide are synthesized, two of which are metastable phases. Using *in situ* diagnostics, the reaction pathways are characterized to identity intermediates and the temperature regimes at which they react. Using this information we identify *why* different polymorphs form using different precursors. Additionally, small functional organosilicon molecules are shown to catalyze the formation of iron(II) sulfide using metathesis reactions. Here we show that the Si−O functional group stabilizes intermediate species along the pathway to avoid forming more stable intermediates. The result is higher yields of FeS_2 at lower temperatures

and times. The included chapters will hopefully better inform future solid-state chemists when exploring new composition spaces and reaction pathways.

ACKNOWLEDGEMENTS

Throughout my graduate studies, I have been blessed with funding to perform this research across the country. Specifically, I would like to acknowledge the National Science Foundation (DMR-1653863) and GENESIS: A Next Generation Synthesis Center, an Energy Frontier Research Center funded by the U.S. Department of Energy, Office of Science, Basic Energy Sciences under Award Number DE-SC0019212. Theoretical calculations completed in this research used resources of the National Energy Research Scientific Computing Center (NERSC), a U.S. Department of Energy Office of Science User Facility operated under Contract No. DE-AC02-05CH11231. This research used resources at beamline 28-ID-2 of the National Synchrotron Light Source II, a U.S. Department of Energy (DOE) Office of Science User Facility operated for the DOE Office of Science by Brookhaven National Laboratory under Contract No. DE-SC0012704. Research was performed at Oak Ridge National Laboratory (ORNL), managed by UT Battelle, LLC for the U.S. Department of Energy (DOE) under contract DE-AC05-00OR22725. A portion of this research used resources at the Spallation Neutron Source a DOE Office of Science User Facility operated by the Oak Ridge National Laboratory.

There are so many individuals that have shaped the person I am today that it will be hard to keep this short. My journey to pursue chemistry was far from normal and I would like to thank a few teachers that really inspired me. First, I want to thank my advisor Jamie for being such a great teacher and mentor. To describe myself as stubborn is lenient and I appreciate all of the patience that Jamie has had in teaching me about chemistry and about being a professional scientist. I really appreciate how Jamie enabled self-motivation

and discovery through being in the lab. I never felt like he was over my shoulder at any point in my time at CSU. Well, may be when I needed to write more papers but other than that he was always encouraging me to explore new ideas and reactions. I hope he always remembers to stay pitted.

I would also like to thank some mentors at Colorado College where I really discovered a love for chemistry. To Dr. Murphy Brasuel, thank you for taking me on as a mentee when I was really lost. Your love for that Chemistry Department is inspiring. To Dr. Nate Bower, thank you for the conversations about life choices and . You were an inspiration for pursuing this PhD. To Dr. Sally Meyer, thank you for helping me find jobs and for generally treating me like a friend. You really made me feel like I was apart of a family at CC. I would also like to thank my high school chemistry teacher Dr. Igor Stefanic for making it seem cool to be a chemist. This is mostly a joke but he was an ex-sniper in the Croatian military that was also an expert swordsman who dabbled in chemistry.

To my all of my lab mates, thank you for all the support and help along the way. In particular, I would like to thank Dr. Andrew Martinolich for the "hard love" when I first joined the lab. You taught me to always keep running reactions. To Dr. Annalise Maughan, thank you for being the best lab Mom and for always inspiring me to make better figures/presentations. To Eve Mozur, thank you for being my twin and coming into the Neilson world together. To Dr. Iain Oswald, thank you for your friendship and skills in making a boat load of precursors for beam time. To Dr. Allison Wustrow, thank you for making sure my project stays alive and reaches new heights. I would also like to thank two amazing undergraduate researchers, Erik Rognerud and Antoinette Smith. A big THANK YOU to everyone who helped me on crazy beamline experiments. Specifically, Andy, Chris

Rom (x2), Allison, and Thinh Tran. These experiments will be forever seared into my brain.

I would like to give a special acknowledgement to all of the staff at DOE User Facilities. Specifically, I would like to thank Dr. Andrey Yakovenko, Dr. Wenqian Wu, Dr. Kamila Wiaderek, Dr. Olaf Borkiewicz, Dr. Kevin Beyer, and Dr. Dan Olds. All of these people have saved the day on numerous experiments. To the GENESIS team, I would like to thank many collaborators including Dr. Rebecca McAuliffe, Matthew McDermott, Dr. Tim Liu, and Michelle Beauvais. To Dr. Karena Chapman, thank you for being a superstar and always helping me out, especially at 3AM when I break your instrument! Thank you to Dr. John Parise, Dr. Peter Khalifah, Dr. Peter Chupas, and Dr. Simon Billinge for great discussion along the way. You all taught me the beauty of collaboration and the power of combined resources for science.

My friends have been so supportive though this whole process. Thank you to my chemistry family for teaching me the importance of work intermissions and family dinners. To all of my ski and bike partners, thank you for the escape into the mountains. It is one of the most important parts of who I am. To Brendan, thank you for always being there and supporting my pursuit of science. Also, thank you for trying to get me to talk about my science. To Max and Amy, thank you so much for being the best roommates. Your friendship has meant so much to me. To Tol-by and Blaque, thank you for being great roommates and always watching anime with me. To Kyle and Dana, thank you for teaching me so much about life and gardening.

My family has been through the thick and thin with me and I will always love them. Thank you to my parents, for always supporting me and allowing me to pursue something

so foreign to them. You both have been instrumental in shaping the person I am today. Mom, thank you for being yourself, ALWAYS, and for teaching me to lead by example. Dad, thank you for being my role model and teaching me the importance of family and responsibility. To my brother, you are my best friend and I love you. Thanks for always supporting me. To my sister and her family, thank you for allowing me to be apart of raising your children. I hope to one day have as beautiful of a family as you do.

Finally, I want to acknowledge my amazing partner Kelen. I love you. Thank you for loving me and helping me understand what I am capable of. I love the little family we have and it means the world to me to come home and be with you, Momo and Sydney. Your creativity and joy inspire me daily and bring me out from the dark places when I am down. I am excited for our future together and building a forever home with you.

TABLE OF CONTENTS

ABSTRACT ii
ACKNOWLEDGEMENTS iv
LIST OF FIGURES x
1 Introduction 1
2 Selective formation of yttrium manganese oxides through kinetically competent assisted metathesis reactions 13
2.1 Introduction 14
2.2 Results and Discussion 16
2.3 Conclusions 22
2.4 Methods 23
3 Yttrium manganese oxide phase stability and selectivity using lithium carbonate assisted metathesis reactions 26
3.1 Author Contributions 27
3.2 Introduction 27
3.3 Methods 30
3.4 Results 33
3.5 Discussion 43
3.6 Conclusion 48
4 Sodium catalyzed and selective synthesis of "metastable" $Y_2Mn_2O_7$ 49
4.1 Author Contributions 50
4.2 Introduction 50
4.3 Methods 52
4.4 Results 56
4.5 Discussion 65
4.6 Conclusion 68
5 Low temperature synthesis of $YMnO_3$ via defect accommodating intermediates . . 69
5.1 Author Contributions 70
5.2 Introduction 70
5.3 Methods 73
5.3.1 Precursor Synthesis 73
5.3.2 *Ex situ* reactions 75
5.3.3 *Ex post facto* SXRD reactions 75
5.3.4 *In situ* NPD reactions 76
5.3.5 *In situ* SXRD reactions 77
5.3.6 Rietveld refinements 78
5.3.7 Computational methods 78
5.4 Results 81
5.5 Discussion 91
5.6 Conclusions 99
6 Catalytic behavior of hexaphenyldisiloxane in the synthesis of pyrite FeS_2 101
6.1 Author Contributions 102

6.2 Introduction . . . 102
6.3 Materials and Methods . . . 104
6.4 Results and Discussion . . . 107
6.5 Conclusions . . . 118
7 Outlook and Proposed Future Directions . . . 120
7.1 Exploring selectivity in yttrium iron oxides: a reversal of yttrium manganese oxide phase stability . . . 120
7.2 Using chemometrics to enhance material discovery: increasing the PhD to *in situ* SXRD dataset ratio . . . 121
7.3 Evaluating the role of organosilane molecules in other metathesis systems . 123
7.4 Multi-modal *in situ* characterization of metathesis reactions . . . 125
8 Bibliography . . . 128
A Appendix . . . 155
A.1 Assisted Metathesis Control Reactions . . . 155
A.2 Thermochemical Calculations . . . 175
A.3 Ternary Metathesis Control Reactions . . . 178
A.4 Binary Metathesis Control Reactions . . . 187

LIST OF FIGURES

1.1 Schematic illustrating how the spectating alkali cation changes the observed products in assisted metathesis reactions. 9

2.1 PXRD patterns and crystal structures of products obtained from Mn_2O_3+2 YCl_3+ A_2CO_3 using different alkali cations: (a) Li_2CO_3: $Pbnm$ $YMnO_3$, 850 °C (b) Na_2CO_3: $Fd\bar{3}m$ $Y_2Mn_2O_7$, 650 °C (c) K_2CO_3: $P6_3cm$ $YMnO_3$ $T >$850 °C. In the structures: oxygen: orange, manganese: navy and yttrium: teal. Tick marks denote expected peak positions. 16
2.2 Temperature dependent magnetic susceptibility of (a) o-$YMnO_3$ and (b) $Y_2Mn_2O_7$ showing both ZFC and FC measurements. Curie Weiss analyses of the linear portion of the inverse magnetic susceptibility after correcting for temperature dependent paramagnetism ($\chi_0 = 10^{-6}$ Oe mol Mn emu^{-1}) are shown in orange. 19
2.3 SEM images of the products from assisted metathesis reactions: (a,b) o-$YMnO_3$ from Eq.1; (c) NaCl and $Y_2Mn_2O_7$ from Eq. 2; (d) $Y_2Mn_2O_7$ from Eq. 2. (a,c) show the products before washing with 0.6M HCl while (b,d) show the products after washing with 0.6M HCl. 22

3.1 *In situ* PXRD results of the reaction: $Mn_2O_3 + 2.2\,YCl_3 \cdot 6\,H_2O + 3\,Li_2CO_3$ under flowing oxygen. (a) Powder diffraction patterns as a function of temperature (b) Weighted scale factor of each phase during the reaction pathway from Rietveld refinement as a function of temperature. Both (a) and (b) are separated into three reactive zones: I Reactivity of yttrium chloride and formation of YOCl; II Oxygenation of YOCl and formation of $LiMnO_2$; III Melting of LiCl and $YMnO_3$ formation. Each sub-panel in (b) is separated by cation for visualization purposes with the gray lines denoting phases with other cations. 34
3.2 (a) mass spectrometry and (b) thermogravimetric analysis on the reaction: $Mn_2O_3 + 2\,YCl_3 \cdot 6\,H_2O + 3\,Li_2CO_3$. The reaction was heated at 10 °C/min to 850 °C with reaction zones I, II, and III presented for comparison to Figure 1. The theoretical mass loss from the reaction are shown as solid black lines in (b). Release of H_2O and CO_2 vapor during the reaction matches the reactivity observed in the *in situ* SXRD data. 35
3.3 *In situ* PXRD results of the reaction: $Mn_2O_3 + 2.2\,YCl_3 \cdot 6\,H_2O + 3\,Li_2CO_3$ under flowing helium. (a) Powder diffraction patterns as a function of temperature (b) Weighted scale factor of each phase during the reaction pathway from Rietveld refinement as a function of temperature. Both (a) and (b) are separated into three reactive zones: I Reactivity of yttrium chloride and formation of YOCl; II Oxidation of YOCl and formation of $LiMnO_2$; III Melting of LiCl and $YMnO_3$ formation. Each sub-panel in (b) is separated by cation for visualization purposes with the gray lines denoting phases with other cations. Quotation marks denote that Mn_3O_4 is poorly resolved from $Li_2Mn_2O_4$ in our refinement. . 37

3.4 (a) $YMnO_3$ products calculated from $ex\ situ$ assisted metathesis reactions at 850 °C (Eq 1.) under flowing argon (green) versus oxygen (orange) at various reaction times. Open symbols represent the calculated phase fraction of o-$YMnO_{3+\delta}$ while solid symbols show the phase fraction of h-$YMnO_3$. (b) Calculated volumes of o-$YMnO_{3+\delta}$ products from the reactions in (a). The reactions performed under flowing oxygen show a decrease in reaction volume as a function of time. 39

3.5 (a) $YMnO_3$ products calculated from $ex\ situ$ assisted metathesis reactions at various temperatures and oxygen partial pressures (Eq 1.). Each pie chart denotes the relative molar phase fraction of each $YMnO_3$ phase as calculated from Rietveld refinements after 24 h reactions: navy = h-$YMnO_3$, red = o-$YMnO_3$, and orange = o-$YMnO_{3+\delta}$. Shaded regions illustrate the qualitative change in phase formation under the presented conditions. At high temperatures, h-$YMnO_3$ dominates. At high oxygen partial pressures and temperatures below 850 °C the over-oxidized o-$YMnO_{3+\delta}$ forms selectively. At temperatures below 750 °C and lower oxygen partial pressures, a mixture of h-$YMnO_3$ and o-$YMnO_3$ are observed. 40

3.6 Comparison of $ex\ situ$ reactions (a) $LiMnO_2 + YOCl$, 500 °C, 24 h, < 10 mTorr; and (b) $Mn_2O_3 + 2.2\,YCl_3 \cdot 6\,H_2O + 3\,Li_2CO_3$, 850 °C, 24 h, Flowing O_2. Both reactions were heated at 10 °C/min. The calculated X-ray diffraction pattern is provided for o-$YMnO_3$ from the ICSD. The product in (a) matches the stoichiometric o-$YMnO_3$ while the pattern in (b) shows differences in peak position and shape for the o-$YMnO_{3+\delta}$ phase. 41

3.7 Comparison of $ex\ situ$ reactions from the reaction: $Y_2O_3 + Mn_2O_3 \xrightarrow{6LiCl}$ at (a) 550 °C (b) 600 °C (c) 850 °C. All reactions were heated at 10 °C/min to the reaction temperatrue for 24 h under vacuum in a sealed quartz ampule. Reported structures from ICSD are denoted as tick marks. Main reflections for $LiCl \cdot H_2O$: $+$ and LiCl: $*$ are present but not identified using tick marks. 42

3.8 Comparison of the structures for the proposed intermediate reactions in Equations 5 & 6 as derived from characterization of the assisted metathesis reaction pathway. Yttrium-containing intermediates were derived from characterizing the the assisted metathesis reaction pathways (Fig. 3.1 & 3.3). From $ex\ situ$ control reactions the ternary metathesis reaction ($YOCl + LiMnO_2$) is the kinetically controlling reaction pathway and, while still a competent reaction pathway, the reaction from binary oxides in a lithium chloride flux ($Y_2O_3 + Mn_2O_3 \xrightarrow{6LiCl}$) requires longer reaction times to arrive at the orthorhombic $YMnO_3$ product. 46

4.1 Schematic illustrating the hypothesized mechanism to form $Y_2Mn_2O_7$ catalyzed by sodium via the Na_xMnO_2 intermediate. The reactive [MnO_2] species produced in the elementary steps in Eqn. 4.9a-4.9d react directly with small particles of Y_2O_3 at the reaction interface. 53

4.2 *In situ* PXRD data as a function of time for the reaction: $Mn_2O_3 + 2\,YCl_3 + 3\,Na_2CO_3 + \frac{1}{2}\,O_2 \longrightarrow Y_2Mn_2O_7 + 6\,NaCl + 3\,CO_2$ under flowing oxygen. The reaction is separated by a dotted line for (a) heating at 10 °C/min to 650°C and (b) dwelling at 650 °C for 60 min. 57
4.3 Calculated Weighted Scale Factor phase present from the data in Figure 1. Each vertical panel is separated by reaction schedule: (a-c) heating at 10 °C/min to 650 °C and (d-f) dwelling at 650 °C for 60 min. Horizontally, the sequential refinement is separated by cation for visualization: (a,d). Sodium, (b,e). Manganese , and (c,f). Yttrium. The gray lines denote all other phases present during the reaction. The shaded region, i.,ii., and iii., correspond to trajectories highlighted in Figure 4.4. 58
4.4 f^* diagram of atomic coordinates calculated from Rietveld refinement of $Cmcm$ Na_xMnO_2 in which each axis denotes a crystallographic Wyckoff atom position within the lattice. For reference, calculated trajectories that correspond to the different stoichiometries of Na_xMnO_2 are provided as black lines. The color bar in the figure follows the lifetime of the Na_xMnO_2 intermediate in the assisted metathesis reaction presented in Figure 4.3 with highlighted trajectories (i-iii) reflecting shaded regions in Figure 4.3(i-iii). The diameter of each circle mirrors the calculated Weighted Scale Factor in Figure 4.3 for Na_xMnO_2. The structure of $Cmcm$ Na_xMnO_2 is shown with Wyckoff atom sites labeled. 60
4.5 Predominance phase diagram for material phases in the Y-Mn-O chemical system as a function of oxygen and yttrium chemical potentials, μ_O and μ_Y. $Y_2Mn_2O_7$ appears to be preferentially synthesized under high oxygen chemical potentials. The phase diagram was calculated using DFT thermochemistry data on the Materials Project[1] and the NIST-JANAF thermochemical tables.[2] The entropic temperature contribution towards phase stability at 900 K is estimated by the Gibbs descriptor from Bartel et al.[3] 64

5.1 Calculated weight fractions of crystalline materials at different reaction temperatures reveals the reaction pathway of the ternary metathesis reaction, $LiMnO_2 + YOCl \longrightarrow LiCl + YMnO_3$ when changing the $LiMnO_2$ precursor. Each row highlights the structure of $LiMnO_2$ precursor and the reaction pathway as a function of temperature: (a-c) m-$LiMnO_2$ ($C2/m$), (d-f) o-$LiMnO_2$ ($Pmnm$) and (g-i) t-$LiMnO_2$ ($I4_1/amd$). Each column shows the phase fractions (Weight Percent) of crystalline phases present along the pathway. For clarity, the presented phases are separated into the reactants, $LiMnO_2$ (green square) and t-YOCl (red circle) (a,d,g); the intermediates, Y_3O_4Cl (burgundy cross), r-YOCl (rose x), t′-spinel (blue triangle) and c′-spinel (aqua triangle) (b,e,h); and the products LiCl (goldenrod square), h$-YMnO_3$ (purple hexagon) and o-$YMnO_3$ (lilac cross) (c,f,i). 82
5.2 Occupancy of crystallographic sites that correspond to lithium-rich (left), manganese-rich (center) and oxygen (right) site within the crystal lattice for the o-$LiMnO_2$ (red) m-$LiMnO_2$ (blue) and t-$LiMnO_2$ (green). As all occupancies were refined together with the scale factor for the phase, values should be considered relative rather than absolute. 84

5.3 Diffraction patterns that illustrate the presence of two unique manganese-containing spinel intermediates in these ternary metathesis reactions: a) SXRD patterns of o-$LiMnO_2$+YOCl at 500 °C and b) NPD pattern of t-$LiMnO_2$+YOCl at 400°C. The contributions of each lithium manganese oxide phase are highlighted: $LiMnO_2$ precursor (top), t′-spinel (second from top), and c′-spinel (third from top). The overall fit from Rietveld refinement (bottom) also contains t-YOCl, r-YOCl, Y_3O_4Cl and LiCl (red) along with a difference pattern (gray). 85
5.4 Structural relationship between a) cubic $Fd\bar{3}m$ spinel and b) tetragonal $I4_1/amd$ spinel. The geometric relationship between unit cells is shown the Wyckoff positions highlighted. The tetrahedral cation sites ($(8c)_c$ and $(4c)_t$), octahedral cation sites ($(16d)_c$ and $(8c)_t$), and oxygen site ($(32e)_c$ and $(16h)_t$) are highighted. Finally, the local [MnO_6] octahedra are shown for each structure with the axial and equatorial bond distances labeled to highlight the Jahn-Teller distortion in tetragonal spinels 86
5.5 Calculated fraction of reaction products taken from laboratory PXRD data of *ex situ* ternary metathesis reactions ($LiMnO_2$ + YOCl) at 550 °C comparing short and long duration reactions. The results are separated by $LiMnO_2$ precursor: a) monoclinic ($C2/m$), b) orthorhombic ($Pmnm$) and c) tetragonal ($I4_1/amd$). . . 88
5.6 Calculated fraction of reaction products taken from laboratory PXRD data of *ex situ* ternary metathesis reactions ($LiMnO_2$ + YOCl) at varied temperatures and reaction times. Subplots (a-c) show the progression of reaction products when starting with monoclinic ($C2/m$) m-$LiMnO_2$ at (a) 500 °C, (b) 550 °C, and (c) 600 °C. As the temperature increases, the hexagonal $YMnO_3$ product selectivity increases over the orthorhombic product. 89
5.7 DFT-calculated phase diagram of cation-deficient $YMnO_3$ polymorphs with respect to temperature, T, and a fixed, equal concentration of cation (Y,Mn) vacancies, x in $Y_{1-x}Mn_{1-x}O_3$. All structures are initialized with AFM magnetic orderings, and the Fermi energy of electrons is fixed at $E_F = 1.0$ eV. 92

6.1 PXRD results with Rietveld refinements from metathesis reactions of $FeCl_2$ + Na_2S_2 at 150 °C for 24h under Argon: Top to Bottom: Neat reaction, 12mol% Ph_3SiCl, 13mol% Ph_3SiOH, 4.5 $(C_6H_5)_6Si_2O$. + denotes (206) reflection of Fe_7S_8 107
6.2 (a) PXRD results with Rietveld refinements from metathesis reactions of $FeCl_2$ and Na_2S_2 at 150 °C for 24h under Argon: varying mol% $(C_6H_5)_6Si_2O$; (+) denote Na_2S_4 (*) denote Na_2S_2. (b) Mole fraction from Rietveld refinements of PXRD data as a result of varying the mol% concentration of $(C_6H_5)_6Si_2O$. The inset shows reaction pellets of 4.5 mol% $(C_6H_5)_6Si_2O$ and 0.5 mol% metathesis pellets with yellow sulfur condensate at 0.5 mol%. 109
6.3 *in situ* SXRD results of the reaction Na_2S_2+$FeCl_2$ a) using 4.5 mol% $(C_6H_5)_6Si_2O$ and b) with no molecular additive heating at 10 °C/min to 300 °C. Differential Scanning Calorimetry plots are appended to a) and b) to compare crystallization exotherms. Dotted lines denote the start and stop of reactive zones in the diffraction data. The reaction proceeds from precursors reactive intermediates, and finally products. 111

6.4 PXRD results from the reaction: $Na_2S_2 + FeCl_2$ at 150°C for 24hr with various small molecule additives. The reflections for Na_2S_2, FeS_2, and NaCl are shown as tick marks above and reflections are highlighted by colored rectangles for comparison. All concentrations are at 10 wt% of each molecule. 114
6.5 ^1H NMR spectra of relevant $(C_6H_5)_3SiOH$ control reactions. All reactions were heated at 150°C for 24hr. (a) $(C_6H_5)_3SiOH$ standard, $(C_6H_5)_3SiOH$ decomposition after heating, $(C_6H_5)_3SiOH$ washes from the reaction $Na_2S_2 + FeCl_2$. (b): $(C_6H_5)_3SiOH$ and $(C_6H_5)_6Si_2O$ standards as compared to $(C_6H_5)_3SiOH$ reactions with each reaction precursor. 115

7.1 Synchrotron X-ray diffraction patterns for the ternary metathesis reaction: $LiMnO_2$+ YOCl $\longrightarrow$ $YMnO_3$ + LiCl collected in situ and the corresponding Rietveld refinements of the NMF-derived components (left). The corresponding the weight ratios associated with the 5 NMF components as horizontal bar charts, track the state of the metathesis reaction. 122
7.2 Mole phase fraction calculated from Rietveld refinements of PXRD data in the reaction $CuCl_2 + Na_2Se_2$ with varying mol% $[(C_6H_5)_6Si_2O]$ NaCl phase fraction maintains a range between 65-75mol% phase fraction and is omitted to clarify the copper selenide products. 124
7.3 Comparison of Synchrotron X-ray diffraction patterns (LEFT), Pair Distribution Function analysis (CENTER), and DRIFTS IR Sepctroscopy (RIGHT) in the metathesis reaction: Na_2S_2+$FeCl_2$ $\xrightarrow{H_2O}$ FeS_2+2 NaCl. The dotted lines describe different labeled events during the reaction. 126
7.4 Quantitative phase identification from SXRD and PDF of the metathesis reaction: $Na_2S_2 + FeCl_2$ $\xrightarrow{H_2O}$ $FeS_2 + 2\,NaCl$. The relevant intermediates are labeled by color. 127

A.1 PXRD results from the reaction: Mn_2O_3 + Y_2O_3 at 650 °C and 850 °C. Reactivity is not observed until 850 °C and the product formed is YMn_2O_5, suggesting Y_2O_3 is less reactive than Mn_2O_3 at 850 °C 155
A.2 PXRD results from assisted metathesis reactions using Li_2CO_3 showing the effect of temperature on the reaction products. At temperatures lower than 550 °C no $Y-Mn-O$ phases are present, between 550-850 °C o-$YMnO_3$ is the predominate product, and at 950°C h-$YMnO_3$ is the predominate product. 157
A.3 PXRD results from assisted metathesis reactions using Li_2CO_3 showing the effect of excess hydrated yttrium chloride on the reaction products. As the yttrium chloride excess increases, the YMn_2O_5 brownmillerite phase decreases in intensity.158
A.4 Neutron diffraction data and laboratory PXRD data for o-$YMnO_3$. Rietveld co-refinements were performed concomitantly against neutron and X-ray diffraction data to confirm the structure and composition of the metastable phases. Tick marks above denote the expected peak positions. 159
A.5 ATR-IR spectroscopy on washed products of the assisted metathesis reactions using (a) Li_2CO_3: o-$YMnO_3$ (Eq.2) (b) Na_2CO_3: $Y_2Mn_2O_7$ (Eq.3). Asymmetric stretching modes (1500-1400cm^{-1}) and out of plane bending vibrations (850cm^{-1}) due to CO_3^{2-} are not present in the assisted metathesis products. . . 160

A.6 Magnetization measurements as a function of applied field for (a) o-$YMnO_3$ and (b) $Y_2Mn_2O_7$ at 2 K and 300 K. Both samples display magnetization consistent with ferromagnetic, Brillion-like field dependence, with o-$YMnO_3$ having slight hysteresis. 160
A.7 PXRD results from control reactions on washed o-$YMnO_3$ under various environments and times. Under oxidizing conditions, the o-$YMnO_{3+\delta}$ is stable while under flowing argon, the o-$YMnO_{3+\delta}$ converts to o-$YMnO_3$ and h-$YMnO_3$. In a sealed ampoule ($<$ 5 mTorr) for 30d the product is o-$YMnO_{3+\delta}$ If the assisted metathesis reaction, $Mn_2O_3 + 2.2\,YCl_3 \cdot 6\,H_2O + 3\,Li_2CO_3$, is heated to 850 °C for 7 days, the o-$YMnO_{3+\delta}$ forms and persists. 161
A.8 PXRD results from the assisted metathesis reactions using sodium carbonate illustrating the effect of time on the reaction products at 650 °C. Heating the reaction for longer time periods results in decomposition of the $Y_2Mn_2O_7$ to Mn_2O_3 and Y_2O_3. NaCl is present in both reactions, which suggests that it does not stabilize the metastable pyrochlore. 162
A.9 Neutron diffraction data and laboratory PXRD data for $Y_2Mn_2O_7$. Rietveld co-refinements were performed concomitantly against both neutrons and X-ray diffraction data to confirm the structure and composition of the $Y_2Mn_2O_7$. Tick marks denote the expected peak positions. 163
A.10 SEM-EDS analysis of Li_2CO_3 assisted reaction at 850 °C and yttrium chloride hexahydrate precursor to form o-$YMnO_3$ product. Color maps show atomic distribution while the table shows the corresponding atom% from EDS. The percentage of carbon can be attributed to advantageous surface species 164
A.11 SEM-EDS analysis of Li_2CO_3 assisted reaction at 850 °C and yttrium chloride hexahydrate precursor. o-$YMnO_3$ product was washed with 0.6 M HCl prior to imaging. Color maps show atomic distribution while the table shows the corresponding atom% from EDS. The percentage of carbon can be attributed to advantageous surface species 165
A.12 SEM-EDS analysis of Na_2CO_3 assisted reaction at 650 °C and anhydrous yttrium chloride precursor to produce $Y_2Mn_2O_7$. Color maps show atomic distribution while the table shows the corresponding atom% from EDS. The percentage of carbon can be attributed to advantageous surface species 166
A.13 SEM-EDS analysis of Na_2CO_3 assisted reaction at 650 °C and anhydrous yttrium chloride precursor. $Y_2Mn_2O_7$ product was washed with 0.6 M HCl prior to imaging. Color maps show atomic distribution while the table shows the corresponding atom% from EDS. The percentage of carbon can be attributed to advantageous surface species 167
A.14 Structural parameters for the $Cmcm$ Na_xMnO_2 intermediate as a function of reaction time. Refined occupancies of each atomic site that were used in calculating the f_* ternary diagrams are shown on the right while Unit cell parameters for the orthorhombic cell are shown on the left.The colored regions (i,ii,iii) are taken from Figure 4.3 and Figure 4.4 168

A.15 Ternary f^* diagram of atomic coordinates calculated from Rietveld refinement of $Ia\overline{3}$ Y_2O_3. Each axis denotes atom identity and crystallographic Wyckoff position within the lattice. For reference, the calculated value of Y_2O_3 is provided. The color bar in the figure follows the lifetime of the Y_2O_3 intermediate in the assisted metathesis reaction presented in Figure 4.3. The diameter of each circle mirrors the calculated Weighted Scale Factor in Figure 4.3 for Y_2O_3. 169
A.16 The calculated size of the coherently diffracting domains of Y_2O_3 intermediates as calculated from the Scherrer equation with error bars using the Integral Breadth method for peak width. The colored regions (i,ii,iii) are taken from Figure 4.3 and Figure 4.4 170
A.17 Bar graphs representing the mole percent amounts of products calculated from $ex\ situ$ PXRD Rietveld refinements of the reaction: (a) $Mn_2O_3 + Y_2O_3 \xrightarrow{O_2}$ and (b) $2\,MnO_2 + Y_2O_3 \xrightarrow{O_2}$. The reactions were heated at 10 °C/min to 650 °C for 24, 72, and 128 hours under flowing oxygen. Each color bar is represented in the legend as a different product phase. 171
A.18 Bar graphs representing the mole percent amounts of products calculated from $ex\ situ$ PXRD Rietveld refinements of the reaction: (a) $Mn_2O_3 + Y_2O_3 \xrightarrow{6NaCl,O_2}$ and (b) $2\,MnO_2 + Y_2O_3 \xrightarrow{6NaCl,O_2}$. The reactions were heated at 10 °C/min to 650 °C for 24, 72, and 128 hours under flowing oxygen. Each color bar is represented in the legend as a different product phase. Mole fractions are presented after subtracting the contribution from NaCl for comparison. 172
A.19 Bar graphs representing the mole percent amounts of products calculated from $ex\ situ$ PXRD Rietveld refinements of $Y_2Mn_2O_7$. The reactions were heated at 10 °C/min to 650 °C for 24, 72, 128, and 336 hours under flowing oxygen. Each color bar is represented in the legend as a different calculated phase. . . . 172
A.20 PXRD results from the reaction: $C2/m$ $NaMnO_2 + YOCl \xrightarrow{O_2}$. The reaction was performed by heating at 10 °C/min to 650 °C and dwelling for 24 h. Raw data: black circles, Rietveld refinement: orange, background: green, difference: navy. Tick marks denote the majority phases and are highlighted by color and mole percent as calculated from Rietveld refinements. All other product mole percents are highlighted in black without tick marks. 173
A.21 PXRD results from the reaction: $Cmcm$ $Na_{0.7}MnO_2 + YOCl \xrightarrow{O_2}$. The reaction was performed by heating at 10 °C/min to 650 °C and dwelling for 24 h. Raw data: black circles, Rietveld refinement: orange, background: green, difference: navy. Tick marks denote the majority phases and are highlighted by color and mole percent as calculated from Rietveld refinements. All other product mole percents are highlighted in black without tick marks. 174
A.22 Calculated difference in reaction enthalpies ($\Delta\Delta$H) when changing the alkali carbonate precursor in the reaction: $3\,A_2CO_3 + 2\,YCl_3 + Mn_2O_3 \longrightarrow 6\,ACl + 2\,YMnO_3 + 3\,CO_2$.The difference is taken with respect to Li_2CO_3 assisted reactions. As the size of the alkali cation increases from lithium to potassium, the reaction enthalpy becomes more exothermic. 175

A.23 Predominance phase diagram for material phases in the Y-Mn-O chemical system as a function of oxygen and manganese chemical potentials, μ_O and μ_{Mn}. . 176
A.24 Predominance phase diagram for material phases in the Y-Mn-O chemical system as a function of manganese and yttrium chemical potentials, μ_{Mn} and μ_Y. . 177
A.25 Gibbs free energies and heat capacities as a function of temperature for $YMnO_3$ polymorphs 178
A.26 Comparison of calculated and experimental heat capacities for h-$YMnO_3$ ($P6_3cm$). Experimental heat capacity data is acquired from Satoh et al.[4] 179
A.27 Y, Mn vacancy formation energies as a function of Fermi energy for $YMnO_3$ polymorphs for different chemical potentials, μ_Y and μ_{Mn}. The dashed lines represent the valence band maximum (VBM) and conduction band minimum (CBM). (a) The upper bounds, and (b) the lower bounds, of the window of chemical potential stability of $YMnO_3$ as determined by simplexes in the Y-Mn-O phase diagram (0 K) constructed from the MP database. 180
A.28 Calculated phase stability of $YMnO_3$ polymorphs with respect to temperature and an equal concentration of cation (Y,Mn) vacancies, *x*. The phase diagram is constructed for all values of Fermi energy, E_F, within the band gap to show how the sensitivity of the phase boundary position with E_F. 181
A.29 Quantitative phase analysis of crystalline materials calculated from synchrotron X-ray diffraction experiments of the ternary metathesis reaction $LiMnO_2$+YOCl $\longrightarrow$ $YMnO_3$ + LiCl when starting from monoclinic ($C2/m$) $LiMnO_2$. Reactions were heated at 10 °C/min to 600 °C. Each row of subpanels presents a) precursors, b) intermediates, and c) products as calculated from Rietveld analysis. 182
A.30 Weighted scale factor of crystalline materials from neutron refinement at different reaction temperatures reveals the reaction pathway of the ternary metathesis reaction, $LiMnO_2$+YOCl $\longrightarrow$ LiCl+$YMnO_3$. Each row of subpanels is from a single precursor: (a-c) monoclinic ($C2/m$), (d-f) orthorhombic ($Pmnm$) and(g-i) tetragonal [($I4_1/amd$)]. Each column highlights phase fractions containing a specific cation to provide clarity with many overlapping phases: (a,d,g) Lithium, (b,e,h) Manganese, (c,f,i) Yttrium. 183
A.31 The contributions of the manganese containing phases $LiMnO_2$(top), t′-spinel (second from top), and c′-spinel (third from top) are overlayed on the pattern. The overall fit (bottom) also contains t-YOCl, r-YOCl, Y_3O_4Cl and LiCl (red) along with a difference pattern (gray) for reactions of o-$LiMnO_2$ (SXRD (a), NPD (b)),m-$LiMnO_2$ (SXRD (c), NPD (d)), and t-$LiMnO_2$ (SXRD (e), NPD (f)). . 185
A.32 Ratio of the c and a lattice parameters for (a) c′-spinel and (b) t′-spinel from X-ray diffraction patterns used in Figure 5.1. Data points are separated by $LiMnO_2$ precursor: o-$LiMnO_2$ (red squares), m-$LiMnO_2$ (blue circles) and t-$LiMnO_2$ (green triangles). 186
A.33 ^{1}H NMR spectra of the phenyl region in the $(C_6H_5)_6Si_2O$ standard and a wash from the metathesis reaction Na_2S_2 + $FeCl_2$ with 4.5mol% $(C_6H_5)_6Si_2O$. Deuterated methylene chloride (CD_2Cl_2) was used as the solvent 189

A.34 Vapor transport reaction to test the effect of water vapor from the decomposition/polymerization of $(C_6H_5)_3SiOH$ on the metathesis reaction: $Na_2S_2 + FeCl_2 \longrightarrow FeS_2 + 2\,NaCl$. a) Experimental set-up showing the separation of each reaction physically in a sealed ampule. b) PXRD pattern of reaction products performed under polyimide tape. 191
A.35 Differential Scanning Calorimetry results from the reaction $Na_2S_2 + FeCl_2$ with (a) no additive and (b) 4.5mol% $(C_6H_5)_6Si_2O$. Heating rate was changed from 1 °C/min to 10 °C/min. 191

1. Introduction

In molecular chemistry, the reaction mechanism is foundational to the synthesis of new molecules. Understanding the elementary steps along a pathway from precursor to product allows for more control of the reaction kinetics, which ultimately increase the number of possible outcomes. In solid-state inorganic chemistry, reactions are limited by diffusion, where high temperatures and long reaction times are requisite for the reaction to proceed. If the reaction pathway is considered in these traditional ceramic syntheses, the energy barrier of diffusion is often the largest.[5] Therefore, one typically runs a reaction with enough thermal energy to sample the full potential energy surface and the product of these reactions will equilibrate at the global energy minimum under the thermodynamic control. If additional products exist at higher positions on the global energy landscape, alternate pathways must be developed that selectively overcome or circumvent the barrier of diffusion.[6] Only then can kinetics play a role in the outcome of the reaction. Thus, there is a demand to develop low-temperature solid-state reactions where kinetics determines product selectivity. To address this demand, we must first be able to predict new functional materials that are *synthetically accessible*, or identify synthetic targets that lie close in energy to the global minimum. These kinetically stable, or metastable, products will have the highest probability for success.

Theory provides a powerful tool for predicting new materials. In fact, computational theory has led to the prediction of millions of unexplored inorganic materials, yet many of these predictions focus on a desired property and not on synthetic accessibility.[7] While

identifying functional materials is important, it is also important to address predictions on which products are accessible using our current synthetic techniques. There are examples of synthetically-realized materials based solely on structure-property predictions,[8] yet many there are orders of magnitude more of these predicted materials are most likely synthetically inaccessible due to their position on a particular free energy landscape.[9] Computational studies have begun working towards modeling the "synthesizability" of new inorganic materials,[3,10] but the focus remains on describing the thermodynamic range of the products' stability in relation to a thermodynamic energy ground-state.[11–13] While understanding the relative thermodynamic energetic position of a desired material is useful in accessing the probability of synthesizing a material,[14] current computational tools cannot predict synthetic variables as they relate to reaction kinetics, precursor competence, and non-equilibrium phase behavior.[3] Also, there is a growing list of stable compounds previously thought to not exist or be unstable, owing to their decomposition under traditional synthesis conditions (e.g., $MgCr_2S_4$).[15] Thus, theory has begun to address where products lie on the global energy landscape as well as the widths of potential energy basins[16] yet we lack the requisite knowledge of available reaction pathways available to navigate this energy landscape. I propose that the first step to addressing this problem is to develop low-temperature reactions where kinetic control determines product selectivity. Then, these reaction pathways can be studied using *in situ* diagnostics to identify the relevant steps along these kinetically controlled reaction pathways. This information will be used to inform future theory and synthesis.

A solid-state reaction pathway is dependent on the following steps: (1) precursors of a given stoichiometry diffuse across a solid-solid gradient to a reaction interface, (2) reaction

intermediates form of local composition to minimize their chemical potential, and (3) atoms rearrange at the reaction interface to nucleate the product phase.[17,18] Traditionally, the role of kinetics in solid-state chemistry has been used to describe reactions that are not fully equilibrated. Oftentimes, the state of the reaction is assessed by the homogeneity of the product. Traditional high-temperature ceramic syntheses often employ multiple steps of heating, mechanically grinding, and reheating to facilitate diffusion. Here the kinetics of the reaction impede the arrival at the desired product. While effective for reactions under thermodynamic control, these ceramic syntheses are crude for selectively synthesizing metastable materials.

Metastable phases can be kinetically trapped in solid-state synthesis using extrinsic parameters such as pressure (graphite vs. diamond). Changing the thermodynamic conditions can move the energy levels of desired products and quenching from high pressure traps the metastable product. The formation of glasses are another example of products that are in a kinetically trapped state where the reaction product is quenched from a liquid state. Manipulation of particle surface area is another way to kinetically trap different products. Titanium dioxide has three naturally occurring polymorphs that can be synthesized by manipulating the particle size. There, the thermodynamic stability of the product changes with the surface area of the particle.[19] In these examples of kinetic trapping, the energy levels of the products are manipulated then trapped, whereas kinetic control implies that the barriers along the reaction pathway can change.

In order to implement kinetic control in the solid-state, there is demand for reactions that have precursors that react at low-temperatures where kinetic energy barriers along the reaction pathway are manipulated synthetically to select for a given product.[20] One

way in which to lower diffusion barriers is using topotactic reactions, where a redox-active metal within a rigid structural motif (e.g., layers, channels) provides a scaffold for which more labile ions can be inserted or removed.[21] While the structure remains intact, the electronic properties of the material change, as the transition metal is oxidized or reduced.[22–27] This soft-chemistry approach enables tunable electronic properties in superconducting oxides,[28] dehydration reactions to metastable hexagonal MoO_3,[29,30] and labile anion removal/reduction reactions in the preparation of metastable $SrFeO_2$.[31] Furthermore, these topotactic reactions can be expanded to perform multi-step cation exchange reactions.[32–34]

Kinetically, these *chimie douce* reactions are limited by diffusion of a cation either into a specific lattice site or between layers of a material. Taking advantage of the topotactic similarities between reactant and product structures provides a rational approach in the synthesis of a desired structure. Here rigid structural units (e.g., layers, pillars, channels) and the choice of labile ion (Alkali cation, H_2O, H^+, O^{2-}) affects the structure, and therefore the properties, of the resulting final product.[21] The structure of a material can also inhibit a chemical reaction, as is the case in $LiAlO_2$ where lithium can only be replaced with cations such as H^+ in one of the three known polymorphs.[35] In battery electrodes, the starting polymorph structure is critical in controlling these topotactic pathways, affecting the voltage, accessible capacity, and lifetime of the device. It can also provide a starting point for a number of structural transitions, as is the case in the "devil's staircase" of $NaMoO_2$, which exhibits 13 unique structural transitions as sodium deintercalates.[36]

While these topotactic syntheses rely on a rigid structural framework, other examples enable product selectivity through fabrication of prenucleation clusters or oligomeric

species to arrive at different reaction products.[37,38] Here, the outcome of the reaction is determined by the composition and local structure of each cluster, which aggregate to yield the desired product.

Inorganic salts that melt at relatively low temperatures can be used as a reactive flux to increase diffusion. Alkali sulfides are commonly used not only as a molten flux, but also as a reactive source sulfur.[39] Alkali halide salts are commonly used in fluxes for single crystal growth[40] as they are relatively unreactive and their behavior in eutectic mixtures is well studied for fine temperature control. In more challenging syntheses, such as the preparation of metal nitrides, molten sodium has been shown to increase the solubility of diatomic nitrogen.[41] These flux environments also provide a hotbed for material discovery. Using *In situ* characterization techniques, like thermodiffraction, new potassium tin sulfide materials were discovered when monitoring the crystalline phases that emerged upon cooling a reactive potassium sulfide flux.[42]

Other strategies use weak Lewis acid or base additives like trioctylphosphine (TOP) or pyridine, as a source, solvent, and stabilizer for atom transfer in synthesizing transition metal phosphides and chalcogenides.[43,44] By isolating functional groups that can target specific structural transformations, tunable syntheses can be designed akin to retrosynthetic organic syntheses. For example, a CdO template can be converted to a Cu_xS product through step-wise cation/anion exchange reactions that incorporate specific molecular additives like $(CH_3)_3Si-(S/Se)$ and TOP to coordinate and transfer specific atoms into isolated cation/anion lattice sites.[32,33]

Another way to overcome diffusion is to reduce the length scales to the atomistic scale. Examples include thin film deposition techniques, where the composition of the product

can be finely tuned through layered deposition of individual atoms.[18,45] This modulated elemental approach can be used to precisely tune the product composition and can lead to exquisite control in the formation of complex ternary and multinary compounds,[46,47] as well as metastable phases[48,49] By annealing at low-temperatures, the reaction pathway becomes nucleation-limited, which can lead to metastable phase formation. This strategy has led to kinetic control in the synthesis of metastable phases in high temperature superconductors[50] and mechanistic understanding of the barriers of product nucleation.[48]

Kinetic control can also be accessible at low temperatures in solid-state metathesis reactions, or double ion exchange reactions. By tuning the initial reactant composition, solid-state reactions can be designed using the large enthalpic driving force to form the alkali-metal halide product to overcome diffusion activation barriers.[51,52] These metathesis reactions are particularly useful for synthesizing very refractory, or "ultra-hard", materials like transition metal borides,[53] nitrides,[54,55] and carbides[56] that may not be particularly accessible when using traditional ceramic methods from the elements. Oftentimes, metathesis reactions are used to target binary compositions, yet recent studies have expanded to target more complex materials including ternary nitrides,[57] ternary oxides,[58] hydroxyapatites,[59] and rare-earth nitridophosphates.[60] While most of these examples involve purely inorganic precursors, metathesis chemistry can also include the use of functional organic species as precursors such as alkylamides,[61] silylamides,[62] and thiosilanes[62] to target inorganic products. While the diversity of these reactions is endless, the utility of solid-state metathesis reactions is in their ability to proceed to completion at temperatures where kinetic control is possible.

Metathesis reactions proceed to completion at low temperatures and short reaction times, which affords an opportunity to study and control kinetic pathways in the solid-state. Canonical examples of solid-state metathesis reactions include the preparation of MoS_2, where the reaction between $MoCl_5 + \frac{5}{2} Na_2S$ proceeds through self-ignition or detonation, in part due to the large enthalpy of formation for the alkali halide byproduct.[63] Here the reaction proceeds through propagation and oftentimes reaches temperatures in excess of 1300 °C. This spike in temperature is useful in synthesizing refractory materials, yet the are too rapid to study *in situ*. Fortuitously, metathesis reactions need not propagate and can proceed to completion under mild reaction conditions, which is crucial if kinetic control is desired. The maximum adiabatic temperature of the internal system can be tuned through changes in composition (Hess's Law), correlated with the heat capacities of the precursors. By changing this adiabatic temperature, different kinetic pathways are observed. This had led to the identification of two extreme hypothetical reaction mechanisms: (1) a pathway that proceeds through direct ionic exchange and (2) the reductive recombination of the the elements at high temperatures.[64] Previous studies have identified that the non-propagating reactions can proceed through both elemental and ionic pathways depending on the targeted product.[65] Also, the reaction pathways can be kinetically controlled through simple changes to reaction preparation, such as grinding precursors in a humid atmosphere versus under inert conditions.[66] By kinetically controlling the reaction pathway, metastable polymorphs like superconducting pyrite $CuSe_2$ can be prepared at low-temperatures.[67] *In situ* identification of the reaction pathway in low-temperature metathesis reactions can also lead to targeted manipulation of the kinetic pathway, such as the use of functional molecules like triphenylphosphine to controllably shuttle anions to

synthesize metastable superconducting selenides.[68,69] Overall, these metathesis reactions provide a diverse set of potential reactions when targeting new or metastable materials.

This dissertation explores low-temperature kinetic pathway in solid-state metathesis reactions with the goal of controlling the outcome of a solid-state reaction simply by changing the steps by which the pathway proceeds. The following chapters details work on two different model systems where kinetic control is hypothesized to be possible. The first project (Ch. 2-5) details product selectivity of yttrium manganese oxide, including the formation of two metastable polymorphs. The second project (Ch. 6) describes the use of the role of functional organosilicon molecules in catalyzing iron(II) disulfide formation. Using *in situ* synchrotron X-ray diffraction (SXRD), the reaction pathway of each system is studied to understand the relevant crystalline intermediates that form and the temperature regimes at which they exist. $In\ situ$ X-ray diffraction provides a powerful characterization tool for analyzing these kinetic factors in solid-state inorganic synthesis.[6,70] Temperature-dependent diffraction experiments have been used in characterizing kinetic control in solids,[66] thin films,[46] polymorph metastability,[67] battery kinetics,[71] hydrothermal crystal growth,[72] and the discovery of new materials in flux-mediated synthesis.[42] Analysis of this information is used to understand how metastable phases form *in situ*, identify catalysts in solid-state reactions, and design new, low-temperature syntheses to increase selectivity in the solid-state.

The first project details product selectivity in the synthesis of different yttrium manganese oxide products using assisted metathesis reactions:

$$\mathrm{Mn_2O_3 + 2\,YCl_3 + 3\,A_2CO_3 \xrightarrow{O_2} YMnO_3 + 6\,ACl + 3\,CO_2,} \tag{1.1}$$

where A = Li, Na, and K. In Chapter 2, we demonstrate that assisted metathesis reactions provide selectivity in synthesizing three different Y-Mn-O products: hexagonal $YMnO_3$, metastable orthorhombic $YMnO_3$, and the metastable pyrochlore $Y_2Mn_2O_7$. Changing the nominally spectating alkali cation changes the reaction products (Figure 1.1). This observation is discussed in terms of the competence of the assisted metathesis precursors in forming reaction products at low temperatures and reaction times.

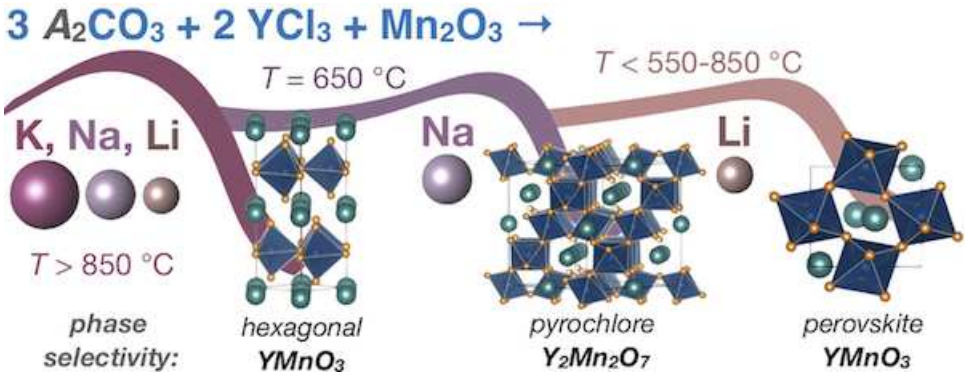


Figure 1.1: Schematic illustrating how the spectating alkali cation changes the observed products in assisted metathesis reactions.

In Chapters 3 & 4, we detail the reaction pathway of these assisted metathesis reactions in Eqn. 1.1 to better understand the product selectivity observed. Chapter 3 expands on the lithium carbonate assisted metathesis reactions which yield the over-oxidized perovskite $YMnO_{3+\delta}$. *In situ* SXRD reveals a reaction pathway that is kinetically controlled through the formation of ternary intermediates: $LiMnO_2$ and YOCl. The direct reaction between these ternary intermediates results in the synthesis of stoichiometric orthorhombic $YMnO_3$ at

relatively low-temperatures. Using these lithium carbonate assisted metathesis reactions, the phase stability of $YMnO_3$ is examined, as well. By changing the oxygen fugacity in these reactions, the $YMnO_3$ product and material properties change as a function of temperature.

In Chapter 4, we describe a novel reaction pathway in solid-state chemistry using sodium carbonate assisted metathesis reactions. Sodium selectively synthesizes the metastable pyrochlore $Y_2Mn_2O_7$. Here, we identify the key intermediates as Y_2O_3 and Na_xMnO_2, which react directly to form $Y_2Mn_2O_7$. Analysis of the composition of Na_xMnO_2 during formation and reaction reveals a pathway dependent on a series of defect reactions. These defect reactions are hypothesized to produce reactive species of $[MnO_2]$ that react directly with small particles of Y_2O_3. Here, we construct a series of pseudo-elementary reactions to illustrate how $[MnO_2]$ species are produced. We discover the presence of sodium catalyzes these defect reactions by anchoring the Na_xMnO_2 structure and increasing the selectivity of $Y_2Mn_2O_7$.

The ternary intermediates identified in assisted metathesis reactions can be used directly as precursors as well. Chapter 5 details these ternary metathesis reactions using lithium manganese oxide:

$$\mathrm{LiMnO_2 + YOCl \longrightarrow LiCl + YMnO_3,} \tag{1.2}$$

where three different $LiMnO_2$ precursors are studied. The three $LiMnO_2$ precursors have different starting structures based on the rock salt structure. Here, *in situ* X-ray diffraction and neutron diffraction are used to understand how the precursor structure and composi-

tion affect the reaction pathway. Regardless of polymorph structure, the reaction pathway proceeds through the same intermediates: r-YOCl, Y_3O_4Cl and two lithium manganese oxide spinels. The two spinels form as a result of a disproportionation Jahn Teller active Mn(III) octahedra, which results in a tetragonal Mn(II,III) spinel resembling Mn_3O_4 and a Mn(III,IV) spinel resembling $LiMn_2O_4$. Changing the $LiMnO_2$ precursors changes the temperatures at which the intermediates, and resulting products, form along the pathway. Monoclinic $C2/m$ $LiMnO_2$ is shown to demonstrate the lowest onset temperatures for $YMnO_3$ and the shortest reaction times. The stability of the orthorhombic $YMnO_3$ polymorphs is shown to be dependent on small concentrations of cation defects that result from the different oxidation states observed in the manganese-containing spinel intermediates. Over time, o-$YMnO_3$ is shown to be stable below 600 °C at relatively low defect concentrations. The differences in reactivity of each $LiMnO_2$ precursor suggest that increased product selectivity can be controlled through careful tuning of defects in these spinel intermediates. Then post-synthetic treatment at low-temperatures can be used to influence or remove these defects, resulting in new step-wise reactions of solids.

In Chapter Six, the focus shifts to the second project of this dissertation which describes the use of organosilicon molecules as a catalyst in preparing FeS_2 using solid-state metathesis reactions. Specifically, hexaphenyldisiloxane is shown to change the kinetics of the reaction pathway as a function of concentration. *In situ* SXRD reveals that hexaphenyldisiloxane reduces the barrier of diffusion by facilitating the formation of FeS_2 directly. Reactions with no molecular additive proceed through a diffusion-limited pathway, as evidenced by numerous intermediate phases in the SXRD data. Characterization of the hexaphenyldisiloxane *ex post facto* shows that the molecule remains unchanged, while the

Si−O functional group is responsible for increasing FeS_2 yields. We hypothesize that the polarizable silicon-oxygen bond stabilizes intermediate species as NaCl forms, thus preventing the formation of crystalline intermediates observed previously.[65,66]

The final chapter discusses future outlooks for the presented body of work. In the preceding chapters, model systems were identified and targeted using metathesis reactions. In the preparation of complex oxides, other compositions will be targeted using both assisted metathesis and ternary metathesis reactions. Even changing the transition metal from manganese to iron in YMO_3 has pronounced effect on the stability of the products. Understanding how the identity and stability of intermediates changes with transition metal will hopefully promote selectivity in other other complex oxides.The functionality of the organosilicon molecules also needs to be expanded to other metal chalcogenides to assess it's universal application as a catalyst. Here, we present initial results on copper selenides using hexaphenyldisiloxane. Finally, the rich amount of chemistry to be discovered in these *in situ* data sets is enormous, yet more efficient strategies are required to digest these large datasets. A brief look at a chemometric approach using multivariate analysis is discussed for identifying reaction intermediates and reactive temperature regimes.

2. Selective formation of yttrium manganese oxides through kinetically competent assisted metathesis reactions*

Overview

The synthesis of complex oxides requires high temperatures to overcome barriers imparted by solid-state diffusion; as such, reactions typically yield the most stable polymorph for a given composition. To synthesize new or metastable complex oxides, kinetically competent reactions with lower initial energy barriers must be devised to control the reaction pathway and resulting products. This contribution details the selective synthesis of different yttrium manganese oxides through assisted metathesis reactions between Mn_2O_3, YCl_3, and A_2CO_3 under flowing oxygen; where A = Li, Na, K. With lithium carbonate, the orthorhombic perovskite o-$YMnO_3$ (o-$YMnO_{3+\delta}$), forms over the temperature range of 550-850 °C. With sodium carbonate, the pyrochlore $Y_2Mn_2O_7$ forms at 650 °C. No apparent selectivity is observed with K_2CO_3, and all alkalis yields hexagonal $YMnO_3$ at $T > 950$ °C. The alkali species modify the reaction pathway and thus impart kinetic control in the formation of both phases.

*Substantial portions of this chapter have been reproduced with permission from P. K. Todd and J. R. Neilson, *J. Am. Chem. Soc.* **2019**, *141*, 1191–1195, reference 73, © 2019 the American Chemical Society

2.1. Introduction

Computational predictions for functional materials continue to outpace our ability to synthesize them.[74] Traditional ceramic syntheses use high temperatures to overcome the energy barriers of solid-state diffusion; as such, the high reaction temperatures permit the formation of the lowest energy product with little control over the reaction pathway.[5] Metastable products can be kinetically trapped by quenching from applied extrinsic parameters such as pressure. Synthesis of metastable phases without the use of extrinsic parameters requires kinetic control: selective manipulation of the energy barriers along a reaction pathway.[6] The discovery and development of solid-state reactions that exhibit kinetic control will lead to greater understanding of the energy barriers along the pathway, as well as the discovery of materials above the energetic "convex hull".[11,20]

Solid-state metathesis chemistry enables reactions with low thermal barriers. While they provide self-propagating, exothermic synthesis of sulfides, oxides, and nitrides,[52,63] solid-state metathesis reactions need not self propagate[58,59,75] and can be performed under kinetic control[65,76] to selectively produce metastable products.[66,67] "Assisted" metathesis reactions[77,78] are exemplified by the reaction between $PbSO_4$, K_2CO_3, and TiO_2, which form $PbTiO_3$ along with K_2SO_4 and CO_2(g) as byproducts.[79] These reactions are *kinetically competent*: they proceed to stoichiometric completion, and the temperature at which they proceed is low enough that the reaction pathway could influence the outcome. This kinetic competence results from differences in precursor reactivity and is distinct from the lability of ligands to soluble coordination complexes,[80] as materials synthesis require concerted bond breaking/making and diffusion of many species.

The yttrium-manganese-oxide family of materials provides an ideal energetic landscape to explore the role of reaction pathways in assisted metathesis reactions. These materials have garnered significant interest for their magnetic and electronic properties.[81–86] Reaction of the binary oxides yields hexagonal $YMnO_3$ at high temperatures (>1100 °C).[87] Small lanthanides (Ln = Yb, Er, Y) produces this hexagonal structure; larger lanthanides form an orthorhombic perovskite. $YMnO_3$ exhibits the smallest difference in Gibbs free energy between stable hexagonal and metastable perovskite polymorphs at $T = 1200$ °C.[88] The small difference in free energy suggests that kinetic factors can play a determining role in the reaction pathway. As such, the orthorhombic perovskite $YMnO_3$ has been synthesized through citrate decomposition routes,[89,90] kinetic trapping,[91,92] and hydrothermal reactions.[83,93] Furthermore, pyrochlore $Y_2Mn_2O_7$ has been reported as a metastable phase and has been synthesized through kinetic trapping reactions from oxidizing hydrothermal conditions.[94]

Using the nominal assisted metathesis reaction: $Mn_2O_3 + 2\,YCl_3 + 3\,A_2CO_3 \longrightarrow 2\,YMnO_3 + 6\,ACl + 3\,CO_2$ under flowing oxygen (where A = Li, Na, K), we observe different Y-Mn-O products using different alkali carbonates. Lithium carbonate reactions selectively form o-$YMnO_3$ over the temperature range of 550-850 °C, while sodium carbonate selectively forms the metastable pyrochlore $Y_2Mn_2O_7$ at 650 °C. Reactions heated to T >900 °C forms hexagonal $YMnO_3$, regardless of alkali carbonate. The ability to form these two phases through relatively simple changes to the reaction preparation illustrates the competence of assisted metathesis to kinetically control solid-state reactions.

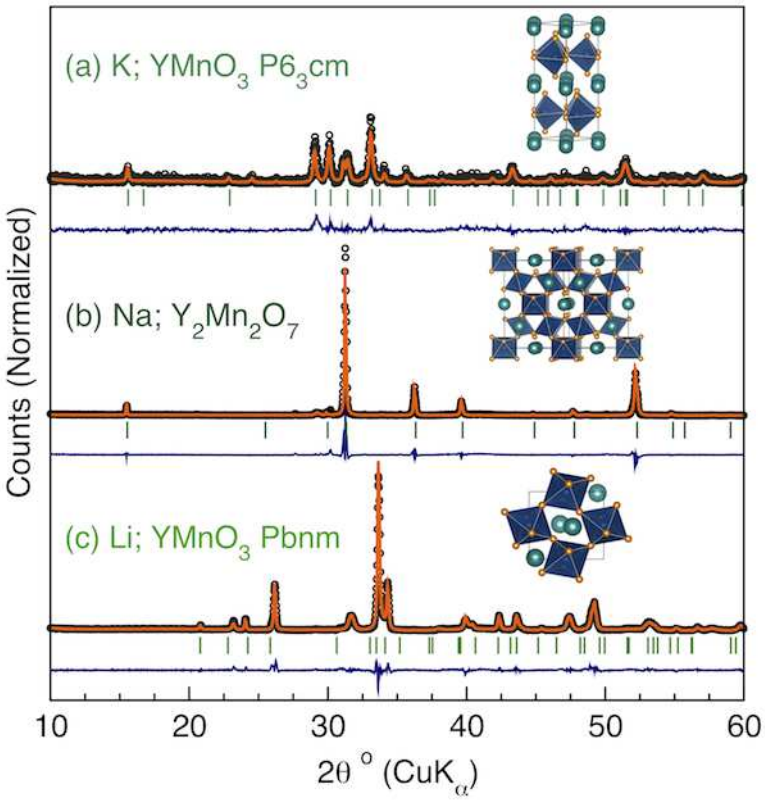


Figure 2.1: PXRD patterns and crystal structures of products obtained from $Mn_2O_3 + 2\,YCl_3 + A_2CO_3$ using different alkali cations: (a) Li_2CO_3: $Pbnm$ $YMnO_3$, 850 °C (b) Na_2CO_3: $Fd\bar{3}m$ $Y_2Mn_2O_7$, 650 °C (c) K_2CO_3: $P6_3cm$ $YMnO_3$ T >850 °C. In the structures: oxygen: orange, manganese: navy and yttrium: teal. Tick marks denote expected peak positions.

2.2. Results and Discussion

The assisted metathesis reactions presented have a lower reaction temperature than traditional ceramic routes. When using the binary oxides (Mn_2O_3 and Y_2O_3), reactivity is not observed until T_{rxn} = 850 °C. Figure 2.1 depicts PXRD results from the reaction of binary oxides after 96 h. Even at 850 °C, the reaction has not proceeded to completion, with most of the identifiable phases being comprised of the reactants.

By lowering the energy barrier to reactivity of yttrium manganese oxide phases, the reaction pathway can be changed to access phases other than hexagonal $YMnO_3$. Figure 2.1

shows PXRD data and Rietveld analysis of the optimized products using different alkali carbonate precursors. With Li_2CO_3, orthorhombic ($Pnma$) $YMnO_3$ forms via the reaction:

$$\begin{aligned} &\mathrm{Mn_2O_3} + 2.2\,\mathrm{YCl_3 \cdot 6\,H_2O} + 3\,\mathrm{Li_2CO_3} \xrightarrow{\mathrm{O_2}} \\ &2\,\mathrm{YMnO_3} + 5.8\,\mathrm{LiCl} + 0.2\,\mathrm{LiYCl_4(g)} \\ &+ 3\,\mathrm{CO_2(g)} + 12.4\,\mathrm{H_2O(g)} \cdot \end{aligned} \tag{2.1}$$

This optimized reaction yields >99% conversion to the perovskite phase. o-$YMnO_3$ is the predominate product over the temperature range of 550-850 °C, with higher temperatures yielding improved crystallinity (Figure A.2). With reactions performed at 450 °C, the reaction products are Mn_2O_3, Y_2O_3, and Y_3O_4Cl. At reaction temperatures above 850 °C, the hexagonal polymorph of $YMnO_3$ is produced. Flowing dry oxygen suppresses the formation of Li_2MnO_3, which is produced when the reaction is performed in air.

Myriad control reactions were performed to test the stability of these phases by varying the reaction temperature, atmosphere, and precursor composition (Table A.1). The synthesis of o-$YMnO_3$ (Eq. 2) requires a 20 mol% excess of $YCl_3 \cdot 6\,H_2O$ to avoid yttrium-poor YMn_2O_5 (Figure A.3). YCl_3 is likely lost from the reaction mixture by complexing with LiCl to form $LiYCl_4$ (g) at high temperatures, as supported by the presence of residue on the downstream end of the process tube.[95] This loss of YCl_3 is exacerbated when using anhydrous YCl_3; this result is explained by the coordination of yttrium by oxygen rather than chlorine in $YCl_3 \cdot 6\,H_2O$ to prevent reaction with LiCl.[96]

Joint refinement against X-ray and neutron powder diffraction data reveals the crystal structure and composition of o-$YMnO_3$ (Figure A.4). The unit cell volume is contracted as

Table 2.1: Calculated crystallographic and magnetic data for o-$YMnO_3$ and $Y_2Mn_2O_7$

	Crystallographic Data*			
Compound	a (Å)	b (Å)	c (Å)	V (Å^3)
o-$YMnO_3$	$(Pbnm)$			
Present	5.6451(4)	7.3943(4)	5.2218(3)	217.97(2)
[90]	5.826(2)	7.369(2)	5.254(2)	225.586
$Y_2Mn_2O_7$	$(Fd\bar{3}m)$			
Present	9.9096(3)	–	–	973.1(1)
[94]	9.902(1)	–	–	970.92(1)

* co-refined Rietveld analysis of X-ray and neutron diffraction data

compared to stoichiometric o-$YMnO_3$ (Table 2.1, Table A.2).[83,89,90,97,98] Other $LnMnO_{3+\delta}$ phases (Ln = La, Pr, Nd) show a similar volume contraction,[99–102] while expansion is observed with oxygen substoichiometry.[101,103,104] The presence of smaller Mn(IV) and significant cation vacancies in o-$YMnO_{3+\delta}$ accounts for the observed contraction. Furthermore, anisotropic broadening of Bragg reflections (e.g., (100) and (101) planes) likely results from cation vacancies. Rietveld analysis was performed to determine the structure and oxygen site occupancy (O1: 1.062(9), O2: 1.024(8)), which yields an overall chemical formula: $YMnO_{3.11(4)}$. IR spectroscopy does not detect incorporation of CO_3^{2-} into the o-$YMnO_3$ lattice (Figure A.5).

The magnetic susceptibility supports this stoichiometric deviation. Previous studies report antiferromagnetic interactions for o-$YMnO_3$ and an effective moment consistent with $3d^4$ Mn(III).[83,89,97,98] Curie-Weiss analysis of the linear portion of the inverse magnetic susceptibility, after correcting for temperature-dependent paramagnetism (χ_0 = 10^{-6}Oe mol Mn emu^{-1}), reveals weak mean-field ferromagnetic interactions (Figure 2.2, $\Theta = 8.28(5)$ K), consistent with observed weak ferromagnetic hysteresis ($T = 2$ K, Figure A.6). Mean-field ferromagnetic interactions arise in presence of a mixed valence Mn(III)/Mn(IV)

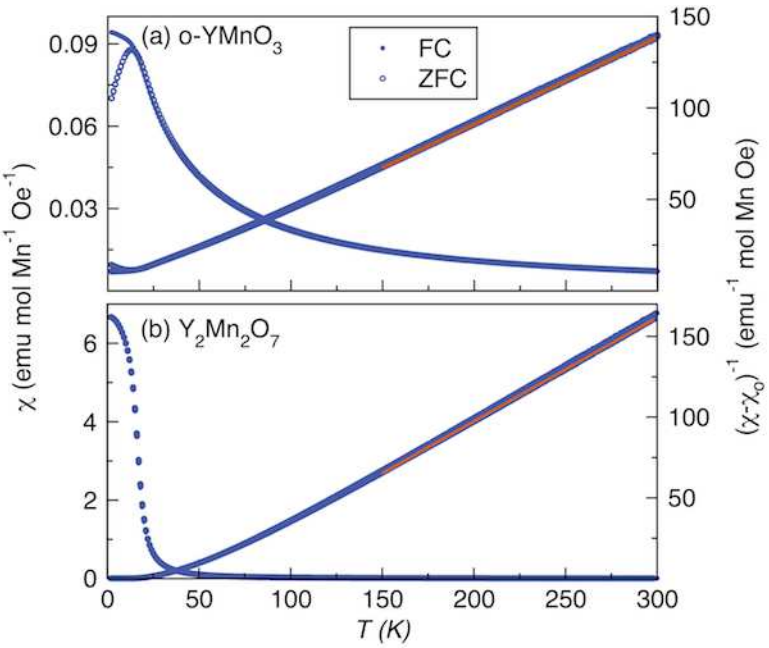


Figure 2.2: Temperature dependent magnetic susceptibility of (a) o-$YMnO_3$ and (b) $Y_2Mn_2O_7$ showing both ZFC and FC measurements. Curie Weiss analyses of the linear portion of the inverse magnetic susceptibility after correcting for temperature dependent paramagnetism ($\chi_0 = 10^{-6}$ Oe mol Mn emu^{-1}) are shown in orange.

system due to double exchange.[105] Furthermore, the effective moment, μ_{eff} = 4.104(4), is reduced from the expected value for $3d^4$ Mn(III) (μ_{eff} = 4.90). Incorporation of 17.23(2) mol% $3d^3$ Mn(IV) (μ_{eff}=3.87) into a Mn(III) lattice reproduces the experimental effective moment and is comparable to the 19.55(5)% Mn(IV) determined from Rietveld analysis (e.g., $YMnO_{3.11(4)}$).

Control reactions suggest that o-$YMnO_{3+\delta}$ is thermodynamically stable for $T < 900$ °C under flowing oxygen, and formation of o-$YMnO_{3+\delta}$ requires kinetically-competent reactants. When Li_2CO_3-based reactions are run for 7 d at 850 °C, the same o-$YMnO_{3+\delta}$ is observed (Table A.3). High oxygen chemical potential is required for the stability of o-$YMnO_{3+\delta}$, as the washed o-$YMnO_{3+\delta}$ product decomposes into h-$YMnO_3$ and o-$YMnO_3$ when heated to 850 °C under flowing argon (Figure A.7, Table A.3); annealing for 30

d at 850 °C in an evacuated ampoule does not lead to decomposition; however, a slight increase of unit cell volume is observed, suggestive of a release of some oxygen. When o-$YMnO_{3+\delta}$ recovered from the assisted metathesis reaction is annealed in a LiCl flux with a 1:3 YMnO3:LiCl ratio to 850 °C under flowing O_2 for 24 h, o-$YMnO_{3+\delta}$ is also observed (vol = 218.20(3) $Å^3$). This shows that that presence or absence of LiCl is not a strong influence on the stability of the structure. Given that only Li_2CO_3 shows selectivity for o-$YMnO_{3+\delta}$, kinetic control does play a role in these reactions even if the perovskite phase is most stable at these temperatures.

Formation of $Fd\bar{3}m$ $Y_2Mn_2O_7$ occurs when using Na_2CO_3 in the assisted metathesis reaction:

$$\begin{aligned} &\mathrm{Mn_2O_3 + 2\,YCl_3 + 3\,Na_2CO_3} \xrightarrow{\mathrm{O_2}} \\ &\mathrm{Y_2Mn_2O_7 + 6\,NaCl + 3\,CO_2(g)} \end{aligned} \tag{2.2}$$

The reaction proceeds stoichiometrically using anhydrous yttrium chloride to form $Y_2Mn_2O_7$ and 6 NaCl. Anhydrous yttrium chloride is necessary to avoid the formation of unreactive Y_2O_3, as is observed with $YCl_3 \cdot 6\,H_2O$. Higher reaction temperature (850 °C) and/or longer times (48 h) lead to partial decomposition (Table A.1, Figure A.8); these controls substantiate the kinetically-controlled synthesis of a metastable product.[6]

Co-refinement of X-ray and neutron powder diffraction data reveal a stoichiometric compound after refinement of the O′ position (8b) in the pyrochlore lattice (Table 2.1 and Figure A.9). IR spectroscopy does not detect CO_3^{2-} incorporation into the lattice (Figure A.5). The magnetic susceptibility of $Y_2Mn_2O_7$ is consistent with the previously

reported ferromagnetic behavior (Figure 2.2). Curie Weiss analysis on $Y_2Mn_2O_7$ is consistent with the previously reported ferromagnetic interaction strength and effective moment ($\Theta = 48.70(5)$ K, $\mu_{\text{eff}} = 3.526(3)$),[94] as well as Brillouin-like functions in the isothermal magnetization at low temperature (Figure A.6).

K_2CO_3 was also used in these assisted metathesis reactions. At reaction temperatures above 850 °C, the hexagonal $YMnO_3$ polymorph is observed (Table A.1). At temperatures below 850 °C, o-$YMnO_3$, $Y_2Mn_2O_7$, h-$YMnO_3$, and YMn_2O_5 are produced simultaneously in mixtures, but no phase selectivity is observed. It is interesting to note that $Y_2Mn_2O_7$ and h-$YMnO_3$ appear to be metastable at $T <$ 850 °C when using K_2CO_3.

Although changing the precursor changes the thermodynamic landscape, the observed products do not reflect the assertion that more exothermic reactions should yield more stable products. As the alkali cation size increases, the overall reaction enthalpy becomes more favorable (Figure A.22). It is unclear how or if the changes in the reaction enthalpy can affect polymorph stability. Therefore, the fact that the most stable product only forms with lithium suggests that the reaction pathway dictates the reaction product.

SEM-EDS analysis shows a porous o-$YMnO_3$ product when using Li_2CO_3 (Figure 2.3(a,b)). Compositional analysis (EDS, Figure A.10) shows the product is composed of only yttrium manganese oxide phases, suggesting LiCl melts or volatilizes during the reaction (T_m(LiCl) = 605 °C). Washed o-$YMnO_3$ products are virtually identical (Figure 2.3(a) vs (b); Figure A.10 vs A.11). SEM-EDS images of products using Na_2CO_3 show larger densified particles with NaCl present (Figure 2.3(c), Figure A.12). Washing product reveals a distribution of smaller $Y_2Mn_2O_7$ particles without NaCl (Figure 2.3(d); Figure A.13). Phase stability is dependent on specific surface area (e.g., particle size), as

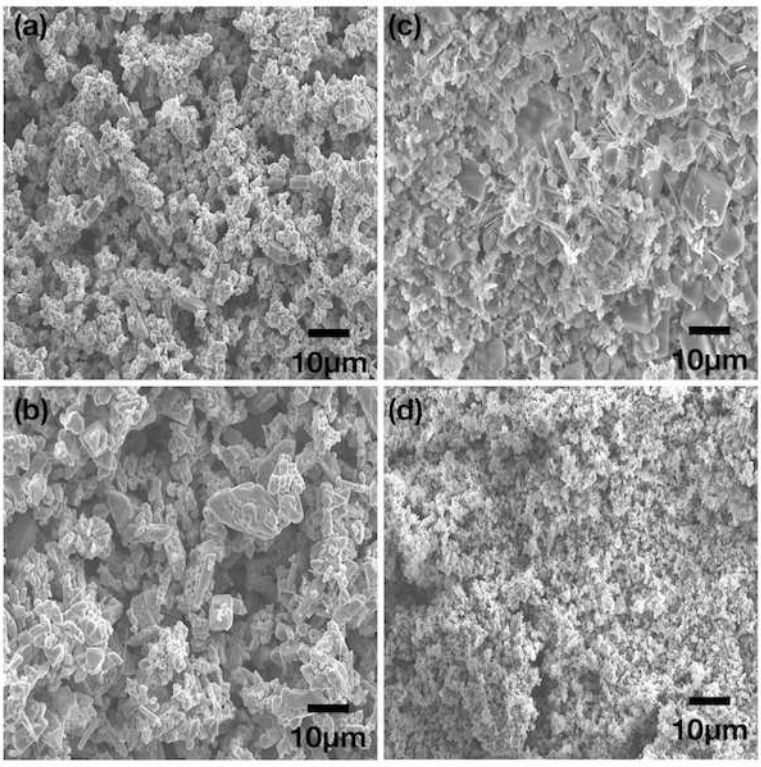


Figure 2.3: SEM images of the products from assisted metathesis reactions: (a,b) o-$YMnO_3$ from Eq.1; (c) NaCl and $Y_2Mn_2O_7$ from Eq. 2; (d) $Y_2Mn_2O_7$ from Eq. 2. (a,c) show the products before washing with 0.6M HCl while (b,d) show the products after washing with 0.6M HCl.

demonstrated for the different polymorphs of TiO_2 and FeS_2;[19,106] these observations invoke the concept of 'remnant' metastability'.[11] It is possible that the phases presented here are stabilized by small, high surface area particles due to the large mass loss experienced during the reaction pathway. However, it is unclear how porosity is influenced by the presence of different alkalis. Elucidation of the reaction pathway is likely to reveal the origin of the selectivity.

2.3. Conclusions

Assisted solid-state metathesis reactions are kinetically competent; they permit low temperature synthesis of yttrium manganese oxide ceramics. Li_2CO_3 assisted reactions

selectively form the orthorhombic perovskite $YMnO_3$ over a wide temperature range (550-900 °C) and at long reaction times; we infer from this that the perovskite is, in fact, stable at lower temperatures. Na_2CO_3 yields the metastable pyrochlore $Y_2Mn_2O_7$ at T_{rxn} = 650 °C but only at short reaction times. K_2CO_3 forms a mixture of products including o-$YMnO_3$, $Y_2Mn_2O_7$, and h-$YMnO_3$ (metastable at the reaction temperature). Therefore, we conclude that the alkali species plays a larger role in shaping the reaction pathway than in changing the thermodynamic landscape of polymorph selectivity. Understanding how the reaction pathway promotes this selectivity will hopefully lead to more prescriptive solid-state reactions for complex oxides.

2.4. Methods

All reagents were prepared, stored, and weighed in an argon-filled glovebox with O_2 and H_2O levels $\leq$ 0.1ppm. Manganese(III) oxide (Sigma Aldrich 99%) was purified by heating in an alumina boat at 1 °C/min to 700 °C for 16 h in air and quenched into the glovebox; purity was verified by powder X-ray diffraction (PXRD). Alkali carbonates were stored in a 160 °C convection oven and transferred to the glovebox. Anhydrous YCl_3 (Alfa Aesar 99.9%) and $YCl_3 \cdot 6\,H_2O$ (Alfa Aesar 99.9%) were purchased and stored under argon. All gases (O_2, Ar) were purchased through Airgas at the Ultra High Purity grade (99.999%).

To prepare the assisted metathesis reactions, precursors were mixed in an agate mortar and pestle for approximately 15 minutes in the glovebox followed by pelleting in a 5mm die under $\sim$1 ton. Pellets were placed in an alumina reaction boat atop a sacrificial layer

of reactant powder. Still in the argon-filled glovebox, the alumina boat was inserted into a 24 mm i.d. mullite process tube affixed with self-sealing gas connection ports. The entire reaction apparatus was removed from the glovebox and placed in a tube furnace with appropriate dry gas connections (after purging for > 1 min at $\sim$0.2 cc/min). Reactions heated at 10 °C/min to the reaction temperature. All reactions were furnace cooled, and products were processed under ambient conditions. Samples were washed with 0.6 M HCl, filtered, then dried at 80 °C for 12 h.

To synthesize o-$YMnO_3$, 20% molar excess of yttrium chloride hexahydrate was added to manganese(III) oxide and lithium carbonate. Precursors were heated to 850 °C for 24 h under flowing oxygen producing a black and porous product. To synthesize $Y_2Mn_2O_7$, anhydrous yttrium chloride was added to manganese(III) oxide and sodium carbonate. The precursors were heated to 650 °C for 24 h under flowing oxygen producing a dense brown/black pellet.

Laboratory Powder X-Ray Diffraction (PXRD) was performed on a Bruker D8 DaVinci with CuK_α radiation. All samples were prepared on a zero-diffraction silicon wafer. Rietveld analysis was performed using EXPGUI/GSAS or TOPAS.[107,108]

Neutron powder diffraction (NPD) experiments were performed at HB2A ($\lambda = 1.54$Å) at the High Flux Isotope Reactor at Oak Ridge National Laboratory. NPD samples were made in batches to yield 250 mg of desired product and combined to make approximately 5 g of material. After each batch reaction, samples were washed with 0.6M HCl and PXRD was run to ensure sample purity. Then, batches were combined and PXRD was run again to ensure a total purity of product. Instrument parameters were extracted from a silicon standard.

Scanning electron microscopy (SEM) analyses were done using a JEOL JSM-6500F microscope. Energy-dispersive X-ray spectroscopy (EDS) was performed at a 15keV accelerating voltage at three different spots to obtain an average composition. SEM images were taken at a 10mm working distance and processed to enhance contrast for reproduction. Magnetic measurements were performed using the Vibrating Sample Magnetometer (VSM) option on a Quantum Design Inc. PPMS DynaCool. Magnetic susceptibilities were measured under zero field cooled (ZFC) and field cooled (FC) conditions using 0.0155(1) g and 0.0100(1) g of $Y_2Mn_2O_7$ and o-$YMnO_3$, respectively. IR spectroscopy was performed on solid samples using a ThermoScientific Nicolet i550 FT-IR using the SMART iTR module. Powders were placed on an ATR crystal and purged with nitrogen before measurement.

All thermochemical calculations were performed using tabulated values from the NIST Webbook.[109]

3. Yttrium manganese oxide phase stability and selectivity using lithium carbonate assisted metathesis reactions[†]

Overview

In solid-state chemistry, stable phases are often missed if their synthesis is impractical, such as when decomposition or a polymorphic transition occurs at relative low temperature. In the preparation of complex oxides, reaction temperatures commonly exceed 1000 °C with little to no control of the reaction pathway. Thus, a prerequisite for exploring the synthesis of complex oxides is to identify reactions with intermediates that are kinetically competent at low temperatures, as provided by assisted metathesis reactions. Here, we study the assisted metathesis reaction: $Mn_2O_3 + 2.2\,YCl_3 \cdot 6\,H_2O + 3\,Li_2CO_3 \longrightarrow 2\,YMnO_3 + 5.8\,LiCl + 0.2\,LiYCl_4 + 3\,CO_2$ using $in\ situ$ synchrotron X-ray diffraction. By changing the atmosphere, oxygen vs. inert gas, the reaction product changes from the over-oxidized perovskite $YMnO_{3+\delta}$ to the hexagonal $YMnO_3$ polymorph at the reaction temperature of 850 °C, respectively. Analysis of the reaction pathways reveals two parallel reaction pathways in forming $YMnO_3$ phases: (1) the slow reaction of metal oxides in a LiCl flux ($Y_2O_3 + Mn_2O_3 \xrightarrow{6LiCl} 2\,YMnO_3$) and (2) the fast reaction from ternary intermediates ($YOCl + LiMnO_2 \longrightarrow LiCl + YMnO_3$) . Control reactions reveal that both proposed

[†]Substantial portions of this chapter have been reproduced with permission from P. K. Todd, A. M. M. Smith and J. R. Neilson, *Inorg. Chem.* **2019**, *58*, 15166–15174, reference 110, © 2019 the American Chemical Society

pathways in isolation result in product formation, but the direct preparation of ternary intermediates ($YOCl + LiMnO_2 \longrightarrow LiCl + YMnO_3$) occurs at lower temperatures (500 °C), shorter times ($<$ 24 h), and forms nominally-stoichiometric orthorhombic $YMnO_3$. These ternary intermediates react at a faster rate than the slow step-wise oxygenation of yttrium chloride to Y_2O_3 ($YCl_3 \longrightarrow YOCl \longrightarrow Y_3O_4Cl \longrightarrow Y_2O_3$), which is relatively inert. These results support a kinetically controlled reaction pathway to form $YMnO_3$ phases in assisted metathesis reactions with phase selectivity achievable through changes to reaction atmosphere.

3.1. Author Contributions

PKT synthesized all precursors, performed the majority of all reported experiments, conducted on-site experiments at ANL-APS 17-BM-B, and wrote the manuscript. AMMS assisted in ternary metathesis reactions, including data analysis. JRN provided guidance and assistance in writing the manuscript.

3.2. Introduction

Current computational studies are able to predict millions of new functional materials,[7] but they are unable to successfully predict the synthetic pathways by which they proceed.[20] While computational studies have begun working towards modeling the "synthesizability" of new inorganic materials,[3,10] the focus remains on describing the thermodynamic range of the products' stability in relation to a thermodynamic energy ground-state.[11–13] While understanding the relative thermodynamic energetic position of a desired material is use-

ful in accessing the probability of synthesizing a material,[14] current computational tools cannot predict synthetic variables as they relate to reaction kinetics, precursor competence, and non-equilibrium phase behavior.[3] Also, there is a growing list of stable compounds previously thought to not exist or be unstable, owing to their decomposition under traditional synthesis conditions (e.g., $MgCr_2S_4$).[15] Thus, more diagnostic studies are required that focus on characterizing these transient steps in material synthesis so that kinetic factors can be applied to these valuable data-driven endeavors.

In situ X-ray diffraction provides a powerful characterization tool for analyzing these kinetic factors in solid-state inorganic synthesis.[6,70] Temperature-dependent diffraction experiments have been used in characterizing kinetic control in solids,[66] thin films,[46] polymorph metastability,[67] battery kinetics,[71] hydrothermal crystal growth,[72] and the discovery of new materials in flux-mediated synthesis.[42] As a system for these diagnostic studies, metathesis reactions provide diverse compositional control in the synthesis of oxides, sulfides, and nitrides.[52] By tuning the reaction composition, energetics can be modulated from rapid, exothermic propagation events[63] to reactions that require continual heating.[58,59,75] These kinetically slower, non-propagating pathways provide opportunities for kinetic control at low-temperatures[65,76] and have been shown to synthesize metastable products.[66,67]

Previously, "assisted" metathesis reactions were shown to exhibit selective polymorph formation in the yttrium manganese oxide family of materials through changes in precursor reactivity.[73] Changing the alkali cation in the reaction between Mn_2O_3, YCl_3, and A_2CO_3 (where A = Li, Na, K) creates different kinetic pathways that result in three distinct yttrium manganese oxide products: orthorhombic $YMnO_{3+\delta}$, $Y_2Mn_2O_7$, and hexagonal

$YMnO_3$. Each reaction involving an alkali cation represents a different set of synthesis conditions and nuances that lead to polymorph selectivity in this system. This contribution elaborates on lithium carbonate assisted-metathesis reactions.

Using lithium carbonate, the over-oxidized o-$YMnO_{3+\delta}$ appears to be the thermodynamically-stable product at reaction temperatures below 850 °C using oxidizing conditions and long reaction times (7 d):

$$\begin{aligned} &\mathrm{Mn_2O_3} + 2.2\,\mathrm{YCl_3 \cdot 6\,H_2O} + 3\,\mathrm{Li_2CO_3} \xrightarrow{\mathrm{O_2}} \\ &2\,\mathrm{YMnO_{3+\delta}} + 5.8\,\mathrm{LiCl} + 0.2\,\mathrm{LiYCl_4(g)} \\ &+ 3\,\mathrm{CO_2(g)} + 12.4\,\mathrm{H_2O(g)} \cdot \end{aligned} \tag{3.1}$$

At temperatures above 850 °C, or under inert conditions, the hexagonal $YMnO_3$ product dominates over long reaction times (7 d). While the over-oxidized perovskite phase is accessible via assisted metathesis, the stoichiometric o-$YMnO_3$ phase remains inaccessible using assisted metathesis at any temperature. Stoichiometric o-$YMnO_3$ has been labeled as metastable via citrate decomposition routes,[89,90] kinetic trapping,[91,92] and hydrothermal reactions,[83,93] but the kinetic factors that dictate why o-$YMnO_3$ forms over h-$YMnO_3$ are unclear.

The assisted metathesis reactions using lithium carbonate form the o-$YMnO_{3+\delta}$ polymorph, but understanding the kinetic factors in selecting between this over-oxidized orthorhombic phase and the hexagonal polymorph may provide clarity on how to access stoichiometric o-$YMnO_3$. The assisted metathesis reactions are undoubtedly affected by

oxygen fugacity, which suggests the over-oxidized o-$YMnO_{3+\delta}$ may be stabilized solely through inclusions of Mn(IV) defects and cation vacancies which have been observed in other rare-earth manganese oxides ($LnMnO_3$ where Ln = La, Pr, Nd).[99–102] While both orthorhombic phases form in the same space group ($Pbnm$), the over-oxidized phase exhibits a slightly contracted unit cell volume and exhibits different magnetic properties.[73]

Using $in\ situ$ synchrotron X-ray diffraction, temperature-dependent assisted-metathesis reactions (Eq. 1) are examined under different reaction environments (O_2 vs. noble gas). Identification of the crystalline transient intermediates leads to the identification of two reaction pathways that explain the observation of o-$YMnO_3$ formation: The formation and subsequent reaction of (i) ternary intermediates YOCl and $LiMnO_2$ and/or (ii) binary oxides in a lithium chloride flux. In testing these hypotheses using $ex\ situ$ control reactions, we identify both pathways as competent intermediates but discover that the ternary metathesis reaction between yttrium oxychloride and lithium manganese oxide is much more kinetically competent (i.e., it is faster). Using the discovered "ternary" metathesis between YOCl and $LiMnO_2$, stoichiometric o-$YMnO_3$ is shown to be synthetically accessible at low-temperatures (500 °C).

3.3. Methods

All reagents were prepared, stored, and weighed in an argon-filled glovebox with O_2 and H_2O levels $\leq$ 0.1ppm. Manganese(III) oxide (Sigma Aldrich 99%) was purified by heating Mn_2O_3 in an alumina boat at 1 °C/min to 700 °C for 16 h in air and quenched into the glovebox; purity was verified by powder X-ray diffraction (PXRD). $YCl_3 \cdot 6\,H_2O$

(Alfa Aesar 99.9%), lithium carbonate (Sigma Aldrich 99.9%), lithium iodide (Alfa Aesar 99.5%), and lithium choride (Alfa Aesar 99.5%), were purchased and stored under argon. All gases (O_2, Ar, He) were purchased through Airgas at the Ultra High Purity grade (99.999%). $NaMnO_2$ ($C2/m$) was prepared by mixing manganese (III) oxide and sodium carbonate (Sigma Aldrich 99.9%) in a 1:1 molar ratio, grinding for 15 minutes in an agate mortar and pestle, and pelleting using $\sim$1 tn of force. The pellet was placed upon a sacrificial layer of powder in an alumina crucible and heated in a muffle furnace at 1 °C/min to 700 °C for 10 h. The reaction was subsequently quenched into the antechamber of the glovebox and stored under argon. $LiMnO_2$ ($C2/m$) was prepared through a solid-state ion exchange from $NaMnO_2$ and LiI. Sodium manganese oxide was mixed with three molar equivalents of lithium iodide, placed in an alumina crucible, which was sealed in a quartz ampule under vacuum (> 10 mTorr). The reaction was heated at 1 °C/min to 460 °C for 4 h and cooled at 1 °C/min to room temperature. The product was washed with deionized water, filtered, and dried at 80 °C for 6 h. YOCl was prepared by heating $YCl_3 \cdot 6\,H_2O$ in an alumina boat to 350 °C at 10 °C/min for 4 h in air. The YOCl product formed is the $P4/nmn$ PbClF structure-type. All prepared reactants were confirmed using laboratory PXRD. Preparations for $ex\ situ$ assisted metathesis reactions have been described in detail previously.[73] Oxygen partial pressure was controlled using mass flow controllers to achieve a 1:100 dilution of oxygen in argon ($pO_2 \sim 10^{-2}$ atm), flowing argon ($pO_2 \sim 10^{-6}$ atm), and flowing oxygen (pO_2~0.8 atm).

For temperature-dependent $in\ situ$ assisted metathesis reactions that produce carbon dioxide as a by-product, open-ended quartz capillary (1.1 mm OD) were packed in a glovebag under argon using glass wool as a plug. Synchrotron X-ray diffraction experiments

were performed at beamline 17-BM-B (λ = 0.2415 $\mathring{A}$) at the Advanced Photon Source at Argonne National Laboratory using a Perkin Elmer plate detector at a distance of 700 mm. All capillaries were loaded into a flow-cell apparatus equipped with resistive heating elements and heated at 10 °C/min.[111] Gas flow (O_2, He) was supplied at APS and controlled through mass flow controllers at a rate of 0.2 cc/min. Assisted-metathesis reactions were heated to a maximum temperature of 850 °C while the sample continuously rocked at $\pm$ 5° about the length of the capillary. Diffraction patterns were collected every two seconds and summed every 20 seconds for powder averaging. Plate detector images were integrated using GSAS-II and calibrated using a LaB_6 standard. Laboratory PXRD data were collected on a Bruker D8 Discover diffractometer using Cu Kα radiation and a Lynxeye XE-T position-sensitive detector.

All Rietveld refinements were performed using TOPAS v6. Due to the number and positional overlap of intermediates during the sequential refinements, all thermal displacement parameters were fixed at 5Å^2 and the full-width-half-max was fixed at 178 nm to better account for changes in peak intensity during the reaction. In order to compare the relative fractions of phases determined from Rietveld calculations, a weighted scale factor is defined as: $Q_p = S_p \cdot V_p \cdot M_p$ where Q_p = weighted scale factor of phase p, S_p = Scale factor calculated from Rietveld for phase p, V_p is the volume of the unit cell for phase p, and M_p is the atomic mass of the unit cell for phase p. It should be noted that we omit the Brindley coefficient for microabsorption correction in our calculation of weighted scale factor due to the inability to successfully refine our particle sizes for individual phases. Amorphous material and product lost as vapor are not accounted for in the sequential refinement. We reference all phases by their stoichiometric formula; however, the actual chemical for-

mula may be distinct from the written formula as XRD data alone cannot typically resolve non-stoichiometric compounds.

3.4. Results

In situ synchrotron X-ray diffraction experiments were performed to study reaction progress as a function of temperature (25 °C $\geq$ T $\leq$ 850 °C; 10 °C/min) and environment (O_2 vs. Ar/He). Figure 1(a) shows the integrated SXRD patterns from the assisted metathesis reaction (Eq. 1) under flowing oxygen as a function of temperature. As precursors are heated, the reaction progress can be segmented into discrete reactive zones (I, II, III). To quantitatively visualize these reactive zones, sequential Rietveld refinements were performed over the range of diffraction patterns and the results are represented in Figure 1(b), where each horizontal sub-panel highlights a different cation (Y, Mn, Li) for clarity.

Reactive zone I describes the reaction of yttrium chloride with lithium carbonate (T_{rxn}=25-320 °C). The first reaction in Zone I is the dehydration of $YCl_3 \cdot 6\,H_2O$ which occurs in the two-step process:

$$\mathrm{YCl_3 \cdot 6\,H_2O \longrightarrow YCl_3 \cdot H_2O + 5\,H_2O(g)} \tag{3.2a}$$

$$\mathrm{YCl_3 \cdot H_2O \longrightarrow YCl_3 + H_2O(g)} \tag{3.2b}$$

TGA-MS results (Figure 3.2) support the two-step dehydration of yttrium chloride which agrees with previous studies on the decomposition of rare-earth chloride hydrates in air.[112]

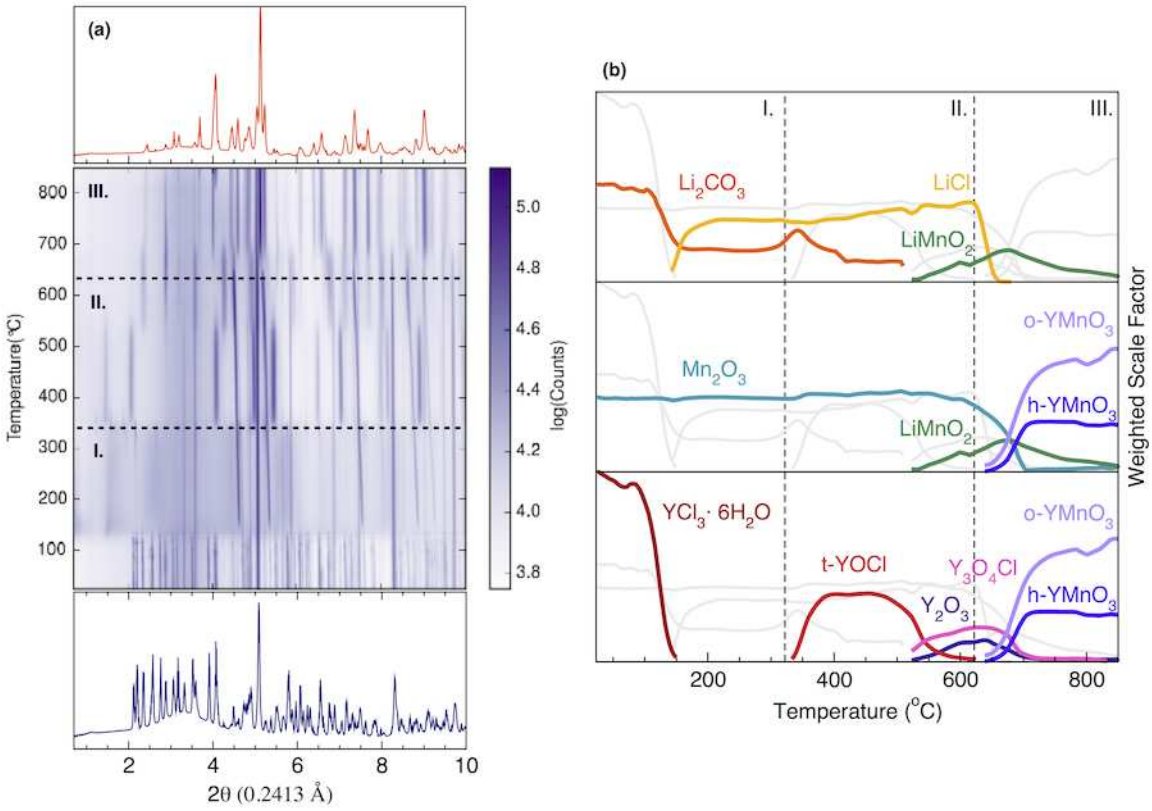


Figure 3.1: *In situ* PXRD results of the reaction: $Mn_2O_3 + 2.2\,YCl_3 \cdot 6\,H_2O + 3\,Li_2CO_3$ under flowing oxygen. (a) Powder diffraction patterns as a function of temperature (b) Weighted scale factor of each phase during the reaction pathway from Rietveld refinement as a function of temperature. Both (a) and (b) are separated into three reactive zones: I Reactivity of yttrium chloride and formation of YOCl; II Oxygenation of YOCl and formation of $LiMnO_2$; III Melting of LiCl and $YMnO_3$ formation. Each sub-panel in (b) is separated by cation for visualization purposes with the gray lines denoting phases with other cations.

Upon dehydration, the yttrium chloride reacts with two moles of lithium carbonate according to the following reaction at T_{rxn}=155-320 °C:

$$2\,YCl_3 + 2\,Li_2CO_3 \longrightarrow 2\,YOCl + 4\,LiCl + 2\,CO_2 \tag{3.3}$$

The formation of LiCl at 136 °C and decrease in Li_2CO_3 peak intensity over this temperature range is supported in Rietveld analysis (Figure 3.1) and mass loss with an increase

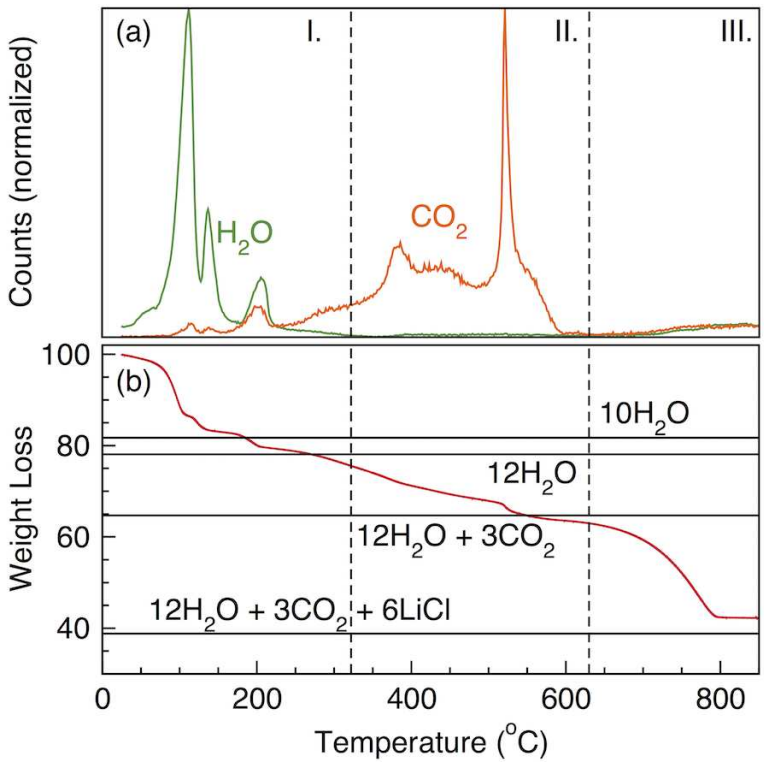


Figure 3.2: (a) mass spectrometry and (b) thermogravimetric analysis on the reaction: $Mn_2O_3 + 2\,YCl_3 \cdot 6\,H_2O + 3\,Li_2CO_3$. The reaction was heated at 10 °C/min to 850 °C with reaction zones I, II, and III presented for comparison to Figure 1. The theoretical mass loss from the reaction are shown as solid black lines in (b). Release of H_2O and CO_2 vapor during the reaction matches the reactivity observed in the *in situ* SXRD data.

in CO_2 ion count (Figure 3.2). Interestingly, there is a discontinuity in crystalline yttrium containing phases (Figure 3.1) after the loss of intensity of yttrium chloride hexahydrate. Visual inspection of the SXRD data also shows an increase in intensity near the background that correspond to poorly resolved YOCl ($R\bar{3}m$) reflections. These reflections grow (155 -322 °C) before this YOCl phase undergoes a phase transition to the $P4/mnm$ structure at 322 °C. During Zone I, the manganese(III) oxide remains unchanged.

Reaction Zone II (322-630 °C) describes the behavior of ternary intermediates along the reaction pathway. During this temperature range, lithium chloride continues to increase in intensity and lithium carbonate decreases slowly in intensity (Figure 3.1). TGA-MS

(Figure 3.2) supports the reactivity of lithium carbonate as both mass loss and the ion count of CO_2 steadily increases over this range. An increase in lithium carbonate intensity is observed at 350 °C in Figure 3.1 due to the overlapping peak positions with $P4/mnm$ YOCl, which grows in rapidly at this temperature. The behavior of the yttrium-containing intermediates over this range is indicative of the conversion to Y_2O_3 under flowing oxygen; as $P4/mnm$ YOCl reacts, Y_3O_4Cl and Y_2O_3 emerge while LiCl continues to grow.

At 515 °C, Mn_2O_3 reacts with the remaining Li_2CO_3 according to the reaction in Equation 4:

$$\mathrm{Mn_2O_3 + Li_2CO_3 \longrightarrow 2\,LiMnO_2 + CO_2} \tag{3.4}$$

TGA-MS (Figure 3.2) shows a sharp increase in the CO_2 signal at this temperature, supporting the reaction with Mn_2O_3. Crystalline $LiMnO_2$ ($C2/m$, Figure 3.1) begins to grow at 515 °C, while the Mn_2O_3 begins to lose intensity.

Reactive Zone III (620-650 °C) begins with the melting of lithium chloride at 620 °C and ends with the formation of $YMnO_3$ products. During this zone, the Mn_2O_3 loses intensity rapidly as LiCl melts. Concomitantly, the intensity of $LiMnO_2$ grows over this range. At 630 °C, the nucleation and growth of both h-$YMnO_3$ and o-$YMnO_{3+\delta}$ occurs. Above this temperature, all remaining ternary intermediates react while both $YMnO_3$ phases grow. TGA-MS (Figure 3.2) shows a large mass loss above this temperature that is associated with the volatilization of lithium chloride, which has been observed previously in assisted metathesis reactions involving lithium carbonate.[73] Unfortunately, lithium chloride also

corrodes the quartz capillary at this temperature, as evidenced by the increase in crystalline SiO_2 at $\sim 4^\circ$ 2θ (Figure 3.1). Thus, $in\ situ$ isothermal studies at such elevated reaction temperatures are not viable as the capillary disintegrates over time. The formation of both hexagonal and orthorhombic $YMnO_3$ polymorphs occurs simultaneously at 630 °C. As temperature increases, the amount of o-$YMnO_{3+\delta}$ increases at a faster rate than the hexagonal polymorph.

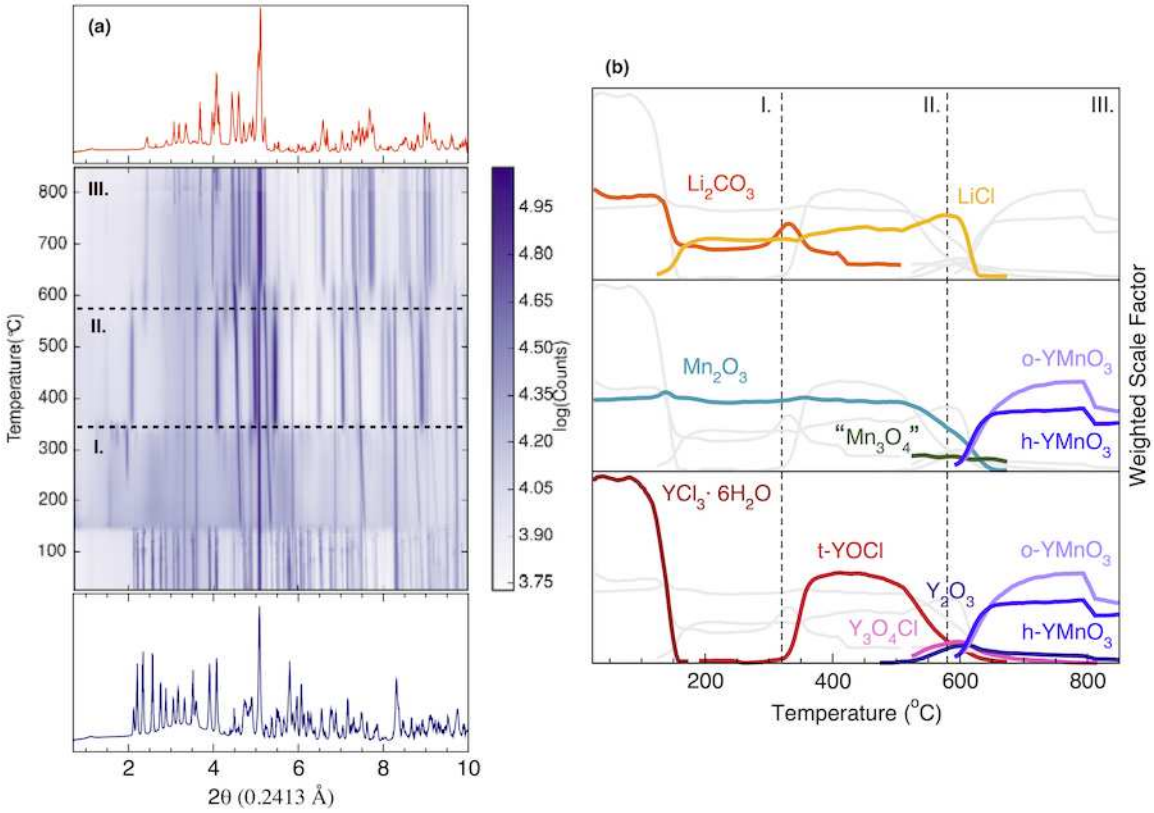


Figure 3.3: $In\ situ$ PXRD results of the reaction: $Mn_2O_3 + 2.2\,YCl_3 \cdot 6\,H_2O + 3\,Li_2CO_3$ under flowing helium. (a) Powder diffraction patterns as a function of temperature (b) Weighted scale factor of each phase during the reaction pathway from Rietveld refinement as a function of temperature. Both (a) and (b) are separated into three reactive zones: I Reactivity of yttrium chloride and formation of YOCl; II Oxidation of YOCl and formation of $LiMnO_2$; III Melting of LiCl and $YMnO_3$ formation. Each sub-panel in (b) is separated by cation for visualization purposes with the gray lines denoting phases with other cations. Quotation marks denote that Mn_3O_4 is poorly resolved from $Li_2Mn_2O_4$ in our refinement.

To test the role of reaction atmosphere on the observed products, the assisted metathesis reaction in Equation 1 was performed under flowing helium while monitoring the re-

action progress with $in\ situ$ SXRD. Figure 3.3 shows the integrated diffraction patterns as a function of temperature along with the calculated scale of relevant phases from Rietveld analysis during the reaction. Reactive zones I, II, and III (Figure 3.3) follow the same general trends as Figure 3.1 with the exception of two major differences. First, there is no distinguishable formation of the ternary intermediate $LiMnO_2$ during the reaction under helium. During Zone II, the only crystalline intermediate that forms when Mn_2O_3 reacts is the spinel Mn_3O_4. It should be noted that this phase is poorly resolved in the diffraction data and possesses the same space group as the tetragonal spinel "$Li_2Mn_2O_4$" ($I4_1/amd$) with comparable unit cell parameters. The second difference is observed upon the formation and growth of $YMnO_3$ phases in Zone III Under flowing helium, where the formation of $YMnO_3$ phases occurs at 580 °C as compared to 630 °C under flowing oxygen. Also, both hexagonal and orthorhombic polymorphs seem to grow at comparable rates during heating. This contrasts with the reaction performed in O_2 (g) (Figure 3.1), where the orthorhombic polymorph grows at a much faster rate as compared to the hexagonal polymorph. A drop in intensity of all phases is observed above 800 °C in Figure 3.3 due to degradation of the capillary.

$Ex\ situ$ reactions show that the atmosphere changes which phase of $YMnO_3$ dominates after extended duration reactions. Under flowing oxygen, the orthorhombic phase selectively forms after 4 hours (Fig. 3.4(a)). Reactions performed at 850 °C under flowing argon show both h-$YMnO_3$ and o-$YMnO_3$ form upon heating while longer reactions form h-$YMnO_3$ as the observed product. Analysis of the calculated unit cell volume (Fig. 3.4(b)) using different environments supports the oxidation to o-$YMnO_{3+\delta}$ when performing the reaction under flowing oxygen.

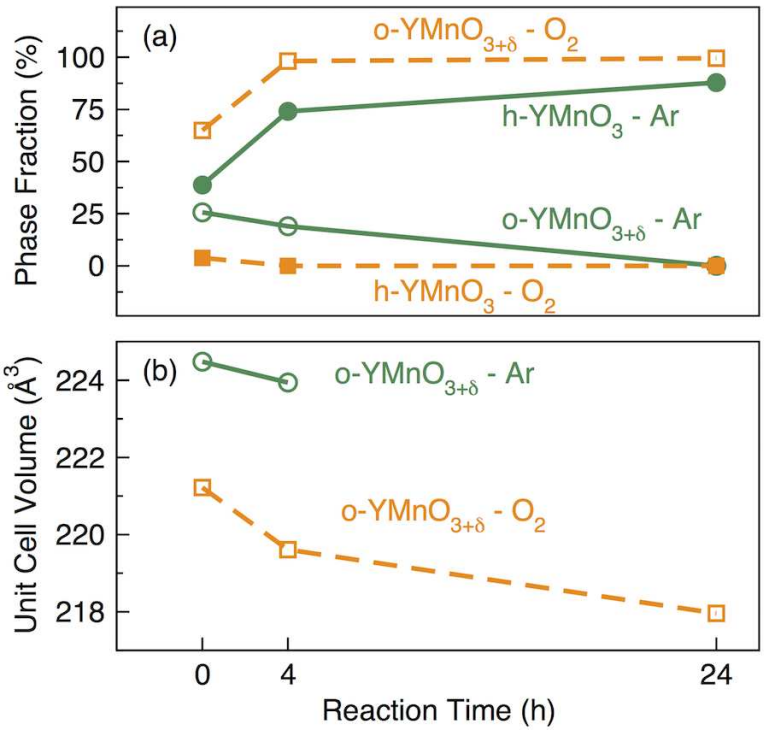


Figure 3.4: (a) $YMnO_3$ products calculated from *ex situ* assisted metathesis reactions at 850 °C (Eq 1.) under flowing argon (green) versus oxygen (orange) at various reaction times. Open symbols represent the calculated phase fraction of o-$YMnO_{3+\delta}$ while solid symbols show the phase fraction of h-$YMnO_3$. (b) Calculated volumes of o-$YMnO_{3+\delta}$ products from the reactions in (a). The reactions performed under flowing oxygen show a decrease in reaction volume as a function of time.

Additionally, control reactions were performed at various temperatures and oxygen partial pressures to understand how oxygen fugacity affects phase formation. The relative amounts of each $YMnO_3$ product are displayed in Figure 3.5 as individual pie charts. It is likely that these reactions do not fully equilibrate after 24 h; as such, we assume the majority product to be most stable under the experimental conditions. At high temperatures, regardless of oxygen partial pressure, the hexagonal polymorph dominates. At high oxygen partial pressures the o-$YMnO_3$ phase forms over the temperature range of 550-850 °C. At temperatures below 700 °C and $pO_2 < 1$atm, mixed products of h-$YMnO_3$ and

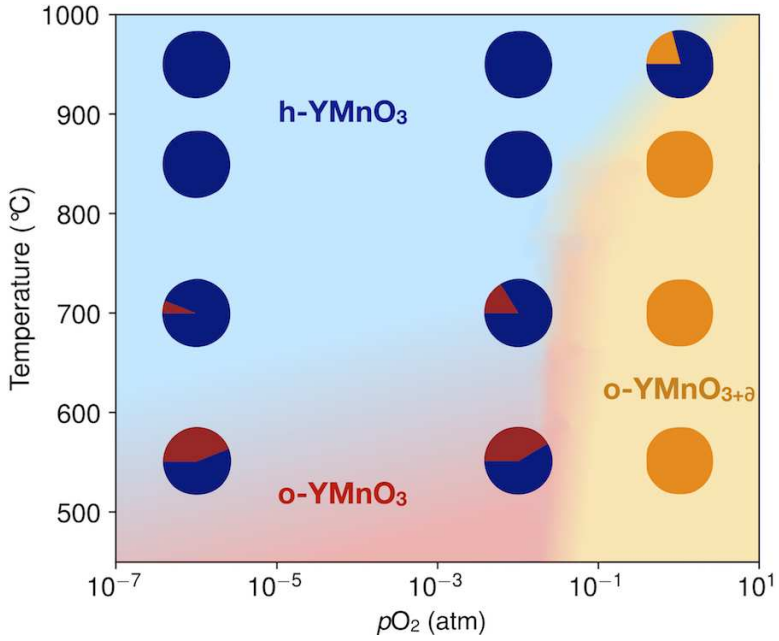


Figure 3.5: (a) $YMnO_3$ products calculated from $ex\ situ$ assisted metathesis reactions at various temperatures and oxygen partial pressures (Eq 1.). Each pie chart denotes the relative molar phase fraction of each $YMnO_3$ phase as calculated from Rietveld refinements after 24 h reactions: navy = h-$YMnO_3$, red = o-$YMnO_3$, and orange = o-$YMnO_{3+\delta}$. Shaded regions illustrate the qualitative change in phase formation under the presented conditions. At high temperatures, h-$YMnO_3$ dominates. At high oxygen partial pressures and temperatures below 850 °C the over-oxidized o-$YMnO_{3+\delta}$ forms selectively. At temperatures below 750 °C and lower oxygen partial pressures, a mixture of h-$YMnO_3$ and o-$YMnO_3$ are observed.

stoichiometric o-$YMnO_3$ appear. At temperatures below 550 °C no $YMnO_3$ products are observed.

Analysis of the crystalline intermediates along the reaction pathway leads to the construction of two primary hypotheses that lead to $YMnO_3$ formation:

$$\mathrm{YOCl} + \mathrm{LiMnO_2} \longrightarrow \mathrm{LiCl} + \mathrm{YMnO_3} \tag{3.5}$$

$$\mathrm{Y_2O_3} + \mathrm{Mn_2O_3} \xrightarrow{6LiCl} 2\,\mathrm{YMnO_3} \tag{3.6}$$

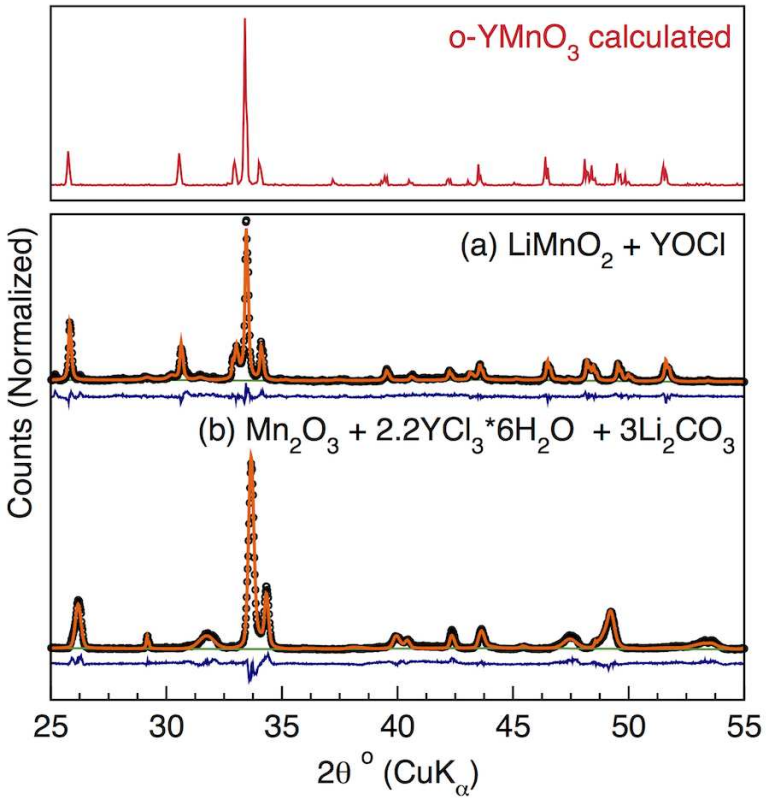


Figure 3.6: Comparison of $ex\ situ$ reactions (a) $LiMnO_2 + YOCl$, 500 °C, 24 h, $<$ 10 mTorr; and (b) $Mn_2O_3 + 2.2\,YCl_3 \cdot 6\,H_2O + 3\,Li_2CO_3$, 850 °C, 24 h, Flowing O_2. Both reactions were heated at 10 °C/min. The calculated X-ray diffraction pattern is provided for o-$YMnO_3$ from the ICSD. The product in (a) matches the stoichiometric o-$YMnO_3$ while the pattern in (b) shows differences in peak position and shape for the o-$YMnO_{3+\delta}$ phase.

In order to test the viability of each hypothesized reaction, $ex\ situ$ control reactions were performed and the diffraction patterns of the products are shown in Figure 3.6 & 3.7. The reaction between ternary intermediates (Eq. 5, 500 °C, 24 h, *in vacuo*) shows the formation of o-$YMnO_3$ as the main product (Fig 3.6(a)) while the reaction from the oxides in a lithium chloride flux (Eq. 6) remains predominately binary oxides (Fig. 3.7(a)). If the temperature for the flux reaction is increased to 600 °C for 24 h, o-$YMnO_3$ partially forms (Fig. 3.7(b)), while at 850 °C h-$YMnO_3$ is the major product after 24 h (Fig. 3.7(c)). Compared to the reaction shown in Equation 5, the reaction from the oxides requires higher

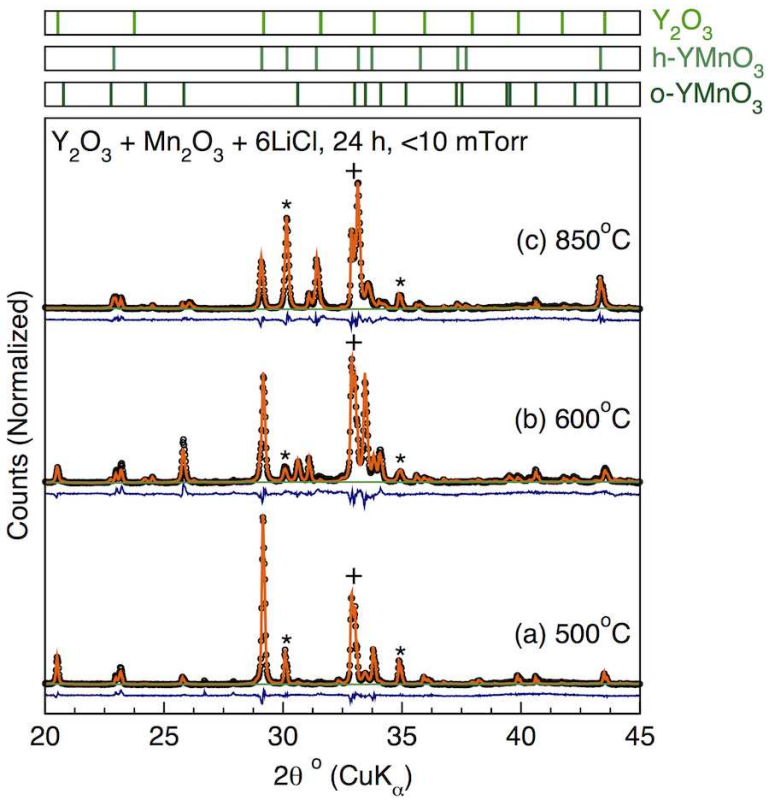


Figure 3.7: Comparison of $ex\ situ$ reactions from the reaction: $Y_2O_3 + Mn_2O_3 \xrightarrow{6LiCl}$ at (a) 550 °C (b) 600 °C (c) 850 °C. All reactions were heated at 10 °C/min to the reaction temperatrue for 24 h under vacuum in a sealed quartz ampule. Reported structures from ICSD are denoted as tick marks. Main reflections for $LiCl \cdot H_2O$: $+$ and LiCl: $*$ are present but not identified using tick marks.

temperatures and longer times than the reaction from ternary intermediates, even in a LiCl flux. In the assisted metathesis reactions formation of the orthorhombic product depends on an oxygen-rich reaction environment, but the control reactions shown in Figure 3.6 both are performed $in\ vacuo$. Unit cell volumes calculated from Rietveld refinements confirmed that the unit cell volume of the o-$YMnO_3$ formed in Equation 5 (225.39 Å^3) matches that of single crystal o-$YMnO_3$ (225.56Å^3);[83] over-oxidized $YMnO_{3.11}$ has a unit cell volume contraction (219.97Å^3).[73] Comparison of the PXRD data of $YMnO_{3.11}$ from assisted metathesis reactions at 850 °C for 24 h in flowing oxygen is displayed in Figure 3.6(b) to show the change in peak position and anisotropic peak broadening of the over-oxidized

phase. The calculated orthorhombic $YMnO_3$ matches the o-$YMnO_3$ product from ternary metathesis (Fig. 3.6(a)). Therefore, we conclude that the orthorhombic phase formed in Figure 3.6(a) is stoichiometric and not the over-oxidized polymorph (Fig. 3.6(b)).

3.5. Discussion

The collective results from these $in\ situ$ SXRD experiments using assisted metathesis reveal a kinetically-controlled reaction pathway that proceeds through transient intermediates. Analysis of these crystalline intermediates and their reaction temperature regimes illustrates the competence of assisted metathesis precursors to overcome diffusion limitations in the formation of complex oxides. Previous studies on the kinetics of complex oxide formation are inherently limited to studying diffusion, whether that be in the bulk,[113] thin-films,[114] or hydrothermally.[115] The sluggish reaction kinetics in oxides can be attributed to the slow rate of diffusivity of larger cations within the oxygen sub-lattice, as seen in the synthesis of ternary metal titanates ($BaTiO_3$, $SrTiO_3$) and rare-earth chromium oxides ($LaCrO_3$, $YCrO_3$).[116–118] These observations are supported in previous studies on $YMnO_3$ formation, where reactions from the binary oxides ($Y_2O_3 + Mn_2O_3$) are limited by the refractory nature of yttrium oxide. Even at elevated temperatures and times (900 °C, 96 h) the reaction products include unreacted Y_2O_3 and yttrium-poor YMn_2O_5.[73] Assisted metathesis reactions overcome this diffusion barrier by starting with labile precursors (e.g., YCl_3) that react at lower temperatures.

The presented results illustrate that the choice of reaction environment in the assisted metathesis reactions changes the thermodynamic stability of the product. Previous studies

have shown that oxygen fugacity can affect polymorph stability in TiO_2 polymorphs by favoring defect states in the anatase polymorph at high oxygen fugacities.[119] We have demonstrated that high oxygen fugacity (Fig. 3.5) in assisted metathesis reactions results in the formation of o-$YMnO_{3+\delta}$ at high oxygen partial pressures. At partial pressures below 1 atm, the hexagonal polymorph dominates at all temperatures, although at 550 °C, nominally o-$YMnO_3$ forms as a minority product. These data suggest that o-$YMnO_3$ may be accessible at low temperatures and oxygen partial pressures. Unfortunately, assisted metathesis reactions do not form any yttrium manganese oxide products below 550 °C as Mn_2O_3 is not reactive at this temperature. Thus, if o-$YMnO_3$ is the desired product, a different reaction pathway is needed that competently forms $YMnO_3$ products below 550 °C.

Analysis of the reaction intermediates from Figures 3.1 and 3.3 provide two hypothetical reactions (Eq. 5 & 6) for the formation of $YMnO_3$ products. Equation 5 proposes a metathesis reaction from ternary intermediates that are observed along the reaction pathway. While YOCl forms and reacts comparably under flowing oxygen and argon, the formation of $LiMnO_2$ is only apparent in the reaction pathway under flowing oxygen. When Mn_2O_3 begins to react under flowing helium in Figure 3.3, Mn_3O_4 appears as the only manganese containing intermediate. The mixed-valent Mn_3O_4 spinel ($I4_1/amd$) is poorly resolved in the diffraction data over the temperature range observed (580-680 °C) due to a large number of present phases that overlap in intensity. Interestingly, the nominally tetragonal spinel "$Li_2Mn_2O_4$" ($I4_1/amd$) also exists with similar lattice parameters as Mn_3O_4. Mn_3O_4 is used in the sequential refinement as the intermediate in Figure 3.3 as the Rietveld calculations have improved statistics (Mn_3O_4 R_wp = 9.886, $Li_2Mn_2O_4$ R_wp =

10.356) during this temperature range. While Mn_3O_4 provides the best statistical fit to the data, we cannot rule out that $Li_2Mn_2O_4$ is not present in some amount at this temperature under flowing helium. Thus, we deduce that the ternary metathesis reaction in Equation 5 is a plausible pathway for the formation of $YMnO_3$, regardless of environment.

The reaction from binary oxides in a lithium chloride flux (Eq. 6) is derived from the two observations from the reaction pathways: (1) the eventual formation of Y_2O_3 from yttrium chloride precursors and (2) the observed T_{rxn} of Mn_2O_3 coinciding with the melting of LiCl. Alkali halide fluxes have been used previously to accelerate the synthesis of yttrium silicates[120] and are used extensively as fluxes in the growth of single crystal complex oxides.[121] Thus, if both binary oxides are present in a molten, reactive environment (LiCl T_m = 605 °C), the activation barrier of yttrium oxide diffusion can be lowered to form $YMnO_3$.

While each proposed hypothesis can explain the observed formation of $YMnO_3$, $ex\ situ$ control reactions reveal that the rate at which each reaction proceeds differs. The reaction from the ternary intermediates (Eq. 5, Fig. 3.6(a)) proceeds at lower temperatures and shorter times than the reaction from the binary oxides using a lithium chloride flux (Eq. 6, Fig. 3.7(a)). Even at higher temperatures (Figure 3.7(b,c)), the reaction from the oxides is still incomplete after 24 h. The assisted metathesis reactions proceed to completion at reaction times as low as 4 h at 850 °C suggesting that the formation and reaction between ternary intermediates is kinetically-controlling the reaction pathway.

Analysis of these ternary reaction intermediates reveals why they are kinetically competent at lower temperatures. Both $P4/nmn$ YOCl and $C2/m$ $LiMnO_2$ adopt layered structures (Fig. 3.8) that facilitate and increase diffusion as compared to the structurally dense

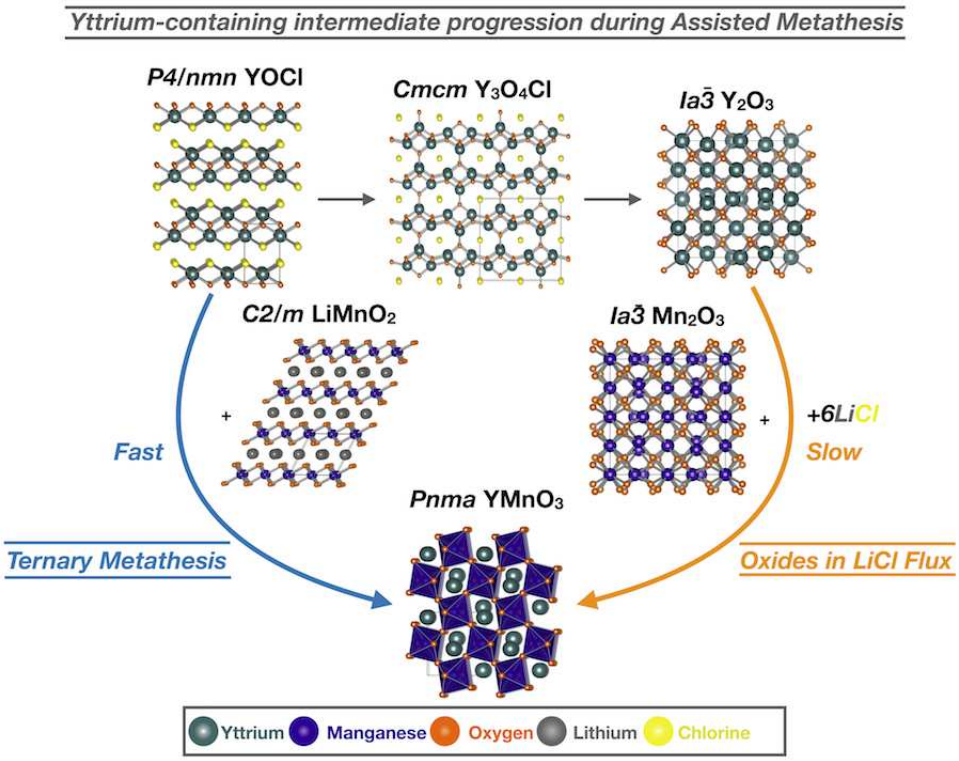


Figure 3.8: Comparison of the structures for the proposed intermediate reactions in Equations 5 & 6 as derived from characterization of the assisted metathesis reaction pathway. Yttrium-containing intermediates were derived from characterizing the the assisted metathesis reaction pathways (Fig. 3.1 & 3.3). From $ex\ situ$ control reactions the ternary metathesis reaction ($YOCl + LiMnO_2$) is the kinetically controlling reaction pathway and, while still a competent reaction pathway, the reaction from binary oxides in a lithium chloride flux ($Y_2O_3 + Mn_2O_3 \xrightarrow{6LiCl}$) requires longer reaction times to arrive at the orthorhombic $YMnO_3$ product.

binary oxides which adopt the cubic $Ia\bar{3}$ structure (Fig. 3.8). The $C2/m$ $LiMnO_2$ adopts a disordered α-$NaFeO_2$-type structure with slight site mixing between the lithium and manganese. All yttrium containing intermediates ($R\bar{3}m$ YOCl, $P4/nmn$ YOCl, $Cmcm$ Y_3O_4Cl) form ordered layers of alternating oxygen and chlorine bilayers separated by yttrium. The YOCl begins forming at temperatures much lower than the formation of $LiMnO_2$, but the slow conversion to Y_2O_3 allows for these layered intermediates to persist long enough to react to form $YMnO_3$. The structurally-dense $Ia\bar{3}$ Y_2O_3 does form during the reaction pathway but reacts upon the melting of LiCl. Therefore, the ternary metathesis reaction

Table 3.1: Conditions for selective synthesis of $YMnO_3$ phases

Phase	o-$YMnO_3$	o-$YMnO_{3+\delta}$	h-$YMnO_3$
Space Group	$Pbnm$	$Pbnm$	$P6_3cm$
Reaction Type	Ternary metathesis (Eq. 5)	Assisted Metathesis (Eq. 1) Ternary metathesis (Eq. 5) LiCl flux (Eq. 6)	Assisted Metathesis (Eq. 1) Ternary metathesis (Eq. 5) LiCl flux (Eq. 6)
Conditions	T <600 °C	T = 500 - 850 °C	T > 600 °C
Evironment	Vacuum, inert gas	O_2, air	Vacuum, inert gas

between $LiMnO_2$ and YOCl is the most competent pathway, but it is not the only reaction pathway possible during an assisted metathesis reaction.

Taken together, three unique reaction conditions enable competent low-temperature, selective syntheses of three different $YMnO_3$ phases (Table 1). The identification and development of ternary metathesis reactions has been previously shown using lithium manganese oxide and lanthanum oxychloride to form $LaMnO_3$ at 850 °C for 12 h.[58] By reducing the reaction temperature even further (850 °C to 500 °C), the ternary metathesis permits the formation of o-$YMnO_3$, which appears to be thermodynamically stable at these lower temperatures. Previous studies using hydrothermal[83,93] or citrate decomposition[89,90] pathways have resulted in the formation of o-$YMnO_3$ at similar temperatures, but the kinetic factors governing these reactions are more difficult to elucidate than the solid-state reactions studied here. The ternary metathesis reactions pose another system of kinetically competent reactions when considering new complex oxides: they are less complex than the three-component assisted metathesis systems and can be performed $in\ vacuo$, reducing the compositional complexity and improving phase selectivity. Future studies will aim to expand the compositional space of these reactions.

3.6. Conclusion

In situ SXRD has been used to characterize the reaction pathway in the assisted metathesis reaction: $Mn_2O_3 + 2.2\,YCl_3 \cdot 6\,H_2O + 3\,Li_2CO_3$ $\longrightarrow 2\,YMnO_3 + 5.8\,LiCl + 0.2\,LiYCl_4(g) + 3\,CO_2 + 12.4\,H_2O$. It has been determined that the selectivity of reaction products is dependent on the reaction atmosphere. The over-oxidized perovskite o-$YMnO_{3+\delta}$ forms under flowing oxygen while the hexagonal $YMnO_3$ forms under inert conditions at 850 °C at long time points. While reaction atmosphere determines the product stability in assisted-metathesis, *in situ* analysis of the reaction progress identifies YOCl and $LiMnO_2$ as the intermediates that kinetically control formation of o-$YMnO_3$. Using these intermediates as precursors to perform ternary metathesis leads to the formation of nominally stoichiometric o-$YMnO_3$ at 500 °C. While molten LiCl may also enhance mass transport in the reaction, the ternary metathesis reaction yields products in a shorter amount of time and at temperatures lower than the melting point of LiCl, as confirmed by *ex situ* control experiments.

4. Sodium catalyzed and selective synthesis of "metastable" $Y_2Mn_2O_7$[‡]

Overview

There are few examples of solid-state chemical reactions where a catalyst enables product selectivity. Inherently, solid-state chemistry is limited by diffusion, where high thermal energy barriers dominate the potential energy landscape resulting in the product at the global or local energy minimum (i.e., thermodynamic control). To selectively synthesize products away from equilibrium, reactions must proceed to completion at temperatures where kinetics can influence the outcome. Here, we present a solid-state reaction that selectively yields reportedly "metastable" $Y_2Mn_2O_7$ through a sodium catalyzed pathway at relatively low temperatures. By characterizing reaction intermediates using *in situ* synchrotron X-ray diffraction experiments, we observe Y_2O_3 and Na_xMnO_2 as the intermediates that form the pyrochlore $Y_2Mn_2O_7$. Analysis of the composition of these intermediates yields a series of pseudo-elementary steps dependent on a series of defect reactions in the Na_xMnO_2 intermediate. This cascade of defect reactions results in reactive [MnO_2] species that react with small particles of Y_2O_3 to selectively yield the pyrochlore. Sodium acts catalytically in forming the Na_xMnO_2 intermediate and anchoring the structure as [MnO_2]

[‡]Substantial portions of this chapter have been reproduced with permission from P. K. Todd, M. J. McDermott, C. L. Rom, A. A. Corrao, J. Denney, S. S. Dwaraknath, P. Khalifah, K. A. Persson and J. R. Neilson, *Prepared Manuscript* **2020**

fragments are removed. This discovery highlights a new kinetically-controlled reaction mechanism that permits the synthesis of complex oxides at low-temperatures.

4.1. Author Contributions

PKT performed all experiments and coordinated results between researchers. CLR assisted with synchrotron experiments. MJM, SSD and KAP performed all thermochemistry-based calculations. JD and PGK assisted in f^* calculations, analysis, and visualization. AC assisted in writing scripts for data analysis. PKT and MJM wrote the manuscript with the guidance of JRN, SSD, KAP, and PGK.

4.2. Introduction

In molecular chemistry, the understanding of reaction mechanisms is the foundation to synthesizing metastable products; the use of catalysts to direct and control the outcome of reactions at their transition states is routine. In solid-state materials synthesis, reactions are limited by diffusion, where high initial energy barriers limit reaction selectivity, which results in the formation of the lowest energy product.[5] Metastable phases can be kinetically trapped in solid-state synthesis by changing thermodynamic variables such as pressure (diamond vs. graphite) or manipulation of particle surface area (TiO_2 [19]), however this requires that targeted phases become the most stable phase under a specific set of environmental conditions. Instead, kinetic control permits the synthesis of materials that are not the most stable phase under any thermodynamic conditions.[6] In order to implement kinetic control in material synthesis, precursors must react at moderately

low temperatures in order to impart selectivity through the manipulation of *kinetic* energy barriers along the reaction pathway.[20]

Kinetic control in material synthesis is thought to originate with topotactic reactions in which labile ions are inserted or removed within a rigid structural motif (e.g., layers, channels).[21,122] This "soft-chemistry approach" enables tunable electronic properties in superconducting copper and nickel oxides[28,123] and labile anion removal/reduction reactions in the preparation of metastable $SrFeO_2$.[31] Another strategy involves reducing diffusion lengths of reactants to the atomistic scale through thin film deposition techniques, where reaction pathways are instead limited by nucleation of a particular phase at a targeted composition,[18,48] which has led to kinetic control in the synthesis of metastable phases in high-temperature superconductors[50] Previously, we have shown that solid-state metathesis reactions circumvent diffusion depending on the preparation method of reactants[66] which permits kinetic control in the synthesis of metastable oxides,[73] nitrides,[55] and chalcogenides.[68,76] In the preparation of complex oxides, "assisted" metathesis reactions exhibit selectivity in yielding metastable polymorphs through changes to the alkali carbonate precursor in the reaction: $3\,A_2CO_3 + 2\,YCl_3 + Mn_2O_3$, where A = Li, Na, K.[73] When starting with lithium carbonate, the identitication of reaction intermediates, $LiMnO_2 + YOCl$, leads to a kinetically faster reaction pathway and improved product selectivity of the nominally metastable perovskite $YMnO_3$.[110]

This contribution details the sodium *catalyzed* assisted metathesis reactions which selectively yields metastable $Y_2Mn_2O_7$:

$$\mathrm{Mn_2O_3 + 2\,YCl_3 + 3\,Na_2CO_3 + \frac{1}{2}\,O_2 \longrightarrow Y_2Mn_2O_7 + 6\,NaCl + 3\,CO_2.} \tag{4.1}$$

Previous reports have synthesized $Y_2Mn_2O_7$ using high temperatures and pressures[92] or hydrothermally under oxidizing conditions,[94] yet it remains unclear the synthetic variables that select for these high-pressure pyrochlores.[124] Using temperature-dependent synchrotron X-ray diffraction (SXRD) experiments, we identify a reaction pathway dependent on the formation of Y_2O_3 and Na_xMnO_2 intermediates. Crystallographic analysis of Na_xMnO_2 along the pathway reveals pseudo-elementary steps that produce [MnO_2] species, which react with small particles of Y_2O_3 to yield the pyrochlore (Fig. 4.1). DFT-based thermochemistry reveals an equilibrium-like progression of the reaction as the pseudo-elementary steps yield precise control over the chemical potential of each component, as supported by myriad control reactions. The result is the identification of a new mechanism to selectively synthesize metastable complex oxides at low-temperatures in solid-state chemistry.

4.3. Methods

All reagents were prepared, stored, and weighed in an argon-filled glovebox with O_2 and H_2O levels $\leq$ 0.1ppm. Manganese(III) oxide (Sigma Aldrich 99%) was purified by heating Mn_2O_3 in an alumina boat at 1 °C/min to 700 °C for 16 h in air and quenched into the glovebox; purity was verified by powder X-ray diffraction (PXRD). Manganese (IV) ox-

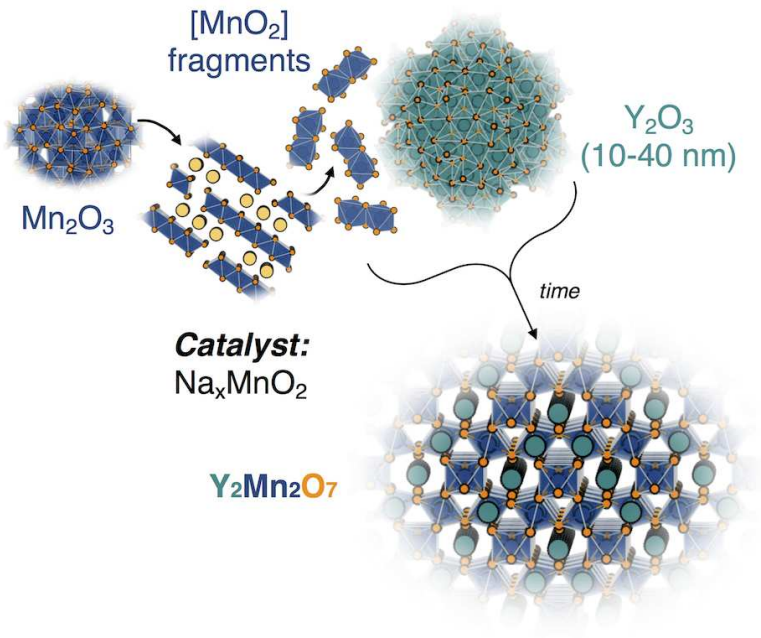


Figure 4.1: Schematic illustrating the hypothesized mechanism to form $Y_2Mn_2O_7$ catalyzed by sodium via the Na_xMnO_2 intermediate. The reactive $[MnO_2]$ species produced in the elementary steps in Eqn. 4.9a-4.9d react directly with small particles of Y_2O_3 at the reaction interface.

ide (Sigma Aldrich $\geq$ 99%), YCl_3 (Alfa Aesar 99.9%), sodium carbonate (ACROS Organics 99.5%), and manganese (II) carbonate (Sigma Aldrich $\geq$ 99.99%) were purchased and stored under argon. All gases (O_2, Ar, He) were purchased through Airgas at the Ultra High Purity grade (99.999%). $NaMnO_2$ ($C2/m$) was prepared by mixing manganese (III) oxide and sodium carbonate in a 1:1 molar ratio, grinding for 15 minutes in an agate mortar and pestle, and pelleting using a $1/4$ in die under $\sim$1 tn of force. The pellet was placed upon a sacrificial layer of powder in an alumina crucible and heated in a muffle furnace at 1 °C/min to 700 °C for 10 h. The reaction was subsequently quenched into the antechamber of the glovebox and stored under argon. Similarly, $Na_{0.7}Mn_2O_4$ ($Cmcm$) was prepared by mixing manganese (II) carbonate and sodium carbonate in a 0.70:2 Na:Mn ratio following the same pellet preparation as $NaMnO_2$. The reaction was performed by heating at 5 °C/min to 1050 °C for 15 h and then quenching into the antechamber of a

glovebox and stored under argon. Y_2O_3 was purified of hydroxide in an alumina boat at 1 °C/min to 900 °C for 4 h in air, cooled to 200 °C at 1 °C/min for 12 h, and quenching into the glovebox. YOCl was prepared by heating $YCl_3 \cdot 6\,H_2O$ in an alumina boat to 350 °C at 10 °C/min for 4 h in air. The YOCl product formed as the $P4/nmn$ PbClF structure-type. All prepared reactants were confirmed using laboratory PXRD. Preparations for $ex\ situ$ assisted metathesis reactions have been described in detail previously.[73] Laboratory PXRD data were collected on a Bruker D8 Discover diffractometer using Cu Kα radiation and a Lynxeye XE-T position-sensitive detector.

For temperature-dependent $in\ situ$ assisted metathesis reactions that produce carbon dioxide as a by-product, open-ended quartz capillaries (1.1 mm OD) were packed in a glove-bag under argon using glass wool as a plug. Synchrotron X-ray diffraction experiments were performed at beamline 17-BM-B (λ = 0.2415 Å) at the Advanced Photon Source (APS) at Argonne National Laboratory using a Perkin Elmer plate detector at a distance of 700 mm. All capillaries were loaded into a flow-cell apparatus equipped with resistive heating elements and heated at 10 °C/min.[111] Gas flow (O_2, He) was controlled through mass flow controllers at a rate of 0.2 cc/min. Assisted-metathesis reactions were heated to a maximum temperature of 850 °C while the sample continuously rocked at $\pm$ 5° around the axis of the capillary. Diffraction patterns were collected every two seconds and summed every 20 seconds for powder averaging. Plate detector images were integrated using GSAS-II and calibrated using a LaB_6 standard.

All Rietveld refinements were performed using TOPAS v6. Due to the number and positional overlap of intermediates during the sequential refinements, thermal displacement parameters were fixed at 5Å^2 and the full-width-half-max using a Lorentzian polynomial

was fixed at 178 nm to better account for changes in peak intensity during the reaction. In order to compare the relative fractions of phases determined from Rietveld calculations,[70] a weighted scale factor (WSF) is defined as: $Q_p = S_p \cdot V_p \cdot M_p$ where Q_p = weighted scale factor of phase p, S_p = Scale factor calculated from Rietveld for phase p, V_p is the volume of the unit cell for phase p, and M_p is the atomic mass of the unit cell for phase p. It should be noted that we omit the Brindley coefficient for microabsorption correction in our calculation of weighted scale factor due to the unreliable refinement of particle sizes for individual phases. Amorphous material and product lost as vapor are not accounted for in the sequential refinement. We reference all phases by their nominal stoichiometric formula; however, the actual chemical formula may be distinct from the written formula as XRD data alone cannot typically resolve non-stoichiometric compounds.

It has been recently demonstrated by some of us that f^* diagrams are a powerful tool for understanding defects in chemical systems with three different crystallographic sites, allowing a diffraction analogue of a ternary phase diagram to be calculated in which each axis represents the relative scattering power of each crystallographic site (at $2\theta = 0$) rather than the chemical composition.[125,126] The f^* diagram method is applied here with a slight modification to understand the evolution of defects within the $Cmcm$ Birnessite phasesNa_xMnO_2. Since this phase has four distinct crystallographic sites (2 Na, 1 Mn, 1 O) rather than three, a pseudo-ternary (in which the scattering power of the two Na sites was summed together) rather than a proper ternary diffraction phase diagram was constructed.

DFT thermochemistry data for material phases in the Y-Mn-O chemical system were acquired from the *Materials Project* database.[1] The *pymatgen* package was used to perform convex hull stability analysis and construct predominance phase diagrams.[127] Tem-

perature dependent phase stability was estimated using the Gibbs free energy descriptor, $G^{\delta}_{SISSO}(T)$ created with the SISSO (sure independence screening and sparisfying operator)[128] approach implemented by Bartel, et al.[3]

4.4. Results

To characterize the crystalline materials present during the sodium carbonate assisted metathesis reactions, $in\ situ$ synchrotron X-ray diffraction (SXRD) was performed upon heating (25 °C $\leq$ T $\leq$ 650 °C; 10 °C/min) and dwelling (650 °C, 1 h). Figure 4.2 presents the integrated SXRD diffraction patterns from the reaction in Equation 4.1 as a function of reaction time (125 min) where the dotted line separates heating from dwelling. Visually, the diffraction patterns in Figure 4.2(a) reveal discrete intermediate reactions that occur upon heating precursors to products. After dwelling (Fig. 4.2(b)), the data reflect gradual changes in product intensity at the expense of relevant intermediate phases.

Quantitative phase analysis using the Rietveld method reveals identities and phase fractions of the intermediates associated with forming metastable pyrochlore $Y_2Mn_2O_7$. The results are summarized in Figure 4.3, where each horizontal subpanel highlights the crystalline phases containing one of three cations present in these reactions (a,d. Sodium, b,e. Manganese, c,f. Yttrium). Together, the results in Figure 4.3(a) describe the reactivity of precursors upon heating to 650 °C.

The first intermediate step that is observed along the pathway is formation of yttrium oxychloride and sodium chloride from the reaction between YCl_3 and Na_2CO_3 at 230 °C:

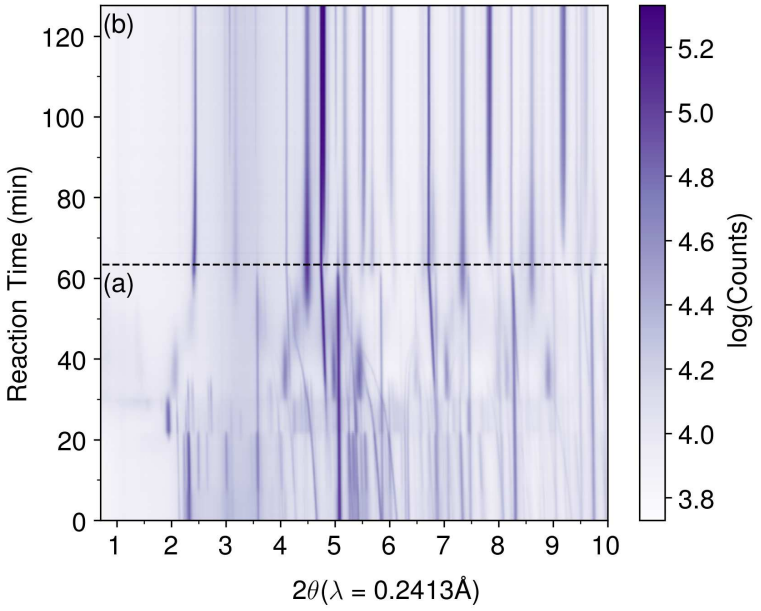


Figure 4.2: $In\ situ$ PXRD data as a function of time for the reaction: $Mn_2O_3 + 2\,YCl_3 + 3\,Na_2CO_3 + \frac{1}{2}\,O_2 \longrightarrow Y_2Mn_2O_7 + 6\,NaCl + 3\,CO_2$ under flowing oxygen. The reaction is separated by a dotted line for (a) heating at 10 °C/min to 650°C and (b) dwelling at 650 °C for 60 min.

$$2\,YCl_3 + 2\,Na_2CO_3 \longrightarrow 2\,YOCl + 4\,NaCl + 2\,CO_2, \tag{4.2}$$

The formation of NaCl at 230 °C corresponds directly with the increase in intensity of the $P4/mnm$ YOCl phase and loss of Na_2CO_3 phase intensity, consistent with lithium carbonate assisted metathesis reactions.[110] YOCl persists over the temperature range 260-490 °C, reacting with more sodium carbonate to form Y_3O_4Cl at 450 °C, and eventually yielding Y_2O_3 at 500 °C.

The relevant intermediates for the formation of $Y_2Mn_2O_7$ appear to be Y_2O_3, Na_xMnO_2, and a small amount of Mn_2O_3. The precursor Mn_2O_3 remains unreacted until 540 °C when remaining Na_2CO_3 reacts to form the Birnessite-type $Cmcm$ Na_xMnO_2 intermediate:

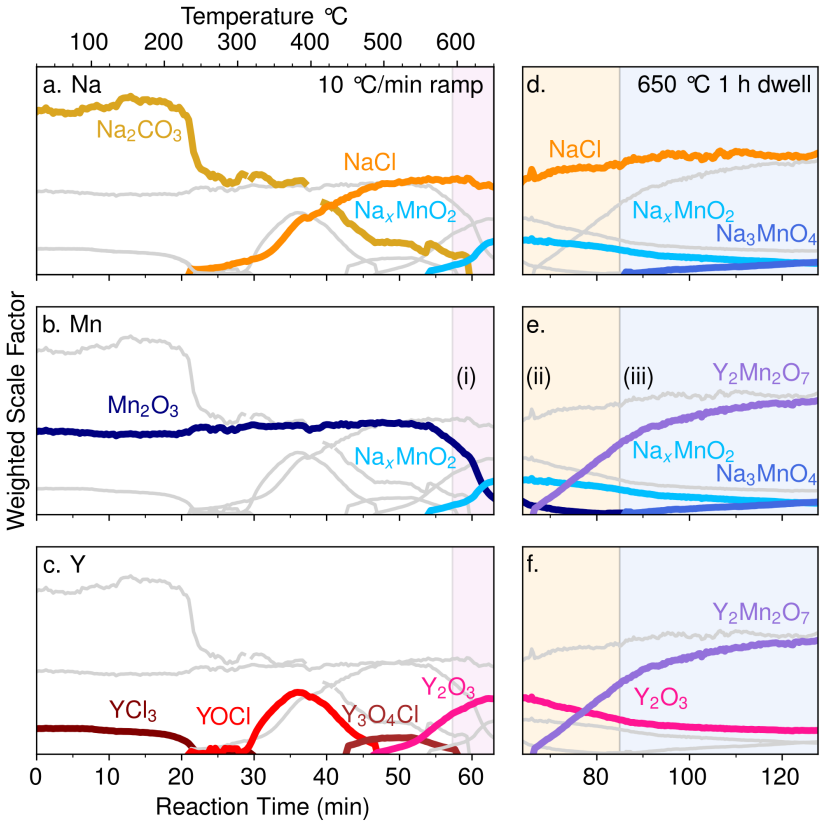


Figure 4.3: Calculated Weighted Scale Factor phase present from the data in Figure 1. Each vertical panel is separated by reaction schedule: (a-c) heating at 10 °C/min to 650 °C and (d-f) dwelling at 650 °C for 60 min. Horizontally, the sequential refinement is separated by cation for visualization: (a,d). Sodium, (b,e). Manganese , and (c,f). Yttrium. The gray lines denote all other phases present during the reaction. The shaded region, i.,ii., and iii., correspond to trajectories highlighted in Figure 4.4.

$$x\mathrm{Na_2CO_3} + \mathrm{Mn_2O_3} \longrightarrow 2\,\mathrm{Na_xMnO_2} + x\mathrm{CO_2} \tag{4.3}$$

Upon reaching the dwell temperature of 650 °C, the pyrochlore $Y_2Mn_2O_7$ starts to form (Fig. 4.3(b)), while the phase fractions of Y_2O_3, Mn_2O_3, and Na_xMnO_2 slowly decrease. The fraction of NaCl does not significantly change. From the identity of these interme-

diates, the destination for sodium from Na_xMnO_2 upon formation of $Y_2Mn_2O_7$ is unclear. Therefore closer inspection of the structural evolution of these intermediates is required.

The Na_xMnO_2 intermediate is best described by the orthorhombic *Cmcm* P2′ layering. The P2′ designation occurs from a slight shift of the MO_2 layers at high temperatures from the P2-$P6_3/mmc$ structure, and sodium occupies both the prismatic and octahedral sites at fractional occupancy.[129–131] During the reaction, no O3-type polymorphs were observed upon formation of Na_xMnO_2, and attempts to fit a monoclinic $C2/m$ α-$NaMnO_2$ phase or orthorhombic $Pmnm$ β-$NaMnO_2$ to the SXRD data were unsuccessful. Thus, we only observe the $Cmcm$, P2′ polytype of Na_xMnO_2 during the formation of $Y_2Mn_2O_7$.

Analysis of the composition and defect chemistry of the Na_xMnO_2 intermediate reveals discrete reaction steps concomitant with $Y_2Mn_2O_7$ formation. Free refinement of the crystallographic site occupancies of all three elements in Na_xMnO_2 and subsequent analysis on an f^* diagram[125] reveals how the stoichiometry of Na_xMnO_2 evolves through three different defect reactions. The distinct compositional trajectories of the Na_xMnO_2 phase, delineated on Figure 4.4, follow three major processes during the reaction pathway: (i) Na_xMnO_2 formation, (ii) a crossover region of continued Na_xMnO_2 formation and initial $Y_2Mn_2O_7$ formation, and (iii) extended $Y_2Mn_2O_7$ production.

The initial formation of Na_xMnO_2 results in a highly defective and oxidized intermediate. Trajectory (i) in Figure 4.4 describes the defect rearrangement reaction:

$$[\mathrm{Na}_{1-\mathrm{y}}\mathrm{Mn}_{\mathrm{z}}][\mathrm{Mn}_{1-\mathrm{x}}]\mathrm{O}_2 \longrightarrow [\mathrm{Na}_{1-\mathrm{y}}][\mathrm{Mn}_{1-\mathrm{x}+\mathrm{z}}]\mathrm{O}_2, \tag{4.4}$$

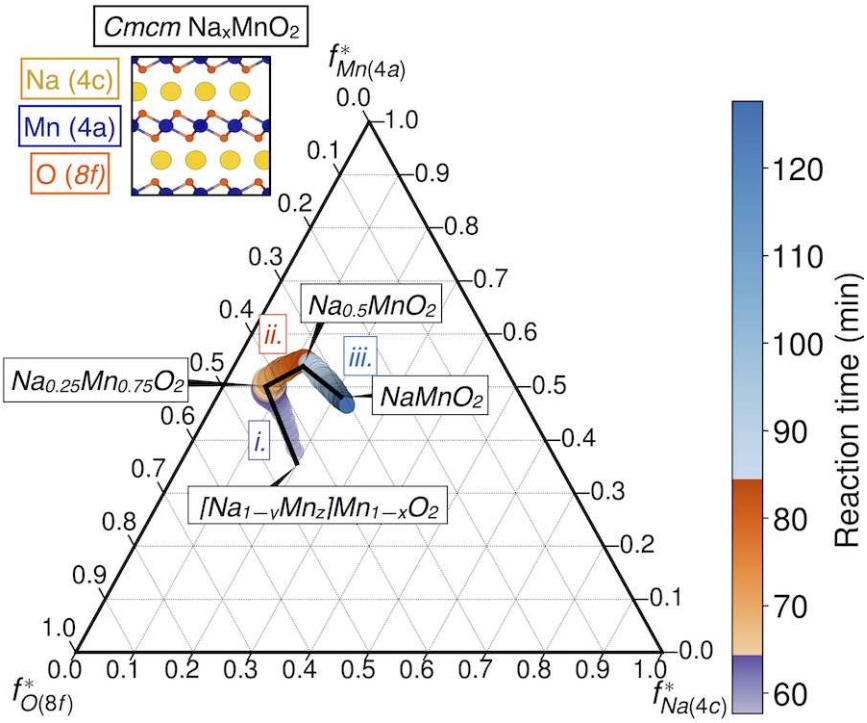


Figure 4.4: f^* diagram of atomic coordinates calculated from Rietveld refinement of $Cmcm$ Na_xMnO_2 in which each axis denotes a crystallographic Wyckoff atom position within the lattice. For reference, calculated trajectories that correspond to the different stoichiometries of Na_xMnO_2 are provided as black lines. The color bar in the figure follows the lifetime of the Na_xMnO_2 intermediate in the assisted metathesis reaction presented in Figure 4.3 with highlighted trajectories (i-iii) reflecting shaded regions in Figure 4.3(i-iii). The diameter of each circle mirrors the calculated Weighted Scale Factor in Figure 4.3 for Na_xMnO_2. The structure of $Cmcm$ Na_xMnO_2 is shown with Wyckoff atom sites labeled.

where the first set of brackets describes the composition of the ideal sodium sites, and the second set of brackets describes that of manganese. The position of the starting composition indicates significant excess of scattering intensity on the sodium site relative to the manganese site suggestive of anti-site disorder. Additionally, there is decreased scattering intensity of the metal sites relative to oxygen, which suggests of overall cation deficiencies in the structure. Movement along trajectory (i) yields site ordering of this cation deficient structure during its formation, which is analytically calculated as the black line overlaid on these data in Figure 4.4 (Eqn. 4.4). This ordering reaction proceeds as Na_xMnO_2 forms in Figure 4.3. At that point in the overall reaction, the nominal composition of

the sodium manganese oxide intermediate resembles a site ordered, but cation-deficient $Na_{0.25}Mn_{0.75}O_2$, which formally describes manganese as Mn(V). Therefore, this analysis revises Eqn. 4.3 as:

$$\frac{3}{2}\,\mathrm{Mn_2O_3} + \frac{1}{2}\,\mathrm{Na_2CO_3} + \frac{3}{2}\,\mathrm{O_2} \longrightarrow 4\,\mathrm{Na_{0.25}Mn_{0.75}O_2} + \frac{1}{2}\,\mathrm{CO_2}, \tag{4.5}$$

as the reaction is performed in flowing O_2. This high defect concentration intermediate then reacts to form $Y_2Mn_2O_7$.

At the point $Y_2Mn_2O_7$ starts to form (Fig. 4.3), we observe a change in the defect chemistry of Na_xMnO_2 concomitant with consumption of Mn_2O_3 and Y_2O_3. The change in defect chemistry in Figure 4.4 proceeds along trajectory (ii) from a cation-deficient $Na_{0.25}Mn_{0.75}O_2$ composition to that of $Na_{0.5}MnO_2$. This result is observed from the decrease in relative electron density from the oxygen site (8f), as well as an increase in the sodium to manganese site ratio. Paired with the reduction in WSF of Na_xMnO_2, Mn_2O_3, and Y_2O_3 (Figure 4.3), the following balanced equation summarizes the progression along trajectory (ii) in Figure 4.4:

$$4\mathrm{Na_{0.25}Mn_{0.75}O_2} + \mathrm{Y_2O_3} + \frac{1}{2}\,\mathrm{Mn_2O_3} \longrightarrow \mathrm{Y_2Mn_2O_7} + 2\mathrm{Na_{0.5}MnO_2} + \frac{3}{2}\mathrm{O_2}, \tag{4.6}$$

where the sodium manganese oxide intermediate is both reacting to form $Y_2Mn_2O_7$ and consuming the remaining Mn_2O_3 precursor. During the reaction in Eqn. 4.6, the pyrochlore

grows rapidly (Fig. 4.3 (70–90 min) before tapering off at the end of the second trajectory in Figure 4.4. No other yttrium manganese oxide polymorphs are observed.

The defect reaction trajectory (iii) in Figure 4.4 illustrates how the selective formation $Y_2Mn_2O_7$ is sustained through the reaction of the sodium manganese oxide intermediate. The composition of the intermediate moves from nominally $Na_{0.5}MnO_2$ to $NaMnO_2$, as summarized by Equation 4.7:

$$4\mathrm{Na_{0.5}MnO_2} + \mathrm{Y_2O_3} \longrightarrow \mathrm{Y_2Mn_2O_7} + 2\,\mathrm{NaMnO_2}, \tag{4.7}$$

where there is an observed decrease in electron density of oxygen and manganese sites relative to sodium (Fig. 4.4, consistent with the overall decrease in WSF of Na_xMnO_2 and Y_2O_3 shown in Figure 4.3. Once the intermediate reaches the composition $NaMnO_2$, the phase fraction of $Y_2Mn_2O_7$ continues to increase; yet, movement in the f^* diagram ceases at $NaMnO_2$ as a different crystallographic phase, Na_3MnO_4, forms in small quantities (Fig. 4.3(b)):

$$3\,\mathrm{NaMnO_2} + \mathrm{Y_2O_3} + \mathrm{O_2} \longrightarrow \mathrm{Y_2Mn_2O_7} + \mathrm{Na_3MnO_4} \tag{4.8}$$

It is of note that Na_3MnO_4 does not appear in reaction products of $ex\ situ$ studies of these assisted metathesis reactions, though it may be present as a trace quantity.[73]

The *in situ* SXRD data also provide insight to the reactivity of Y_2O_3. While Y_2O_3 maintains its nominal composition throughout the reaction (Fig. A.15), the broad diffraction peaks of Y_2O_3 reveal the formation of small, high surface area Y_2O_3 crystalline domains ranging from $\sim$5 to 40 nm, even up to 650 °C (Figure A.16). This lends support to the high reactivity of Y_2O_3 described in Eqns. 4.6-4.8.

The calculated phase equilibria provide a thermochemical origin of the differentiation of the reaction towards $Y_2Mn_2O_7$. Thermochemical data acquired from Materials Project density functional theory calculations[1] and NIST-JANAF experimental database,[2] along with application of the Gibbs descriptor from Bartel, et al.,[3] were used to create a predominance phase diagram of material phases in the Y-Mn-O chemical system as a function of yttrium and oxygen chemical potentials (Fig. 4.5) at 900 K. $Y_2Mn_2O_7$ is predicted to be thermodynamically stable up to a temperature of 1400 K, above which application of the Gibbs descriptor suggests the destabilization of $Y_2Mn_2O_7$. The predominance diagram in Fig. 4.5 suggests that $Y_2Mn_2O_7$ is stable at high oxygen chemical potentials and low temperatures. This is a critical insight into understanding the formation of the phase. Thus if the *local* oxygen chemical potential is sufficiently high along the reaction pathway, we would expect $Y_2Mn_2O_7$ to preferentially form.

Control reactions of binary yttrium and manganese oxides reveal that the sodium carbonate assisted metathesis reaction pathway is selective for $Y_2Mn_2O_7$. Analysis of *ex situ* control reactions, $2\,MnO_2 + Y_2O_3$ and $Mn_2O_3 + Y_2O_3$, performed at 650 °C under flowing O_2 at ambient pressure (Figure A.17) reveal that the reactions contain a finite fraction of $Y_2Mn_2O_7$ at initial time points (i.e., no selectivity), and the phase fraction of $Y_2Mn_2O_7$

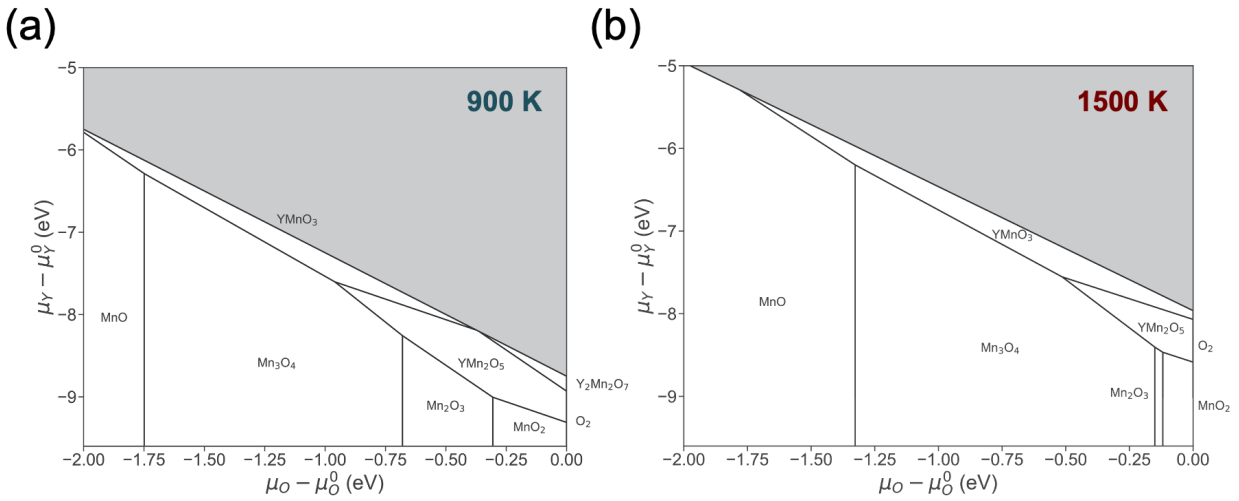


Figure 4.5: Predominance phase diagram for material phases in the Y-Mn-O chemical system as a function of oxygen and yttrium chemical potentials, μ_O and μ_Y. $Y_2Mn_2O_7$ appears to be preferentially synthesized under high oxygen chemical potentials. The phase diagram was calculated using DFT thermochemistry data on the Materials Project[1] and the NIST-JANAF thermochemical tables.[2] The entropic temperature contribution towards phase stability at 900 K is estimated by the Gibbs descriptor from Bartel et al.[3]

decreases at longer times in favor of YMn_2O_5. Based on Figure 4.5 this suggests that the true μ_O is near the border between YMn_2O_5 and $Y_2Mn_2O_7$.

Additionally, the presence of a six molar equivalent of sodium chloride does increase the initial yield of $Y_2Mn_2O_7$, but YMn_2O_5 increases in phase fraction at long reaction times (Figure A.18). In order to access the stability of pyrochlore, washed $Y_2Mn_2O_7$ was heated at 650 °C under flowing oxygen for long duration reactions, which results in the partial, slow decomposition to binary oxides, $Mn_2O_3 + Y_2O_3$ (Fig. A.19).

Control ternary metathesis reactions performed using nominally stoichiometric, ideal sodium manganese oxide precursors does not yield selectivity for $Y_2Mn_2O_7$. In the case of Li_2CO_3-based assisted metathesis reactions,[73] we previously identified that the ternary metathesis reaction, $LiMnO_2 + YOCl \longrightarrow YMnO_3 + LiCl$ yielded improved selectivity for orthorhombic $YMnO_3$ over the analogous assisted metathesis reactions.[110] However, the

reaction, $2\,NaMnO_2 + 2\,YOCl \xrightarrow{O_2}$, results in a mixture of Y-Mn-O products (Fig. A.20). Furthermore, using a partially-oxidized precursor in the reaction, $2\,Na_{0.7}MnO_2$ with 2 YOCl selectively yields $Y_2Mn_2O_7$, but it is incomplete after 24 h (Fig. A.21). Together, these control reactions lend support to the reported metastability of $Y_2Mn_2O_7$ and the importance of the sodium-based reaction pathway in selectively yielding $Y_2Mn_2O_7$.

4.5. Discussion

The presented results permit the construction of pseudo-elementary reactions that explain the selective formation of $Y_2Mn_2O_7$ as facilitated by the Na_xMnO_2 intermediate. The trajectories from the f^* diagram of Na_xMnO_2 (Fig. 4.4) paired with changes in phase fraction from Figure 4.3 provide a mechanistic view of the reaction pathway. These reaction trajectories can be described in the following pseudo-elementary steps:

$$4Na_{0.25}Mn_{0.75}O_2 + \frac{1}{2}\,Mn_2O_3 \longrightarrow 2Na_{0.5}MnO_2 + \frac{3}{2}O_2 + 2[MnO_2] \tag{4.9a}$$

$$4Na_{0.5}MnO_2 \longrightarrow 2NaMnO_2 + 2[MnO_2] \tag{4.9b}$$

$$3\,NaMnO_2 + O_2 \longrightarrow Na_3MnO_4 + 2[MnO_2] \tag{4.9c}$$

$$2[MnO_2] + Y_2O_3 \longrightarrow Y_2Mn_2O_7 \tag{4.9d}$$

where the production of $[MnO_2]$ species (e.g., fragments, clusters) react directly with Y_2O_3 to form $Y_2Mn_2O_7$ (Eqn. 4.9d). Writing the pseudo-elementary reactions illustrates how the Na_xMnO_2 intermediate structure facilitates the release of reactive $[MnO_2]$ species through

a cascade of defect reactions. The starting composition in Eqn. 4.9a, $Na_{0.25}Mn_{0.75}O_2$, has a high concentration of defects and readily reacts towards ordered $Na_{0.5}MnO_2$ to yield $Y_2Mn_2O_7$. Concomitantly, the remaining Mn_2O_3 is consumed and the pyrochlore forms. While oxygen is consumed to produce $Na_{0.25}Mn_{0.75}O_2$ (Eqn. 4.5), oxygen is released in Eqn. 4.9a when the pyrochlore forms, thus producing a local molar concentration of O_2 more consistent with a condensed phase than that of a gas ($\sim$1000 times less dense). This locally high μ_O can stabilize the nascent formation of $Y_2Mn_2O_7$ as suggested by Fig. 4.5. Paired with small, reactive particles of Y_2O_3, the [MnO_2] species react rapidly to form the pyrochlore in these assisted metathesis reactions yielding high conversion after short duration reactions.

In such a reaction (Eqn. 4.9d), manganese is always the limiting reagent, as such, the local chemical potential of yttrium is high. This allows the the reaction to avoid the formation of the less reactive (more inert) YMn_2O_5, as indicated to prevail when the μ_Y is too low (Fig. 4.5) and as observed in our myriad control reactions (Figs. A.17, A.18, and A.19). Avoidance of unreactive intermediates has also been documented in other ternary metathesis reactions yielding $MgCr_2S_4$.[15,40] Figure 4.1 schematically summarizes the overall process to form $Y_2Mn_2O_7$ through the direct reaction of Y_2O_3 and the hypothesized [MnO_2] species at the reaction interface.

Previous studies have denoted $Y_2Mn_2O_7$ as metastable, yet $Y_2Mn_2O_7$ forms selectively using a sodium carbonate assisted metathesis reaction. Due to the small ionic radius of Mn(IV) compared to other transition metals, all manganese-containing pyrochlores are categorized as high-pressure metastable phases.[124] As such, previous studies have synthesized $Y_2Mn_2O_7$ through kinetic trapping at high oxygen chemical potential ($KIO_4 \longrightarrow$

$KIO_3 + O_2 \cdot$ at 1100 °C and 4 GPa)[92] and hydrothermal conditions (NaOH, $NaClO_3$ in H_2O at 500 °C and 3 GPa),[94] which agrees with the thermochemical calculations presented in Figure 4.5. Interestingly, the washed pyrochlore product is relatively stable under flowing oxygen at 650 °C for two weeks (Fig. S6). This observation is supported in previous thermogravimetric analysis where the pyrochlore is stable up to 800 °C, where it decomposes to the perovskite $YMnO_3$.[94] In all of the reported syntheses of $Y_2Mn_2O_7$, the reaction conditions are performed in conditions that drastically increase the chemical potential of oxygen. Figure 4.5 (a) and (b), support that to synthetically access the pyrochlore, the chemical potential of oxygen must be high and the reaction must proceed at low temperatures. Thus, we hypothesize that the pyrochlore is not metastable at 650 °C and $P = 1$ atm, but inaccessible through most synthetic methods. The reaction pathway in these assisted metathesis reactions proceeds through kinetic control, as we previously showed that long duration metathesis reactions yield decomposition of $Y_2Mn_2O_7$.[73] Therefore, the selectivity observed over short reaction times indicates the intermediate Na_xMnO_2 structure is critical for imparting reactivity and selectivity in these reactions.

Here we show that sodium effectively catalyzes the defect cascade pathways presented in Figure 4.1 (Eqn. 4.9a) to selectively yield $Y_2Mn_2O_7$. Many kinetically-controlled reactions are selective due to the mobility of a particular cation or anion in a topochemcial process.[21] While the calculated occupancy of sodium increases in this reaction, analogous to intercalation of sodium into the structure (Figure A.14),[132] the identified reaction pathway does not take place via simple intercalation. Instead, sodium appears to anchor the layered Na_xMnO_2 structure thus catalyzing the removal of $[MnO_2]$ species and O_2, which proceeds to react with Y_2O_3 under conditions with high local yttrium and oxygen chemical

potentials to form $Y_2Mn_2O_7$. Analysis of the pseudo-elementary steps identified from the f^* diagram and the observed phase fractions support this mechanism. The selectivity of these sodium-catalyzed reactions via the Na_xMnO_2 intermediate is analogous to base-catalyzed hydrolysis of esters (e.g., saponification) where selectivity depends on the identity and the eventual consumption of the hydroxyl intermediate. We suspect that this catalyst-defined selectivity in inorganic materials synthesis is not uncommon but remains to be identified at the mechanistic level described in this work. This contribution is the next step in "turning down the heat" to synthesize new metastable functional materials.

4.6. Conclusion

In the presented assisted metathesis reactions, the presence of sodium catalyzes the formation of metastable $Y_2Mn_2O_7$. *In situ* temperature-dependent SXRD experiments reveal a reaction pathway dependent on Na_xMnO_2 and Y_2O_3 intermediates. Analysis of the composition of Na_xMnO_2 along the reaction pathway reveals pseudo-elementary steps that describe a cascading defect pathway resulting in the release of $[MnO_2]$ species that react with small particles of Y_2O_3 at a high local chemical potential of yttrium and oxygen. DFT thermochemical calculations and myriad control reactions support the stabilization of $Y_2Mn_2O_7$ through control of the local chemical potential of each component at 650 °C. Sodium acts catalytically by anchoring the Na_xMnO_2 intermediate during the cascading defect pathway which results in high yields of $Y_2Mn_2O_7$. This mechanistic description of a solid-state reaction shows promise for developing new, low-temperature syntheses with increased product selectivity.

5. Low temperature synthesis of $YMnO_3$ via defect accommodating intermediates[§]

Overview

In the synthesis of complex oxides, solid-state metathesis provides low-temperature reactions where product selectivity can be achieved through simple changes in precursor composition. The influence of precursor structure is less understood in these metathesis reactions. Here we present on the ternary metathesis reaction: $LiMnO_2 + YOCl \longrightarrow YMnO_3 + LiCl$ to target two yttrium manganese oxide products, hexagonal and orthorhombic $YMnO_3$, when starting from three different $LiMnO_2$ precursors. Using temperature-dependent synchrotron X-ray and neutron diffraction, we identified the relevant intermediates and temperature regimes of reactions along the pathway to $YMnO_3$. We discovered that, regardless of $LiMnO_2$ precursor, the reaction proceeds through the same intermediates: r-YOCl, Y_3O_4Cl, and two lithium manganese oxide spinels that result from a disproportionation reaction of Mn(III). Depending on the identity of the $LiMnO_2$ precursor, the kinetics of intermediate formation differed, resulting in varying amounts of reduced Mn(II,III) tetragonal spinel and oxidized Mn(III,IV) cubic spinel. Changing the relative oxidation state in each spinel results in different observed amounts of h-$YMnO_3$ versus o-$YMnO_3$ in these metathesis reactions. Thermochemical calculations reveal that small

[§]Substantial portions of this chapter have been reproduced with permission from P. K. Todd, A. Wustrow, R. D. McAuliffe, M. J. McDermott, G. T. Tran, B. C. McBride, D. O'Nolan, C. H. Liu, S. S. Dwaraknath, K. W. Chapman, S. J. L. Billinge, K. A. Persson, A. Huq, G. M. Veith, and J. R. Neilson, *Prepared Manuscript* **2020**

concentrations of cation defects change the stability from h-$YMnO_3$ to o-$YMnO_3$, suggesting the kinetics of spinel formation kinetically control $YMnO_3$ selectivity at short reaction times. Long reaction times yield o-$YMnO_3$ as the majority product at temperatures below 600 °C supporting an equilibration of these cation defects over time. Controlling the composition and structure of these defect-accommodating intermediates provides new strategies for selective synthesis of complex oxides at low-temperatures.

5.1. Author Contributions

PKT, AW, and RDM synthesized and characterized precursors. PKT and AW performed and analyzed ex situ reactions. PKT, AW, GTT and BCM performed SXRD experiments. DO and KC assisted with using the gradient furnace, and CL wrote scripts to assist with SXRD collection under the supervision of SB. AW and PKT analyzed SXRD data. RDM performed and analyzed NPD experiments assisted by AH. MJM, SSD, and KAP performed calculations relating the stability of the two polymorphs. PKT, AW, RDM, and MJM wrote the manuscript with the guidance of JRN, GMV, and KAP.

5.2. Introduction

In molecular chemistry, the understanding of precursor structure and composition permits product selectivity under mild reaction conditions. In comparison, product selectivity in inorganic materials synthesis is often limited to the product at a global or deep local minimum on a potential energy landscape due to the large thermal energy barrier of diffusion.[5] For more kinetic variables to influence the pathway, like the effect of precursor

structure on product selectivity, the reaction must proceed to completion at low temperatures.[20]

A good starting point when synthesizing extended crystalline solids at low temperatures is to use a structural framework that retain geometric motifs from precursor to product. Specific examples include intercalation/deintercalation of cations or anions from a rigid inorganic framework.[21,22] Here, the precursor structure of a material determines the outcome of the reaction, such as achieving high capacities when cycling battery electrodes,[36] or selective replacement of interstitial cations in layered polymorphs of $LiAlO_2$.[35] Those topotactic examples are limited to the removal of labile ions from a rigid host structure, whereas most inorganic materials synthesis involves more complex reaction pathways where the structural similarities between precursor and product are less clear.

Solid-state metathesis provides a low-temperature route to crystalline materials where precursor composition and preparation can influence product selectivity.[6,133] In the preparation of complex oxides, we have shown that assisted metathesis reactions of the form $3A_2CO_3 + 2YCl_3 + Mn_2O_3 \xrightarrow{O_2} 2YMnO_3 + 6ACl + 3CO_2$ (A = Li, Na, K) selectively synthesized three unique yttrium manganese oxide products depending on the identity of the alkali carbonate precursor.[73] When using lithium, we identified $LiMnO_2$ and YOCl as intermediates that kinetically yield orthorhombic $YMnO_3$ at temperatures below 850 °C, rather than hexagonal $YMnO_3$ produced from reactions of the binary oxides at temperatures above 900 °C. By starting with these ternary materials as precursors, metathesis reactions can be performed directly:

$$\mathrm{LiMnO_2 + YOCl \longrightarrow LiCl + YMnO_3}, \tag{5.1}$$

to yield o-$YMnO_3$ at temperatures as low as 500 °C. This contribution expands on these ternary metathesis reaction by analyzing the effect of changing the $LiMnO_2$ precursor structure on the resulting reaction pathway.

The three polymorphs of $LiMnO_2$ crystallize as derivatives of the rock salt structure with octahedrally coordinated cation sites; however, the transition metal polyhedral connectivity varies between the structures. The monoclinic polymorph ($C2/m$, m-$LiMnO_2$) forms as a slightly distorted analog to $R\bar{3}m$ $LiCoO_2$, where the Jahn-Teller active Mn(III) induces a slight shift in the manganese oxide layering. m-$LiMnO_2$ is the most disordered of the three, with 10% of lithium sitting on manganese sites and vice versa.[134] The orthorhombic polymorph ($Pmnm$, o-$LiMnO_2$) is also a layered structure where the manganese oxide layers adopt a corrugated rock salt layering as compared to m-$LiMnO_2$. o-$LiMnO_2$ also has somewhat less site mixing, with only 5% cation inversion.[135] The tetragonal polymorph ($I4_1/amd$, t-$LiMnO_2$) orders with manganese sites forming the octahedral framework of a spinel and lithium occupying the remainder of the octahedral sites.[136] As this phase is formed by chemical insertion of Li into $LiMn_2O_4$ under mild conditions, it does not exhibit any notable site mixing in its pristine form.

Using *in situ* and recovered (*ex post facto*) temperature-dependent synchrotron X-ray diffraction (SXRD) along with neutron powder diffraction (NPD) data, we identify reaction intermediates and compare the temperature ranges by which they react to form $YMnO_3$

products. We discover that each reaction pathway when starting with different $LiMnO_2$ proceeds through a series of defect accommodating intermediates: r-YOCl, Y_3O_4Cl, and two lithium manganese oxide spinels. The spinel intermediates form from a disproportionation reaction resulting in a reduced Mn(II,III) spinel and an oxidized Mn(III,IV). The relative amount of these two spinels changes as a function of reaction progress (e.g., how much LiCl had formed). In all reaction pathways, varying amounts of h-$YMnO_3$ and o-$YMnO_3$ were observed at short reaction times depending on which precursor was used. Density functional theory (DFT) based calculations reveal that o-$YMnO_3$ is stablized through small concentrations of cation defects in our observed products, which we correlate to the amount of oxidized Mn(III,IV) spinel present at the temperature when $YMnO_3$ forms. Over long duration reactions, these ternary metathesis reactions yield the slightly cation deficient o-$YMnO_3$. Controlling the composition and subsequent oxidation state of manganese in these spinel intermediates affords opportunities for increased kinetic control in the synthesis of complex oxides at low-temperatures.

5.3. Methods

5.3.1 Precursor Synthesis

YOCl was synthesized by heating yttrium chloride hexahydrate (Acros Organics, 99.9%) in an alumina crucible in air at 400 °C for 4 h with heating and cooling rates of 5 °C/min.[112]

$LiMn_2O_4$ was synthesized by reacting stoichiometric amounts of Li_2CO_3 (Baker, 99.3%) and Mn_2O_3. Mn_2O_3 was synthesized by heating $MnCO_3$ (Sigma Aldrich, 99.9%) in an alumina crucible in air at 850 °C for 12 h with heating and cooling rates of 10 °C/min.

The Li_2CO_3 and Mn_2O_3 powders were mixed using a mortar and pestle and heated in an alumina crucible at 800 °C for 24 h with heating and cooling rates of 10 °C/min. To prepare t-$LiMnO_2$, $LiMn_2O_4$ powder was refluxed under nitrogen in a 4 M acetonitrile solution with LiI (Alfa Aesar, 99.9%) where the overall Li:Mn ratio was 6:1.[137,138] The reflux was performed at 82 °C using an oil bath to maintain the correct temperature. After refluxing, the powder was filtered and washed with acetonitrile to remove LiI and I_2 and dried under vacuum at 80 °C.

m-$LiMnO_2$ was synthesized by ion exchange from $NaMnO_2$.[139] $NaMnO_2$ was synthesized by reacting stoichiometric amounts of Na_2CO_3 (Macron Chemicals, 99.5%) and MnO_2 (Trinox 95%). The powders were mixed using a mortar and pestle and heated in an alumina crucible to 700 °C for 24 h with heating and cooling rates of 5 °C/min. The resulting black powder was moved into a glovebox antechamber while hot to prevent corrosion due to ambient humidity. $NaMnO_2$ was mixed with 3 times the stoichiometric amount of LiI using a mortar and pestle inside an Ar-filled glovebox. The mixture was heated to 460 °C for 4 h in an alumina crucible inside a sealed quartz ampule. The reaction was cooled for 9 h (1 °C/min). Excess LiI and NaI were removed by washing with water.

o-$LiMnO_2$ was synthesized by reacting Li_2CO_3 (Baker, 99.3%) and MnO_2 (Alfa Aesar, 99.9%) with 15 mol% excess Li_2CO_3. The powders were milled using an 8000M Spex MixerMill within a 30 mL polypropylene bottle placed inside the steel Spex jar. The powders were milled for 90 min with 5 mm spherical yttria-stabilized zirconia milling media in a 2:1 weight ratio of media to sample. The resulting gray powder was pelleted using $\sim$1 short ton of force. The pellets were placed inside beds of sacrificial powder in an alumina

boat and heated under flowing argon. The samples were heated at 600 °C for 4 h and 900 °C for 48 h with heating and cooling rates of 10 °C/min.

5.3.2 *Ex situ* reactions

Ex situ control reactions were prepared by mixing $LiMnO_2$ and YOCl in a mortar and pestle for 15 min under argon. This homogenized mixture was pelleted using $\sim$ 1 short ton of force, placed in a cylindrical alumina crucible, and sealed in an evacuated quartz ampule ($\leq$ 15 mTorr). Reactions were heated at 10 °C/min to the dwell temperature (500-600 °C). To avoid exposure to ambient oxygen due to the propensity for lithium chloride to chemically react with quartz at temperatures above 600 °C, long duration reaction ampules were placed into a larger diameter evacuated quartz ampule (e.g., double-sealed). Sample purity and product identification was verified by laboratory powder X-ray diffraction (PXRD) data collected on a Bruker D8 Discover diffractometer using Cu Kα radiation and a Lynxeye XE-T position-sensitive detector.

5.3.3 *Ex post facto* SXRD reactions

Synchrotron X-ray diffraction (SXRD) data were collected at beamline 28-ID-2 at the National Synchrotron Light Source II at Brookhaven National Laboratory. Data for all reactions were obtained using a gradient furnace, where the calibrated horizontal beam position defines the sample temperature.[140] In the gradient furnace, varying density of heating elements along the device allow for a single capillary to be simultaneously heated to a range of temperatures as a function of position along the capillary. Samples were

loaded into a 1.1 mm OD quartz capillary and sealed with epoxy (Aremco-Bond™ 570). Calibration of detector curvature was performed using CeO_2 at all points along the gradient furnace using pyFAI. A single characteristic position was set to 450 °C (using a PID-controlled power source) which created a reproducible temperature range from 300 °C to 750 °C along the capillary. Position was related to temperature with a calibration run based on the thermal expansion of NaCl.[141] Samples were held at temperature for 40 min before being cooled to room temperature. *Ex post facto* diffraction patterns were then taken along the length of the capillary with a wavelength of 0.1949 Å for m-$LiMnO_2$ and o-$LiMnO_2$ and 0.19319 Å for t-$LiMnO_2$. SXRD data were collected on a Perkin Elmer plate detector at a distance of 1400 mm. The experimental data was reduced in real-time using analysis software xpdAn and xpdTools that are open source projects in the xpdAcq organization on GitHub (https://github.com/xpdAcq).

5.3.4 *In situ* NPD reactions

Neutron powder diffraction (NPD) experiments were performed at beamline BL-11A POWGEN at the Spallation Neutron Source at Oak Ridge National Laboratory. The samples were measured using the MICAS vacuum furnace with the AGES gas handling insert.[142] Stoichiometric mixtures of $LiMnO_2$ and YOCl were mixed with an agate mortar and pestle in an argon-filled glovebox. Then, the homogenized powder was loaded into quartz baskets lined with Al_2O_3 cloth (Zircar Zirconia, Tricon Knit Cloth). The Al_2O_3 cloth was used to minimize Li-containing compounds from reacting with the quartz holder. For *in situ* measurements, the samples were heated in argon at a rate of 1 °C/min and 1 h dwell

scans were collected every 50 °C starting at 100 °C for the t-$LiMnO_2$ mixture and 250 °C for the o-$LiMnO_2$ and m-$LiMnO_2$ mixtures. The t-$LiMnO_2$ mixture was kept below the melting point of LiCl, reaching a maximum temperature of 500 °C to prevent leakage of molten LiCl through the glass frit holding up the sample. The glass baskets were redesigned with a closed bottom for subsequent experiments with m-$LiMnO_2$ and o-$LiMnO_2$ to access higher temperature and observe the formation of $YMnO_3$. NPD patterns of empty quartz baskets lined with Al_2O_3 cloth were collected every 100 °C and were subtracted from the *in situ* diffraction patterns.

5.3.5 *In situ* SXRD reactions

In situ SXRD experiments were performed at beamline 17-BM-B (λ = 0.2415 Å) at the Advanced Photon Source (APS) at Argonne National Laboratory using a Perkin Elmer plate detector at a distance of 700 mm. Homogenized metathesis precursors were packed into a quartz capillary (1.1 mm OD, 0.9 mm ID) at CSU in an argon-filled glovebox. Then, capillaries were sealed under vacuum ($<$ 20 mTorr) using a methane-oxygen torch. All capillaries were loaded into a flow-cell apparatus[111] equipped with resistive heating elements and heated at 10 °C/min to 600 °C. While heating, the samples were continuously rocked at $\pm$ 5° around the axis of the capillary. Diffraction patterns were collected every two seconds and summed every 20 seconds. Images collected from the plate detector were integrated using GSAS-II and calibrated using a LaB_6 standard.

5.3.6 Rietveld refinements

Quantitative phase analysis of X-ray and neutron data diffraction data was performed using the Rietveld method as implemented in TOPAS v6. To consistently analyze powder patterns which could contain upwards of five distinct crystallographic phases, the following assumptions were made for analyzing X-ray diffraction data: atomic displacement parameters (ADPs) were fixed using a B_{iso} value of 2.5 Å^2, peak broadening was assumed to be a result of crystal size using a Lorentzian function, and site occupancies were fixed at one. Lattice parameters were held constant when the calculated weight percents was less than 5% due to the large amount of overlap between intermediate phases in the diffraction data. For analyzing weight percents in neutron diffraction data, the ADPs were refined, and peak broadening was fit as a function of Lorentzian and Gaussian functions, and all site occupancies were fixed at full occupancy of 1. To obtain occupancies from neutron diffraction data, the ADPs were fixed at 1.5 Å^2 and the occupancies were refined.

5.3.7 Computational methods

Theoretical calculations were performed to evaluate the thermodynamic stability of $YMnO_3$ polymorphs using density functional theory (DFT) as implemented in the Vienna *Ab initio* Simulation Package (VASP).[143] We used the Generalized Gradient Approximation (GGA) with Perdew-Burke-Ernzerhof (PBE) exchange-correlation functional[144] plus Hubbard-U extension (GGA + U) with $U = 3.9$ eV for Mn.[145,146] The Projector Augmented Wave (PAW) method[147,148] was used for modeling core states with a plane wave basis and a minimum energy cutoff of $\geq$ 520 eV. The Python Materials Genomics package (*pymat-*

gen)[149] was used to create and process all VASP input/output files. The *phonopy*[150] package was used to process force constants, apply the quasiharmonic approximation (QHA), and produce the Gibbs free energy, $G(T, P)$, of each structure.

The original structures for the hexagonal and orthorhombic $YMnO_3$ polymorphs were acquired from the Materials Project (MP) database.[1] Initial results showed that the calculated material properties were particularly sensitive to the initialized magnetic ordering of the structures. For example, all structural relaxations performed using the GGA+U scheme with a ferromagnetic (FM) ordering yield an incorrect zero band gap for both the centrosymmetric (high-temperature) and noncentrosymmetric (low-temperature) h-$YMnO_3$ structures. Previous studies suggest that below their Néel temperatures, the hexagonal and orthorhombic phases acquire triangular and sinusoidally-modulated antiferromagnetic (AFM) orderings, respectively.[89,151] To initialize an appropriate magnetic ordering in our calculations, we enumerated many possible collinear magnetic orderings for each structure using the high-throughput DFT workflow developed by Horton et al.[152] We found several orderings which opened the GGA-calculated band gap to between 1-2 eV for both the hexagonal and orthorhombic phases. Each of these collinear orderings were AFM and slightly higher in energy than the FM orderings, by $\sim$2 meV/atom or less. For each structure, we selected the lowest energy AFM ordering which also resulted in a substantial non-zero band gap. The original MP structures were then re-relaxed with these AFM orderings in 2x2x2 supercells with a k-point grid density of 5000/atom until forces on the atoms were 10^{-4} with eV/Å or less.

Density functional perturbation theory (DFPT) was used to calculate force constants for 11 equally spaced deformations spanning $\pm$ 4% lattice strain of the re-relaxed (primitive)

cells. We used a k-point grid density of 5000/atom, plane wave energy cutoff of 620 eV, and energy convergence criterion of 10^{-8} eV for the self-consistent electronic loop. Force constants were mass-weighted and symmetrized to acquire phonon modes used to approximate the Helmholtz free energy, $F(T, V)$, as a function of volume of the deformed cells. Using *phonopy*, the Vinet equation of state[153] was fit to these free energy curves for each structure at temperatures ranging from $T = 0$ to 1400 K (in 100 K steps) and minimized at a pressure of $P = 1$ atm, yielding the Gibbs free energy curves, $G(T, P)$, of each structure.

Vacancy formation energies for yttrium and manganese cations, $E^f[V_Y]$ and $E^f[V_{Mn}]$, were calculated for each $YMnO_3$ structure via the charged-defect supercell approach with finite-size corrections developed by Freysoldt et al.[154,155] and implemented by Broberg et al.[156] in the *atomate* workflow interface.[157] We used a k-point grid density of 100/atom and supercell dimensions outlined in Table A.5. Using computed defect formation energies, the thermodynamic stability of the polymorphs was modeled using a defect concentration-dependent thermodynamic potential, Φ, defined as:

$$\Phi(T, P, x) = G^{QHA}(T, P) + \left(E^f[V_Y] + E^f[V_{Mn}]\right) x \tag{5.2}$$

Where T is the temperature, P is the pressure, $G^{QHA}(T, P)$ is the Gibbs free energy calculated using QHA, $E^f[V_Y]$ and $E^f[V_{Mn}]$ are the defect formation energies of yttrium and manganese vacancies respectively, and x is the concentration of cation vacancies in $Y_{1-x}Mn_{1-x}O_3$. A paired cation vacancy concentration was used as an equivalent represen-

tation of oxygen hyper-stoichiometry $YMnO_{3+\delta}$, where $x = \delta/(3+\delta)$. This aligns with previous observations that rare-earth perovskite manganites $RMnO_3$ accommodate excess oxygen via cation (R, Mn) vacancies (instead of oxygen interstitials) due to their close-packed structure.[99,100,158,159] It was noted that in $LaMnO_3$, cation vacancies were found in equal proportions for small values of δ,[158] although this is not necessarily true for more oxidizing conditions.[99]

Entropic contributions to vacancy formation were not included in the calculation of vacancy formation energies. Thus the calculated vacancy formation energies, $E^f[V_Y] + E^f[V_{Mn}]$, are independent of temperature. The Fermi energy of electrons, E_F, which is typically solved for self-consistently via charge balance of defect concentrations at equilibrium, was left as a free variable in phase diagram construction.

5.4. Results

To identify how each $LiMnO_2$ precursor affected the reaction intermediates that yield $YMnO_3$, various thermodiffraction experiments were conducted. Synchrotron X-ray diffraction (SXRD) experiments were performed *ex post facto* on ternary metathesis reactions heated isothermally across a temperature gradient ($300 \leq T \leq 750$ °C, 1 h).

The quantitative phase analysis from SXRD experiments is shown in Figure 5.1 with temperature values reported in Tables A.6-A.8. Complementary temperature-dependent neutron powder diffraction (NPD) experiments were also performed to confirm the identity of observed intermediates and to better analyze the composition of lithium containing inter-

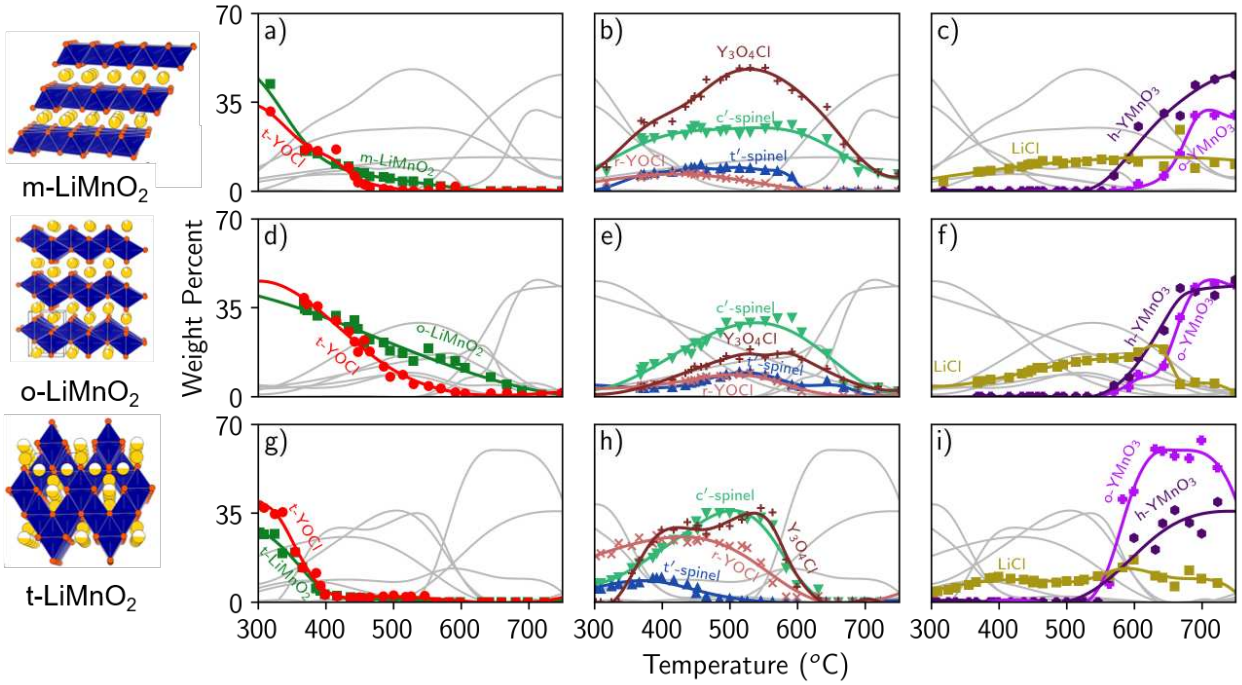


Figure 5.1: Calculated weight fractions of crystalline materials at different reaction temperatures reveals the reaction pathway of the ternary metathesis reaction, $LiMnO_2 + YOCl \longrightarrow LiCl + YMnO_3$ when changing the $LiMnO_2$ precursor. Each row highlights the structure of $LiMnO_2$ precursor and the reaction pathway as a function of temperature: (a-c) m-$LiMnO_2$ ($C2/m$), (d-f) o-$LiMnO_2$ ($Pmnm$) and (g-i) t-$LiMnO_2$ ($I4_1/amd$). Each column shows the phase fractions (Weight Percent) of crystalline phases present along the pathway. For clarity, the presented phases are separated into the reactants, $LiMnO_2$ (green square) and t-YOCl (red circle) (a,d,g); the intermediates, Y_3O_4Cl (burgundy cross), r-YOCl (rose x), t′-spinel (blue triangle) and c′-spinel (aqua triangle) (b,e,h); and the products LiCl (goldenrod square), h$-YMnO_3$ (purple hexagon) and o-$YMnO_3$ (lilac cross) (c,f,i).

mediates. The quantitative phase analysis from NPD experiments is shown in Figure A.30 and details about formation of the phases is provided in Tables A.9-A.8.

Regardless of $LiMnO_2$ precursor, the first observed reaction forms lithium chloride, two manganese-containing spinel phases, and oxygen-rich yttrium oxide chloride (Fig. 5.1 and A.30). The two spinel intermediates form as lithium and oxygen are removed from $LiMnO_2$ to form LiCl and Y_3O_4Cl respectively. Here, a disproportionation of $LiMnO_2$ into two distinct spinel phases is observed: a cubic spinel phase resembling $Fd\bar{3}m$ $LiMn_2O_4$ (c′-spinel) and a tetragonal spinel phase resembling $I4_1/amd$ Mn_3O_4 (t′-spinel). In SXRD

experiments collected *ex post facto* (Fig. 5.1), the relative weight percent of the c′-spinel is greater than the t′-spinel for all reaction pathways, yet *in situ* SXRD and NPD experiments yield more t′-spinel over similar temperature ranges (Fig. A.29 and A.30). Concomitantly, $Cmcm$ Y_3O_4Cl forms through the oxygenation of the t-YOCl precursor. This reaction proceeds through a disordered rhombohedral form of YOCl ($R\bar{3}m$) that is poorly resolved in the diffraction data but has been previously observed in assisted metathesis reactions with lithium.[110] The results in Figure 5.1(b,e,h) confirm the presence of each intermediate, yet subtle differences are observed in the precursor reactivity, the relative amounts of each intermediate, and the temperature range over which the intermediates form and react.

The reaction pathway starting with m-$LiMnO_2$ (Fig. 5.1a-c) yields intermediates at the lowest temperatures, yet react over a broad temperature range. In Figure 5.1b, significant amounts of r-YOCl, Y_3O_4Cl, the two manganese-containing spinel phases, and LiCl form by 300 °C. *In situ* SXRD experiments in Figure A.29 confirm that the relative amounts of each precursor begin decreasing at temperatures as low as 150 °C to yield c′-spinel and r-YOCl. Furthermore, calculated site occupancies from the *in situ* NPD experiments reveal the occupancy of the (2d) lithium site of m-$LiMnO_2$ in Figure 5.2a had decreased by ∼24% by 300 °C compared to o-$LiMnO_2$, which does not begin to react until 300 °C. The m-$LiMnO_2$ and YOCl precursors continue to react until depleted at 570 °C and 443 °C, respectively. Near 500 °C, the relative amount of the reaction intermediates is the highest, with Y_3O_4Cl representing the largest fraction at 48 wt%. Here, the intermediates react to yield different polymorphs of $YMnO_3$. First, r-YOCl and t′-spinel react at lower temperatures (t′-spinel: 570 °C; r-YOCl: 465 °C) followed by Y_3O_4Cl and c′-spinel (Y_3O_4Cl: 592 °C; c′-spinel: 644 °C). As the intermediates start to decrease, the h-$YMnO_3$ phase forms at 570 °C fol-

lowed by the formation of o-$YMnO_3$ at 644 °C. More h-$YMnO_3$ is formed as a result of this reaction with 50% more h-$YMnO_3$ present at 750 °C.

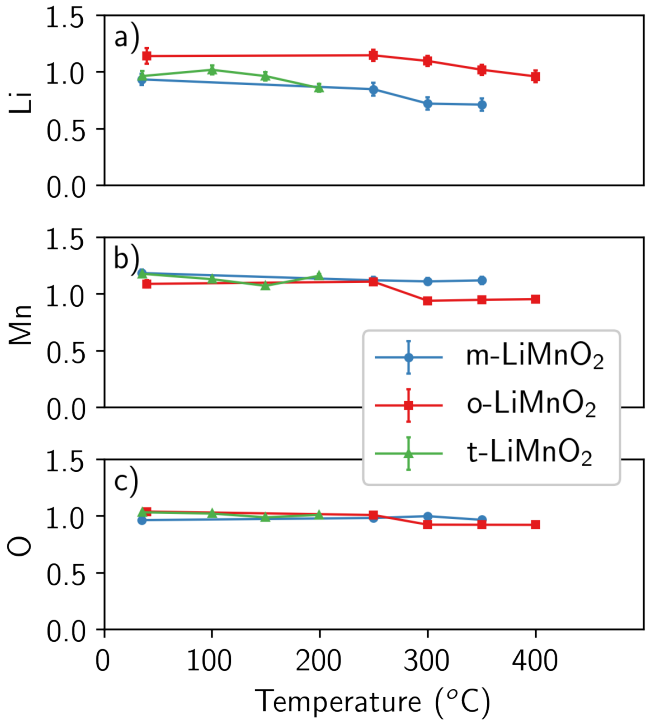


Figure 5.2: Occupancy of crystallographic sites that correspond to lithium-rich (left), manganese-rich (center) and oxygen (right) site within the crystal lattice for the o-$LiMnO_2$ (red) m-$LiMnO_2$ (blue) and t-$LiMnO_2$ (green). As all occupancies were refined together with the scale factor for the phase, values should be considered relative rather than absolute.

The reaction starting from o-$LiMnO_2$ (Fig. 5.1 d-f), yields a pathway where the precursors begin to react near 300 °C and persist to the highest observed temperatures (o-$LiMnO_2$: 668 °C; YOCl: 495 °C). Compared to m-$LiMnO_2$, o-$LiMnO_2$ begins reacting at higher temperatures, as supported in the calculated lithium site occupancies in Figure 5.2 and *in situ* NPD results in Figure A.30. As precursor react, the same intermediates are formed; however, there is significantly less Y_3O_4Cl formed at a maximum of 18 wt% at 530 °C as compared to 48 wt% at the same temperature for reactions starting with m-$LiMnO_2$. Also, the t′-spinel intermediate was observed up to 606 °C. Here, a concomitant

decrease of phase fraction for all intermediate phase fraction is observed resulting in equal amounts of h-$YMnO_3$ and o-$YMnO_3$ form at 570 °C and 606 °C, respectively.

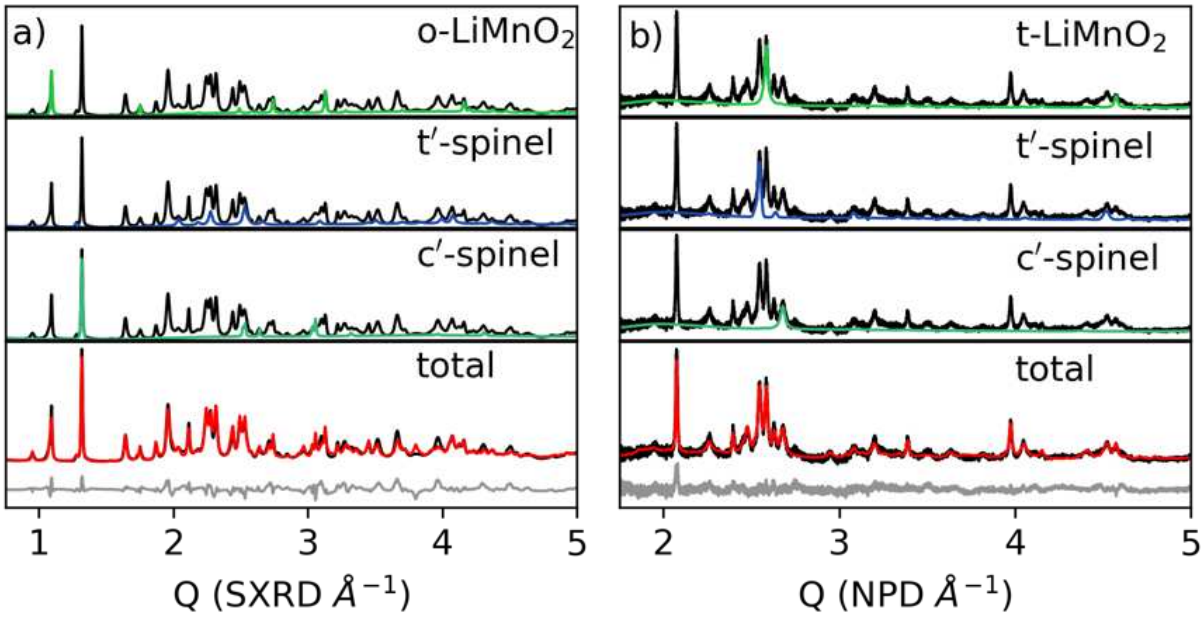


Figure 5.3: Diffraction patterns that illustrate the presence of two unique manganese-containing spinel intermediates in these ternary metathesis reactions: a) SXRD patterns of o-$LiMnO_2$ + YOCl at 500 °C and b) NPD pattern of t-$LiMnO_2$ + YOCl at 400°C. The contributions of each lithium manganese oxide phase are highlighted: $LiMnO_2$ precursor (top), t′-spinel (second from top), and c′-spinel (third from top). The overall fit from Rietveld refinement (bottom) also contains t-YOCl, r-YOCl, Y_3O_4Cl and LiCl (red) along with a difference pattern (gray).

For reactions starting with the t-$LiMnO_2$ polymorph, the precursors react over a narrower temperature range relative to the other $LiMnO_2$ precursors. Here, t-$LiMnO_2$ and YOCl are completely depleted by 392 °C in Figure 5.1g), whereas m-$LiMnO_2$ and o-$LiMnO_2$ persist to higher temperatures. This is evident in the calculated site occupancies in Figure 5.2, where the (4a) lithium site occupancy appears to decrease below 300 °C, yet is completly reacted by 300 °C. Contrary to the other $LiMnO_2$ polymorphs, there is a significant fraction of t′-spinel compared to c′-spinel at 300 °C which reacts at 400 °C to yield more c′-spinel in Figure 5.1h. Also, r-YOCl forms in a relatively large amount reaching

26 wt% as opposed to a maximum of 7 wt% and 9 wt% for reactions with m-$LiMnO_2$ and o-$LiMnO_2$ respectively. Near 500 °C, Y_3O_4Cl, r-YOCl, and c′-spinel react completely by 560 °C to yield o-$YMnO_3$ and h-$YMnO_3$. Here, more o-$YMnO_3$ was observed with 25% more o-$YMnO_3$ than h-$YMnO_3$ present at 725 °C.

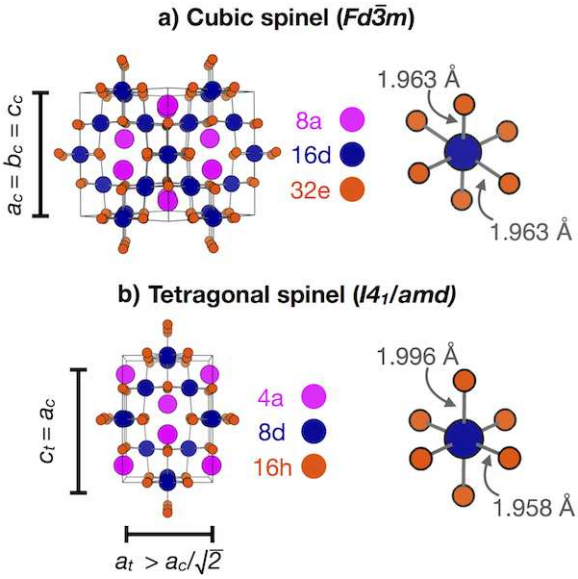


Figure 5.4: Structural relationship between a) cubic $Fd\bar{3}m$ spinel and b) tetragonal $I4_1/amd$ spinel. The geometric relationship between unit cells is shown the Wyckoff positions highlighted. The tetrahedral cation sites ((8c)$_c$ and (4c)$_t$), octahedral cation sites ((16d)$_c$ and (8c)$_t$), and oxygen site ((32e)$_c$ and (16h)$_t$) are highighted. Finally, the local [MnO_6] octahedra are shown for each structure with the axial and equatorial bond distances labeled to highlight the Jahn-Teller distortion in tetragonal spinels

Central to understanding the reaction pathway in these ternary metathesis reactions is the disproportionation of spinel intermediates into a c′-spinel and t′-spinel (Fig. 5.1 b,e,h). To properly identify the two phases both SXRD and NPD were needed. In the SXRD results, this spinel disproportionation is most easily observed in diffraction patterns taken from the reaction o-$LiMnO_2$ + YOCl (Figure 5.3), as Bragg peaks from both the monoclinic and tetragonal polymorphs of $LiMnO_2$ overlap with those of the t′-spinel phase (Fig. A.31). The c′-spinel is most evident in the X-ray diffraction patterns (Fig. 5.3a, Fig. A.31) by the strong (111) reflection at Q = 1.33 $Å^{-1}$. The t′-spinel is harder to distinguish with X-rays,

as evidenced by the small $(112)_t$ peak at Q = 2.04 Å^{-1}, or by a small shoulder on the $(111)_c$ peak of c′-spinel corresponding to the $(101)_t$ peak at Q = 1.28 Å^{-1}. In the neutron diffraction pattern (t-$LiMnO_2$ + YOCl) presented in Figure 5.3b the t′-spinel is easily identifiable by a strong (202) reflection at 2.55 Å^{-1} and the c′-spinel is identified by the (202) reflection at 2.64 Å^{-1}. The site occupancies of the t′-spinel phase were refined from the neutron data and indicated the presence of lithium on the tetrahedral (4c) manganese site of Mn_3O_4, with a refined Li occupancy of 0.43 ± 0.15 at 450 °C. The intensity of Bragg peaks from the c′-spinel in NPD results was not high enough to successfully refine occupancies of this phase. We hypothesize that the two spinel structures observed is directly related to to composition of each phase along the reaction pathway.

The geometric relationship between these two spinel structures is shown in Figure 5.4. The tetragonal spinel unit cell is distinguishable crystallographically by an contraction of the a_t axis due to a Jahn-Teller distortion of Mn(III) containing [MnO_6] octahedra. To ensure the validity of refining both cubic and tetragonal spinel phases, we fitted the c′-spinel using a formally tetragonal setting ($I4_1/amd$ $LiMn_2O_4$) which refined to a metrically cubic unit cell when a_t=b_t= $\sqrt{2}\times$ c_t (e.g., the c_t/a_t ratio remained close to the expected value of 1.41 for a cubic spinel in Fig. A.32 a)). For comparison, the t′-spinel c_t/a_t ratio yielded a tetragonal ($I4_1/amd$) cell with a c_t/a_t ratio of 1.63 (Fig. A.32b).

While the relative amounts of $YMnO_3$ products differed between each reaction pathway in Figure 5.1, longer duration reactions are required to understand how the relative amount of each polymorph changed as a function of $LiMnO_2$ precursor. Control reactions were performed at 550 °C, for each $LiMnO_2$ precursor, to determine product selectivity in these ternary metathesis reactions. Figure 5.5 depicts the phase fractions from PXRD

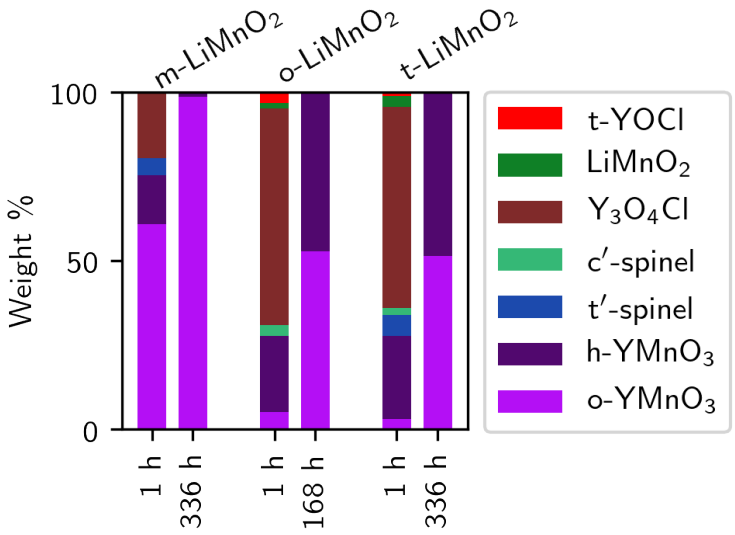


Figure 5.5: Calculated fraction of reaction products taken from laboratory PXRD data of *ex situ* ternary metathesis reactions ($LiMnO_2 + YOCl$) at 550 °C comparing short and long duration reactions. The results are separated by $LiMnO_2$ precursor: a) monoclinic ($C2/m$), b) orthorhombic ($Pmnm$) and c) tetragonal ($I4_1/amd$).

results after short (1 h) and long (168 or 336 h) duration reactions. After dwelling for 1 h at 550 °C, reactions starting with m-$LiMnO_2$ yielded the highest conversion to products, which supports the lower onset temperature for $YMnO_3$ in Figure 5.1c. Interestingly, o-$YMnO_3$ was observed as the majority phase over h-$YMnO_3$ after 1 h (Figure 5.5a). Both t-$LiMnO_2$ and o-$LiMnO_2$ reactions yielded little conversion to $YMnO_3$ after one hour, which also supports the results in Figure 5.1f and i, where 550 °C was near the onset temperature of $YMnO_3$ for both reactions. After long duration reactions with m-$LiMnO_2$, o-$YMnO_3$ was the only product observed, whereas o-$LiMnO_2$ and t-$LiMnO_2$ yielded mixtures of hexagonal and orthorhombic $YMnO_3$ after one week at 550 °C. The presence of two $YMnO_3$ products suggests that these reactions may not be at equilibrium after 1 week.

As reactions starting with m-$LiMnO_2$ yield $YMnO_3$ products at the lowest temperatures and reaction times, control reactions were performed varying reaction temperature

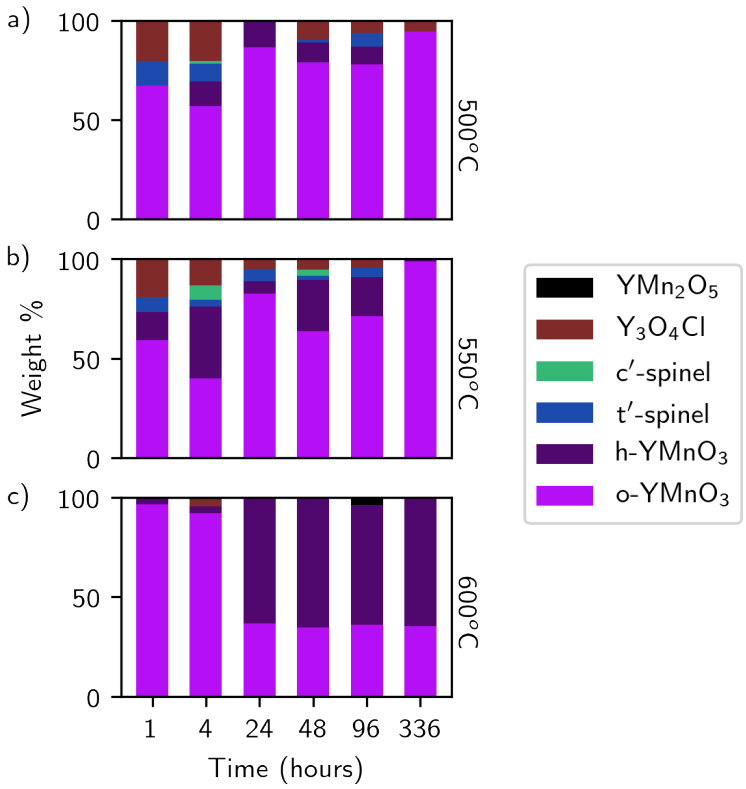


Figure 5.6: Calculated fraction of reaction products taken from laboratory PXRD data of *ex situ* ternary metathesis reactions ($LiMnO_2 + YOCl$) at varied temperatures and reaction times. Subplots (a-c) show the progression of reaction products when starting with monoclinic ($C2/m$) m-$LiMnO_2$ at (a) 500 °C, (b) 550 °C, and (c) 600 °C. As the temperature increases, the hexagonal $YMnO_3$ product selectivity increases over the orthorhombic product.

to better understand how $YMnO_3$ phase selectivity changes with reaction temperature. Figure 5.6(a-c) shows the product distribution calculated from Rietveld refinements of laboratory PXRD data at different reaction temperatures (500 - 600 °C) as a function of time of reaction (without re-mixing). Taken together, the results from these *ex situ* reactions reveal a change in phase selectivity of $YMnO_3$ products as a function of temperature. Below 600 °C, the orthorhombic phase dominates after long duration reactions. At 600 °C or above, the product fraction shifts to favor h-$YMnO_3$ at longer time point reactions, but a mixture of polymorphs still exists after two weeks at 600 °C.

Density functional theory calculations were performed to compare the sensitivity of polymorph selection in $YMnO_3$ to the concentration of defects arising from different synthesis conditions. A previous study[90] showed that the orthorhombic polymorph o-$YMnO_3$ is readily produced and stabilized in oxygen-rich environments. As with other perovskite manganites, excess oxygen, δ, in o-$YMnO_{3+\delta}$, has been shown to manifest as the formation of nearly-equivalent amount cation (yttrium and manganese) vacancies, x, in $Y_{1-x}Mn_{1-x}O_3$. It was hypothesized by Bergum, et al. that excess oxygen stabilizes the orthorhombic phase via an increase in perovskite geometric stability resulting from the decrease in ionic radius that occurs with partial oxidation of Mn^{3+} to Mn^{4+}.[160] To computationally test this hypothesis, we first calculated the defect-free Gibbs free energies, $G(T, P)$, for the hexagonal and orthorhombic polymorphs using the QHA approach for considering phonon vibrational entropy contributions. We also considered the centrosymmetric hexagonal structure ($P6_3/mmc$), which through a ferroelectric phase transition is stable at temperatures above $T \sim 1250$ K.[87] In our calculations we found that the typical ground-state hexagonal ($P6_3cm$) structure was thermodynamically stable at all temperatures considered, $T < 1400$ K, and a pressure of $P = 1$ atm. The orthorhombic ($Pnma$) polymorph and centrosymmetric hexagonal polymorph ($P6_3/mmc$) Gibbs free energies were approximately +23.0 and +19.9 meV/atom higher than that of the hexagonal phase at $T = 0$ K, decreasing to +7 and +11 meV/atom at $T = 1400$ K, respectively. The Gibbs free energies and heat capacities, $c_p(T)$, are shown as a function of temperature in Figure A.25.

The defect-dependent thermodynamic potential, $\Phi(T, P, x)$, given by Eq. 5.2, was minimized at $P = 1$ atm resulting in the phase diagram in Figure 5.7. The cation-deficient orthorhombic polymorph, o-$Y_{1-x}Mn_{1-x}O_3$, is predicted to be stable above a threshold de-

fect concentration of approximately $x \simeq 0.0045$ at $T = 0$ K, which appears to decrease with temperature. The centrosymmetric hexagonal structure h-$YMnO_3$ ($P6_3/mmc$) was not found to be the minimum energy phase of the three structures at any values of T or x and hence does not appear in the diagram. Figure A.28 shows the sensitivity of this phase boundary to the value of Fermi energy, E_F. Lower values of E_F merely shift the location of the phase boundary towards slightly higher values, near $x \sim 0.007$ at $T = 0$ K. Furthermore, changes in the values of chemical potentials have no effect on the phase diagram (with the caveat that negative defect formation energies are unphysical) since the polymorphs are compared with *identical* compositions at all points on the diagram.

Importantly, and in agreement with the hypothesis by Bergum, et al., the significantly lower cation vacancy formation energies in the orthorhombic phase offset the difference in energies due to polymorphism (~ 20 meV) between the hexagonal ($P6_3cm$) and orthorhombic structures. According to the defect formation energy curves, which are shown in Figure A.27, o-$YMnO_3$ exhibits significantly lower cation vacancy formation energies than h$-YMnO_3$ ($P6_3cm$). This difference, of 2.5 eV and 2.6 eV for Y and Mn vacancies respectively at $E_F = 1.0$ eV, appears to stabilize the orthorhombic phase even at very small cation vacancy concentrations, on the order of $\sim 0.5\%$.

5.5. Discussion

Regardless of $LiMnO_2$ precursor in these ternary metathesis reactions, the formation of $YMnO_3$ products proceeds through the same defect accommodating intermediates that can

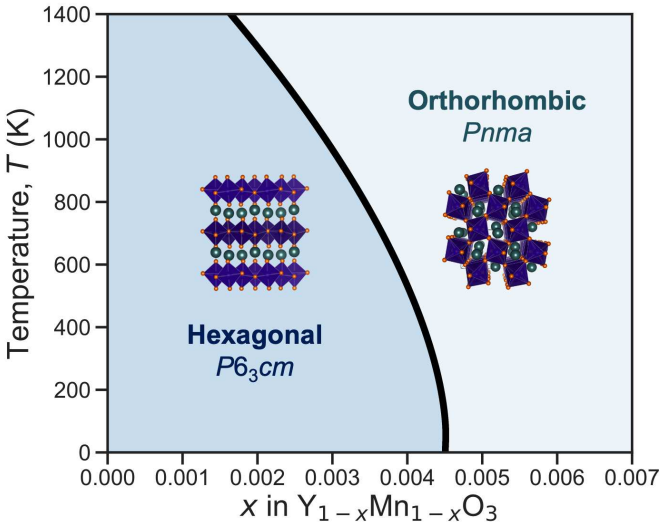


Figure 5.7: DFT-calculated phase diagram of cation-deficient $YMnO_3$ polymorphs with respect to temperature, T, and a fixed, equal concentration of cation (Y,Mn) vacancies, x in $Y_{1-x}Mn_{1-x}O_3$. All structures are initialized with AFM magnetic orderings, and the Fermi energy of electrons is fixed at $E_F = 1.0$ eV.

be generally described as:

$$\mathrm{LiMnO_2 + YOCl \longrightarrow \epsilon LiCl + Li_{1-\epsilon}MnO_{2-\epsilon/2} + YO_{1+\epsilon/2}Cl_{1-\epsilon} \longrightarrow LiCl + YMnO_3}, \quad (5.3)$$

where ϵ describes the amount of lithium chloride that has formed at a particular temperature or time and $Li_{1-\epsilon}MnO_{2-\epsilon/2}$ and $YO_{1+\epsilon/2}Cl_{1-\epsilon}$ describe the average composition of the disproportionated spinel phases and oxygen-rich yttrium oxychloride intermediates, respectively. As the value of ϵ changes over the progress of the reaction, we observe different crystalline intermediates that describe these average compositions.

As the reaction progresses, the yttrium oxychloride precursor loses chlorine to LiCl and replaces it with oxygen obtained from lithium manganese oxide species in the reaction. The intermediate $YO_{1+\epsilon/2}Cl_{1-\epsilon}$ crystallizes into two distinct phases. At low values of ϵ the more chlorine rich rhombohedral r-YOCl forms. As more chlorine in the structure

is replaced with oxygen, an orthorhombic Y_3O_4Cl type phase forms with the composition $YO_{1+\epsilon/2}Cl_{1-\epsilon}$ with a maximum ϵ of 2/3. Beyond $\epsilon = 2/3$, we hypothesized Y_2O_3 will form, yet we do not observe this phase as an intermediate, yet previous studies have observed this transition in metathesis reactions $Y_3O_4Cl \longrightarrow Y_2O_3$,[110] as well as in thermogravimetric studies of rare-earth halides.[112,161] In these previous studies, oxygenation occurred when performing the reactions in air or under flowing oxygen. In a sealed environment where oxygen must come from lithium manganese oxide phases, further chlorine loss and oxygen abstraction from lithium manganese oxide phases past the point of ϵ=2/3 requires conversion to an oxide.

In equation 5.3, the Li-Mn-O intermediates are represented generally as $Li_{1-\epsilon}MnO_{2-\epsilon/2}$, yet we observe two distinct spinel intermediates: a c′-spinel resembling cubic $Fd\bar{3}m$ $LiMn_2O_4$ and a t′-spinel resembling tetragonal $I4_1/amd$ Mn_3O_4. Here, the two spinel intermediates form from a disproportionation reaction as lithium and oxygen leave the phase to form LiCl and oxygenated $YO_{1+\epsilon/2}Cl_{1-\epsilon}$. The observation of two spinels can be attributed to the well-known propensity of Jahn-Teller active Mn(III) to distort the [MnO_6] octahedra in these spinels, as presented in Figure 5.4. This disproportionation can manifest in different ways in these Li-Mn-O spinels as a function of composition and oxidation state of manganese. The effect of losing either oxygen or lithium from $LiMnO_2$ has been previously investigated. With all Mn(III), $Li_2Mn_2O_4$ adopts the tetragonal $I4_1/amd$ spinel structure, where all [MnO_6] are distorted. Upon delithiation, a phase transition to the cubic spinel, $Fd\bar{3}m$ $LiMn_2O_4$, is observed. This cubic spinel is observed electrochemically over the range $0.24 < Li_xMn_2O_4 < 1$, or when the manganese oxidation state is greater than 3.5.[162] When $x = 0.24$, a disproportionation reaction occurs, resulting in a Mn(IV)

cubic spinel ($Li_4Mn_5O_{12}$), and a mixed Mn(II,III) tetragonal spinel (Mn_3O_4).[163] Alternatively, the presence of oxygen vacancies in the cubic spinel $LiMn_2O_{4-\delta}$ also results in a similar disproportionation. Here, the cubic spinel is observed when (4-δ) $>$ 3.833. Then, a disproportionation reaction occurs to yield tetragonal Mn_3O_4, cubic $LiMn_2O_{4-\delta}$, and tetragonal $Li_2Mn_2O_4$ over the range 3.33 (4-δ) $>$ 3.833.[164] The disproportionation reaction in the ternary metathesis reactions studied here differs from those cases, as both lithium and oxygen vacancies are introduced simultaneously. Therefore we define a range in manganese oxidation states for cubic spinels, $+3.33 <$ Mn $< +3.88$, where the endpoints represent $LiMn_2O_{3.833}$ and $Li_{0.24}Mn_2O_4$, respectively. Then, we apply these constraints to describe the presented disproportionation reaction into c′-spinel and t′-spinel intermediates:

$$\mathrm{Li_{1-\epsilon}MnO_{2-\epsilon/2}} \longrightarrow \mathrm{y(t'{-}Li_xMn_{3-x}O_{4+z})} + \mathrm{c'{-}Li_{1-\epsilon-yx}Mn_{1-3y+yx}O_{2-\epsilon/2-4y-zy}}, \qquad (5.4)$$

where x is the degree of site mixing on tetrahedral site of the t′ spinel and y represents the amount of t′ spinel relative to c′ spinel upon disproportionation. The variable z determines the amount of cation vacancies in t′-spinel, which is related to the extent of charge disproportionation of Mn(III) to Mn(II) and Mn (IV). In Equation 5.4, we assume some concentration of lithium on the tetrahedral site of the t′ spinel, as evidenced from neutron diffraction data; yet, the disproportionation reaction could plausibly yield Mn_3O_4 when $x = 0$. As constructed, the composition of these spinels can exist up to $x = 0.5$. At $x = 0.5$, the t′-spinel would formally be $Li_{0.5}Mn_{0.5}Mn_2O_4$ where the oxidation state of manganese would remain Mn(III), thus making disproportionation redundant. The value of y in Equa-

tion 5.4 then becomes directly influenced by the amount of lithium on the tetrahedral site of the t′-spinel. Lower values of x will result in more t′-spinel Mn_3O_4 with Mn(II,III), whereas higher values of x will result in a more equal phase fraction of each spinel intermediate. The varying degree of spinel disproportionation may explain why we observe different ratios of t′-spinel to c′-spinel in the presented experiments. For example, experiments collected *ex post facto* after one hour at each temperature observe more c′-spinel (Fig. 5.1), whereas *in situ* NPD and SXRD experiments the samples are at elevated temperatures for longer times in aggregate may have more conversion to the t′-spinel (Fig. A.29 and A.30). This supports control reactions as well at longer dwell times where the t′-spinel is often always the observed spinel in XRD results.

The progress of the reaction (ϵ) and the degree of disproportionation (y) determine which $YMnO_3$ polymorph is observed. Figure 5.7 shows that the stability of $YMnO_3$ is directly influenced by cation defects, specifically the oxidation state of manganese. This observation is supported in previous studies on assisted metathesis reactions to yield $YMnO_{3+\delta}$, where Mn(IV) defects result in the orthorhombic product over h-$YMnO_3$ at temperatures below 850 °C. The value of ϵ in Eqn. 5.4 influences the composition of the spinel intermediates, specifically, the ratio of lithium to manganese. As more lithium chloride and Y_3O_4Cl forms, the value of y in Eqn. 5.4 should increase, resulting in a higher relative fraction of *reduced* Mn(II,III) t′-spinel. If less LiCl and Y_3O_4Cl have formed, a greater fraction of *oxidized* Mn(III,IV) c′-spinel will be observed relative to t′-spinel. The observed results suggest that the spinel intermediates react individually with the yttrium oxychloride intermediates to yield different $YMnO_3$ product. Here, Mn(II,III) t′-spinel will yield a

product resembling h-$YMnO_{3-\delta}$[104] and the Mn(III,IV) c′-spinel will result in o-$YMnO_{3+\delta}$, as supported by the calculated phase diagram in Figure 5.7.

The identity of the $LiMnO_2$ precursor kinetically controls the composition and relative amount of each intermediate when they react to form $YMnO_3$. The results collectively support a relatively slow reaction pathway to spinel intermediates when starting with the layered m-$LiMnO_2$ or o-$LiMnO_2$ as opposed to starting with the spinel t-$LiMnO_2$. Previous electrochemical studies have identified the mechanism of the layered-to-spinel transition as proceeding slowly to the cubic spinel $LiMn_2O_4$ through a disordered "splayered" intermediate ($R\bar{3}m$ $LiMnO_2$) where manganese moves from manganese oxide layers into the octahedral spinel sites vacated by lithium.[165–167] The presented results proceed through a similar kinetic pathway where the layered precursors react over a broad temperature range to yield the spinel intermediates, although we do not observe the "splayered" intermediate in our diffraction data as this level of resolution is limited within a multi-phased sample. Both m-$LiMnO_2$ and o-$LiMnO_2$ are slow to transition to the spinel intermediates, yet the m-$LiMnO_2$ precursor reacts at a lower temperature. The reason for the differences in reactivity between o-$LiMnO_2$ and m-$LiMnO_2$ is due to the degree of structural rearrangement necessary to adopt the spinel structure. As lithium is removed from o-$LiMnO_2$ and m-$LiMnO_2$, manganese must move to fill the octahedral (16d) site in the spinel intermediates. The o-$LiMnO_2$ structure adopts a corrugated rocksalt ordering of manganese oxide layers which requires 50 % of the manganese atoms to migrate into the octahedral spinel site, whereas in the monoclinic $C2/m$ structure, only 25 % of the manganese must move to accommodate the reaction to the spinel intermediate. Thus, starting with m-$LiMnO_2$ results in higher values of ϵ at lower temperatures, or a greater value of Y_3O_4Cl and Mn(II,III)

t′-spinel at 450 °C when h-$YMnO_3$ forms. As there is more reduced spinel intermediate, the fraction of h-$YMnO_3$ to o-$YMnO_3$ is greatest. In comparison, the value of ϵ is lower when starting with o-$LiMnO_2$, or less Y_3O_4Cl and Mn(II,III) t′-spinel have formed at 500 °C. Then, the amounts of c′-spinel, t′-spinel, r-YOCl, and Y_3O_4Cl all decreased, which results in equal amounts of o-$YMnO_3$ and h-$YMnO_3$.

The reaction pathway starting with t-$LiMnO_2$ yields a different reaction to spinel intermediates. The results in Figure 5.1g,h denote the same t′-spinel, yet the temperature at which the t′-spinel reacts corresponds to an increase in c′-spinel and not h-$YMnO_3$, which was observed when starting with m-$LiMnO_2$. We hypothesize that the observed t′-spinel resembles a tetragonal spinel closer to $Li_{2-\epsilon}Mn_2O_{4-\epsilon/2}$, where $1 < \epsilon < 2$, and not a t′-spinel resembling Mn_3O_4. Thus, we are observing a disproportionation regime that was not present in the diffraction patterns starting from the layered $LiMnO_2$ precursors where a spinel is observed only when $\epsilon \geq 1$. Instead, more o-$LiMnO_2$ and m-$LiMnO_2$ precursor persisted over this $1 < \epsilon < 2$ range when starting with the layered phases whereas the transition from t-$LiMnO_2$ to spinel intermediates was discrete, supporting the formation of a unique spinel intermediate over this region. This observation results in a pathway where the amount of Mn(III,IV) c′-spinel is greatest; or the value of ϵ is lowest when $YMnO_3$ is observed resulting in more o-$YMnO_3$ relative to h-$YMnO_3$.

The DFT-calculated phase diagram in Figure 5.7 suggests that the phase stability is correlated to the overall concentration of cation defects in the $YMnO_3$ lattice. Specifically, cation vacancies paired with partial oxidation of Mn^{3+} to Mn^{4+} appear to stabilize the orthorhombic phase due to its significantly lower cation vacancy formation energies. Limitations of our calculated phase diagram include: 1) the assumption that the defect

formation energy does not change with temperature, 2) the prerequisite that structural selectivity in $YMnO_3$ can be modeled assuming an *equal* concentration of cation vacancies, and 3) the lack of consideration of anharmonic phonon effects. It is important to note that Figure 5.7 must be considered from a fixed composition viewpoint; i.e., the phase diagram shows the predicted phase stability as a function of vacancy composition, rather than oxygen partial pressure. This is important in distinguishing the defect mechanisms between the two structures. For example, it is known that hexagonal rare earth manganites $RMnO_{3+\delta}$ synthesized under high oxygen pressure can accommodate excess oxygen via interstitials due to their more open structure.[168] Hence the constructed phase diagram provides a route to understanding thermodynamic stability when approached from a synthesis route in which cation vacancies exist or are likely to form, such as from an intermediate structure containing Mn^{4+}.

We anticipate that the inclusion of anharmonic effects could change the calculated Gibbs free energies of the $YMnO_3$ phases considerably at high temperature. This is likely the explanation of the unexpected negative slope of the phase boundary in Figure 5.7, which is due to the decrease in the free energy difference of the orthorhombic $G(T, P)$ curve with respect to the hexagonal $G(T, P)$ curve at high temperature. Indeed, the heat capacity of h-$YMnO_3$ ($P6_3cm$), which indicates the second derivative of $G(T, P)$ with temperature, underestimates the experimental heat capacity by $\sim 10\%$ at $T = 1400$ K, as seen in Figure A.26. Therefore anharmonic effects are likely required to explain the proposed entropic stabilization of the hexagonal phase at high temperature that has been experimentally observed.[90,160,169] Nevertheless, we believe that the location of the phase boundary at lower temperature is still a reasonable estimate of the order of magnitude of the critical

concentration of cation vacancies which switch the stability between the hexagonal and orthorhombic $YMnO_3$ phases. Even with differing values of Fermi energy within the band gap (Figure A.28) we predict this phase boundary to be located in the range $x \simeq 0.045$-0.07% at $T = 0$ K.

In all of the presented ternary metathesis reactions, long duration reactions yield greater amounts of o-$YMnO_3$ (Fig. 5.5). While the amount of h-$YMnO_3$ and o-$YMnO_3$ depends on the oxidation state of manganese in the spinel intermediates at *short* reaction times, the overall phase stability will reflect the concentration of defects closer to equilibrium, where the overall $YMnO_3$ phase stability will be dependent on the number of defects that are *initially* present in the $LiMnO_2$ precursors. The calculated concentration of cation defects needed to yield o-$YMnO_3$ is small (∼0.5%) which supports that even small amounts of impurities or site defects in the bulk $LiMnO_2$ precursors will result in o-$YMnO_{3+\delta}$ at temperatures below 600 °C, if allowed to equilibrate. At 600 °C, h-$YMnO_3$ begins to dominate, which supports previous phase diagrams above 800 °C.[170]

5.6. Conclusions

The reactions of three polymorphs of $LiMnO_2$ with YOCl to form LiCl and $YMnO_3$ were studied using X-ray and neutron diffraction. The reactions formed a number of crystalline intermediates, including r-YOCl, Y_3O_4Cl and two lithium manganese oxide spinel intermediates. The two spinel intermediates, reduced t′-spinel and oxidized c′-spinel, are the result of manganese disproportionation as lithium and oxygen are removed from $LiMnO_2$ over the course of the reaction. DFT-calculated thermochemistry reveals that small changes in

manganese oxidation state changes the relative stability of the two polymorphs of $YMnO_3$, suggesting that t′-spinel leads to formation of h-$YMnO_3$ while c′-spinel leads to the formation of o-$YMnO_3$. By changing the $LiMnO_2$ precursor, the ratio of reduced to oxidized spinel intermediates changes, which results in different ratios of the observed products. By tuning the composition of these spinel intermediates, the concentration of defects can be synthetically controlled in the resulting $YMnO_3$ products. Paired with additional post-synthesis treatment, these defects can be influenced or removed, which provides increased selectivity in the synthesis of complex oxides.

6. Catalytic behavior of hexaphenyldisiloxane in the synthesis of pyrite FeS_2[¶]

Overview

The use of functional small molecules affords opportunities to direct solid-state inorganic reactions at low-temperatures. Here we use substoichiometric amounts of organosilicon molecules to influence the metathesis reaction: $FeCl_2 + Na_2S_2 \longrightarrow 2\,NaCl + FeS_2$. At 150 °C, with no molecular additive, the reaction is diffusion limited and does not go to completion. Upon addition of hexaphenyldisiloxane, $(C_6H_5)_6Si_2O$, the reaction proceeds to completion at 150 °C after 24 h. *In situ* synchrotron X-ray diffraction experiments reveal that upon addition of the molecule, the reaction proceeds rapidly compared to the diffusion limited "neat" reaction. Differential Scanning Calorimetry reveals that the exotherm that forms the diffusion-limited intermediates is effectively removed in the presence of $(C_6H_5)_6Si_2O$. Control reactions suggest that the observed change in the reaction pathway is due to the $Si{-}O$ functional group. ^1H NMR supports catalytic behavior, as $(C_6H_5)_6Si_2O$ is unchanged *ex post facto*. Taken together, we hypothesize that the polar $Si{-}O$ functional group coordinates to iron chloride species as NaCl and Na_2S_4 form, forming a metastable intermediate state instead of more stable crystalline intermediates. In doing so, diffusion limited intermediates are not observed, leading to direct nucleation of FeS_2 at low-temperatures.

[¶]Substantial portions of this chapter have been reproduced with permission from P. K. Todd, A. J. Martinolich, and J. R. Neilson, *Prepared Manuscript* **2020**

6.1. Author Contributions

PKT conducted all experiments and wrote the manuscript with guidance from AJM and JRN. AJM assisted in experiments performed at ANL.

6.2. Introduction

The use of small functional molecules to direct the outcome of a chemical reaction is foundational to molecular solution-based chemistry, where catalysts and additives change activation barriers along the reaction pathway. Due to the high thermal energy barriers to diffusion, the reaction conditions of solid-state materials synthesis oftentimes exceed the temperatures where most molecules are stable, or where molecules can impart selectivity, thus limiting the degree of kinetic control attainable in these reactions.[6,20] There are examples of inorganic materials syntheses that take advantage of small molecules in solution, such as incorporation of weak Lewis acid or base additives like trioctylphosphine (TOP) or pyridine, as a anion source, solvent, and stabilizer for atom transfer in synthesizing transition metal phosphides and chalcogenides.[43,44] These solution based syntheses permit tunable syntheses, akin to retrosynthetic organic syntheses where inorganic templates, like CdO nanoparticles, can be converted to a Cu_xS product through step-wise cation or anion exchange reactions that incorporate specific molecular additives like $(CH_3)_3Si-(S/Se)$ and TOP to coordinate and transfer specific atoms into isolated cation/anion lattice sites.[32–34] For solid-state synthesis, reactions must proceed at temperatures where these molecules do not decompose in order to take advantage of their targeted functional groups.

Exchange reactions, or metathesis, provide low-temperature solid-state syntheses where reaction kinetics can be controlled using small molecules to direct product selectivity. For example, the addition of molecules like H_2O and $(C_6H_5)_3P$ has been shown to aid in atom transfer and intermediate conversion in metathetical preparations.[65,67,69] Shuttling atoms within the reaction mixture reduces energy barriers to diffusion and stabilizes the formation of metastable phases like pyrite $CuSe_2$ at low temperatures with no applied pressure.[171] By changing the chemical potential of selenium through adduct formation ($(C_6H_5)_3PSe$), synthetically inaccessible phases can be achieved, such as in metathesis reactions that yield phase pure superconducting iron selenide in a triphenylphosphine flux.[69] Exploring more functional molecules and understanding their role in changing reaction kinetics will open new avenues in inorganic materials chemistry.

In this work, we study a metathesis reaction that produces pyrite FeS_2 (Eqn. 6.1) in hopes of influencing the reaction pathway at low temperatures. The reaction in Equation 6.1 proceeds to completion at 350 °C for 24 h without an additive, whereas temperatures lower than 350 °C result in diffusion-limited products (Na_2S_4, Na_2S_5, $NaFeS_2$, and $Fe_{1-x}S$). In order for the reaction to proceed to FeS_2 at 150 °C, the initial energy barrier to product formation and solid-state diffusion must be lowered.

$$\mathrm{Na_2S_2 + FeCl_2 \xrightarrow{x} FeS_2 + 2\,NaCl} \tag{6.1}$$

Organosilane small molecules are considered due to their diverse range of physical properties and role as a mediator for ion transport (e.g., halogen transfer,[172,173] ferrosilox-

ane adducts,[174] Table A.15). By changing the Si−X (Si−O−Si, Si−OH, Si−Cl) moiety, the chemical properties change, providing a tunable variable for understanding changes to the reaction pathway in this metathesis reaction. Herein we show that $(C_6H_5)_6Si_2O$ and $(C_6H_5)_3SiOH$ selectively form crystalline NaCl and FeS_2 at low concentrations (Fig. 6.1). Hexaphenyldisiloxane, a weak Lewis base, appears to catalytically lower the energy barrier to FeS_2. Varying the concentration of $(C_6H_5)_6Si_2O$ changes the reaction kinetics where a finite concentration range (2-5mol%) of the molecule produces the most pyrite. ^{1}H NMR reveals that the remains unchanged *ex post facto*. Thus, $(C_6H_5)_6Si_2O$ is proposed as a catalyst in synthesizing FeS_2 in the solid-state. Analysis of the reaction pathways using *in situ* synchrotron X-ray diffraction (SXRD) reveals that $(C_6H_5)_6Si_2O$ changes the reaction pathway by reducing the observed number of diffusion limited intermediates. Changing the molecule concentration and heating rate are shown to tune the reaction kinetics from vigorous propagation events to a more mild pathway that increases the yield of FeS_2.

6.3. Materials and Methods

All reagents were prepared and stored in an argon-filled glovebox with O_2(g) and H_2O(g) levels less than 0.1ppm. Anhydrous $FeCl_2$ was purchased from Sigma-Aldrich (>98% purity), hexaphenyldisiloxane from Santa Cruz Biotechnology (Lot No. A0417, 99.6%), triphenylsilylchloride from TCI (>95%), triphenylsilanol from Alfa Aesar (99%), triphenylphosphine from Alfa Aesar (99+%), triphenylamine from Sigma Aldrich (98%), trityl chloride (97%), and eicosane ($C_{20}H_{42}$) from Acros Organics (99%). Triphenylphos-

phine sulfide was synthesized by heating triphenylphosphine and elemental sulfur in an evacuated silica ampule for 24 h at 150°C and confirmed by ^{31}P NMR spectroscopy.[68]

Na_2S_2 was prepared through a vapor transport reaction between elemental sodium and sulfur.[65] First, elemental sulfur was purified via vapor transport over a temperature gradient from 400 °C to 550 °C in a sealed silica ampoule under vacuum (<10mtorr). Sulfur was placed on the high end of the gradient and transported via vapor across the gradient where the purified product condensed and recrystallized. Solid sodium metal was stored in the glovebox under argon. Before use of the sodium metal, a razor blade was used to remove slight surface oxidation. Using the proper stoichiometry for Na_2S_2, the elements were weighed and placed in separate alumina crucibles with sulfur on the top to avoid a highly exothermic reaction. The contents were sealed under vacuum in a silica ampoule and heated in a box furnace at 200 °C at a ramp rate of 1 °C/min where the reaction dwelled for 24 h. This initial reaction allowed sulfur vapor to corrode the sodium metal to produce an inhomogeneous solution of Na_2S_2 and Na_2S and S_n. The reaction was readmitted to the glovebox and ground to a homogenous powder, pelleted, and sealed in a silica ampoule. An additional annealing step at 300 °C at a ramp rate of 1 °C/min produced a pure product. Air-free PXRD using a polyimide tape covering the powder sample revealed pure crystalline Na_2S_2.

All metathesis reactions were prepared in an argon-filled glovebox. Reagents were weighed on an analytical balance, ground into a homogeneous mixture (2x, 5 min), and pelleted. The pellet was carefully transferred to a closed system sealing station and sealed in a silica ampoule under vacuum (<10 mTorr). Reactions were heated at 150 °C and dwelled for 24 h. Reactions were placed in a hot convection furnace with no designated

ramp rate. Reactions that are deemed Air-Exposed (AE) refer to the grinding of the reaction mixture in an agate mortar and pestle under ambient atmosphere for 5 min after the heating step. Thus, the only exposure to ambient air and moisture was *ex post facto* grinding and characterization. The Air-Free (AF) reactions were prepared, reacted, processed, and characterized under argon. Neat reactions refer to the reactions performed with no molecular additive.

Synchrotron X-ray diffraction experiments were performed at beamline 17-BM-B (λ = 0.2415 Å) at the Advanced Photon Source (APS) at Argonne National Laboratory using a Perkin Elmer plate detector at a distance of 700 mm. Homogenized metathesis precursors were packed into a quartz capillary (1.1mm OD) at Colorado State University in an argon-filled glovebox. Then, capillaries were sealed under vacuum ($<$ 20 mTorr) using a methane-oxygen torch. All capillaries were loaded into a flow-cell apparatus[111] equipped with resistive heating elements and heated at various heating rates depending on the reaction to 300 °C. Whlie heating the samples were continuously rocked at $\pm$ 5° around the axis of the capillary. Depending on the heating rate, Diffraction patterns were collected every two seconds and summed every 10 s (Heating rate $<$ 160 °C/min) at low heating rates. For rapid heating, the diffraction patterns were not summed and taken every two seconds. Plate detector images were integrated using GSAS-II and calibrated using a LaB_6 standard.

Powder X-Ray Diffraction (PXRD) was performed on a Bruker D8 DaVinci with CuK_α radiation. All samples were prepared on a zero-background disc with polyimide film to protect the samples from the environment. Rietveld analysis was performed using EXPGUI/GSAS or TOPAS.[107,108] ^{1}H NMR was performed on an Agilent (Varian) 400 MHz

NMR spectrometer using deuterated methylene chloride as the solvent (CD_2Cl_2; CIL Inc. 99.96%). All ^1H NMR samples were prepared in a glovebox under nitrogen. NMR tubes were sealed with Parafilm® wax to avoid air exposure during transport and characterization. Differential Scanning Calorimetry (DSC) experiments were performed on a TA Instruments 2500 Discovery DSC. Experiments were prepared by hermetically sealing the homogenized metathesis precursors in an aluminum pan. DSC experiments were performed by heating each experiment at 10 °C/min to 300 °C

6.4. Results and Discussion

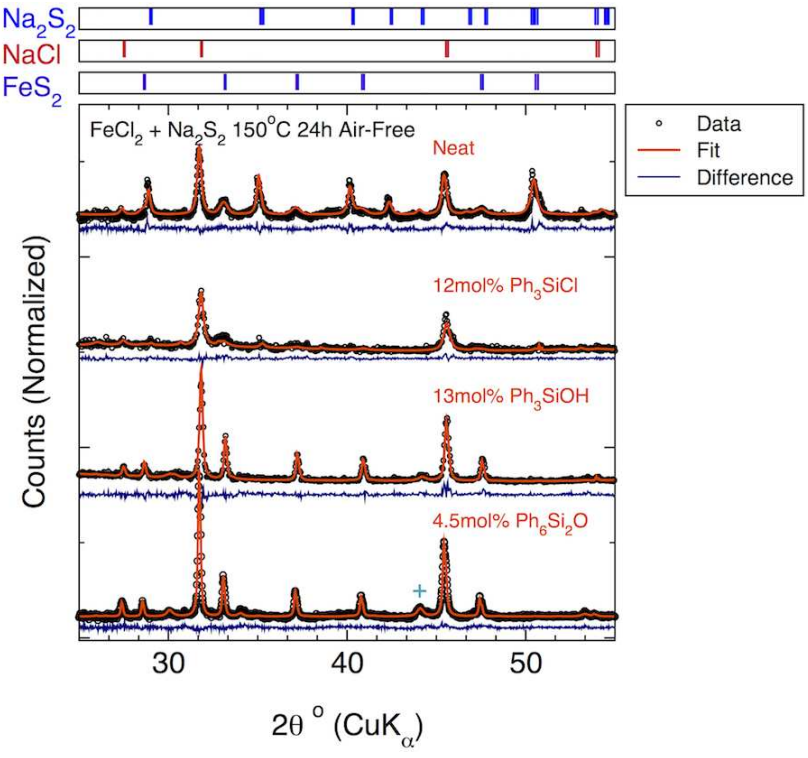


Figure 6.1: PXRD results with Rietveld refinements from metathesis reactions of $FeCl_2 + Na_2S_2$ at 150 °C for 24h under Argon: Top to Bottom: Neat reaction, 12mol% Ph_3SiCl, 13mol% Ph_3SiOH, 4.5 $(C_6H_5)_6Si_2O$. + denotes (206) reflection of Fe_7S_8

PXRD data in Figure 6.1 of the neat metathesis reaction show formation of crystalline NaCl, small amounts of pyrite FeS_2, and high concentrations of unreacted Na_2S_2 precursor (Table 6.1). As compared to the metathesis reaction without a molecular additive, the PXRD results using 4.5mol% $(C_6H_5)_6Si_2O$ (MP: 225 °C) show a dramatic increase in the crystallinity and phase fraction of FeS_2 and NaCl (Fig. 6.1). At 150 °C the metathesis reaction proceeds to completion in Eqn. 6.2:

$$\mathrm{Na_2S_2 + FeCl_2 \xrightarrow{4.5\ mol\%\ (C_6H_5)_6Si_2O} 2\,NaCl + FeS_2} \tag{6.2}$$

where 4.5 mol% $(C_6H_5)_6Si_2O$ results in the highest FeS_2 product yields. Figure 6.2 shows the changes in the products from diffraction patterns under various concentrations of $(C_6H_5)_6Si_2O$. As the $(C_6H_5)_6Si_2O$ concentration increases from 0.5 mol% to 4.5 mol%, the mol% phase fraction of the FeS_2 in the PXRD results increases (Table 6.1; Fig. 6.2). At higher mol% concentrations ($x \geq 4.5$ mol%), the products are comprised of Na_2S_2 and Na_2S_4. Thus, the formation of FeS_2 is highly dependent on the relative amount of $(C_6H_5)_6Si_2O$. At 0.5 mol% $(C_6H_5)_6Si_2O$, the reaction is rapidly exergonic, as indicated by complete pellet deformation and the presence of sulfur condensed on the ampule (Fig 6.2). Previous studies of highly exergonic metathesis reactions have observed similar disproportionation of alkali sulfides which are attributed to diffusion limitations and rapid decomposition of salts with more volatile anion species.[53,63,133,175] PXRD reveals NaCl and Fe_7S_8 but no FeS_2, which suggests that the loss of sulfur from the reaction mixture:

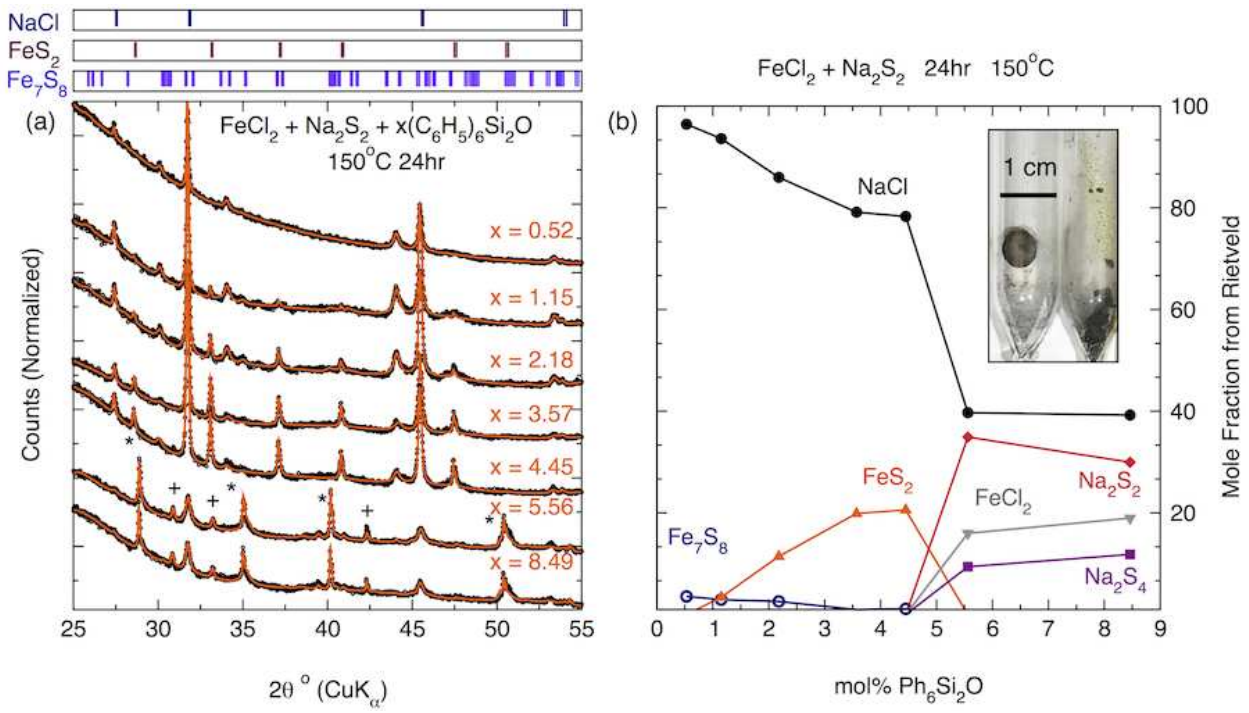


Figure 6.2: (a) PXRD results with Rietveld refinements from metathesis reactions of $FeCl_2$ and Na_2S_2 at 150 °C for 24h under Argon: varying mol% $(C_6H_5)_6Si_2O$; (+) denote Na_2S_4 (*) denote Na_2S_2. (b) Mole fraction from Rietveld refinements of PXRD data as a result of varying the mol% concentration of $(C_6H_5)_6Si_2O$. The inset shows reaction pellets of 4.5 mol% $(C_6H_5)_6Si_2O$ and 0.5 mol% metathesis pellets with yellow sulfur condensate at 0.5 mol%.

$$\mathrm{Na_2S_2 + FeCl_2 \xrightarrow{0.5\ mol\%\ (C_6H_5)_6Si_2O} 2\,NaCl + xFeS + xS + 1 - \mathit{x}FeS_2} \tag{6.3}$$

At 4.5 mol%, the pellet remains intact and results in higher FeS_2 yields suggesting the concentration of $(C_6H_5)_6Si_2O$ changes the reaction kinetics. The observations suggests that $(C_6H_5)_6Si_2O$ is actively involved in determining the pathway and the rate by which it happens.

The decrease in reactivity at higher molecular loadings ($x \geq 4.5$ mol%) can be explained by an decrease in the volumetric percolation reactants. For perspective, 8.5 mol%

Table 6.1: Phase Fraction of Metathesis Products at Various mol% $(C_6H_5)_6Si_2O$ loading as determined by Rietveld analysis of PXRD data.

mol% $(C_6H_5)_6Si_2O$	NaCl	Fe_7S_8	FeS_2	Na_2S_2	Na_2S_4	$FeCl_2$
0.5	96(2)	3.6(1)	–	–	–	–
1.2	93(1)	2.95(8)	3.4(2)	–	–	–
2.2	86(1)	2.58(8)	11.4(4)	–	–	–
3.6	79(1)	0.98(6)	19.9(4)	–	–	–
4.5	78(1)	1.14(7)	20.6(4)	–	–	–
5.6	38(1)	–	–	34(1)	9.4(2)	16.0(3)
8.5	39(2)	–	–	30(1)	11.8(2)	19.0(3)

$(C_6H_5)_6Si_2O$ represents ∼80% by volume of the total precursor mixture, which significantly decreases connectivity between reactants. In previous metathetical preparations of transition-metal borides and nitrides where the reaction is highly exothermic, additional alkali-metal halide salts are added to the precursor mixture to act as a heat sink.[133] Hexaphenyldisiloxane also appears to function similarly. At molecular loadings where the reaction proceeds to iron sulfide products ($0.5 \leq x \leq 4.5$ mol%), the $(C_6H_5)_6Si_2O$ molecule is hypothesized to provide a heat sink to dampen the observed propagation kinetics observed at 0.5mol% (Fig. 6.2). Thus, the reaction with 4.5 mol% does not propagate, yet still permits appropriate mixing of reactants to yield a reaction.

Temperature dependent *in situ* synchrotron X-ray diffraction experiments reveal $(C_6H_5)_6Si_2O$ reduces the number of crystalline intermediates observe along the reaction pathway. Figure 6.3 presents combined *in situ* SXRD and Differential Scanning Calorimetry (DSC) experiments heated at 10 °C/min to 300 °C. Metathesis reactions with 4.5 mol% $(C_6H_5)_6Si_2O$ (Figure 6.3(a)) show a dramatic change from reactants to products below 150 °C. Denoted by dotted lines, the precursors quickly react to yield NaCl and Na_2S_4 as the only observed crystalline intermediates before FeS_2 crystallizes at high temperatures. In

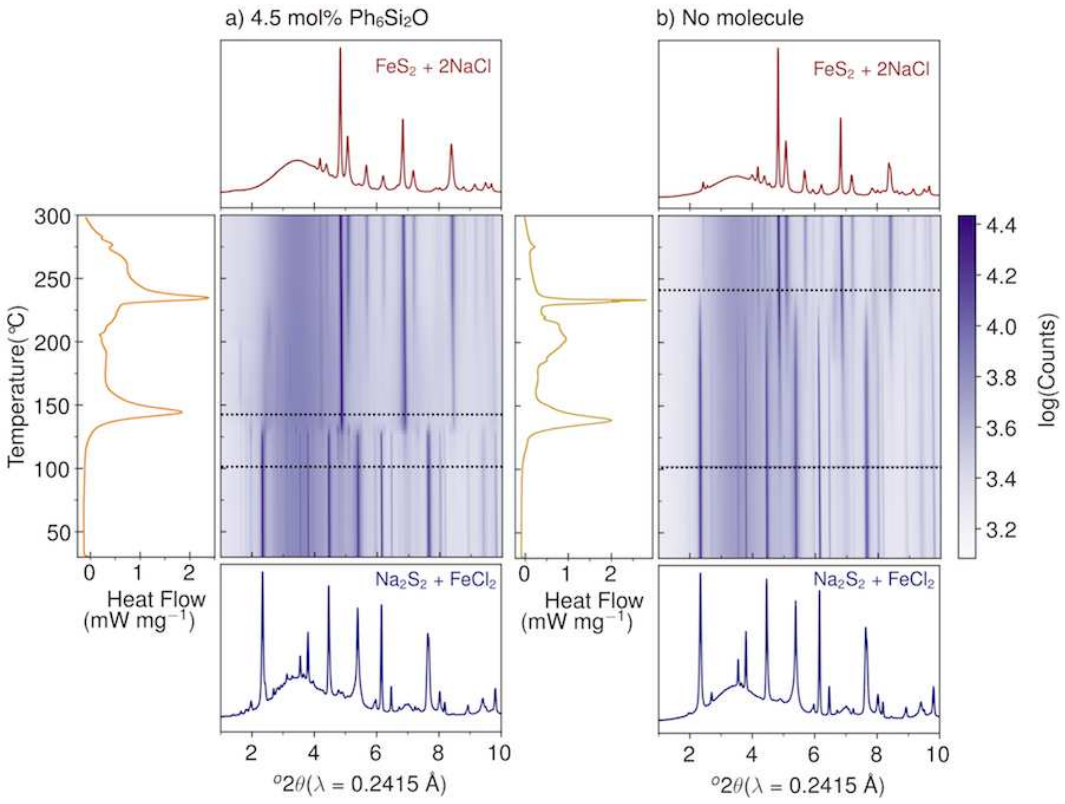


Figure 6.3: *in situ* SXRD results of the reaction $Na_2S_2 + FeCl_2$ a) using 4.5 mol% $(C_6H_5)_6Si_2O$ and b) with no molecular additive heating at 10 °C/min to 300 °C. Differential Scanning Calorimetry plots are appended to a) and b) to compare crystallization exotherms. Dotted lines denote the start and stop of reactive zones in the diffraction data. The reaction proceeds from precursors reactive intermediates, and finally products.

the DSC trace in Figure 6.3 a), two exotherms are observed attributed to the crystallization of NaCl at 150 °C and FeS_2 near 250 °C. Interestingly, an endotherm is observed near 225 °C which coincides with a rapid decrease in a number of low angle Bragg peaks evident in the precursor SXRD pattern. This event is attributed to the melting of the $(C_6H_5)_6Si_2O$. The reaction pathway in Figure 6.3b) presents the metathesis reaction without a molecule. Here, we observe a pathway that proceeds through diffusion-limited intermediates (Na_2S_4, Na_2S_5, $NaFeS_2$, $Fe_{1-x}S$). Compared to Figure 6.3(a), the reaction pathway is more diffuse, without the discreet event observed in Figure 6.3(a). In the DSC trace in Figure 6.3(b), the same exotherms are observed for NaCl and FeS_2, yet an additional broad exotherm

appears (175-225 °C) which we attribute to the crystallization of these diffusion limited intermediates. The absence of this exotherm paired with Na_2S_4 as the only identified crystalline intermediate in Figure 6.3(a) suggests that $(C_6H_5)_6Si_2O$ is actively influencing how the reaction pathway proceeds from precursors to products by circumventing a pathway through these diffusion-limited intermediates. This observation suggests the the molecule may be reacting *in situ* to form or stabilize an intermediate that is not observed crystallographically.

Analysis of the $(C_6H_5)_6Si_2O$ structure *ex post facto* in these ternary metathesis reactions reveals that the molecule remains unchanged. Figure A.33 shows the ^{1}H NMR spectrum of the washed 4.5 mol% $(C_6H_5)_6Si_2O$ assisted metathesis products as compared to a $(C_6H_5)_6Si_2O$ standard. The similarities in the spectra qualitatively suggest the molecule is unchanged during the course of the reaction, supporting catalytic behavior. Considering the physical properties of the molecule, the $(C_6H_5)_6Si_2O$ is hypothesized to (1) increase diffusion at 150 °C by melting at the observed exotherm from NaCl, or later at the molecule's melting point (225 °C), (2) form adducts with precursors as a Lewis base or aryl-based ligand to shuttle atoms within the reaction, (3) or form some transient, metastable intermediate that is directly related to the polarizability of the Si−O−Si moiety that involves Si−X bond breaking and reforming. In order to test these hypotheses, control reactions were performed using other small molecules with targeted functional groups or properties.

In Figure 6.3(a), we observe the melting of $(C_6H_5)_6Si_2O$, which proceeds the crystallization of pyrite in these metathesis reactions. Therefore, Eicosane ($C_{20}H_{42}$ MP: 42°C) was used as a control to identify if the metathesis reaction could proceed through increasing diffusion through a molten, non-specific alkane. The PXRD results in Figure 6.4 show lim-

ited reactivity with NaCl, Na_2S_2, and Na_2S_4 as the identifiable phases. These results show that increasing diffusion is not the only requisite step needed to increase reactivity at low temperatures in these metathesis reactions. Therefore, the $(C_6H_5)_6Si_2O$ must be directly reacting or coordinating to species along the reaction pathway.

Previous work on the metathetical preparation of $CuSe_2$ have shown that the Lewis base $(C_6H_5)_3P$ promotes kinetic control in the formation of the metastable pyrite polymorph by shuttling copper and selenium within the reaction mixture to stabilize pyrite formation.[6,76] $(C_6H_5)_6Si_2O$ should nominally act as a weak Lewis base within the metathesis reaction of FeS_2 as well. To identify how the Lewis basicity affects the kinetic pathway of the formation of FeS_2, triphenylphosphine ($(C_6H_5)_3P$), was added to the precursor reaction mixture at 4.5 mol% loading. The PXRD results in Figure 6.4 show NaCl formation with broad, poorly resolved FeS_2 reflections. Compared to the $(C_6H_5)_6Si_2O$ addition, these results suggest Lewis base addition is not general to product formation. The lack of crystalline Fe−S phases in the diffraction pattern suggests the $(C_6H_5)_3P$ prevents FeS_2 nucleation and growth, perhaps by the same atom-transfer mechanism suggested in the $CuSe_2$ system. If $(C_6H_5)_3P$ is forming an adduct with sulfur, the $(C_6H_5)_3P{-}S$ (BDE: 105.6 kcal/mol) bond will be stronger than the $(C_6H_5)_3P{-}Se$ adduct (BDE: 86.92 kcal/mol). To test the hypothesis that a phosphorus-sulfur adduct is limiting FeS_2 crystallization, $(C_6H_5)_3PS$ was tested, yet the PXRD results yielded similar features as $(C_6H_5)_3P$ (Fig. 6.4). These results suggest that the basicity of phosphorus may be limiting the reaction pathway to FeS_2. Therefore, we conducted metathesis reactions with a less basic molecule, $(C_6H_5)_3N$. Once again, the FeS_2 Bragg peaks in Figure 6.4 are poorly crystalline, suggesting that Lewis basicity may not be the determining factor when using $(C_6H_5)_6Si_2O$.

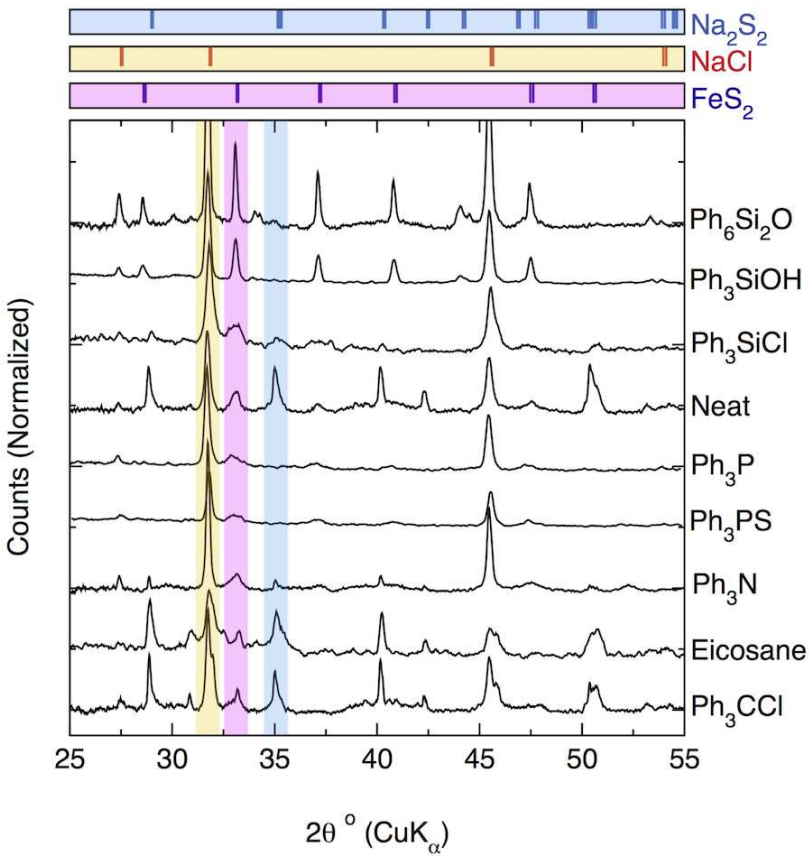


Figure 6.4: PXRD results from the reaction: $Na_2S_2 + FeCl_2$ at 150°C for 24hr with various small molecule additives. The reflections for Na_2S_2, FeS_2, and NaCl are shown as tick marks above and reflections are highlighted by colored rectangles for comparison. All concentrations are at 10 wt% of each molecule.

The control reactions support a reaction pathway that is dependent on the Si−O moiety being present. In Figure 6.4, 13 mol% $(C_6H_5)_3SiOH$ reveals crystalline pyrite and NaCl, similar to the results using $(C_6H_5)_6Si_2O$. The air-free addition of $(C_6H_5)_3SiCl$ in Figure 6.4 also supports the hypothesis of a Si−O dependent reaction pathway as iron sulfide phases are poorly resolved in the PXRD data. While the R-group of these organosilicon molecules may be influencing the pathway, the hexamethyl- and hexaethyl- disiloxane derivatives are both liquids and have weaker Si−R bond dissociation energies, which convolutes the role of these R-groups influencing the pathway. Nonetheless, many of the organic molecules tested here, the presence of phenyl groups does not lead to consistent

trends in the PXRD results, which further supports a dependence on the presence of the Si−O functional group.

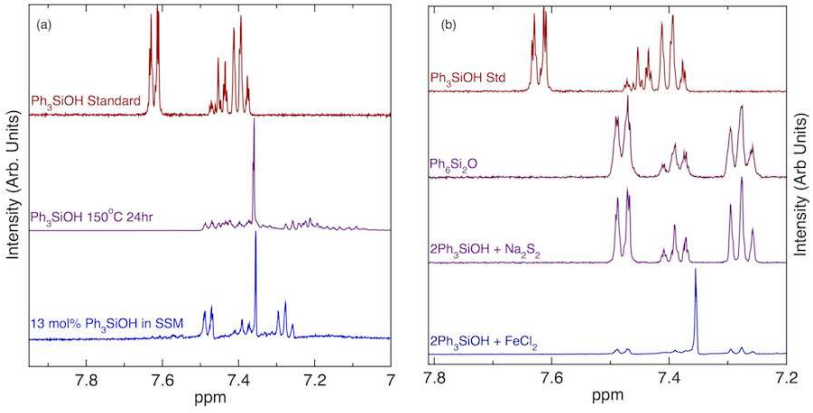


Figure 6.5: ^{1}H NMR spectra of relevant $(C_6H_5)_3SiOH$ control reactions. All reactions were heated at 150°C for 24hr. (a) $(C_6H_5)_3SiOH$ standard, $(C_6H_5)_3SiOH$ decomposition after heating, $(C_6H_5)_3SiOH$ washes from the reaction $Na_2S_2 + FeCl_2$. (b): $(C_6H_5)_3SiOH$ and $(C_6H_5)_6Si_2O$ standards as compared to $(C_6H_5)_3SiOH$ reactions with each reaction precursor.

^{1}H NMR studies of the reaction products in deuterated methylene chloride, reveal that the $(C_6H_5)_3SiOH$ polymerizes/decomposes upon heating (Fig. 6.5(a)). As explained in detail in the Supplementary Information, a self condensation reaction forms $(C_6H_5)_6Si_2O$, yet experiences nucleophillic attack from water resulting in a polymerization to a silicone-like polymer. Interestingly, the formation of water from the self-condensation reactions induces similar behavior to previous studies on this metathesis reaction where grinding the reactants in humid air circumvents diffusion-limited intermediates.[66] To test the hypothesis that water is influencing the reaction pathway, a vapor transport reaction was performed where the self-condensation reaction was separated from the metathesis precursors physically. The results and experimental set-up are shown in Figure A.34, where the presence of water vapor does not result in FeS_2. While direct contact with the water may influence

the pathway more, the results with pure $(C_6H_5)_6Si_2O$ suggest a pathway more dependent on the Si−O functional group.

Control reactions with $(C_6H_5)_3SiCl$ support a direct reaction with Na_2S_2 resulting in some NaCl formation (Fig. 6.1) and a hypothesized thiosilane product (Fig. A.35) ^{1}H NMR spectroscopy reveals two unique phenyl environments in washed products from metathesis reactions *and* from reactions between $(C_6H_5)_3SiCl$ and Na_2S_2. Interestingly, the molecule remains unchanged upon heating and in control reactions between $(C_6H_5)_3SiCl$ and $FeCl_2$. Organosilylchlorides are common precursors for producing various organothiosilane molecules and thiosilicone polymers.[176] Furthermore, if $(C_6H_5)_3CCl$ is used in these metathesis reactions (Fig. 6.4), the reaction products are similar to those without a molecule. Therefore, the formation of a thiosilane product impedes the nucleation of FeS_2 by extracting sulfur. These results further support the importance of the Si−O functional group influencing the reaction pathway towards crystalline FeS_2.

The presented results show that $(C_6H_5)_6Si_2O$ behaves catalytically in reducing the activation barriers in these metathesis reactions. Currently, our knowledge of *how* the $(C_6H_5)_6Si_2O$ interacts with species present along the pathway is not well defined, yet we can hypothesize the pseudo-elementary steps to product formation based on related observations:

$$2\,Na_2S_2 + 2\,FeCl_2 + (C_6H_5)_6Si_2O \longrightarrow 2\,NaCl + [(C_6H_5)_6Si_2O{-}(FeCl)_2] + Na_2S_4 \quad (6.4a)$$

$$[(C_6H_5)_6Si_2O{-}(FeCl)_2] + Na_2S_4 \longrightarrow 2\,NaCl + FeS_2 + (C_6H_5)_6Si_2O. \quad (6.4b)$$

where an unknown, putative $[(C_6H_5)_6Si_2O{-}(FeCl)_2]$ species stabilizes reactive iron chloride species to avoid alternative reactions that yield diffusion limited intermediates. Previous *in situ* PXRD studies of $Na_2S_2 + FeCl_2$ under air-free conditions show that reactivity is initiated by the decomposition of the $FeCl_2$, or the breaking of $Fe{-}Cl$ bonds.[66] Thus, a valid first hypothesis is that the $(C_6H_5)_6Si_2O$ aids in stabilizing the $Fe{-}Cl$ species as NaCl forms. The $Si{-}O{-}Si$ moiety possesses an unusually high bond angle ($144{\pm}0.9°$) and short $Si{-}O$ bond length ($1.64{\pm}0.3$Å) which has been attributed to the ionic character of the $Si{-}O$ bond in comparison to $C{-}O$ analogs.[177] This polarizability could result in cleavage of the disiloxane bonds by transition-metal halides to form transition-metal silanolates (e.g., $(C_6H_5)_3SiO{-}[FeCl]$[178]). Ferrosiloxanes and ferrosiliconate complexed anions have also been reported that can form salts such as $Na[Fe(OSiMe_3)_4]$,[179] as well as cage-like complexes with iron[174] however, additional studies aer required to identify the nature of the true molecular intermediate. yet we have been unable to find evidence of these molecules in *ex post facto* characterization.

Another plausible hypothesis is that $(C_6H_5)_6Si_2O$ may complex the iron (II) chloride as a weak ligand. As the siloxane functional group is sterically hindered by phenyl groups, we may be observing a haptic-type interaction where the reduced [FeCl] species is stabilized through interaction with the phenyl π system. In such a coordination environment, the phenyl groups would hatpically bond to iron as chloride anions are removed to form NaCl, thus stabilizing the iron (II) environment. Interestingly, the phenyl groups in these disiloxane molecules have been shown to exhibit significant dipole moments along the $(C_6H_5){-}Si{-}O$ bond due to $(p \longrightarrow d)_\pi$ interactions with silicon.[180] The electron withdrawal from the phenyl groups could hypothetically provide more of a η^3 haptic bonding

environment, where a half-sandwich type complex could form such as $Fe(Cl)_3\eta^3-(C_6H_5R)_2$, which obeys the 18 electron rule and maintains the Fe^{2+} oxidation state. This type of coordination complex would explain the absence of crystalline inorganic intermediates containing iron or molecular intermediates. Coordinating reactive iron chloride species would catalyze the nucleation of FeS_2. From the observation of diffusion-limited intermediates in reactions without $(C_6H_5)_6Si_2O$, we hypothesize that the lifetime of these reactive iron chloride species is short-lived. If diffusion is too slow to a reaction interface, the iron chloride species will react with nearby species, resulting in myriad diffusion-limited phases (e.g., $NaFeS_2$, $Fe_{1-x}S$) that will then take more time to diffuse and react to yield FeS_2. By coordinating these iron chloride species, their lifetime is extended to permit nucleation of FeS_2 directly at low temperatures.

6.5. Conclusions

In conclusion, this report has demonstrated kinetic control of the metathesis reaction $Na_2S_2 + FeCl_2 \longrightarrow FeS_2 + 2\,NaCl$ through addition of organosilicon molecules. The identity of the $Si-O-Si$ moiety changes the reaction pathway in the metathetical preparation of FeS_2 at low temperatures (150 °C). Addition of $(C_6H_5)_6Si_2O$ has a catalytic effect on the formation of FeS_2 which is dependent on a specific concentration range (2-5 mol%). Analysis of the reaction pathway with $(C_6H_5)_6Si_2O$ reveals a decrease in the number of diffusion-limited crystalline intermediates. We hypothesize that $(C_6H_5)_6Si_2O$ catalyzes the reaction pathway by stabilizing reactive iron chloride species either through a cleavage of the $Si-O$ bond or through a haptic coordination between iron and phenyl R-groups. The

result is the direct nucleation of FeS_2 without proceeding through diffusion-limited intermediates attributed to the molecular nature of $(C_6H_5)_6Si_2O$. This contribution identifies strategies for rationally designing solid-state reactions at low-temperature by coordinating functional molecules with specific reactant compositions.

7. Outlook and Proposed Future Directions[||]

7.1. Exploring selectivity in yttrium iron oxides: a reversal of yttrium manganese oxide phase stability

Yttrium manganese oxide was used as a model system in this dissertation to due to the number of metastable polymorphs available for synthesis. In the case of $YMnO_3$, the orthorhombic polymorph is metastable, while the hexagonal polymorph is thermodynamically stable. While the assisted metathesis reactions and ternary metathesis reactions were successful in selecting between these two polymorphs using manganese, the same may not be true when the transition metal changes.

In the case of yttrium iron oxides, the same polymorphs are observed, yet the stability changes. for $YFeO_3$ the hexagonal phase is the high-pressure metastable phase, while the orthorhombic perovskite is stable. Probing the $YFeO_3$ products using metathesis reactions will expand on the utility of these reactions in kinetically controlling reaction pathways of complex oxides at low-temperatures. The metastable hexagonal $YFeO_3$ has been prepared previously using complex sol-gel methods[181] at low-temperatures and through rapid self-combustion reactions using glycine as fuel.[182] Also, the stability of these $YFeO_3$ phases changes as a function of temperature and oxygen partial pressure.[183]This suggests that the hexagonal phase may be kinetically stabilized at low-temperatures using metathesis chemistry.

[||]A portion of this chapter has been reproduced with permission from D. O'Nolan, G. Huang, G. E. Kamm, A. Grenier, C-H. Liu, P. K. Todd, A. Wustrow, G. T. Tran, D. Montiel, J. R. Neilson, S. J. L. Billinge, P. J. Chupas, K. S. Thornton, K. W. Chapman, *Prepared Manuscript* **2020**

Another interesting aspect in the metathetical preparation of $YFeO_3$ is the diversity of precursors to select from. In the family of lithium iron oxides, there are four unique structures available to use as precursors. Also, FeOCl exists, which provides affords a unique opportunity to see how changing the identity of the precursor affects the pathway. In this reaction, $LiYO_2 + FeOCl$ would be compared to $LiFeO_2 + YOCl$. While $YFeO_3$ is an interesting system analogous to $YMnO_3$, there are many ternary oxide materials that have not been realized. For example, $YMoO_3$ has not been reported yet Y_2MoO_6 is a known phase. Molybdenum is known to be very refractory and difficult to isolate at Mo(III), so this would be a challenging problem for future projects.

7.2. Using chemometrics to enhance material discovery: increasing the PhD to *in situ* SXRD dataset ratio

Solid-state reactions involve coupled transformations of chemistry and structure that can be complex to understand and predict. Insight into the mechanism and pathway for such reactions can be obtained by characterizing how the structure, chemistry and abundance of multiple crystalline reagents, products, intermediates, possible impurities and polymorphs thereof evolve as a function of time and reaction temperature using in-situ X-ray scattering[42,68,70,110]

For the ternary metathesis reaction, $LiMnO_2 + YOCl \longrightarrow LiCl + YMnO_3$, the time-evolution of 9 discrete crystalline phases was observed at a continuum of temperatures up to 750°C. Variable temperature in situ data X-ray scattering data were collected at beamline 28-ID-2, XPD (λ = 0.1949 Å) at NSLS-II, using a newly developed gradient

heater following isothermal heating for 20 min and 40 min, and following cooling to room temperature. Preparation of the reaction precursors has been described previously (Chapter3).[110]

The scattering data show complex coupled changes in the observed diffraction peaks as a function of time and temperature (Figure 7.1). Non-negative matrix factorization (NMF), implemented using the Python scikit-learn package,[184] was applied to the data to rapidly resolve correlated features as separate components and to quantify their associated weight trends (Figure 7.1). The use of such blind-signal separation has been established for images,[185] audio signals[186] and diffraction patterns.[187,188] Each component groups peaks that are observed in together, that is, all peaks from a given crystalline phase and grouped with other crystalline phases that form and/or disappear at the same time. In this way NMF can effectively monitor the reaction state.

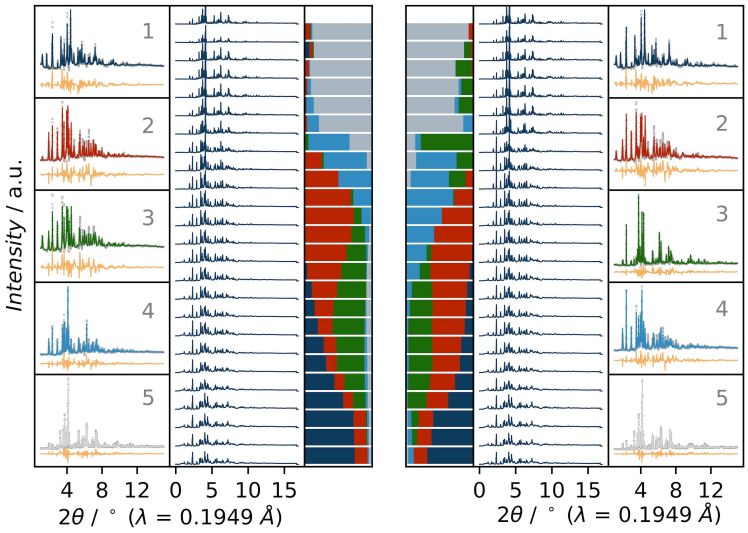


Figure 7.1: Synchrotron X-ray diffraction patterns for the ternary metathesis reaction: $LiMnO_2 + YOCl \longrightarrow YMnO_3 + LiCl$ collected in situ and the corresponding Rietveld refinements of the NMF-derived components (left). The corresponding the weight ratios associated with the 5 NMF components as horizontal bar charts, track the state of the metathesis reaction.

The components from the NMF analysis include features from real crystalline phases and the evolution of the component weightings reflect the progression of intermediate reactions along the reaction pathway; Rietveld refinements were undertaken on the components in TOPAS (Figure 7.1). The analysis corroborates the results presented in Chapter 5, including the identity of all intermediates and products.The analysis shows the time evolution of the reaction at different temperatures, including transformation between different polymorphs, for example, an increasing proportion of o-$YMnO_3$ relative to h-$YMnO_3$ is observed with increasing reaction time.

For the presented body of work, only a handful of *in situ* SXRD experiments were used to construct 5 chapters, yet many more were collected and left unanalyzed. Developing these multivariate analysis tools will alleviate the time demands for analysis and hopefully lead to increased understanding of the kinetic pathways of these complex reactions.

7.3. Evaluating the role of organosilane molecules in other metathesis systems

In this report, the addition of $(C_6H_5)_6Si_2O$ has been used exclusively in the metathesis reaction of $FeCl_2 + Na_2S_2$. Expanding the scope of this work to other metathesis systems will provide insight into (1) how specific the molecule is to individual materials and (2) insight into other solid-state reaction pathways. Currently, $(C_6H_5)_6Si_2O$ is being studied in the $CuCl_2 + Na_2Se_2$ as a means to control polymorph formation. As seen in Figure 7.2, at low concentrations of $(C_6H_5)_6Si_2O$, the metastable pyrite-$CuSe_2$ polymorph is more favorable than the thermodynamically stable marcasite phase. As can be seem from the

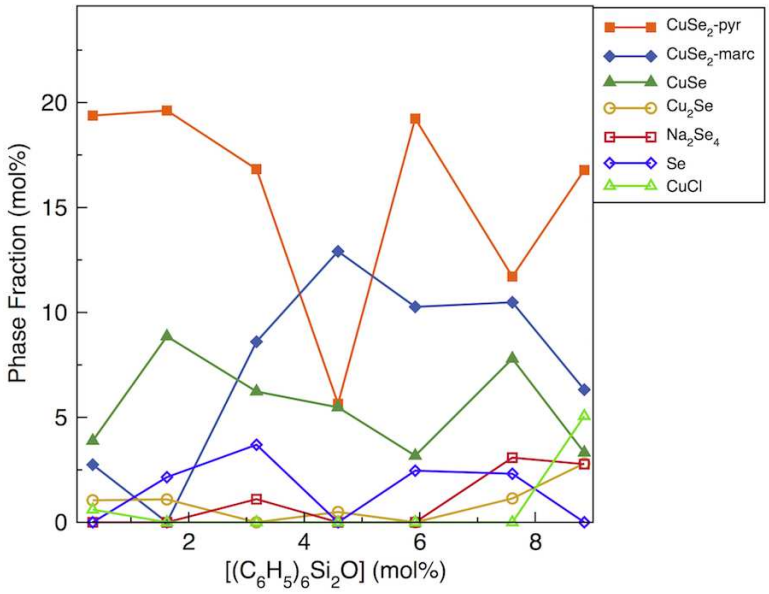


Figure 7.2: Mole phase fraction calculated from Rietveld refinements of PXRD data in the reaction $CuCl_2 + Na_2Se_2$ with varying mol% $[(C_6H_5)_6Si_2O]$ NaCl phase fraction maintains a range between 65-75mol% phase fraction and is omitted to clarify the copper selenide products.

results, the overall trend in this system is not clear above 3 mol% of the molecule. Present work is focusing on optimizing reaction conditions, such as heating rates, in order to control the kinetic formation of metastable pyrite $CuSe_2$. The addition of triphenylphosphine ($(C_6H_5)_3P$) also selectively formed the metastable polymorph, but the proposed atom-transfer pathway was not catalytic, as phosphine-selenium adducts physically remove precursors as the concentration of additive increases. If we can show that $(C_6H_5)_6Si_2O$ is *catalytically* forming the pyrite polymorph, it would provide improved product conversion and efficiency in isolating metastable phases.

Continuing to probe additional metathesis systems will address the utility of the $(C_6H_5)_6Si_2O$ in controlling reaction kinetics. Each molecule used in these solid-state reactions interacts with the precursor materials differently. Increasing our understanding of the types of solids that interact favorably with these molecules will provide more rational

predictions for synthesis. Ideally, a detailed set of rules and a toolbox of reaction conditions can be created for a variety of metathetical preparations based on the precursors.

7.4. Multi-modal *in situ* characterization of metathesis reactions

While X-ray diffraction techniques dominate the characterization of structure in solid-state chemistry, their only provide one technique for characterizing reaction pathways *in situ*. Previous results in the metathetical preparation of transition metal chalcogenides has shown that exposure to water from grinding precursors in air has a catalytic effect on the reaction pathway.[66,67] In these experiments, *in situ* SXRD was used to characterize the reaction pathways *after* the materials had been exposed to water. Thus, characterization of the exposure "event" was undocumented. Even so, diffraction experiments may not be the best characterization tool for looking at this exposure, as the water vapor will be absent in the diffraction patterns. Pair Distribution Function analysis is helpful in looking at changes to the local structure if the reaction contains amorphous material, yet this technique is also used after the exposure event. Recently, the Advanced Photon Source (APS-11-ID-B) has developed multi-modal techniques that pair *in situ* diffraction with IR Spectroscopy.[189] Here, the reaction mixture can be controllably prepared air-free and mounted at the beamline. Then, humid air can be controllably added to the reaction environment and measured simultaneously using IR spectroscopy and SXRD. The IR spectroscopy will look at stretching modes of water to identify how the molecule is affecting the precursors.

Recently, we conducted a preliminary experiment at 11-ID-B using this multi-modal set-up. The results are shown in Figure 7.3 where SXRD, PDF, and IR spectroscopy are

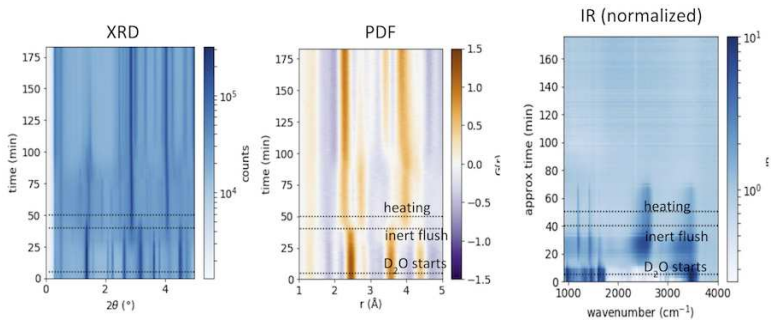


Figure 7.3: Comparison of Synchrotron X-ray diffraction patterns (LEFT), Pair Distribution Function analysis (CENTER), and DRIFTS IR Sepctroscopy (RIGHT) in the metathesis reaction: $Na_2S_2 + FeCl_2 \xrightarrow{H_2O} FeS_2 + 2\,NaCl$. The dotted lines describe different labeled events during the reaction.

shown for the reaction: $Na_2S_2 + FeCl_2 \longrightarrow 2\,NaCl + FeS_2$. The dotted lines denote when the reaction is exposed to humid air. There is a distinct change that occurs when the precursors are exposed to water. Analysis of the intermediates reveals that the water forms hydrated intermediates (Figure 7.3) which promote NaCl formation upon mixing.

Unfortunately, the IR spectroscopy data shows a clear saturation from water, rendering analysis difficult. Also, the experimental set-up takes coordination of many different instruments and preparing the samples in a glovebox is time consuming. Another experiment is needed to fully flesh out the details of how the water interacts at the reaction surface.

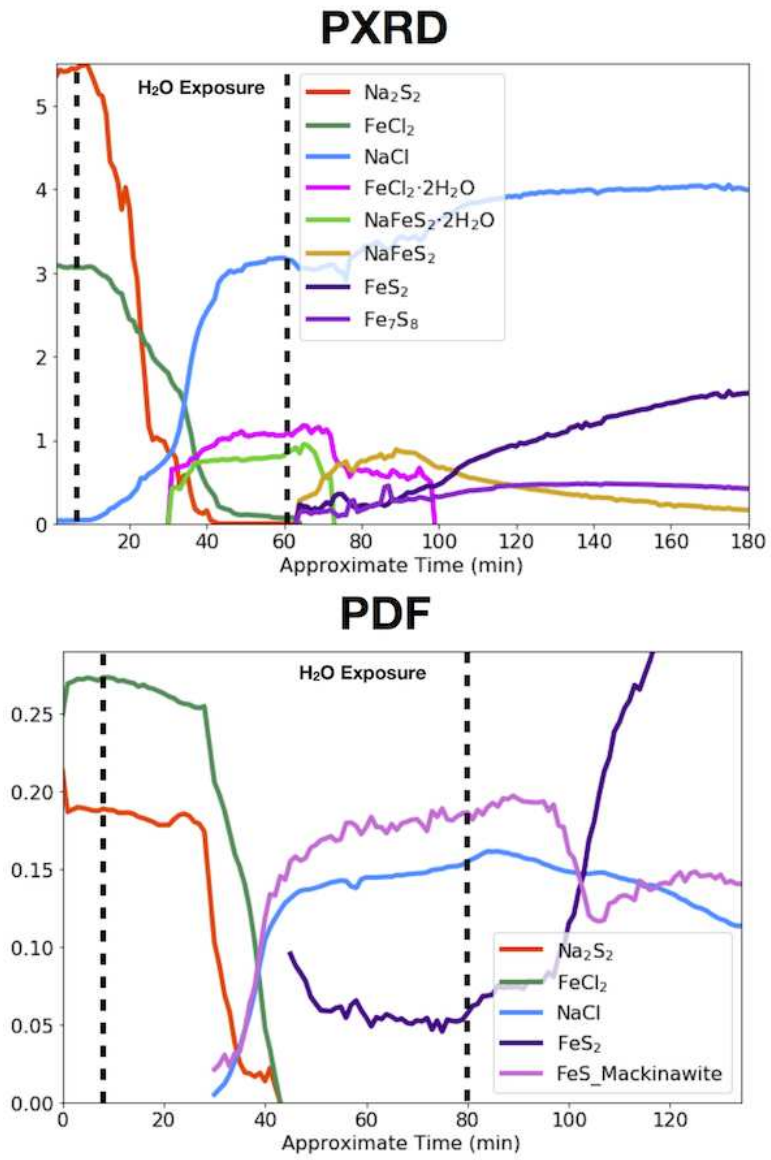


Figure 7.4: Quantitative phase identification from SXRD and PDF of the metathesis reaction: $Na_2S_2 + FeCl_2 \xrightarrow{H_2O} FeS_2 + 2\,NaCl$. The relevant intermediates are labeled by color.

8. Bibliography

[1] Jain, A.; Ong, S. P.; Hautier, G.; Chen, W.; Richards, W. D.; Dacek, S.; Cholia, S.; Gunter, D.; Skinner, D.; Ceder, G.; Persson, K. A. Commentary: The Materials Project: A materials genome approach to accelerating materials innovation. *APL Mater.* **2013**, *1*, 011002.

[2] Malcolm W. Chase, J. *NIST-JANAF thermochemical tables*; Fourth edition. Washington, DC : American Chemical Society ; New York : American Institute of Physics for the National Institute of Standards and Technology, 1998., 1998.

[3] Bartel, C. J.; Millican, S. L.; Deml, A. M.; Rumptz, J. R.; Tumas, W.; Weimer, A. W.; Lany, S.; Stevanović, V.; Musgrave, C. B.; Holder, A. M. Physical descriptor for the Gibbs energy of inorganic crystalline solids and temperature-dependent materials chemistry. *Nat. Commun.* **2018**, *9*.

[4] Satoh, H.; ichi Iwasaki, J.; Kawase, K.; Kamegashira, N. High temperature enthalpies and heat capacities of YbMnO3 and YMnO3. *Journal of Alloys and Compounds* **1998**, *268*, 42 – 46.

[5] Stein, A.; Keller, S. W.; Mallouk, T. E. Turning Down the Heat : Design and Mechanism in Solid-State Synthesis Published by : American Association for the Advancement of Science Turning Down the Heat : Design and Mechanism in Solid State Synthesis. *Science* . **1993**, *259*, 1558–1564.

[6] Martinolich, A. J.; Neilson, J. R. Toward Reaction-by-Design: Achieving Kinetic Control of Solid State Chemistry with Metathesis. *Chem. Mater.* **2017**, *29*, 479–489.

[7] Draxl, C.; Scheffler, M. NOMAD: The FAIR Concept for Big-Data-Driven Materials Science. **2018**, 1–35.

[8] Jain, A.; Shin, Y.; Persson, K. A. Computational predictions of energy materials using density functional theory. *Nature Reviews Materials* **2016**, *1*, 15004.

[9] Jansen, M.; Schön, J. C. Design in Chemical Synthesis- An Illusion? *Angew. Chemie Int. Ed.* **2006**, *45*, 3406–3412.

[10] Curtarolo, S.; Hart, G. L.; Nardelli, M. B.; Mingo, N.; Sanvito, S.; Levy, O. The high-throughput highway to computational materials design. *Nat. Mater.* **2013**, *12*, 191–201.

[11] Sun, W.; Dacek, S. T.; Ong, S. P.; Hautier, G.; Jain, A.; Richards, W. D.; Gamst, A. C.; Persson, K. A.; Ceder, G. The thermodynamic scale of inorganic crystalline metastability. *Sci. Adv.* **2016**, *2*, e1600225–e1600225.

[12] Sun, W.; Holder, A.; Orvañanos, B.; Arca, E.; Zakutayev, A.; Lany, S.; Ceder, G. Thermodynamic Routes to Novel Metastable Nitrogen-Rich Nitrides. *Chem. Mater.* **2017**, *29*, 6936–6946.

[13] Zwijnenburg, M. A.; Bromley, S. T. Structural richness of ionic binary materials: An exploration of the energy landscape of magnesium oxide. *Phys. Rev. B - Condens. Matter Mater. Phys.* **2011**, *83*, 1–9.

[14] Aykol, M.; Hegde, V. I.; Hung, L.; Suram, S.; Herring, P.; Wolverton, C.; Hummelshøj, J. S. Network analysis of synthesizable materials discovery. *Nat. Commun.* **2019**, *10*, 1–20.

[15] Wustrow, A.; Key, B.; Phillips, P. J.; Sa, N.; Lipton, A. S.; Klie, R. F.; Vaughey, J. T.; Poeppelmeier, K. R. Synthesis and Characterization of $MgCr_2S_4$ Thiospinel as a Potential Magnesium Cathode. *Inorg. Chem.* **2018**, *57*, 8634–8638.

[16] Stevanović, V. Sampling Polymorphs of Ionic Solids using Random Superlattices. *Phys. Rev. Lett.* **2016**, *116*, 1–5.

[17] DiSalvo, F. J. Solid-State Chemistry: A Rediscovered Chemical Frontier. *Science.* **1990**, *247*, 649–655.

[18] Johnson, D. C. Controlled synthesis of new compounds using modulated elemental reactants. *Curr. Opin. Solid State Mater. Sci.* **1998**, *3*, 159–167.

[19] Ranade, M. R.; Navrotsky, A.; Zhang, H. Z.; Banfield, J. F.; Elder, S. H.; Zaban, A.; Borse, P. H.; Kulkarni, S. K.; Doran, G. S.; Whitfield, H. J. Energetics of nanocrystalline TiO_2. *Proc. Natl. Acad. Sci.* **2002**, *99*, 6476–6481.

[20] Soderholm, L.; Mitchell, J. F. Perspective: Toward synthesis by design: Exploring atomic correlations during inorganic materials synthesis. *APL Mater.* **2016**, *4*, 053212.

[21] Gopalakrishnan, J. Chimie Douce Approaches to the Synthesis of Metastable Oxide Material. *Chem. Mater.* **1995**, *7*, 1265–1275.

[22] Rouxel, J. Chimie douce with solid precursors, past and present. *Solid State Ionics* **1996**, *84*, 141–149.

[23] Neilson, J. R.; McQueen, T. M. Bonding, Ion Mobility, and Rate-Limiting Steps in Deintercalation Reactions with $ThCr_2Si_2$-type KNi_2Se_2. *J. Am. Chem. Soc.* **2012**, *134*, 7750–7757.

[24] Goodenough, J. B. Evolution of strategies for modern rechargeable batteries. *Acc. Chem. Res.* **2013**, *46*, 1053–61.

[25] Goodenough, J. B.; Park, K. S. The Li-ion rechargeable battery: A perspective. *J. Am. Chem. Soc.* **2013**, *135*, 1167–1176.

[26] Goodenough, J. B.; Kim, Y. Challenges for Rechargeable Li Batteries. *Chem. Mater.* **2010**, *22*, 587–603.

[27] Zhou, X.; Wilfong, B.; Vivanco, H.; Paglione, J.; Brown, C. M.; Rodriguez, E. E. Metastable Layered Cobalt Chalcogenides from Topochemical Deintercalation. *J. Am. Chem. Soc.* **2016**, jacs.6b10229.

[28] Geselbracht, M. J.; Richardson, T. J.; Stacy, A. M. Superconductivity in the layered compound Li_xNbO_2. *Nature* **1990**, *345*, 324–326.

[29] Muraoka, Y.; Grenier, J. C.; Petit, S.; Pouchard, M. Preparation of hexagonal MoO_3 by "Chimie Douce" reaction with NO_2. *Solid State Sci.* **1999**, *1*, 133–148.

[30] Feist, T. P.; Davies, P. K. Soft Chemical Synthesis of New Compounds with the Hexagonal Molybdenum Oxide Structure. *Chem. Mater.* **1991**, *3*, 1011–1012.

[31] Tsujimoto, Y.; Tassel, C.; Hayashi, N.; Watanabe, T.; Kageyama, H.; Yoshimura, K.; Takano, M.; Ceretti, M.; Ritter, C.; Paulus, W. Infinite-layer iron oxide with a square-planar coordination. *Nature* **2007**, *450*, 1062–1065.

[32] Powell, A. E.; Hodges, J. M.; Schaak, R. E. Preserving Both Anion and Cation Sublattice Features during a Nanocrystal Cation-Exchange Reaction: Synthesis of Metastable Wurtzite-Type CoS and MnS. *J. Am. Chem. Soc.* **2016**, *138*, 471–474.

[33] Hodges, J. M.; Kletetschka, K.; Fenton, J. L.; Read, C. G.; Schaak, R. E. Sequential Anion and Cation Exchange Reactions for Complete Material Transformations of Nanoparticles with Morphological Retention. *Angew. Chemie - Int. Ed.* **2015**, *54*, 8669–8672.

[34] Fenton, J. L.; Schaak, R. E. Structure-Selective Cation Exchange in the Synthesis of Zincblende MnS and CoS Nanocrystals. *Angew. Chemie Int. Ed.* **2017**, 1–5.

[35] Poeppelmeier, K. R.; Kipp, D. O. Cation Replacement in α-$LiAlO_2$. *Inorg. Chem.* **1988**, *27*, 766–767.

[36] Vitoux, L.; Guignard, M.; Suchomel, M. R.; Pramudita, J. C.; Sharma, N.; Delmas, C. ï¿The Na_xMoO_2 Phase Diagram ($1/2 \geq x \geq 1$): An Electrochemical Devil's Staircase. *Chem. Mater.* **2017**, *29*, 7243–7254.

[37] Gebauer, D.; Wolf, S. E. Designing Solid Materials from Their Solute State: A Shift in Paradigms toward a Holistic Approach in Functional Materials Chemistry. *J. Am. Chem. Soc.* **2019**, *141*, 4490–4504.

[38] Németh, P.; Mugnaioli, E.; Gemmi, M.; Czuppon, G.; Demény, A.; Spötl, C. A nanocrystalline monoclinic $CaCO_3$ precursor of metastable aragonite. *Sci. Adv.* **2018**, *4*, eaau6178.

[39] Shoemaker, D. P.; Chung, D. Y.; Mitchell, J. F.; Bray, T. H.; Soderholm, L.; Chupas, P. J.; Kanatzidis, M. G. Understanding Fluxes as Media for Directed Synthesis: In Situ Local Structure of Molten Potassium Polysulfides. *Journal of the American Chemical Society* **2012**, *134*, 9456–9463, PMID: 22582976.

[40] Miura, A.; Ito, H.; Bartel, C.; Sun, W.; Rosero-Navarro, N. C.; Tadanaga, K.; Nakata, H.; Maeda, K.; Ceder, G. Selective Metathesis Synthesis of $MgCr_2S_4$ by Control of Thermodynamic Driving Forces. *Preprint* **2019**,

[41] Yamane, H.; DiSalvo, F. J. Sodium flux synthesis of nitrides. *Prog. Solid State Chem.* **2018**, *51*, 27–40.

[42] Shoemaker, D. P.; Hu, Y.-J.; Chung, D. Y.; Halder, G. J.; Chupas, P. J.; Soderholm, L.; Mitchell, J. F.; Kanatzidis, M. G. In situ studies of a platform for metastable inorganic crystal growth and materials discovery. *Proc. Natl. Acad. Sci.* **2014**, *111*, 10922–10927.

[43] Henkes, A. E.; Schaak, R. E. Trioctylphosphine: A general phosphorus source for the low-temperature conversion of metals into metal phosphides. *Chem. Mater.* **2007**, *19*, 4234–4242.

[44] Seefeld, S.; Limpinsel, M.; Liu, Y.; Farhi, N.; Weber, A.; Zhang, Y.; Berry, N.; Kwon, Y. J.; Perkins, C. L.; Hemminger, J. C.; Wu, R.; Law, M. Iron Pyrite Thin Films Synthesized from an $Fe(acac)_3$ Ink. *J. Am. Chem. Soc.* **2013**, *135*, 4412–4424.

[45] Bauers, S. R.; Holder, A.; Sun, W.; Melamed, C. L.; Woods-Robinson, R.; Mangum, J.; Perkins, J.; Tumas, W.; Gorman, B.; Tamboli, A.; Ceder, G.; Lany, S.; Zakutayev, A. Ternary nitride semiconductors in the rocksalt crystal structure. *Proc. Natl. Acad. Sci.* **2019**, *116*, 14829–14834.

[46] Koch, C.; Dankwort, T.; Hansen, A.-L.; Esters, M.; Häußler, D.; Volker, H.; von Hoegen, A.; Wuttig, M.; Johnson, D. C.; Bensch, W.; Kienle, L. Investigation of the phase change mechanism of $Ge_6Sn_2Sb_2Te_11$. *Acta Mater.* **2018**, *152*, 278–287.

[47] Atkins, R.; Moore, D. B.; Johnson, D. C. Insights into the Self-Assembly of Ferecrystalline Compounds from Designed Amorphous Precursors. *Chem. Mater.* **2013**, *25*, 1744–1750.

[48] Bauers, S. R.; Wood, S. R.; Jensen, K. M. Ø.; Blichfeld, A. B.; Iversen, B. B.; Billinge, S. J. L.; Johnson, D. C. Structural Evolution of Iron Antimonides from Amorphous Precursors to Crystalline Products Studied by Total Scattering Techniques. *J. Am. Chem. Soc.* **2015**, *137*, 9652–9658.

[49] Oyelaran, O.; Novet, T.; Johnson, C. D.; Johnson, D. C. Controlling Solid-State Reaction Pathways: Composition Dependence in the Nucleation Energy of InSe. *J. Am. Chem. Soc.* **1996**, *118*, 2422–2426.

[50] Tsuei, C. C.; Gupta, A.; Trafas, G.; Mitzi, D. Superconducting Mercury-Based Cuprate Films with a Zero-Resistance Transition Temperature of 124 Kelvin. *Science* . **1994**, *263*, 1259–1261.

[51] Treece, R.; Gillan, E. G.; Kaner, R. B. Material Synthesis Via Solid-State Metathesis Reactions. *Comments Mod. Chem. Part A Comments Inorg. Chem.* **1995**, *16*, 313–337.

[52] Parkin, I. P.; Kafizas, A. *Compr. Inorg. Chem. II (Second Ed. From Elem. to Appl.*; Elsevier Ltd., 2013; Vol. 2; pp 471–490.

[53] Rao, L.; Gillan, E. G.; Kaner, R. B. Rapid synthesis of transition-metal borides by solid-state metathesis. *J. Mater. Res.* **1995**, *10*, 353–361.

[54] Gillan, E. G.; Kaner, R. B. Rapid Solid-State Synthesis of Refractory Nitrides. *Inorg. Chem.* **1994**, *33*, 5693–5700.

[55] Rognerud, E. G.; Rom, C. L.; Todd, P. K.; Singstock, N. R.; Bartel, C. J.; Holder, A. M.; Neilson, J. R. Kinetically Controlled Low-Temperature Solid-State Metathesis of Manganese Nitride Mn_3N_2 . *Chem. Mater.* **2019**, *31*, 7248–7254.

[56] Nartowski, A. M.; Parkin, I. P.; Mackenzie, M.; Craven, A. J. Solid state metathesis: synthesis of metal carbides from metal oxides. *J. Mater. Chem.* **2001**, *11*, 3116–3119.

[57] Blair, R. G.; Anderson, A.; Kaner, R. B. A solid-state metathesis route to $MgSiN_2$. *Chem. Mater.* **2005**, *17*, 2155–2161.

[58] Mandal, T. K.; Gopalakrishnan, J. From rocksalt to perovskite: a metathesis route for the synthesis of perovskite oxides of current interest. *J. Mater. Chem.* **2004**, *14*, 1273.

[59] Parhi, P.; Ramanan, A.; Ray, A. R. Synthesis of nano-sized alkaline-earth hydroxyapatites through microwave assisted metathesis route. *Mater. Lett.* **2006**, *60*, 218–221.

[60] Kloß, S. D.; Weidmann, N.; Niklaus, R.; Schnick, W. High-Pressure Synthesis of Melilite-type Rare-Earth Nitridophosphates $RE_2P_3N_7$ and a $Ba_2CuSi_2O_7$-type Polymorph. *Inorg. Chem.* **2016**, acs.inorgchem.6b01611.

[61] Parkin, I. P.; Rowley, A. T. Formation of transition-metal nitrides from the reactions of lithium amides and anhydrous transition-metal chlorides. *J. Mater. Chem.* **1995**, *5*, 909.

[62] Baxter, D. V.; Chisholm, M. H.; Gama, G. J.; Distasi, V. F.; Hector, A. L.; Parkin, I. P. Molecular Routes to Metal Carbides , Nitrides , and Oxides . 2 . Studies of the Ammonolysis of Metal Dialkylamides and Hexamethyldisilylamides. *Chem. Mater.* **1996**, *8*, 1222–1228.

[63] Bonneau, P. R.; Jarvis, R. F.; Kaner, R. B. Rapid solid-state synthesis of materials from molybdenum disulphide to refractories. *Nature* **1991**, *349*, 510–512.

[64] Parkin, I. P. Solid state metathesis reaction for metal borides, silicides, pnictides and chalcogenides: ionic or elemental pathways. *Chem. Soc. Rev.* **1996**, *25*, 199.

[65] Martinolich, A. J.; Neilson, J. R. Pyrite Formation via Kinetic Intermediates through Low-Temperature Solid-State Metathesis. *J. Am. Chem. Soc.* **2014**, *136*, 15654–9.

[66] Martinolich, A. J.; Kurzman, J. A.; Neilson, J. R. Circumventing Diffusion in Kinetically Controlled Solid-State Metathesis Reactions. *J. Am. Chem. Soc.* **2016**, *138*, 11031–11037.

[67] Martinolich, A. J.; Kurzman, J. A.; Neilson, J. R. Polymorph Selectivity of Superconducting $CuSe_2$ Through Kinetic Control of Solid-State Metathesis. *J. Am. Chem. Soc.* **2015**, *137*, 3827–3833.

[68] Martinolich, A. J.; Higgins, R. F.; Shores, M. P.; Neilson, J. R. Lewis Base Mediated Polymorph Selectivity of Pyrite $CuSe_2$ through Atom Transfer in Solid-State Metathesis. *Chem. Mater.* **2016**, *28*, 1854–1860.

[69] Fallon, M. J.; Martinolich, A. J.; Maughan, A. E.; Gallington, L. C.; Neilson, J. R. Low-temperature synthesis of superconducting iron selenide using a triphenylphosphine flux. *Dalton Trans.* **2019**, *48*, 16298–16303.

[70] Jiang, Z.; Ramanathan, A.; Shoemaker, D. P. In situ identification of kinetic factors that expedite inorganic crystal formation and discovery. *J. Mater. Chem. C* **2017**, *5*, 5709–5717.

[71] Liu, H.; Kazemiabnavi, S.; Grenier, A.; Vaughan, G.; Di Michiel, M.; Polzin, B. J.; Thornton, K.; Chapman, K. W.; Chupas, P. J. Quantifying Reaction and Rate Heterogeneity in Battery Electrodes in 3D through Operando X-ray Diffraction Computed Tomography. *ACS Appl. Mater. Interfaces* **2019**, *11*, 18386–18394.

[72] Birgisson, S.; Saha, D.; Iversen, B. B. Formation Mechanisms of Nanocrystalline MnO_2 Polymorphs under Hydrothermal Conditions. *Cryst. Growth Des.* **2018**, *18*, 827–838.

[73] Todd, P. K.; Neilson, J. R. Selective Formation of Yttrium Manganese Oxides through Kinetically Competent Assisted Metathesis Reactions. *J. Am. Chem. Soc.* **2019**, *141*, 1191–1195.

[74] Jansen, M. A Concept for Synthesis Planning in Solid-State Chemistry. *Angew. Chemie Int. Ed.* **2002**, *41*, 3746–3766.

[75] Gopalakrishnan, J.; Sivakumar, T.; Ramesha, K.; Thangadurai, V.; Subbanna, G. N. Transformations of Ruddlesden - Popper oxides to new layered perovskite oxides by metathesis reactions. *J. Am. Chem. Soc.* **2000**, *122*, 6237–6241.

[76] Martinolich, A. J.; Higgins, R. F.; Shores, M. P.; Neilson, J. R. Lewis Base Mediated Polymorph Selectivity of Pyrite $CuSe_2$ through Atom Transfer in Solid-State Metathesis. *Chem. Mater.* **2016**, *28*, 1854–1860.

[77] Panda, M.; Seshadri, R.; Gopalakrishnan, J. Preparation of $PbZrO_3$ /ASO_4 Composites (A = Ca, Sr, Ba) and $PbZrO_3$ by Metathetic Reactions in the Solid State: Metathetic Exchange of Divalent Species. *Chem. Mater.* **2003**, *15*, 1554–1559.

[78] Toberer, E. S.; Seshadri, R. Template-free routes to porous inorganic materials. *Chem. Commun.* **2006**, 3159.

[79] Toberer, E. S.; Weaver, J. C.; Ramesha, K.; Seshadri, R. Macroporous Monoliths of Functional Perovskite Materials through Assisted Metathesis. *Chem. Mater.* **2004**, *16*, 2194–2200.

[80] Taube, H. Rates and Mechanisms of Substitution in Inorganic Complexes in Solution. *Chem. Rev.* **1952**, *50*, 69–126.

[81] Chen, H.; Yu, T.; Gao, P.; Bai, J.; Tao, J.; Tyson, T. A.; Wang, L.; Lalancette, R. Synthesis and Structure of Perovskite $ScMnO_3$. *Inorg. Chem.* **2013**, *52*, 9692–9697.

[82] Ishiwata, S.; Kaneko, Y.; Tokunaga, Y.; Taguchi, Y.; Arima, T. H.; Tokura, Y. Perovskite manganites hosting versatile multiferroic phases with symmetric and antisymmetric exchange strictions. *Phys. Rev. B* **2010**, *81*, 4–7.

[83] Ishiwata, S.; Tokunaga, Y.; Taguchi, Y.; Tokura, Y. High-Pressure Hydrothermal Crystal Growth and Multiferroic Properties of a Perovskite $YMnO_3$. *J. Am. Chem. Soc.* **2011**, *133*, 13818–13820.

[84] Lorenz, B.; Wang, Y.-Q.; Chu, C.-W. Ferroelectricity in perovskite $YMnO_3$ and $HoMnO_3$. *Phys. Rev. B* **2007**, *76*, 104405.

[85] Smith, A. E.; Mizoguchi, H.; Delaney, K.; Spaldin, N. A.; Sleight, A. W.; Subramanian, M. A. Mn^{3+} in Trigonal Bipyramidal Coordination: A New Blue Chromophore. *J. Am. Chem. Soc.* **2009**, *131*, 17084–17086.

[86] Okuyama, D.; Ishiwata, S.; Takahashi, Y.; Yamauchi, K.; Picozzi, S.; Sugimoto, K.; Sakai, H.; Takata, M.; Shimano, R.; Taguchi, Y.; Arima, T.; Tokura, Y. Magneti-

cally driven ferroelectric atomic displacements in orthorhombic $YMnO_3$. *Phys. Rev. B* **2011**, *84*, 1–7.

[87] Gibbs, A. S.; Knight, K. S.; Lightfoot, P. High-temperature phase transitions of hexagonal $YMnO_3$. *Phys. Rev. B* **2011**, *83*, 094111.

[88] Kamata, K.; Nakajima, T.; Nakamura, T. Thermogravimetric study of rare earth manganites AMnO3 (A=Sm,Dy,Y,Er,Yb) at 1200Â°C. *Mater. Res. Bull.* **1979**, *14*, 1007–1012.

[89] Muñoz, A.; Alonso, J. a.; Casais, M. T.; Martínez-Lope, M. J.; Martínez, J. L.; Fernández-Díaz, M. T. The magnetic structure of $YMnO_3$ perovskite revisited. *J. Phys. Condens. Matter* **2002**, *14*, 3285–3294.

[90] Gardner, J. S.; Gingras, M. J. P.; Greedan, J. E. Synthesis of Metastable Perovskite-type $YMnO_3$ and $HoMnO_3$. *Rev. Mod. Phys.* **2010**, *82*, 53–107.

[91] Iliev, M. N.; Abrashev, M. V.; Lee, H.-G.; Popov, V. N.; Sun, Y. Y.; Thomsen, C.; Meng, R. L.; Chu, C. W. Raman spectroscopy of orthorhombic perovskite-likeï¿ $YMnO_3$ and $LaMnO_3$. *Phys. Rev. B* **1998**, *57*, 2872–2877.

[92] Fujinaka, H.; Kinomura, N.; Koizumi, M.; Miyamoto, Y.; Kume, S. Syntheses and physical properties of pyrochlore-type $A_2B_2O_7$ (A=Tl,Y; B=Cr,Mn). *Mater. Res. Bull.* **1979**, *14*, 1133–1137.

[93] Giaquinta, D. M.; zur Loye, H.-C. Structural Predictions in the ABO_3 Phase Diagram. *Chem. Mater.* **1994**, *6*, 365–372.

[94] Subramanian, M.; Torardi, C.; Johnson, D.; Pannetier, J.; Sleight, A. Ferromagnetic $R_2Mn_2O_7$ pyrochlores (R = Dy, Lu, Y). *J. Solid State Chem.* **1988**, *72*, 24–30.

[95] Schäfer, H. Gaseous Chloride Complexes with Halogen Bridges-Homo-Complexes and Hetero-Complexes. *Angew. Chemie Int. Ed. English* **1976**, *15*, 713–727.

[96] Bell, A. M. T.; Smith, A. J. Structure of hexaaquadichloroyttrium(III) chloride. *Acta Crystallogr. Sect. C Cryst. Struct. Commun.* **1990**, *46*, 960–962.

[97] Uusi-Esko, K.; Malm, J.; Imamura, N.; Yamauchi, H.; Karppinen, M. Characterization of $RMnO_3$ (R = Sc, Y, Dy-Lu): High-pressure synthesized metastable perovskites and their hexagonal precursor phases. *Mater. Chem. Phys.* **2008**, *112*, 1029–1034.

[98] Alonso, J. A.; Martínez-Lope, M. J.; Casais, M. T.; Fernández-Díaz, M. T. Evolution of the Jahn-Teller distortion of MnO_6 octahedra in $RMnO_3$ perovskites (R = Pr, Nd, Dy, Tb, Ho, Er, Y): A neutron diffraction study. *Inorg. Chem.* **2000**, *39*, 917–923.

[99] Alonso, J. A.; Martínez-lope, M. J.; Casais, M. T.; Macmanus-driscoll, J. L.; de Silva, P. S. I. P. N.; Cohen, L. F.; Fernández-díaz, M. T. Non-stoichiometry, structural defects and properties of $LaMnO_{3+\delta}$ with high δ values ($0.11 \geq \delta \geq 0.29$). *J. Mater. Chem.* **1997**, *7*, 2139–2144.

[100] Tofield, B. C.; Scott, W. R. Oxidative nonstoichiometry in perovskites, an experimental survey; the defect structure of an oxidized lanthanum manganite by powder neutron diffraction. *J. Solid State Chem.* **1974**, *10*, 183–194.

[101] Zuev, A. Y.; Tsvetkov, D. S. Oxygen nonstoichiometry, defect structure and defect-induced expansion of undoped perovskite $LaMnO_{3\pm\delta}$, url = http://dx.doi.org/10.1016/j.ssi.2010.02.024, volume = 181, year = 2010. *Solid State Ionics* 557–563.

[102] Cherepanov, V.; Barkhatova, L.; Petrov, A.; Voronin, V. Oxygen Nonstoichiometry and Crystal and Defect Structure of $PrMnO_{3+y}$ and $NdMnO_{3+y}$. *J. Solid State Chem.* **1995**, *118*, 53–61.

[103] Miyoshi, S.; Hong, J. O.; Yashiro, K.; Kaimai, A.; Nigara, Y.; Kawamura, K.; Kawada, T.; Mizusaki, J. Lattice expansion upon reduction of perovskite-type $LaMnO_3$ with oxygen-deficit nonstoichiometry. *Solid State Ionics* **2003**, *161*, 209–217.

[104] Atsumi, T.; Ohgushi, T.; Namikata, H.; Kamegashira, N. Oxygen nonstoichiometry of $LnMnO_{3-\delta}$ (Ln=La, Pr, Nd, Sm and Y). *J. Alloys Compd.* **1997**, *252*, 67–70.

[105] Spaldin, N. A. *Magnetic materials: fundamentals and applications.*; Cambridge University Press, 2010.

[106] Kitchaev, D. A.; Ceder, G. Evaluating structure selection in the hydrothermal growth of FeS_2 pyrite and marcasite. *Nat. Commun.* **2016**, *7*, 13799.

[107] Toby, B. H. EXPGUI , a graphical user interface for GSAS. *J. Appl. Crystallogr.* **2001**, *34*, 210–213.

[108] Larson, A. C.; Von Dreele, R. B. *General Structure Analysis System (GSAS)*; 2004; pp 1–221.

[109] Burgess, D. In *NIST Chemistry WebBook, NIST Standard Reference Database Number 69*, doi:10.18434/t4d303 ed.; Linstrom, P., Mallard, W., Eds.; National Institute of Standards and Technology: Gaithersburg MD, 20899, Chapter Thermochemical Data.

[110] Todd, P. K.; Smith, A. M. M.; Neilson, J. R. Yttrium Manganese Oxide Phase Stability and Selectivity Using Lithium Carbonate Assisted Metathesis Reactions. *Inorg. Chem.* **2019**, *58*, 15166–15174.

[111] Chupas, P. J.; Chapman, K. W.; Kurtz, C.; Hanson, J. C.; Lee, P. L.; Grey, C. P. A versatile sample-environment cell for non-ambient X-ray scattering experiments. *J. Appl. Crystallogr.* **2008**, *41*, 822–824.

[112] Wendlandt, W. W. The thermal decomposition of yttrium, scandium, and some rare-earth chloride hydrates. *J. Inorg. Nucl. Chem.* **1957**, *5*, 118–122.

[113] Merkle, R.; Maier, J. How is oxygen incorporated into oxides? A comprehensive kinetic study of a simple solid-state reaction with $SrTiO_3$ as a model material. *Angew. Chemie - Int. Ed.* **2008**, *47*, 3874–3894.

[114] Kotula, P. G.; Carter, C. B. Interfacial control of reaction kinetics in oxides. *Phys. Rev. Lett.* **1996**, *77*, 3367–3370.

[115] Eckert, J. O.; Hung-Houston, C. C.; Gersten, B. L.; Lencka, M. M.; Riman, R. E. Kinetics and Mechanisms of Hydrothermal Synthesis of Barium Titanate. *J. Am. Ceram. Soc.* **1996**, *79*, 2929–2939.

[116] Buscaglia, M. T.; Bassoli, M.; Buscaglia, V.; Vormberg, R. Solid-state synthesis of nanocrystalline $BaTiO_3$: Reaction kinetics and powder properties. *J. Am. Ceram. Soc.* **2008**, *91*, 2862–2869.

[117] Akashi, T. Solid-State Reaction Kinetics of $LaCrO_3$ from the Oxides and Determination of La^{3+} Diffusion Coefficient. *J. Electrochem. Soc.* **2006**, *145*, 2090.

[118] Kawamura, K.-i.; Saiki, A.; Maruyama, T.; Nagata, K. SOLID-STATE SCIENCE AND TECHNOLOGY Diffusion Coefficient of Yttrium Ion in $YCrO_3$. **1995**, *142*, 3073–3077.

[119] Heald, E. F.; Weiss, C. W. Kinetics and mechanism of the anatase/rutile transformation, as catalyzed by ferric oxide and reducing conditions. *American Mineralogist* **1972**, *57*, 10–23.

[120] Leskela, M.; Jyrkas, K. Effect of Flux Materials on the Reaction of $Y_2O_3$and SiO_2. *J. Am. Ceram. Soc.* **1987**, *70*, C–160–C–161.

[121] Boltersdorf, J.; King, N.; Maggard, P. A. Flux-mediated crystal growth of metal oxides: Synthetic tunability of particle morphologies, sizes, and surface features for photocatalysis research. *CrystEngComm* **2015**, *17*, 2225–2241.

[122] Murphy, D. W.; Cros, C.; Di Salvo, F. J.; Waszczak, J. V. Preparation and properties of Li_xVS_2 $(0 \leq x \leq 1)$. *Inorg. Chem.* **1977**, *16*, 3027–3031.

[123] Li, D.; Lee, K.; Wang, B. Y.; Osada, M.; Crossley, S.; Lee, H. R.; Cui, Y.; Hikita, Y.; Hwang, H. Y. Superconductivity in an infinite-layer nickelate. *Nature* **2019**, *572*, 624–627.

[124] Gardner, J. S.; Gingras, M. J. P.; Greedan, J. E. Magnetic pyrochlore oxides. *Rev. Mod. Phys.* **2010**, *82*, 53–107.

[125] Yin, L.; Mattei, G. S.; Li, Z.; Zheng, J.; Zhao, W.; Omenya, F.; Fang, C.; Li, W.; Li, J.; Xie, Q.; Zhang, J. G.; Whittingham, M. S.; Meng, Y. S.; Manthiram, A.; Khalifah, P. G. Extending the limits of powder diffraction analysis: Diffraction parameter space, occupancy defects, and atomic form factors. *Rev. Sci. Instrum.* **2018**, *89*.

[126] Yin, L. et al. Thermodynamics of Antisite Defects in Layered NMC Cathodes: Systematic Insights from High-Precision Powder Diffraction Analyses. *Chem. Mater.* **2020**, *32*, 1002–1010.

[127] Ong, S. P.; Jain, A.; Hautier, G.; Kang, B.; Ceder, G. Thermal stabilities of delithiated olivine MPO_4 (M=Fe, Mn) cathodes investigated using first principles calculations. *Electrochem. commun.* **2010**, *12*, 427–430.

[128] Ouyang, R.; Curtarolo, S.; Ahmetcik, E.; Scheffler, M.; Ghiringhelli, L. M. SISSO: A compressed-sensing method for identifying the best low-dimensional descriptor in an immensity of offered candidates. *Phys. Rev. Materials* **2018**, *2*, 083802.

[129] Caballero, A.; Hernán, L.; Morales, J.; Sánchez, L.; Santos Peña, J.; Aranda, M. A. Synthesis and characterization of high-temperature hexagonal P2-$Na_{0.6}MnO_2$ and its electrochemical behaviour as cathode in sodium cells. *J. Mater. Chem.* **2002**, *12*, 1142–1147.

[130] Paulsen, J.; Dahn, J. Studies of the layered manganese bronzes, $Na_{2/3}(Mn_{1-x}M_x)O_2$ with M=Co, Ni, Li, and $Li_{2/3}(Mn_{1-x}M_x)O_2$ prepared by ion-exchange. *Solid State Ionics* **1999**, *126*, 3–24.

[131] Clément, R. J.; Bruce, P. G.; Grey, C. P. Review-Manganese-based P2-type transition metal oxides as sodium-ion battery cathode materials. *J. Electrochem. Soc.* **2015**, *162*, A2589–A2604.

[132] Mendiboure, A.; Delmas, C.; Hagenmuller, P. Electrochemical intercalation and deintercalation of Na_xMnO_2 bronzes. *J. Solid State Chem.* **1985**, *57*, 323–331.

[133] Gillan, E. G.; Kaner, R. B. Synthesis of Refractory Ceramics via Rapid Metathesis Reactions between Solid-State Precursors. *Chem. Mater.* **1996**, *8*, 333–343.

[134] Armstrong, A. R.; Bruce, P. G. Synthesis of layered $LiMnO_2$ as an electrode for rechargeable lithium batteries. *Nature* **1996**, *381*, 499–500.

[135] Croguennec, L.; Deniard, P.; Brec, R.; Lecerf, A. Preparation, physical and structural characterization of $LiMnO_2$ samples with variable cationic disorder. *J. Mater. Chem.* **1995**, *5*, 1919.

[136] Mosbah, A.; Verbaere, A.; Tournoux, M. Phases $Li_xMnO_{2\lambda}$ rattachees au type spinelle. *Materials research bulletin* **1983**, *18*, 1375–1381.

[137] Tarascon, J.; Guyomard, D. Li Metal-Free Rechargeable Batteries Based on $Li_{1+x}Mn_2O_4$ Cathodes ($0 \leq x \leq 1$) and Carbon Anodes. *J. Electrochem. Soc.* **1991**, *138*, 2864–2868.

[138] Wang, M.; Navrotsky, A. $LiMO_2$ (M=Mn, Fe, and Co): Energetics, polymorphism and phase transformation. *J. Solid State Chem.* **2005**, *178*, 1230–1240.

[139] Fuchs, B.; Kemmler-Sack, S. Synthesis of $LiMnO_2$ and $LiFeO_2$ in molten Li halides. *Solid State Ionics* **1994**, *68*, 279–285.

[140] O'Nolan, D.; Huang, G.; Kamm, G. E.; Liu, C.-H.; Grenier, A.; Todd, P. K.; Wustrow, A.; Tran, G. T.; Montiel, D.; Neilson, J. R.; Billinge, S. J. L.; Chupas, P. J.; Thornton, K. S.; Chapman, K. W. Submitted.

[141] Pathak, P.; Vasavada, N. Thermal expansion of NaCl, KCl and CsBr by X-ray diffraction and the law of corresponding states. *Acta Cryst. A* **1970**, *26*, 655–658.

[142] Kirkham, M.; Heroux, L.; Ruiz-Rodriguez, M.; Huq, A. AGES: Automated Gas Environment System for in situ neutron powder diffraction. *Review of Scientific Instruments* **2018**, *89*, 092904.

[143] Kresse, G.; Furthmüller, J. Efficient iterative schemes for ab initio total-energy calculations using a plane-wave basis set. *Phys. Rev. B* **1996**, *54*, 11169–11186.

[144] Perdew, J. P.; Burke, K.; Ernzerhof, M. Generalized Gradient Approximation Made Simple. *Phys. Rev. Lett.* **1996**, *77*, 3865–3868.

[145] Wang, Y.; Fu, Z.-W.; Yue, X.-L.; Qin, Q.-Z. Electrochemical Reactivity Mechanism of Ni_3N with Lithium. *J. Electrochem. Soc.* **2004**, *151*, E162.

[146] Hautier, G.; Ong, S. P.; Jain, A.; Moore, C. J.; Ceder, G. Accuracy of density functional theory in predicting formation energies of ternary oxides from binary oxides and its implication on phase stability. *Phys. Rev. B* **2012**, *85*, 155208.

[147] Blöchl, P. E. Projector augmented-wave method. *Phys. Rev. B* **1994**, *50*, 17953–17979.

[148] Kresse, G.; Joubert, D. From ultrasoft pseudopotentials to the projector augmented-wave method. *Phys. Rev. B* **1999**, *59*, 1758–1775.

[149] Ong, S. P.; Richards, W. D.; Jain, A.; Hautier, G.; Kocher, M.; Cholia, S.; Gunter, D.; Chevrier, V. L.; Persson, K. A.; Ceder, G. Python Materials Genomics (pymatgen): A robust, open-source python library for materials analysis. *Comput. Mater. Sci.* **2013**, *68*, 314–319.

[150] Togo, A.; Tanaka, I. First principles phonon calculations in materials science. *Scr. Mater.* **2015**, *108*, 1–5.

[151] Muñoz, A.; Alonso, J. A.; Martínez-Lope, M. J.; Casáis, M. T.; Martínez, J. L.; Fernández-Díaz, M. T. Magnetic structure of hexagonal $RMnO_3$. *Phys. Rev. B* **2000**, *62*, 9498–9510.

[152] Horton, M. K.; Montoya, J. H.; Liu, M.; Persson, K. A. High-throughput prediction of the ground-state collinear magnetic order of inorganic materials using Density Functional Theory. *npj Computational Materials* **2019**, *5*, 1–11.

[153] Vinet, P.; Rose, J. H.; Ferrante, J.; Smith, J. R. Universal features of the equation of state of solids. *Journal of Physics: Condensed Matter* **1989**, *1*, 1941–1963.

[154] Freysoldt, C.; Neugebauer, J.; Van de Walle, C. G. Fully Ab Initio Finite-Size Corrections for Charged-Defect Supercell Calculations. *Phys. Rev. Lett.* **2009**, *102*, 016402.

[155] Freysoldt, C.; Grabowski, B.; Hickel, T.; Neugebauer, J.; Kresse, G.; Janotti, A.; Van de Walle, C. G. First-principles calculations for point defects in solids. *Rev. Mod. Phys.* **2014**, *86*, 253–305.

[156] Broberg, D.; Medasani, B.; Zimmermann, N. E.; Yu, G.; Canning, A.; Haranczyk, M.; Asta, M.; Hautier, G. PyCDT: A Python toolkit for modeling point defects in semiconductors and insulators. *Computer Physics Communications* **2018**, *226*, 165–179.

[157] Mathew, K. et al. Atomate: A high-level interface to generate, execute, and analyze computational materials science workflows. *Computational Materials Science* **2017**, *139*, 140 – 152.

[158] Roosmalen, J. V.; Cordfunke, E.; Helmholdt, R.; Zandbergen, H. The Defect Chemistry of $LaMnO_{3\pm\ \delta}$: 2. Structural Aspects of $LaMnO_{3+\delta}$. *Journal of Solid State Chemistry* **1994**, *110*, 100 – 105.

[159] Dabrowski, B.; Kolesnik, S.; Baszczuk, A.; Chmaissem, O.; Maxwell, T.; Mais, J. Structural, transport, and magnetic properties of $RMnO_3$ perovskites (R=La, Pr, Nd, Sm, Eu, Dy). *Journal of Solid State Chemistry* **2005**, *178*, 629 – 637.

[160] Bergum, K.; Okamoto, H.; Fjellvåg, H.; Grande, T.; Einarsrud, M.-A.; Selbach, S. M. Synthesis, structure, and magnetic properties of nanocrystalline $YMnO_3$. **2011**, *40*, 7583.

[161] Garcia, E.; Corbett, J. D.; Ford, J. E.; Vary, W. J. Low-Temperature Routes to New Structures for Yttrium, Holmium, Erbium, and Thulium Oxychlorides. *Inorg. Chem.* **1985**, *24*, 494–498.

[162] Ohzuku, T.; Kitagawa, M.; Hirai, T. Electrochemistry of Manganese Dioxide in Lithium Nonaqueous Cell: III. X-Ray Diffractional Study on the Reduction of Spinel-Related Manganese Dioxide. *J. Electrochem. Soc.* **1990**, *137*, 769–775.

[163] Liu, T. et al. Correlation between manganese dissolution and dynamic phase stability in spinel-based lithium-ion battery. *Nat. Commun.* **2019**, *10*, 1–11.

[164] Sugiyama, J.; Atsumi, T.; Hioki, T.; Noda, S.; Kamegashira, N. Nonstoichiometry and defect structure of spinel $LiMn_2O_{4-\delta}$. *J. Power Sources* **1997**, *68*, 641–645.

[165] Reed, J.; Ceder, G.; Van Der Ven, A. Layered-to-spinel phase transition in Li_xMnO_2. *Electrochem. Solid-State Lett.* **2001**, *4*, 2–6.

[166] Armstrong, A. R.; Dupre, N.; Paterson, A. J.; Grey, C. P.; Bruce, P. G. Combined neutron diffraction, NMR, and electrochemical investigation of the layered-to-spinel transformation in $LiMnO_2$. *Chem. Mater.* **2004**, *16*, 3106–3118.

[167] Armstrong, A. R.; Paterson, A. J.; Dupré, N.; Grey, C. P.; Bruce, P. G. Structural evolution of layered $Li_xMn_yO_2$: Combined neutron, NMR, and electrochemical study. *Chem. Mater.* **2007**, *19*, 1016–1023.

[168] Skjaervø, S. L.; Sommer, S.; Nørby, P.; Bøjesen, E. D.; Grande, T.; Iversen, B. B.; Einarsrud, M.-A. Formation mechanism and growth of $MNbO_3$, M=K, Na by in situ X-ray diffraction. *J. Am. Ceram. Soc.* **2017**, *100*, 3835–3842.

[169] Chen, X.-J.; Struzhkin, V. V.; Wu, Z.; Somayazulu, M.; Qian, J.; Kung, S.; Christensen, A. N.; Zhao, Y.; Cohen, R. E.; Mao, H.-k.; Hemley, R. J. Hard superconducting nitrides. *Proc. Natl. Acad. Sci.* **2005**, *102*, 3198–3201.

[170] Balakirev, V. F.; Vedmid', L. B.; Yankin, a. M.; Fedorova, O. M.; Golikov, Y. V. Heterogeneous phase equilibria in the Tb-Mn-O system. *Inorg. Mater.* **2006**, *42*, 1230–1235.

[171] Bither, T.; Prewitt, C.; Gillson, J.; Bierstedt, P.; Flippen, R.; Young, H. New transition metal dichalcogenides formed at high pressure. *Solid State Commun.* **1966**, *4*, 533–535.

[172] GILMAN, H.; BENEDICT, H. N.; HARTZFELD, H. THE PREPARATION AND CLEAVAGE OF SOME HEXASUBSTITUTED DISILOXANES. *J. Org. Chem.* **1954**, *19*, 419–427.

[173] ANDERSON, H. H.; FISCHER, H. METHYLSILICON ESTERS. ESTERS IN AN ORGANOSILICON CONVERSION SERIES. *J. Org. Chem.* **1954**, *19*, 1296–1299.

[174] Nehete, U. N.; Anantharaman, G.; Chandrasekhar, V.; Murugavel, R.; Walawalkar, M. G.; Roesky, H. W.; Vidovic, D.; Magull, J.; Samwer, K.; Sass, B. Polyhedral ferrous and ferric siloxanes. *Angew. Chemie - Int. Ed.* **2004**, *43*, 3832–3835.

[175] Hector, A.; Parkin, I. P. Low-temperature solid-state routes to transition metal oxides via metathesis reactions involving lithium oxide. *Polyhedron* **1993**, *12*, 1855–1862.

[176] Backer, H. J.; Stienstra, F. Chlorotrithioorthosilicoformiate et Chlorotrithioorthogermanioformiate de Butyle Tertiaire (Observations sur L'empêchement St érique). *Recueil des Travaux Chimiques des Pays-Bas* **1935**, *54*, 38–46.

[177] Eaborn, C. 601. Organosilicon compounds. Part II. A conversion series for organosilicon halides, pseudohalides, and sulphides. *J. Chem. Soc.* **1950**, 3077–3089.

[178] Jenkins, L.; Willey, G. Hexamethyldisiloxane and Hexamethyldisilathiane: React ions with Co-valent Metal Halides. *J. Chem. Soc. Dalt.* **1979**, 1697–1700.

[179] Schmidbaur, H.; Schmidt, M. Ferrosiloxanes and Ferrosiliconate Anions. *J. Am. Chem. Soc.* **1962**, *84*, 3600–3601.

[180] Varma, R.; MacDiarmid, A. G.; Miller, J. G. Nature of the silicon-phenyl and silicon-oxygen bonds in hexaphenyldisiloxane: An electric dipole moment study. *J. Organomet. Chem.* **1967**, *9*, 77–81.

[181] Zhang, S.; Tanaka, M.; Yamanaka, S. Superconductivity in electron-doped layered TiNCl with variable interlayer coupling. *Phys. Rev. B* **2012**, *86*, 024516.

[182] Wu, L.; Yu, J. C.; Zhang, L.; Wang, X.; Li, S. Selective self-propagating combustion synthesis of hexagonal and orthorhombic nanocrystalline yttrium iron oxide. *J. Solid State Chem.* **2004**, *177*, 3666–3674.

[183] Vijaya Kumar, M. S.; Nagashio, K.; Hibiya, T.; Kuribayashi, K. Formation of Hexagonal Metastable Phases from an Undercooled $LuFeO_3$ Melt in an Atmosphere with Low Oxygen Partial Pressure. *J. Am. Ceram. Soc.* **2008**, *91*, 806–812.

[184] Pedregosa, F. et al. Scikit-Learn: Machine Learning in Python. *J. Mach. Learn. Res.* **2011**, *12*, 2825–2830.

[185] Lee, D. D.; Seung, H. S. Learning the Parts of Objects by Non-Negative Matrix Factorization. *Nature* **1999**, *401*, 788–791.

[186] Smaragdis, P.; Brown, J. C. Non-Negative Matrix Factorization for Polyphonic Music Transcription. 2003 IEEE Workshop on Applications of Signal Processing to Audio and Acoustics (IEEE Cat. No.03TH8684). 2003; pp 177–180.

[187] Kusne, A. G.; Gao, T.; Mehta, A.; Ke, L.; Nguyen, M. C.; Ho, K.-M.; Antropov, V.; Wang, C.-Z.; Kramer, M. J.; Long, C.; Takeuchi, I. On-the-Fly Machine-Learning for High-Throughput Experiments: Search for Rare-Earth-Free Permanent Magnets. *Sci. Rep.* **2014**, *4*, 6367.

[188] S. Geddes, H.; Blade, H.; F. McCabe, J.; P. Hughes, L.; L. Goodwin, A. Structural Characterisation of Amorphous Solid Dispersions via Metropolis Matrix Factorisation of Pair Distribution Function Data. *Chem. Commun.* **2019**,

[189] Beyer, K. A.; Zhao, H.; Borkiewicz, O. J.; Newton, M. A.; Chupas, P. J.; Chapman, K. W. Simultaneous diffuse reflection infrared spectroscopy and X-ray pair distribution function measurements. *J. Appl. Crystallogr.* **2014**, *47*, 95–101.

[190] Eaborn, C. 537. Organosilicon compounds. Part III. Some sterically hindered compounds. *J. Chem. Soc.* **1952**, 2840.

[191] Chandrasekhar, V.; Boomishankar, R.; Nagendran, S. Recent Developments in the Synthesis and Structure of Organosilanols. *Chem. Rev.* **2004**, *104*, 5847–5910.

[192] Sieckhaus, J.; Scott, R.; Larcher, T. Siloxane Vulcanizates and a Method for the Preparation Thereof. 1975.

[193] Lickiss, P. D. *Adv. Inorg. Chem.*; Elsevier Masson SAS, 1995; Vol. 42; pp 147–262.

[194] Allen, A. D.; Lavery, S. J. Nucleophilic substitution at silicon: the reaction of triphenylsilyl chloride with 2-propanol in CCl_4. *Can. J. Chem.* **1969**, *47*, 1263–1267.

[195] Fulmer, G. R.; Miller, A. J. M.; Sherden, N. H.; Gottlieb, H. E.; Nudelman, A.; Stoltz, B. M.; Bercaw, J. E.; Goldberg, K. I. NMR chemical shifts of trace impurities: Common laboratory solvents, organics, and gases in deuterated solvents relevant to the organometallic chemist. *Organometallics* **2010**, *29*, 2176–2179.

[196] Delaval, J.; Guinet, P.; Morel, J. Process for the Preparation of Linear Organopolysiloxanes. **1969**, 1–10.

[197] Kantor, S. W.; Grubb, W. T.; Osthoff, R. C. The Mechanism of the Acid- and Base-catalyzed Equilibration of Siloxanes. *J. Am. Chem. Soc.* **1954**, *76*, 5190–5197.

A. Appendix

A.1. Assisted Metathesis Control Reactions

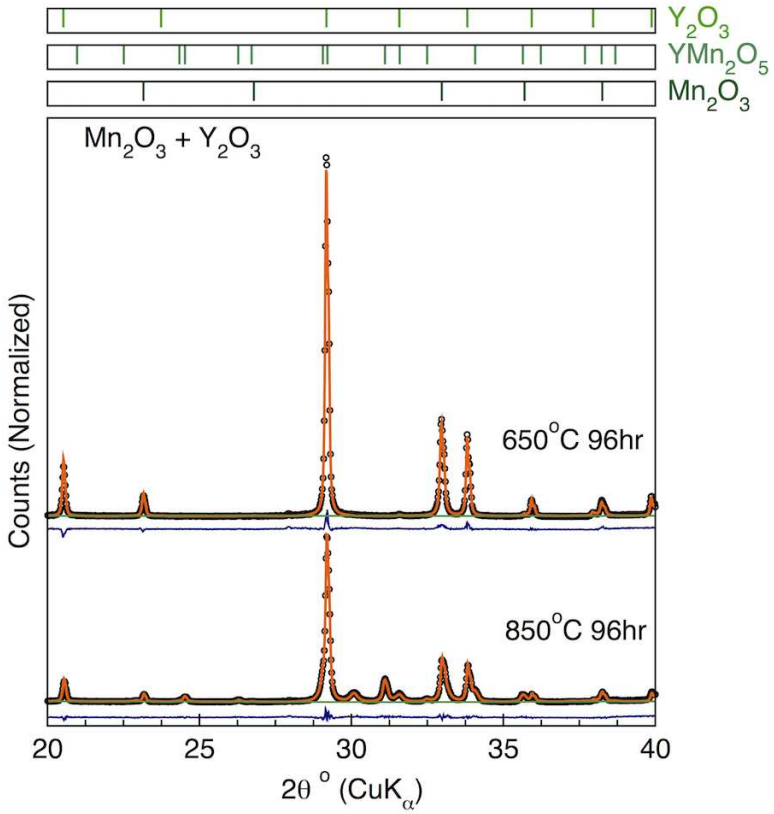


Figure A.1: PXRD results from the reaction: $Mn_2O_3 + Y_2O_3$ at 650 °C and 850 °C. Reactivity is not observed until 850 °C and the product formed is YMn_2O_5, suggesting Y_2O_3 is less reactive than Mn_2O_3 at 850 °C

Table A.1: PXRD phase fractions (mol%) from A_2CO_3 assisted metathesis reactions.†

Precursors	T/ °C	mol% fraction
$3\,Li_2CO_3$ $2\,YCl_3-an$	650 °C	o-$YMnO_3$: 50(1); Li_2MnO_3:39.6(9) Y_2O_3: 0.35(6); $LiCl\cdot H_2O$: 10(1)
$3\,Li_2CO_3$ $2\,YCl_3\cdot 6\,H_2O$	650 °C	o-$YMnO_3$: 84(1); YMn_2O_5: 8.6(5) Li_2MnO_3: 7.5(4)
$3\,Li_2CO_3$ $2\,YCl_3-an$	850 °C	o-$YMnO_3$: 69.9(9); YMn_2O_5: 25.5(5) Li_2MnO_3: 5.5(3)
$3\,Li_2CO_3$ $2.2\,YCl_3\cdot 6\,H_2O$*	850 °C	o-$YMnO_3$: 99.69(6) Y_2O_3: 0.31(3)
$3\,Na_2CO_3$ $2\,YCl_3-an$	650 °C	$Y_2Mn_2O_7$: 14.2(3); NaCl: 85(2) $Na_2Mn_3O_7$: 0.48(6)
$3\,Na_2CO_3$ $2\,YCl_3\cdot 6\,H_2O$	650 °C	$Y_2Mn_2O_7$: 1.9(6); NaCl: 82(1) Y_2O_3: 11.4(2); Mn_2O_3: 4.6(1)
$3\,Na_2CO_3$ $2\,YCl_3-an$	850 °C	o-$YMnO_3$: 56.6(9); YMn_2O_5: 18.3(5) $Y_2Mn_2O_7$: 25.1(5)
$3\,Na_2CO_3$ $2\,YCl_3\cdot 6\,H_2O$	850 °C	o-$YMnO_3$: 51(2); YMn_2O_5: 19.0(9) $Y_2Mn_2O_7$: 5.5(3); NaCl: 24(3)
$3\,K_2CO_3$ $2\,YCl_3-an$	650 °C	$Y_2Mn_2O_7$: 14.2(2); KCl: 78.5(7) K_2MnO_4: 3.55(9); o-$YMnO_3$: 14.2(2)
$3\,K_2CO_3$ $2\,YCl_3\cdot 6\,H_2O$	650 °C	$Y_2Mn_2O_7$: 2(2); KCl: 84(1) Y_2O_3: 7.9(2); Mn_2O_3: 6.0(2)
$3\,K_2CO_3$ $2\,YCl_3-an$	850 °C	o-$YMnO_3$: 44.1(5); YMn_2O_5: 20.6(4) $Y_2Mn_2O_7$: 35.2(3)
$3\,K_2CO_3$ $2\,YCl_3\cdot 6\,H_2O$	850 °C	o-$YMnO_3$: 62(1); YMn_2O_5: 11.3(5) h-$YMnO_3$: 11.3(6); KCl: 15.2(6)

† All reactions include Mn_2O_3 as a precursor and all reactions were carried out over 24 h.
*Stoichiometrically: $3\,Li_2CO_3$, $2\,YCl_3\cdot 6\,H_2O$: o-$YMnO_3$: 79(1); YMn_2O_5: 20.6(6)

Table A.2: Temperature-dependent unit cell volume of o-$YMnO_3$.

T (°C)/Time	Volume (Å^3)
550/24h	215.66(6)
650/24h	213.73(5)
850/24h	217.97(2)
850/7d	217.81(3)

Table A.3: Refined unit cell volume of o-$YMnO_3$ under various post-treatments at 850 °C.

Treatment	Volume (Å^3)
sealed ampoule (< 5mTorr) 30 days	219.19(7)
argon 48 hours	225.8(2) and 221.0(2)†
oxygen 48 hours	217.71(3)
3LiCl* oxygen 24 hours	218.20(3)

† Two individually refined o-$YMnO_3$ phases

*3:1 LiCl:o-$YMnO_3$

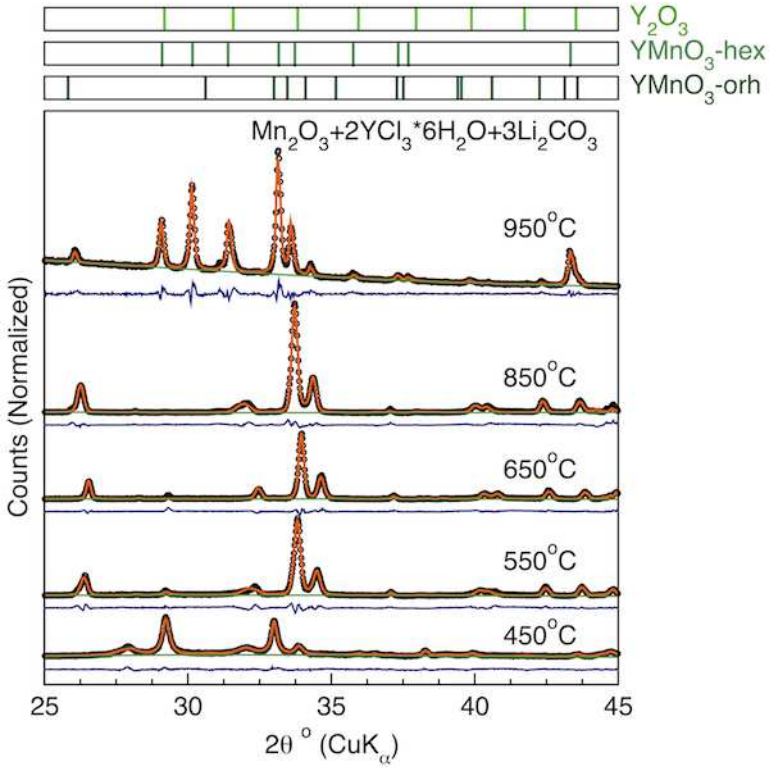


Figure A.2: PXRD results from assisted metathesis reactions using Li_2CO_3 showing the effect of temperature on the reaction products. At temperatures lower than 550 °C no Y−Mn−O phases are present, between 550-850 °C o-$YMnO_3$ is the predominate product, and at 950°C h-$YMnO_3$ is the predominate product.

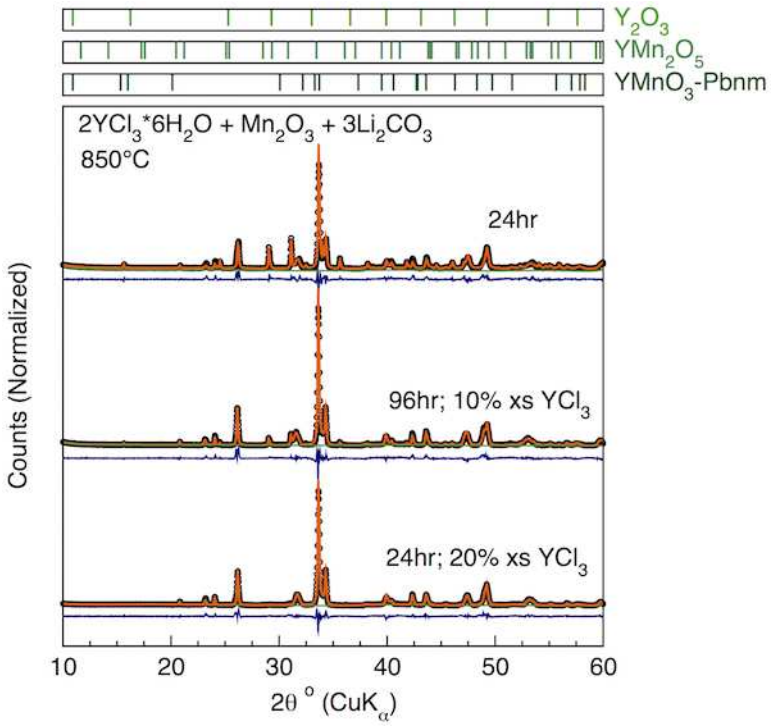


Figure A.3: PXRD results from assisted metathesis reactions using Li_2CO_3 showing the effect of excess hydrated yttrium chloride on the reaction products. As the yttrium chloride excess increases, the YMn_2O_5 brownmillerite phase decreases in intensity.

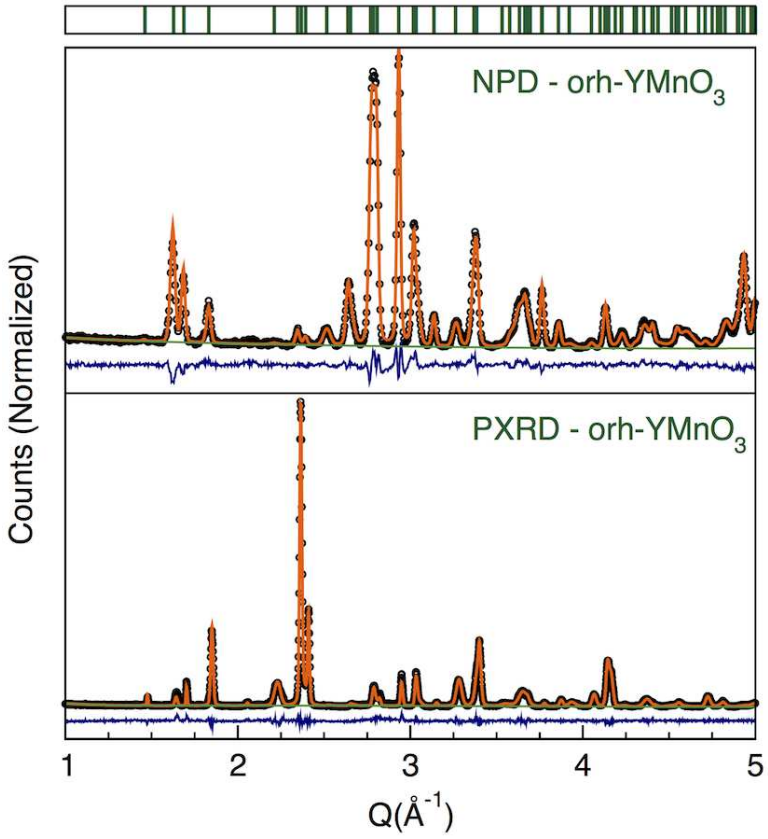


Figure A.4: Neutron diffraction data and laboratory PXRD data for o-$YMnO_3$. Rietveld co-refinements were performed concomitantly against neutron and X-ray diffraction data to confirm the structure and composition of the metastable phases. Tick marks above denote the expected peak positions.

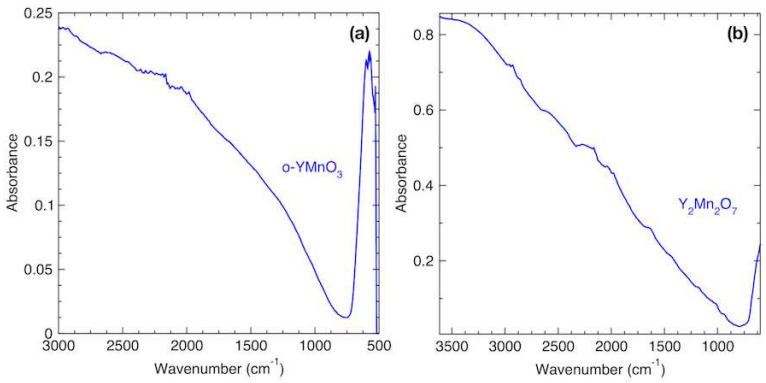


Figure A.5: ATR-IR spectroscopy on washed products of the assisted metathesis reactions using (a) Li_2CO_3: o-$YMnO_3$ (Eq.2) (b) Na_2CO_3: $Y_2Mn_2O_7$ (Eq.3). Asymmetric stretching modes (1500-1400cm^{-1}) and out of plane bending vibrations (850cm^{-1}) due to CO_3^{2-} are not present in the assisted metathesis products.

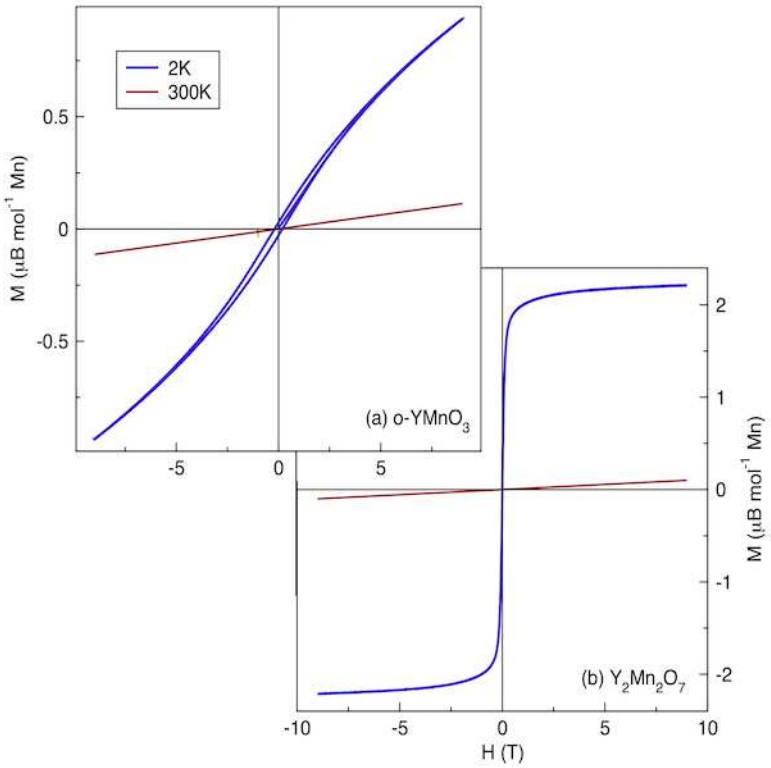


Figure A.6: Magnetization measurements as a function of applied field for (a) o-$YMnO_3$ and (b) $Y_2Mn_2O_7$ at 2 K and 300 K. Both samples display magnetization consistent with ferromagnetic, Brillion-like field dependence, with o-$YMnO_3$ having slight hysteresis.

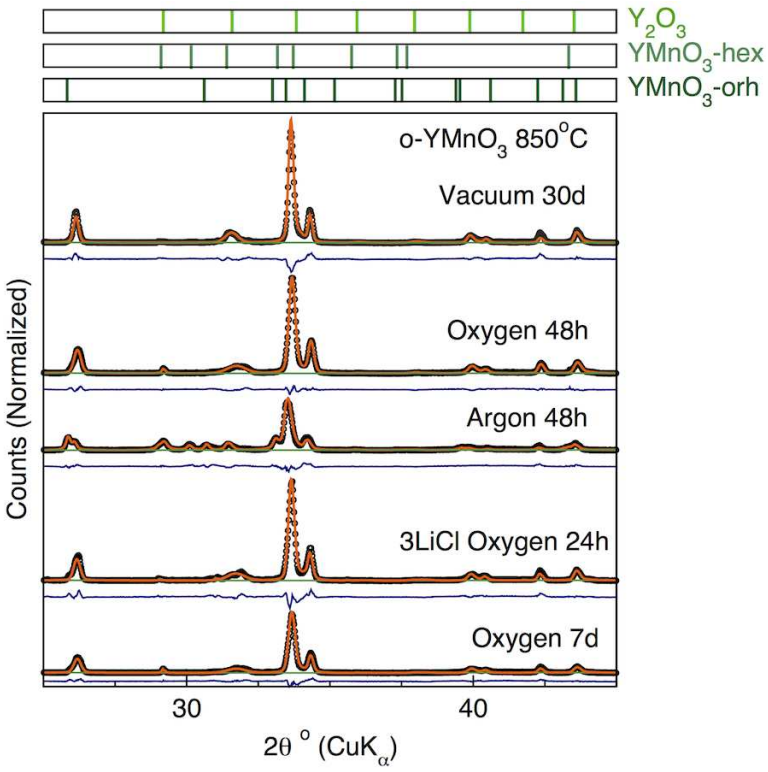


Figure A.7: PXRD results from control reactions on washed o-$YMnO_3$ under various environments and times. Under oxidizing conditions, the o-$YMnO_{3+\delta}$ is stable while under flowing argon, the o-$YMnO_{3+\delta}$ converts to o-$YMnO_3$ and h-$YMnO_3$. In a sealed ampoule ($<$ 5 mTorr) for 30d the product is o-$YMnO_{3+\delta}$ If the assisted metathesis reaction, $Mn_2O_3 + 2.2\,YCl_3 \cdot 6\,H_2O + 3\,Li_2CO_3$, is heated to 850 °C for 7 days, the o-$YMnO_{3+\delta}$ forms and persists.

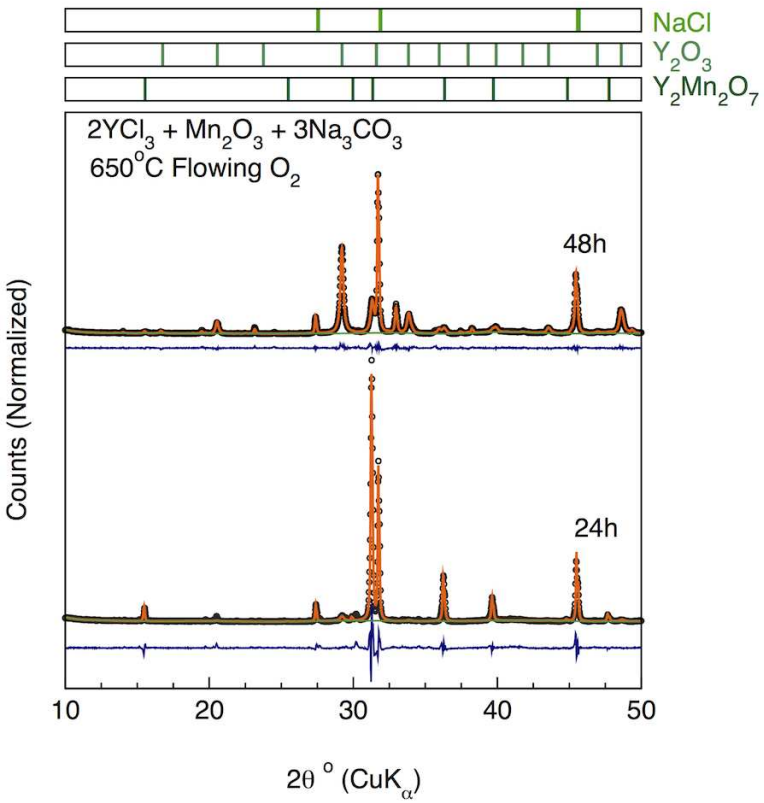


Figure A.8: PXRD results from the assisted metathesis reactions using sodium carbonate illustrating the effect of time on the reaction products at 650 °C. Heating the reaction for longer time periods results in decomposition of the $Y_2Mn_2O_7$ to Mn_2O_3 and Y_2O_3. NaCl is present in both reactions, which suggests that it does not stabilize the metastable pyrochlore.

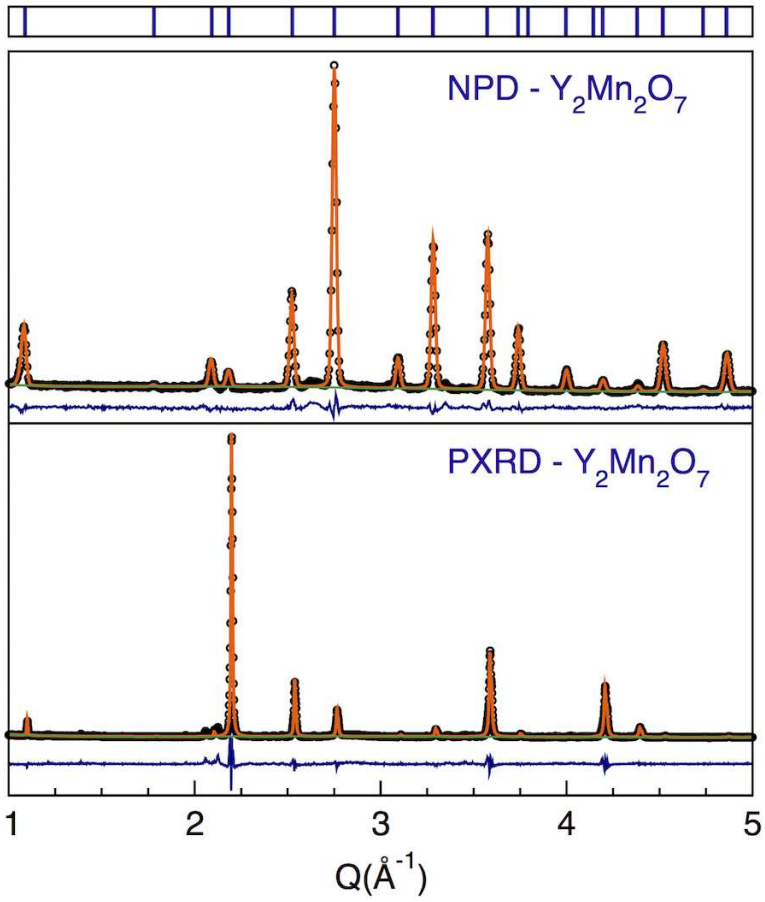
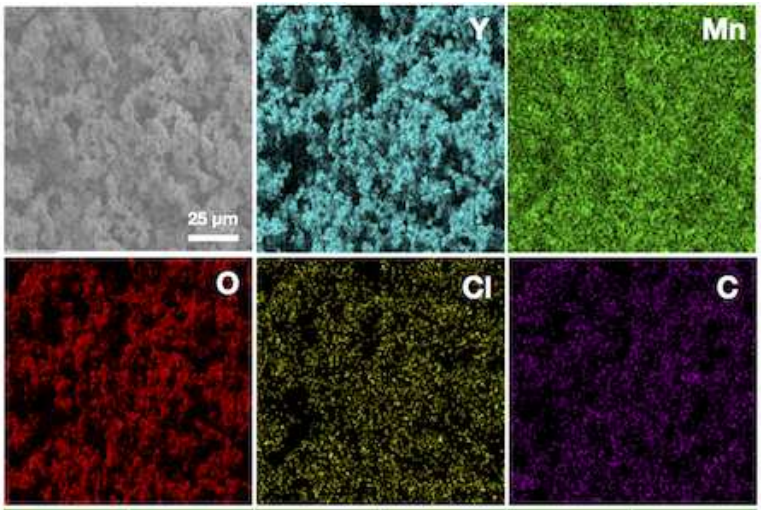
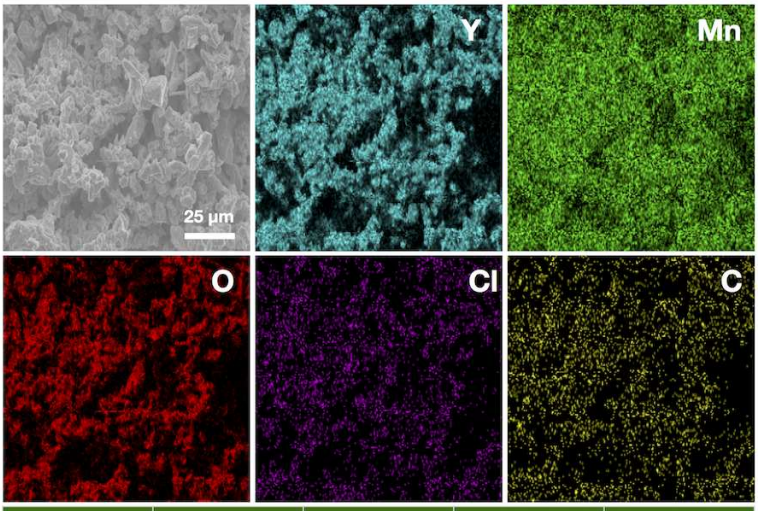


Figure A.9: Neutron diffraction data and laboratory PXRD data for $Y_2Mn_2O_7$. Rietveld co-refinements were performed concomitantly against both neutrons and X-ray diffraction data to confirm the structure and composition of the $Y_2Mn_2O_7$. Tick marks denote the expected peak positions.



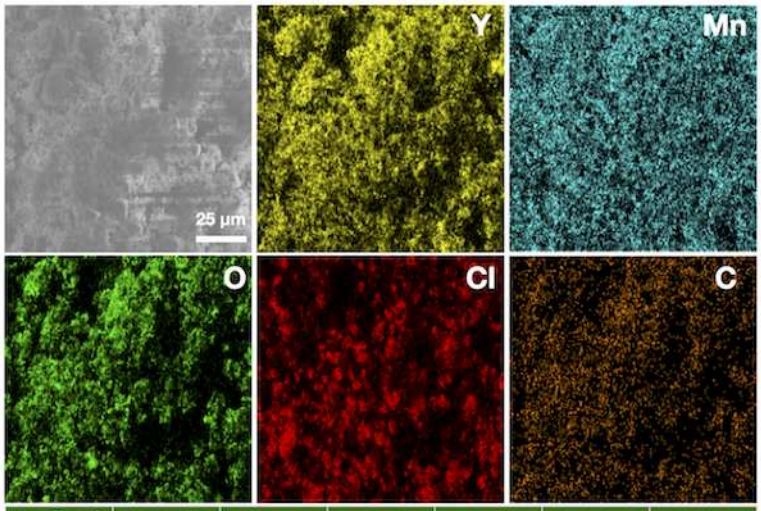
Result Type	Atomic %				
Statistics	C	O	Cl	Mn	Y
Max	10.81	47.21	0.14	25.65	18.53
Min	10.05	45.1	0.09	23.99	18.3
Average	10.4	46.46	0.12	24.61	18.41
Standard Deviation	0.39	1.18	0.03	0.9	0.12

Figure A.10: SEM-EDS analysis of Li_2CO_3 assisted reaction at 850 °C and yttrium chloride hexahydrate precursor to form o-$YMnO_3$ product. Color maps show atomic distribution while the table shows the corresponding atom% from EDS. The percentage of carbon can be attributed to advantageous surface species



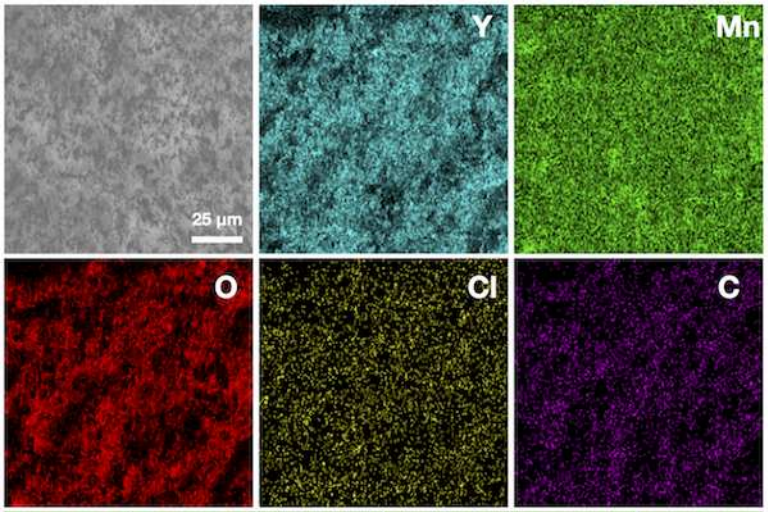
Result Type	Atomic %			
Statistics	C	O	Mn	Y
Max	7.83	50.43	25.96	20.42
Min	6.39	46.09	22.68	20.12
Average	6.98	48.73	24.05	20.24
Standard Deviation	0.75	2.32	1.71	0.16

Figure A.11: SEM-EDS analysis of Li_2CO_3 assisted reaction at 850 °C and yttrium chloride hexahydrate precursor. o-$YMnO_3$ product was washed with 0.6 M HCl prior to imaging. Color maps show atomic distribution while the table shows the corresponding atom% from EDS. The percentage of carbon can be attributed to advantageous surface species



Result Type	Atomic %					
Statistics	C	O	Na	Cl	Mn	Y
Max	15.5	41.95	19.62	16.03	10.79	9.22
Min	14.59	32.37	14.47	8.99	9.41	7.08
Average	14.97	37.64	16.9	12.39	10	8.1
Standard Deviation	0.47	4.86	2.59	3.52	0.71	1.07

Figure A.12: SEM-EDS analysis of Na_2CO_3 assisted reaction at 650 °C and anhydrous yttrium chloride precursor to produce $Y_2Mn_2O_7$. Color maps show atomic distribution while the table shows the corresponding atom% from EDS. The percentage of carbon can be attributed to advantageous surface species



Result Type	Atomic %				
Statistics	C	O	Na	Mn	Y
Max	8.89	52.06	0.54	24.16	17.46
Min	6.81	50.07	0.27	22.01	16.5
Average	8.12	51.09	0.41	23.3	17.08
Standard Deviation	1.13	1	0.13	1.14	0.51

Figure A.13: SEM-EDS analysis of Na_2CO_3 assisted reaction at 650 °C and anhydrous yttrium chloride precursor. $Y_2Mn_2O_7$ product was washed with 0.6 M HCl prior to imaging. Color maps show atomic distribution while the table shows the corresponding atom% from EDS. The percentage of carbon can be attributed to advantageous surface species

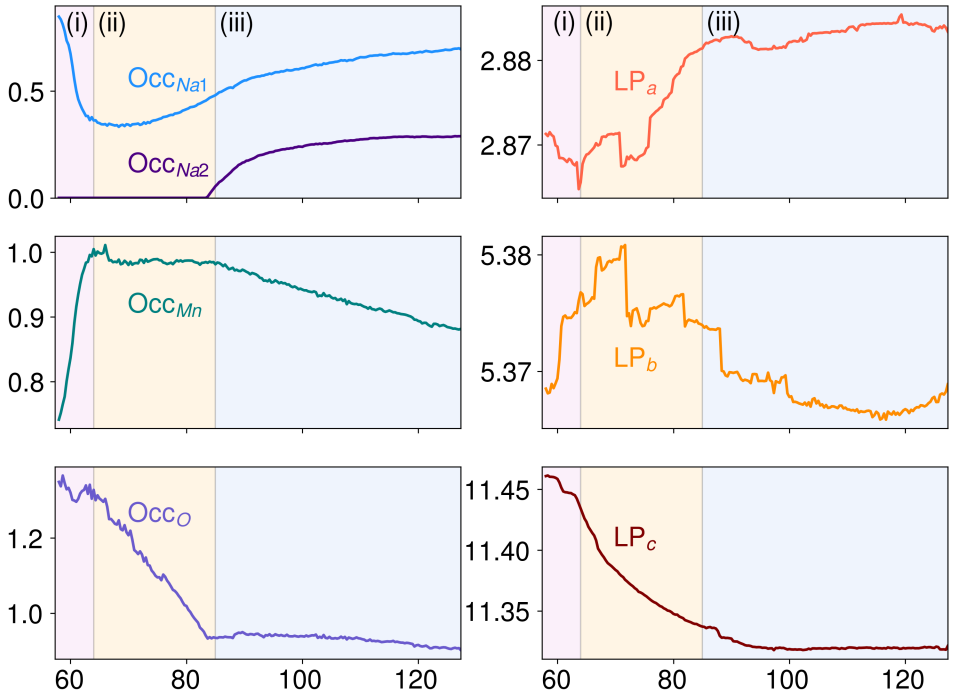


Figure A.14: Structural parameters for the $Cmcm$ Na_xMnO_2 intermediate as a function of reaction time. Refined occupancies of each atomic site that were used in calculating the f_* ternary diagrams are shown on the right while Unit cell parameters for the orthorhombic cell are shown on the left.The colored regions (i,ii,iii) are taken from Figure 4.3 and Figure 4.4

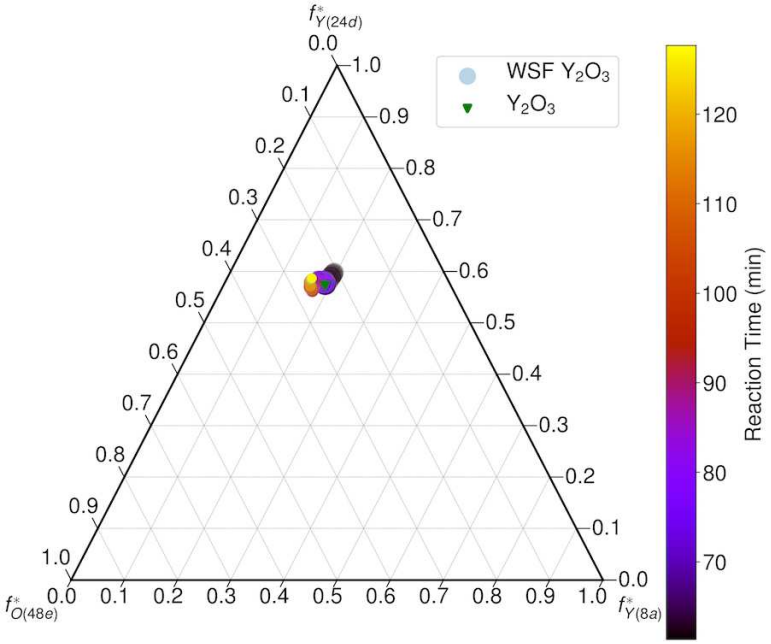


Figure A.15: Ternary f^* diagram of atomic coordinates calculated from Rietveld refinement of $Ia\bar{3}$ Y_2O_3. Each axis denotes atom identity and crystallographic Wyckoff position within the lattice. For reference, the calculated value of Y_2O_3 is provided. The color bar in the figure follows the lifetime of the Y_2O_3 intermediate in the assisted metathesis reaction presented in Figure 4.3. The diameter of each circle mirrors the calculated Weighted Scale Factor in Figure 4.3 for Y_2O_3.

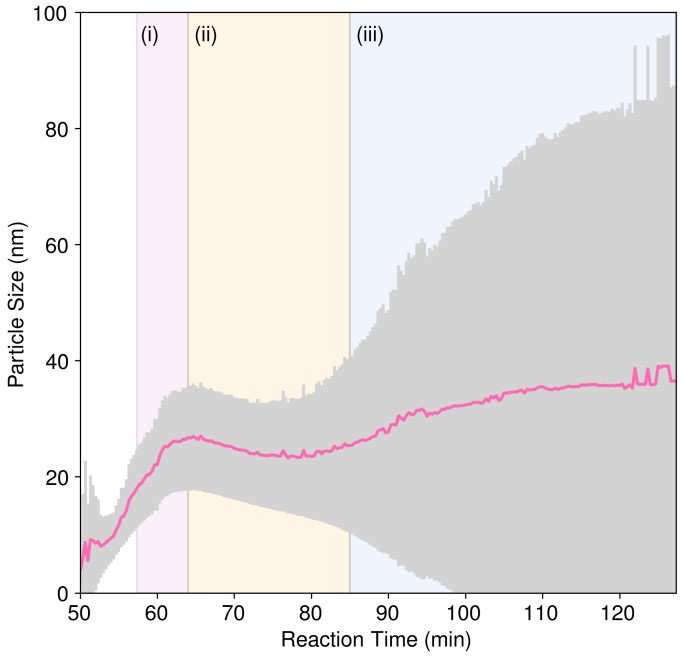


Figure A.16: The calculated size of the coherently diffracting domains of Y_2O_3 intermediates as calculated from the Scherrer equation with error bars using the Integral Breadth method for peak width. The colored regions (i,ii,iii) are taken from Figure 4.3 and Figure 4.4

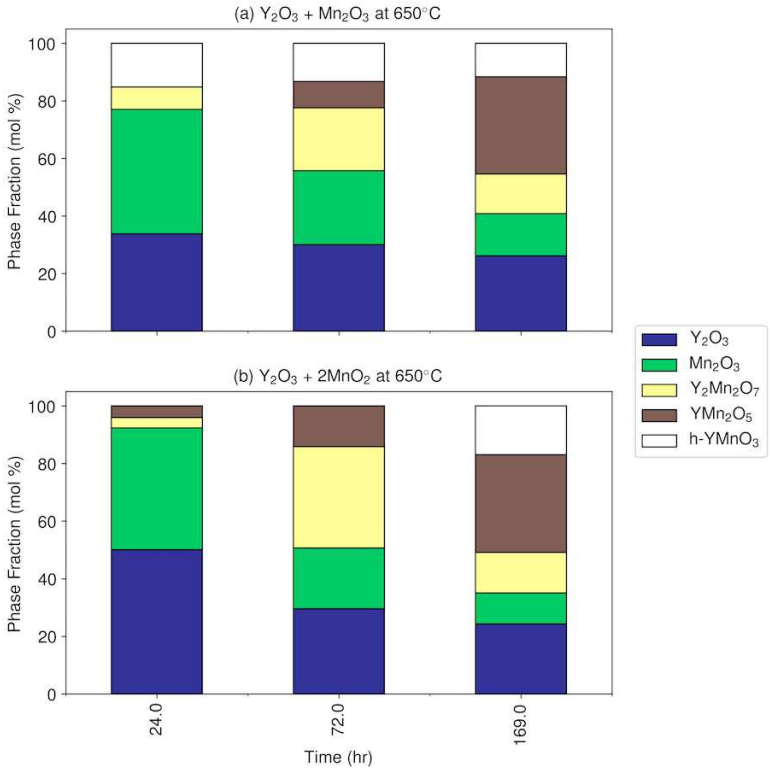


Figure A.17: Bar graphs representing the mole percent amounts of products calculated from $ex\ situ$ PXRD Rietveld refinements of the reaction: (a) $Mn_2O_3 + Y_2O_3 \xrightarrow{O_2}$ and (b) $2\,MnO_2 + Y_2O_3 \xrightarrow{O_2}$. The reactions were heated at 10 °C/min to 650 °C for 24, 72, and 128 hours under flowing oxygen. Each color bar is represented in the legend as a different product phase.

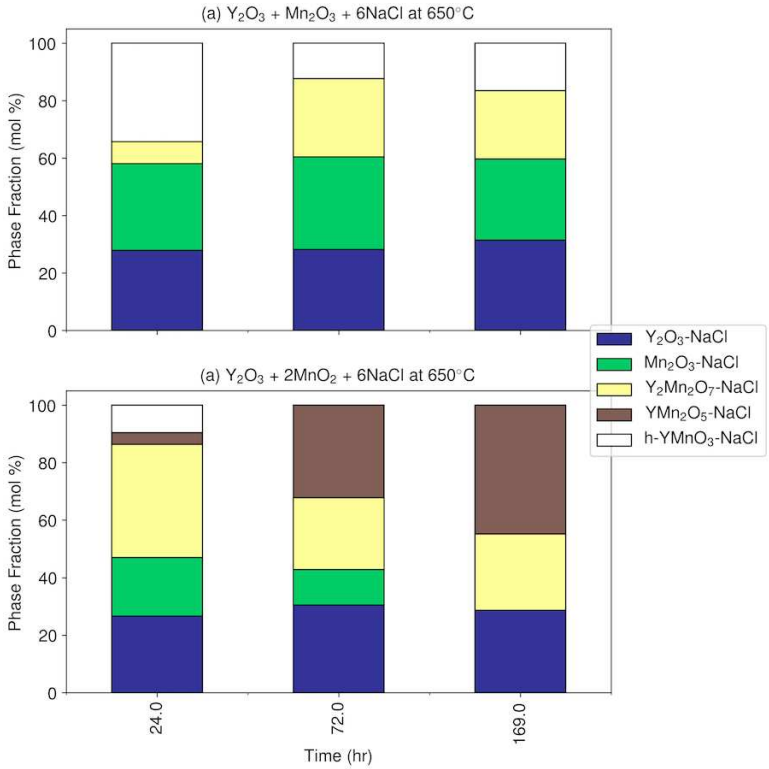


Figure A.18: Bar graphs representing the mole percent amounts of products calculated from $ex\ situ$ PXRD Rietveld refinements of the reaction: (a) $Mn_2O_3 + Y_2O_3 \xrightarrow{6NaCl, O_2}$ and (b) $2\,MnO_2 + Y_2O_3 \xrightarrow{6NaCl, O_2}$. The reactions were heated at 10 °C/min to 650 °C for 24, 72, and 128 hours under flowing oxygen. Each color bar is represented in the legend as a different product phase. Mole fractions are presented after subtracting the contribution from NaCl for comparison.

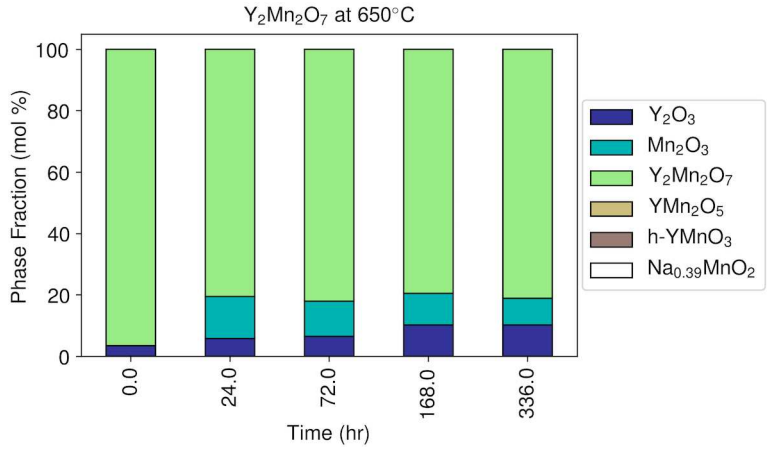


Figure A.19: Bar graphs representing the mole percent amounts of products calculated from $ex\ situ$ PXRD Rietveld refinements of $Y_2Mn_2O_7$. The reactions were heated at 10 °C/min to 650 °C for 24, 72, 128, and 336 hours under flowing oxygen. Each color bar is represented in the legend as a different calculated phase.

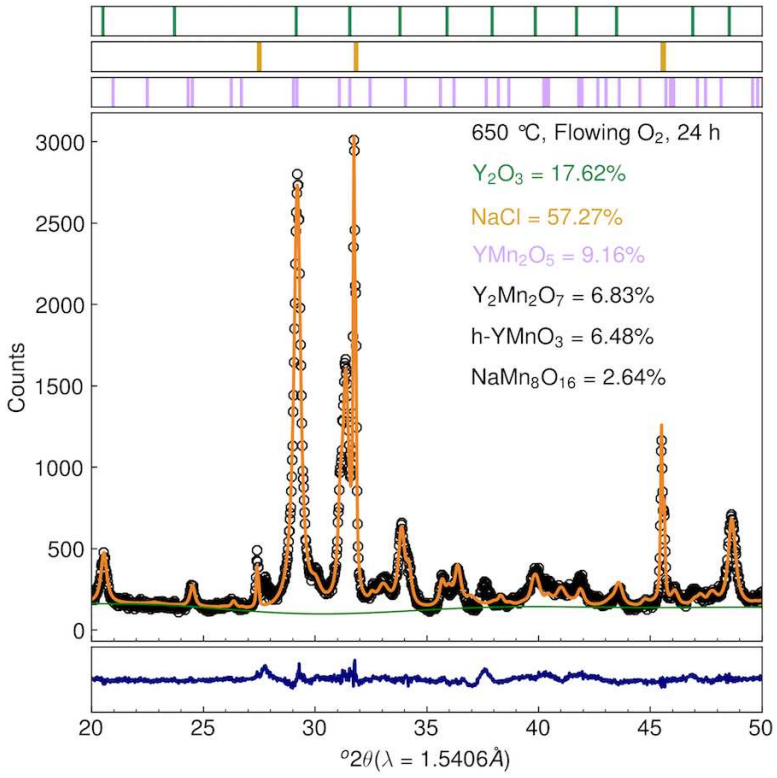


Figure A.20: PXRD results from the reaction: $C2/m$ $NaMnO_2 + YOCl \xrightarrow{O_2}$. The reaction was performed by heating at 10 °C/min to 650 °C and dwelling for 24 h. Raw data: black circles, Rietveld refinement: orange, background: green, difference: navy. Tick marks denote the majority phases and are highlighted by color and mole percent as calculated from Rietveld refinements. All other product mole percents are highlighted in black without tick marks.

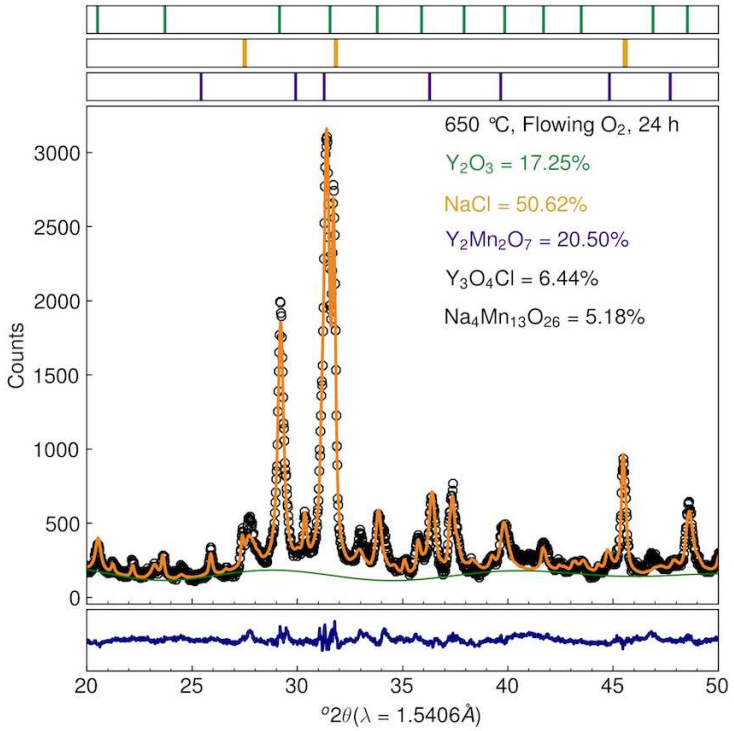


Figure A.21: PXRD results from the reaction: $Cmcm$ $Na_{0.7}MnO_2 + YOCl \xrightarrow{O_2}$. The reaction was performed by heating at 10 ℃/min to 650 ℃ and dwelling for 24 h. Raw data: black circles, Rietveld refinement: orange, background: green, difference: navy. Tick marks denote the majority phases and are highlighted by color and mole percent as calculated from Rietveld refinements. All other product mole percents are highlighted in black without tick marks.

A.2. Thermochemical Calculations

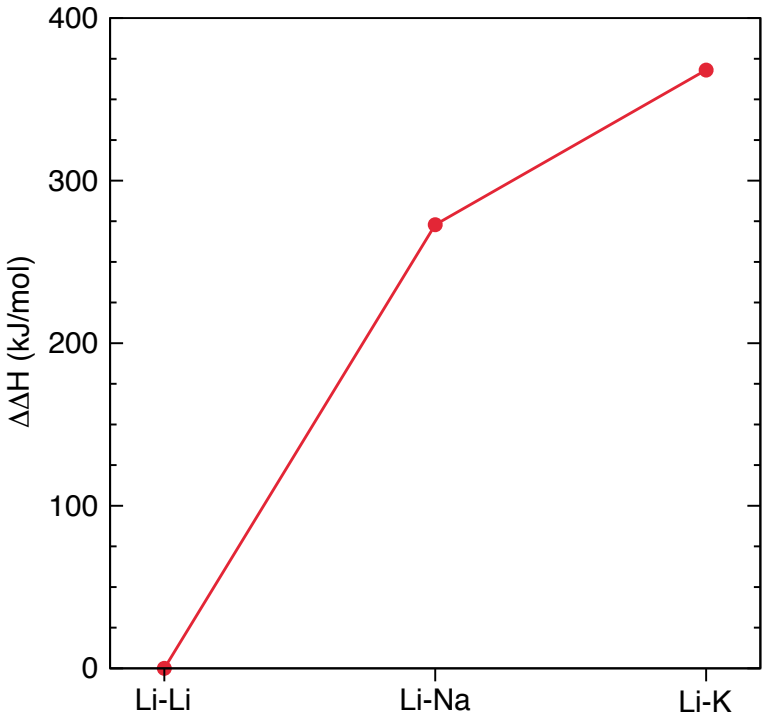


Figure A.22: Calculated difference in reaction enthalpies ($\Delta\Delta H$) when changing the alkali carbonate precursor in the reaction: $3\,A_2CO_3 + 2\,YCl_3 + Mn_2O_3 \longrightarrow 6\,ACl + 2\,YMnO_3 + 3\,CO_2$.The difference is taken with respect to Li_2CO_3 assisted reactions. As the size of the alkali cation increases from lithium to potassium, the reaction enthalpy becomes more exothermic.

Several predominance phase diagrams were created using DFT thermochemistry data on the Materials Project[1] and the NIST-JANAF thermochemical tables.[2] These diagrams are shown in Figures A.23 and A.24. For each figure, the temperature contribution towards phase stability at 900 K is estimated by the Gibbs descriptor from Bartel et al.[3] Both diagrams indicate a very narrow range of chemical potentials where $Y_2Mn_2O_7$ is predicted to be stable. These stability windows correspond to relatively high oxygen chemical potential and low manganese/yttrium chemical potentials.

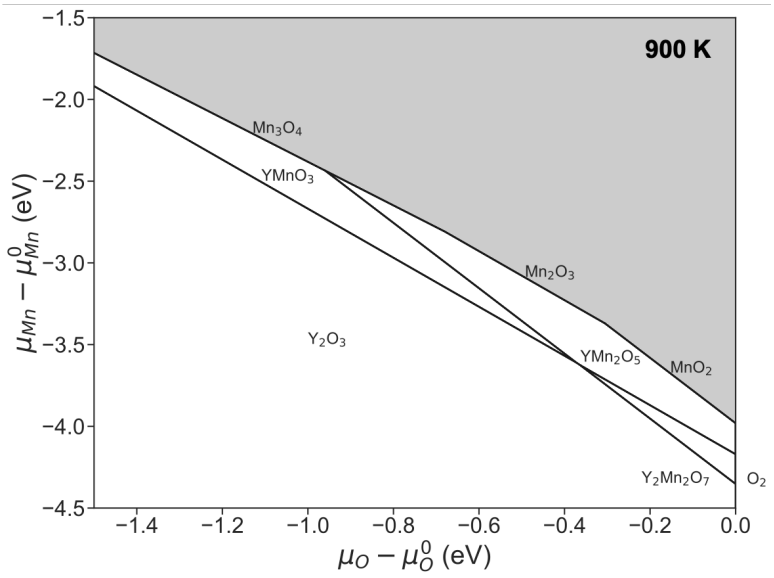


Figure A.23: Predominance phase diagram for material phases in the Y-Mn-O chemical system as a function of oxygen and manganese chemical potentials, μ_O and μ_{Mn}.

Table A.4: Original $YMnO_3$ structures acquired from the Materials Project database

Name	**Spacegroup**	***mpid***	**Energy above hull (eV/atom)**	**Num. atoms**
h-$YMnO_3$	$P6_3cm$	mp-19385	0	30
h-$YMnO_3$	$P6_3/mmc$	mp-19227	0.021	10
o-$YMnO_3$	$Pnma$	mp-20699	0.023	20

The original structures for the $YMnO_3$ polymorphs were acquired from the Materials Project (MP) database.[1] Their properties are shown in Table A.4.

Figure A.25 shows Gibbs free energies, $G(P,T)$, and heat capacities, $c_p(T)$ calculated with quasiharmonic approximation (QHA) for each of the $YMnO_3$ structures. Figure A.26 shows the underestimation of $c_p(T)$ for the h-$YMnO_3$ ($P6_3cm$) which we hypothesize is due to the lack of inclusion of phonon anharmonic effects.

Vacancy formation energies were calculated using the charged defect supercell approach. For each polymorph, we considered Y vacancy charge states ranging from [-4,4] and Mn vacancy charge states ranging from [-7,7]. Corrections to the defect energies were

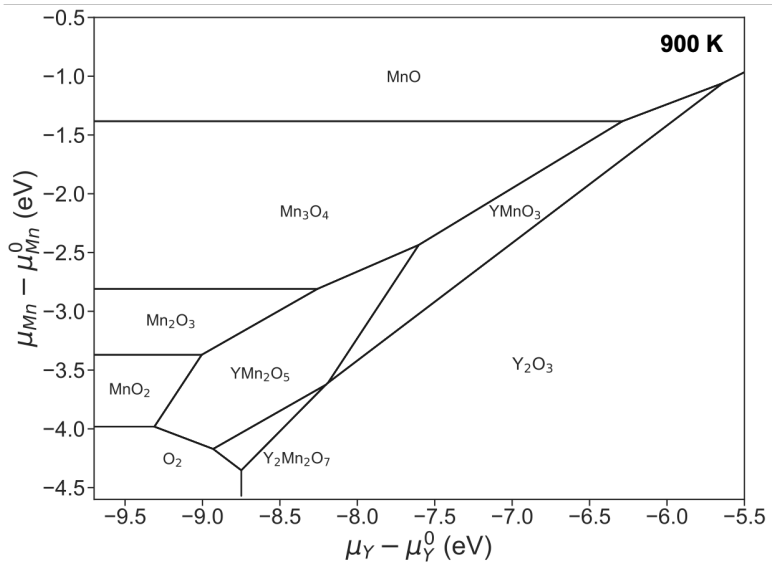


Figure A.24: Predominance phase diagram for material phases in the Y-Mn-O chemical system as a function of manganese and yttrium chemical potentials, μ_{Mn} and μ_Y.

Structure	**Mag. config.**	**Supercell**	**atoms**	**HSE band gap (eV)**	**GGA band gap (eV)**
$YMnO_3$ ($P6_3cm$)	AFM	2x2x1	120	2.38	1.15
$YMnO_3$ ($P6_3/mmc$)	AFM	4x2x1	160	2.1	1.21
ceYMnO3 ($Pnma$)	AFM	2x2x2	160	2.57	1.34

Table A.5: Summary of defect supercells and comparison of the band gaps acquired using the HSE and GGA functionals

made using the band gap of each polymorph calculated with hybrid functional HSE06 and the dielectric tensor; we used the finite-size charge correction from Freysoldt et al.[154] and band edge shifting correction. A summary of the defect calculations is shown in Table A.5.

The defect phase diagrams showing vacancy formation energy as a function of Fermi energy for each polymorph are shown in Figure A.27. Figure A.27(a) is constructed using chemical potentials from the $YMnO_3$-MnO-Y_2O_3 simplex on the Y-Mn-O phase diagram, and Figure A.27(b) using chemical potentials from the $YMnO_3$-YMn_2O_5-Y_2O_3 simplex. The change in chemical potentials simply shifts the vertical position of the defect formation

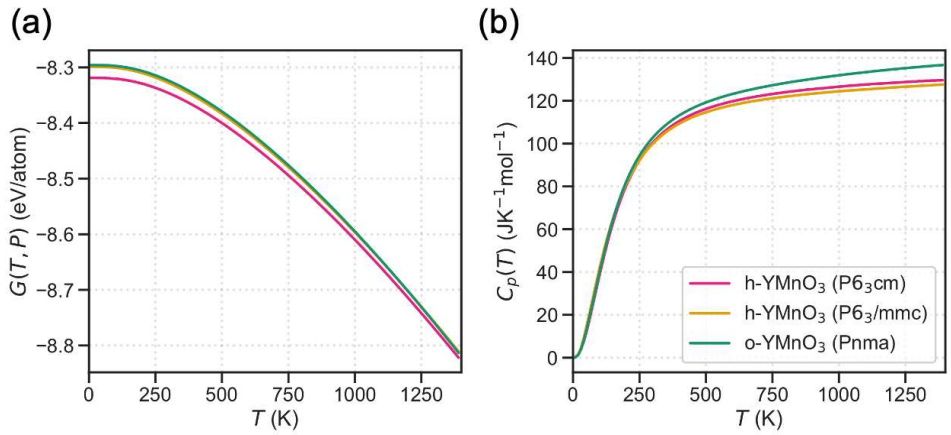


Figure A.25: Gibbs free energies and heat capacities as a function of temperature for $YMnO_3$ polymorphs

Table A.6: Reaction temperatures for m-$LiMnO_2$ X-ray diffraction data in Figure 5.1

Phase	Onset Temp (°C)	Reaction Temp (°C)	Other Notes
m-$LiMnO_2$	–	570	–
YOCl	–	443	–
r−YOCl	–	514	–
t-Mn_3O_4	≤266	690	Plateau T: 415-614 °C
c-$LiMn_2O_4$	≤266	772	Plateau T: 369-644 °C
Y_3O_4Cl	≤266	690	Plateau T: 448-592 °C
h−$YMnO_3$	570	–	Plateau T: 719 °C
o−$YMnO_3$	644	–	Plateau T: 719 °C

energy curves, and hence has no impact on the phase diagram created in Figures 5.7 and A.28.

Finally, the $YMnO_3$ phase diagram is re-plotted in Figure A.28 to show the spread of the phase boundary with different values of Fermi energy, E_F. All Fermi energies lie within the GGA band gaps of all structures considered. Note that the phase boundary shifts rightward towards higher values of vacancy concentration as E_F decreases.

A.3. Ternary Metathesis Control Reactions

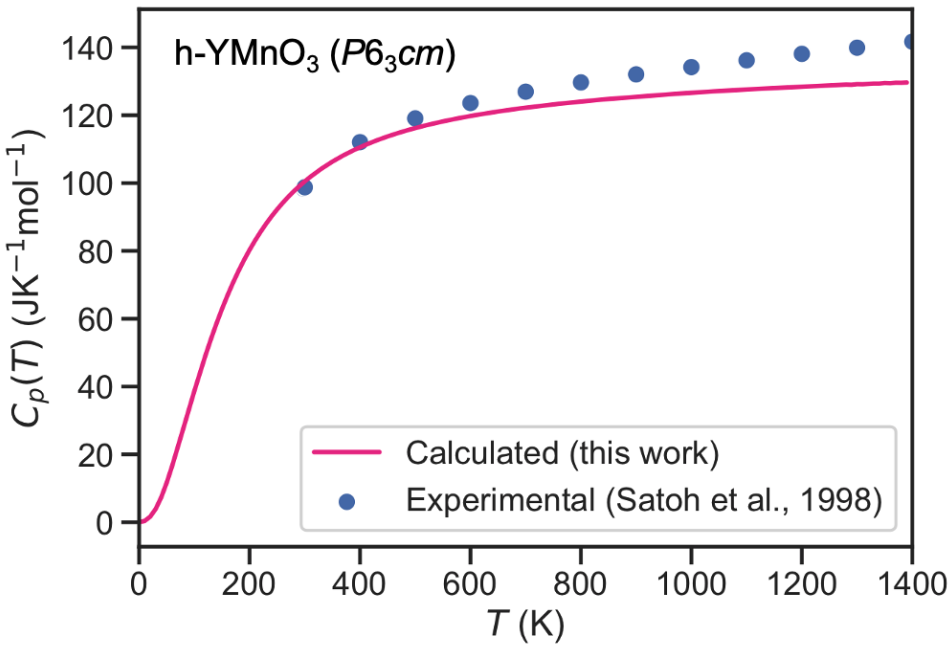


Figure A.26: Comparison of calculated and experimental heat capacities for h-$YMnO_3$ ($P6_3cm$). Experimental heat capacity data is acquired from Satoh et al.[4]

Table A.7: Reaction temperatures for o-$LiMnO_2$ X-ray diffraction data in Figure 5.1

Phase	Onset Temp (°C)	Reaction Temp (°C)	Other Notes
o-$LiMnO_2$	–	668	–
YOCl	–	495	–
r−YOCl	388	570	–
t-Mn_3O_4	443	606	–
c-$LiMn_2O_4$	368	664	Plateau T: 495-592°C
Y_3O_4Cl	388	668	Plateau T: 514-606 °C
h−$YMnO_3$	570	–	Plateau T: 690 °C
o−$YMnO_3$	644	–	Plateau T: 690 °C

Table A.8: Reaction temperatures for t-$LiMnO_2$ X-ray diffraction data in Figure 5.1

Phase	Onset Temp (°C)	Reaction Temp (°C)	Other Notes
t-$LiMnO_2$	–	392	–
YOCl	–	392	–
r−YOCl	–	563	Plateau T: 336-526°C
c-$LiMn_2O_4$	276	631	Plateau T: 465-546°C
t-Mn_3O_4	290	452	–
Y_3O_4Cl	355	583	Plateau T: 417-563°C
h−$YMnO_3$	563	–	–
o−$YMnO_3$	563	–	Plateau T: 642°C

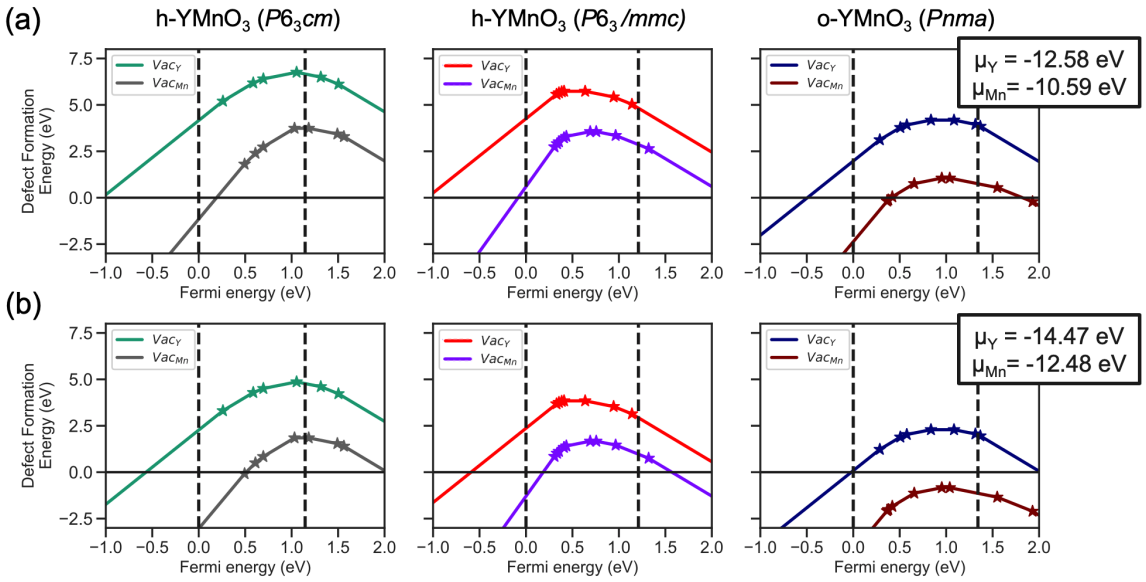


Figure A.27: Y, Mn vacancy formation energies as a function of Fermi energy for $YMnO_3$ polymorphs for different chemical potentials, μ_Y and μ_{Mn}. The dashed lines represent the valence band maximum (VBM) and conduction band minimum (CBM). (a) The upper bounds, and (b) the lower bounds, of the window of chemical potential stability of $YMnO_3$ as determined by simplexes in the Y-Mn-O phase diagram (0 K) constructed from the MP database.

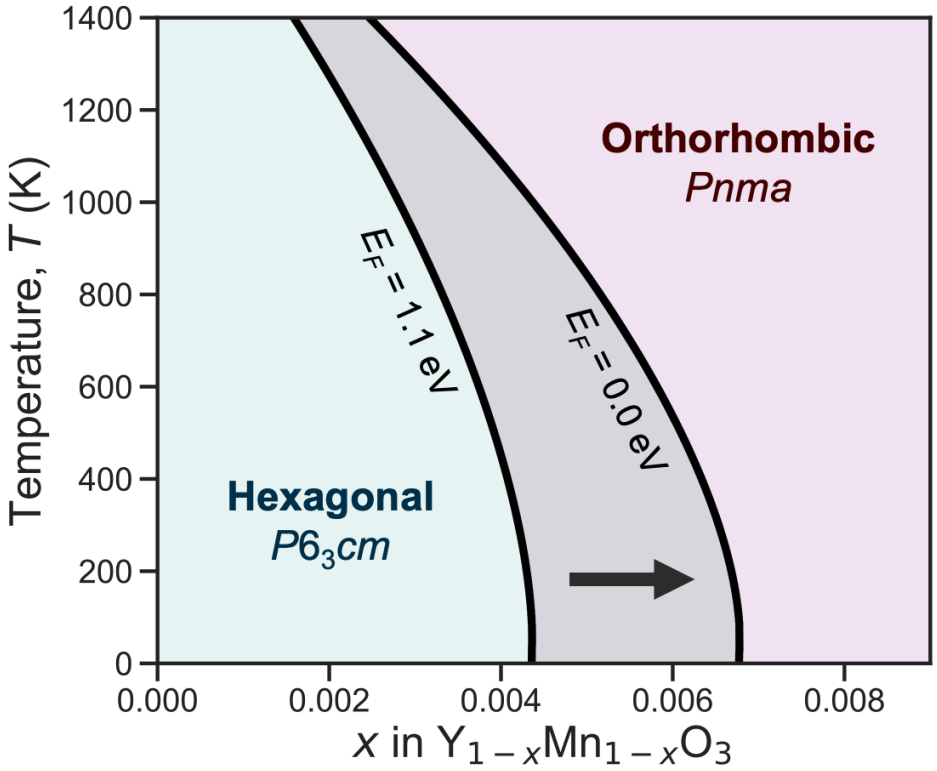


Figure A.28: Calculated phase stability of $YMnO_3$ polymorphs with respect to temperature and an equal concentration of cation (Y,Mn) vacancies, x. The phase diagram is constructed for all values of Fermi energy, E_F, within the band gap to show how the sensitivity of the phase boundary position with E_F.

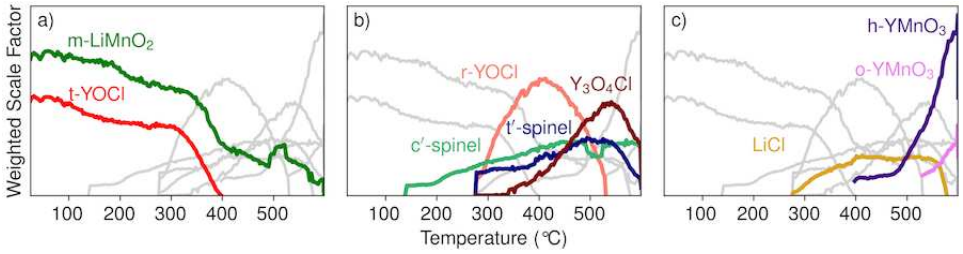


Figure A.29: Quantitative phase analysis of crystalline materials calculated from synchrotron X-ray diffraction experiments of the ternary metathesis reaction $LiMnO_2 + YOCl \longrightarrow YMnO_3 + LiCl$ when starting from monoclinic ($C2/m$) $LiMnO_2$. Reactions were heated at 10 °C/min to 600 °C. Each row of subpanels presents a) precursors, b) intermediates, and c) products as calculated from Rietveld analysis.

The relative amount of the two spinel intermediates provides a metric to analyze the progress of the reaction pathway in this intermediate temperature regime (e.g., how much lithium chloride had formed). In the SXRD results in Figure 5.1, the weight percent of c′-spinel was greater than t′-spinel for all polymorphs, whereas in the neutron diffraction experiments (Fig. A.30), the fraction of t′-spinel was higher. As the NPD was collected *in situ*,the reaction had progressed XX hours upon reaching 500 °C, whereas the SXRD results reflect a one hour reaction for each temperature due to collection across a temperature gradient *ex post facto*. Thus, the greater weight fraction of t′-spinel in the NPD patterns supoorts a reaction pathway where more lithium has been removed from the spinel intermediates and thus, the weight percent of Mn_3O_4 increases.

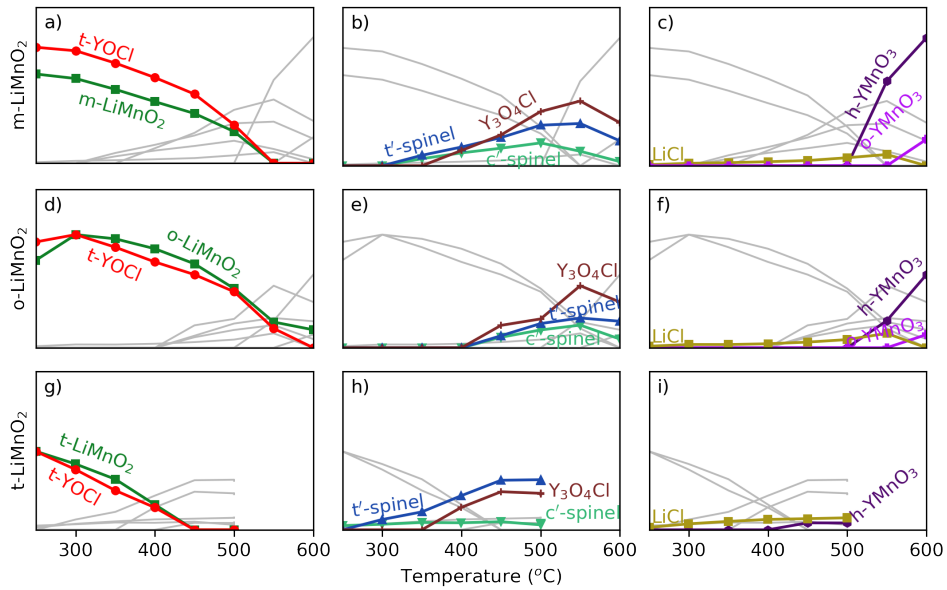


Figure A.30: Weighted scale factor of crystalline materials from neutron refinement at different reaction temperatures reveals the reaction pathway of the ternary metathesis reaction, $LiMnO_2 + YOCl \longrightarrow LiCl + YMnO_3$. Each row of subpanels is from a single precursor: (a-c) monoclinic ($C2/m$), (d-f) orthorhombic ($Pmnm$) and(g-i) tetragonal [($I4_1/amd$)]. Each column highlights phase fractions containing a specific cation to provide clarity with many overlapping phases: (a,d,g) Lithium, (b,e,h) Manganese, (c,f,i) Yttrium.

Table A.9: Reaction temperatures for m-$LiMnO_2$ neutron diffraction data

Phase	Onset Temperature	Reaction Temperature	Other Notes
m-$LiMnO_2$	–	550 °C	–
t-YOCl	–	550 °C	–
LiCl	≤250 °C	600 °C	–
t-$LiMn_2O_4$	350 °C	–	Peak T: 550 °C
c-$LiMn_2O_4$	350 °C	–	Peak T: 500 °C
Y_3O_4Cl	400 °C	–	Peak T: 550 °C
h-$YMnO_3$	550 °C	–	–
o-$YMnO_3$	600 °C	–	–

Table A.10: Reaction temperatures for o-$LiMnO_2$ neutron diffraction data

Phase	Onset Temperature	Reaction Temperature	Other Notes
o-$LiMnO_2$	–	–	–
t-YOCl	–	600 °C	–
LiCl	≤250 °C	600 °C	–
t-$LiMn_2O_4$	450 °C	–	Peak T: 550 °C
c-$LiMn_2O_4$	450 °C	–	–
Y_3O_4Cl	450 °C	–	Peak T: 550 °C
h-$YMnO_3$	550 °C	–	–
o-$YMnO_3$	600 °C	–	–

Table A.11: Reaction temperatures for t-$LiMnO_2$ neutron diffraction data

Phase	Onset Temperature	Reaction Temperature	Other Notes
t-$LiMnO_2$	–	450 °C	–
t-YOCl	–	450 °C	–
LiCl	150 °C	–	–
t-$LiMn_2O_4$	300 °C	–	–
c-$LiMn_2O_4$	400 °C	–	–
Y_3O_4Cl	400 °C	–	Peak T: 450 °C
$LiMn_2O_4$ impurity	–	–	No peak change over T range

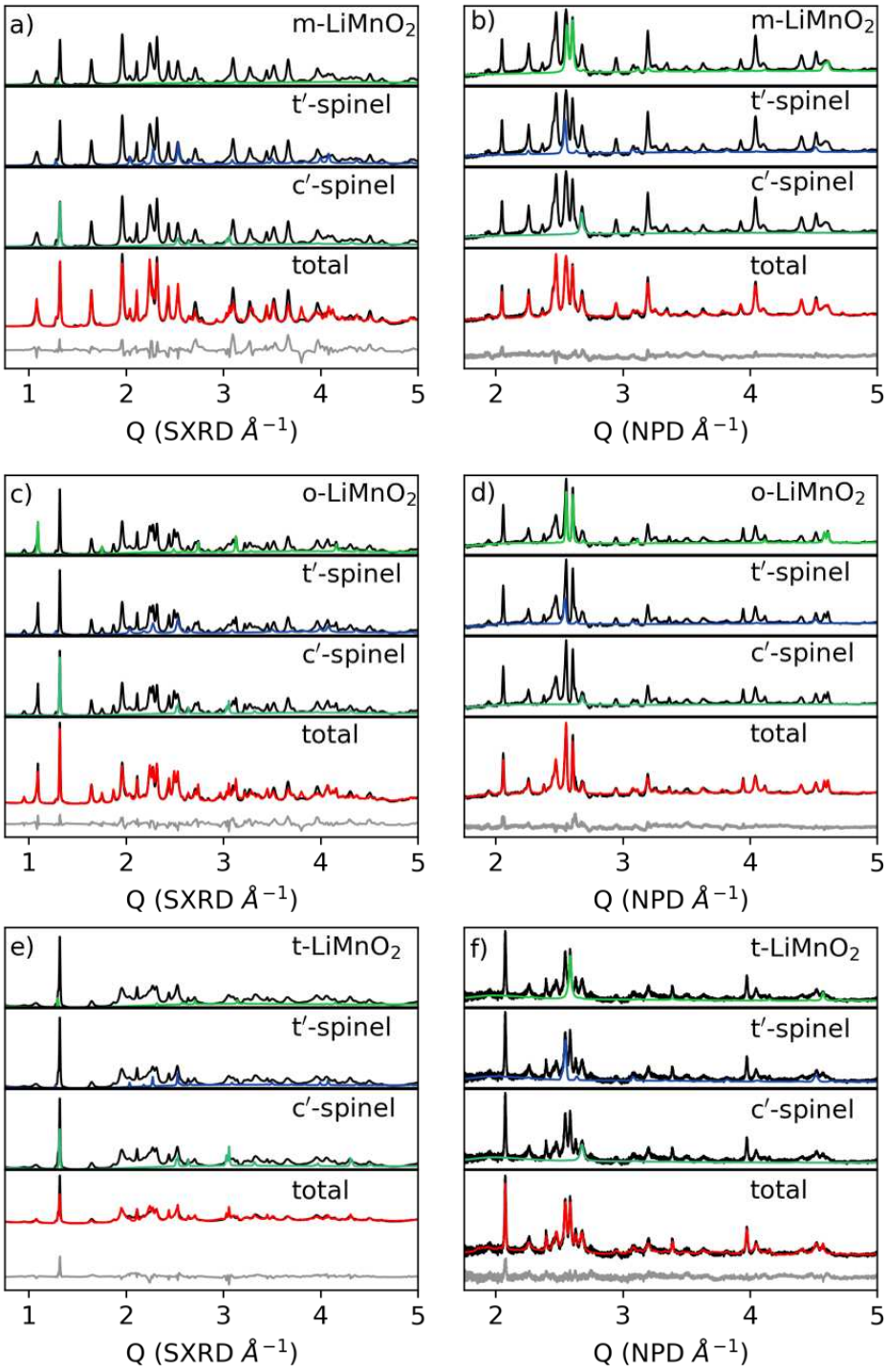


Figure A.31: The contributions of the manganese containing phases $LiMnO_2$(top), t′-spinel (second from top), and c′-spinel (third from top) are overlayed on the pattern. The overall fit (bottom) also contains t-YOCl, r-YOCl, Y_3O_4Cl and LiCl (red) along with a difference pattern (gray) for reactions of o-$LiMnO_2$ (SXRD (a), NPD (b)),m-$LiMnO_2$ (SXRD (c), NPD (d)), and t-$LiMnO_2$ (SXRD (e), NPD (f)).

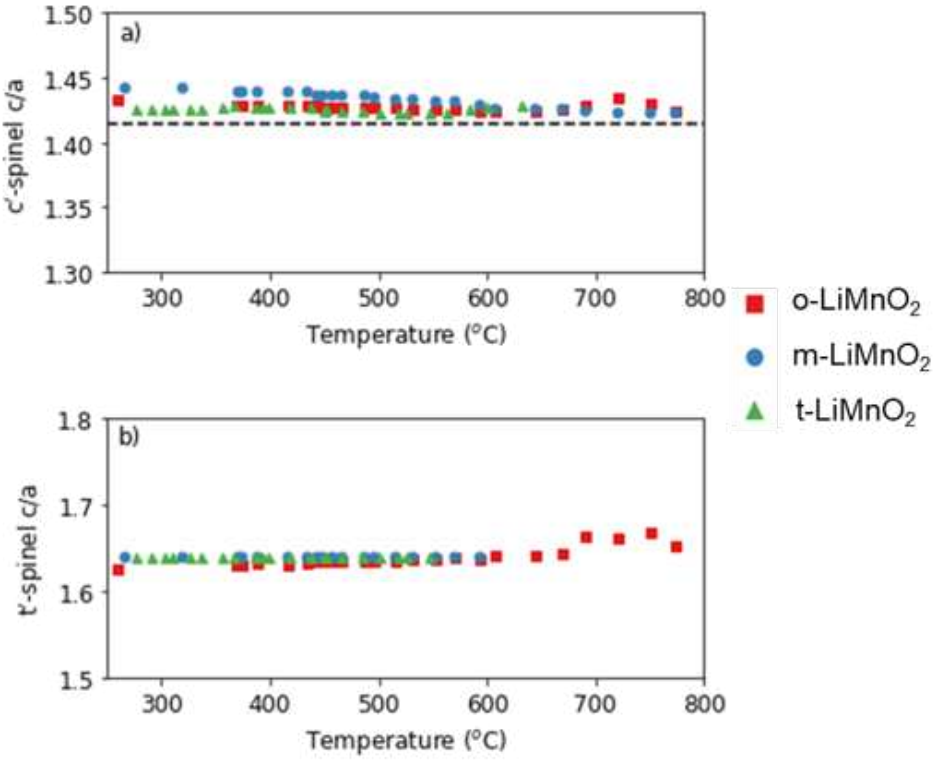


Figure A.32: Ratio of the c and a lattice parameters for (a) c′-spinel and (b) t′-spinel from X-ray diffraction patterns used in Figure 5.1. Data points are separated by $LiMnO_2$ precursor: o-$LiMnO_2$ (red squares), m-$LiMnO_2$ (blue circles) and t-$LiMnO_2$ (green triangles).

A.4. Binary Metathesis Control Reactions

Table A.12: Occupancies for m-$LiMnO_2$ neutron diffraction data

T (°C)	Li occ	Error	Mn occ	Error	O occ	Error	R_{wp}
35	0.931	0.049	1.181	0.029	0.961	0.008	6.620
250	0.845	0.055	1.118	0.030	0.980	0.009	6.044
300	0.718	0.055	1.108	0.030	0.996	0.009	6.273
350	0.709	0.052	1.117	0.031	0.963	0.012	5.657

Table A.13: Occupancies for o-$LiMnO_2$ neutron diffraction data

T (°C)	Li occ	Error	Mn occ	Error	O1 occ	Error	O2 occ	Error	R_{wp}
40	1.137	0.070	1.086	0.033	1.004	0.024	1.069	0.024	8.545
250	1.144	0.051	1.106	0.044	1.021	0.018	0.991	0.018	7.724
300	1.094	0.045	0.937	0.045	0.917	0.016	0.925	0.016	6.578
350	1.026	0.045	0.946	0.042	0.919	0.016	0.921	0.016	5.970
400	0.958	0.051	0.952	0.047	0.931	0.018	0.908	0.019	6.061

Table A.14: Occupancies for t-$LiMnO_2$ neutron diffraction data

T (°C)	Li occ	Error	Mn occ	Error	O occ	Error	R_{wp}
35	0.960	0.046	1.175	0.024	1.030	0.005	3.475
100	1.016	0.039	1.127	0.020	1.019	0.004	4.806
150	0.960	0.037	1.069	0.019	0.986	0.004	3.042
200	0.855	0.034	1.158	0.018	1.007	0.004	3.813

Table A.15: Properties of select organosilane molecules

Name	Formula	Physical Properties	Chemical Properties
Hexaphenyldisiloxane	$(C_6H_5)_6Si_2O$	MP: 224°C Density: 1.20g/cm^3	Weak Lewis Base[177,190] Si−O−Si functional group[172,173] Ferrosiloxanes ($(R_3SiO)_3Fe$)[179]
Triphenylsilanol	$(C_6H_5)_3SiOH$	MP: 150-153°C	Weak Lewis Acid[191] Precursor to silicone[192] hydrogen bonding[193]
Triphenylsilyl chloride	$(C_6H_5)_3SiCl$	MP: 91-94°C	Nucleophilic substitution[194] Precursor: thiosilanes[177,178] Hydrolysis to silanols[191,193]

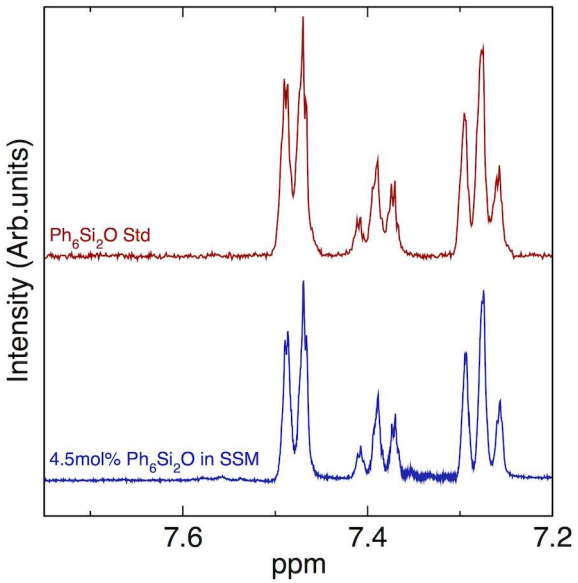


Figure A.33: ^{1}H NMR spectra of the phenyl region in the $(C_6H_5)_6Si_2O$ standard and a wash from the metathesis reaction $Na_2S_2 + FeCl_2$ with 4.5mol% $(C_6H_5)_6Si_2O$. Deuterated methylene chloride (CD_2Cl_2) was used as the solvent

^{1}H NMR studies of the reaction products in deuterated methylene chloride, reveal that the $(C_6H_5)_3SiOH$ polymerizes/decomposes upon heating (Fig. 6.5(a)). Physically, the reaction product mixture becomes difficult to mix, as it contains a viscous silicone-like polymer, even when prepared in the glovebox. ^{1}H NMR spectra of the 13mol% $(C_6H_5)_3SiOH$ assisted metathesis reaction support the polymerization of the $(C_6H_5)_3SiOH$, as there is a sharp benzene signal at 7.36 ppm and multiple unique phenyl environments (Fig. 6.5(a)).[195] This polymerization reaction can be described in the following condensation reaction:

$$2\,(C_6H_5)_3SiOH \longrightarrow H_2O + (C_6H_5)_6Si_2O \tag{A.1a}$$

$$(C_6H_5)_3SiOH + H_2O \longrightarrow C_6H_6 + (C_6H_5)_2Si(OH)_2 \tag{A.1b}$$

$$2\,(C_6H_5)_3SiOH + n(C_6H_5)_2Si(OH)_2 \longrightarrow (C_6H_5)_3SiO{-}[(C_6H_5)_2SiO]_n{-}Si(C_6H_5)_3 \tag{A.1c}$$

where the water produced in the self-condensation reaction acts as a nucleophile and proton donor to form the diphenylsilanediol and benzene. In Eqn. A.1c, $(C_6H_5)_2Si(OH)_2$ is highly unstable and will ultimately react to form higher order siloxanes and silicone polymers as observed previously.[196,197] Self-heating of the $(C_6H_5)_3SiOH$ at 150°C for 24hr reveals a similar result, as the reaction produces a viscous liquid upon cooling and the ^1H NMR spectrum shows the presence of benzene and multiple phenyl environments (Fig. 6.5(a)). Interestingly, if the $(C_6H_5)_3SiOH$ is stoichiometrically mixed and pelleted with Na_2S_2, a downfield shift of the phenyl protons occurs (Fig. 6.5(b)) that matches $(C_6H_5)_6Si_2O$. Na_2S_2 is unstable under ambient conditions, as the salt is hygroscopic, so intuition suggests that the Na_2S_2 acts as a water scavenger after the $(C_6H_5)_3SiOH$ has dimerized, thus preventing the nucleophilic attack of water on silicon in the polymerization step (Eqn. A.1c). Interestingly, $FeCl_2$ does not prevent polymerization (Fig. 6.5(b)), although small intensity peaks are present of some $(C_6H_5)_6Si_2O$. On the other hand, when using $(C_6H_5)_6Si_2O$ in the metathesis reaction, the molecule retains the same phenyl environment as a $(C_6H_5)_6Si_2O$ standard (Fig. A.33). In order for the $(C_6H_5)_3SiOH$ to polymerize, there has to be H_2O present in the reaction mixture, so the self-condensation reaction (Eqn. A.1a) must occur first. Thus, both reactions support the hypothesis that pyrite formation is dependent on the identity of the molecule hexaphenyldisiloxane.

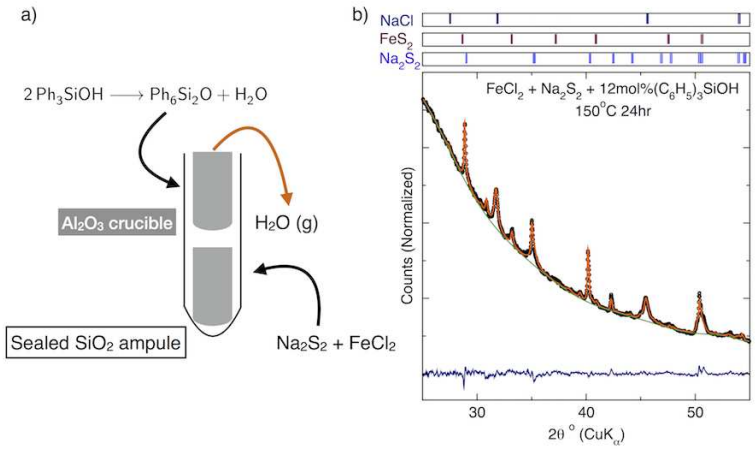


Figure A.34: Vapor transport reaction to test the effect of water vapor from the decomposition/polymerization of $(C_6H_5)_3SiOH$ on the metathesis reaction: $Na_2S_2 + FeCl_2 \longrightarrow FeS_2 + 2\,NaCl$. a) Experimental set-up showing the separation of each reaction physically in a sealed ampule. b) PXRD pattern of reaction products performed under polyimide tape.

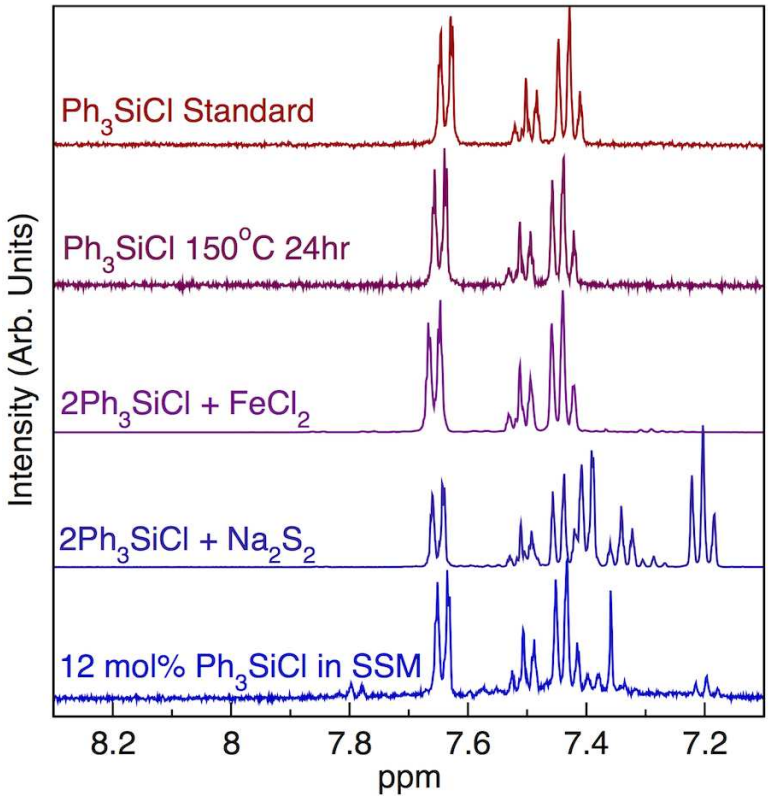


Figure A.35: Differential Scanning Calorimetry results from the reaction $Na_2S_2 + FeCl_2$ with (a) no additive and (b) 4.5mol% $(C_6H_5)_6Si_2O$. Heating rate was changed from 1 °C/min to 10 °C/min.